

Doctoral Thesis
at the
Medical University of Vienna
within the scope of the
"Doctor of Medical Science"
(**"Doktor der Medizinischen Wissenschaft"**)

**Functional Electrical Stimulation
of the Central Nervous System:
Analysis of the Primarily Excited Structures**

by
Dipl.-Ing. Dr. Dr. Frank Rattay

Supervisor:

**Ao. Univ. Prof. Dipl.-Ing. Dr. Winfried Mayr
Center of Biomedical Engineering and Physics**

Vienna, July 2005

Table of Contents

Abstract	4
Kurzfassung	5
Summary	6
1. Introduction	9
<i>Internal cell stimulation by current injection</i>	10
<i>External cell stimulation</i>	12
<i>Models for the cell membrane</i>	13
<i>Axon models of the Hodgkin-Huxley type</i>	14
<i>Influence of temperature</i>	18
2. The activating function concept for CNS neurons	20
<i>Compartment model of an externally stimulated neuron</i>	20
<i>The activating function</i>	21
<i>From which part of a neuron does artificial excitation start?</i>	22
<i>Excitation by a constant field</i>	27
<i>Case study on the human cochlear nerve</i>	28
<i>Discussion</i>	30
<i>Conclusions</i>	31
3. A model of the electrically excited human cochlear neuron	
Part I. Contribution of neural substructures to the generation and propagation of spikes	34
Introduction	34
Material and Methods	36
<i>Morphometry</i>	36
<i>Compartment model</i>	37
<i>Current fluctuations in the active membrane compartments</i>	40
Results	41
<i>Somatic delay</i>	41
<i>Influence of ion channel current fluctuations</i>	42
<i>Excitation in the peripheral and central axons</i>	43
<i>Man versus cat</i>	47
<i>Biphasic pulses, pulse trains</i>	49
Discussion	55
The point of spike generation as predicted by the activating function	58
4. A model of the electrically excited human cochlear neuron	
Part II. Influence of the 3-dimensional cochlear structure on neural excitability	62
Introduction	62
A geometrically simplified model of the human cochlea	64
Calculation of the electric field	66
Results	68
<i>Excitation of the most excitable neuron</i>	68
<i>Excitation of neurons 3-15, monopolar, bipolar and quadrupolar stimulation</i>	71

<i>Excitation of degenerated neurons</i>	77
Discussion	77
5. Effective electrode configuration for selective stimulation with inner eye prostheses	82
Introduction	82
Material and Methods	84
<i>The Fohlmeister - Coleman - Miller (FCM) model</i>	85
Results	87
<i>Avoiding co-stimulation of by-passing axons</i>	87
<i>Influence of dipole distances on axonal excitability</i>	91
<i>Comparison of bipolar and ganglion cell responses</i>	93
Discussion	94
6. Neuromodeling and the human spinal cord motor control: Neural responses to epidural stimulation	96
Introduction	96
Material and Methods	96
Results	98
<i>Biphasic stimulation</i>	105
Discussion	106
<i>Relationship between fiber thresholds and muscle twitch responses</i>	107
<i>Factors limiting the accuracy of the simulations</i>	110
Conclusions	110
References	113

Abstract

Objectives. Individual electric and geometric characteristics of neural substructures have often surprising effects on artificially controlled neural signaling. Rules of thumb approved for the stimulation of long peripheral axons may not hold when the central nervous system is primarily stimulated. This is demonstrated comparing theoretical results with animal experiments and patient data with a focus on cases of the electrically stimulated cochlea, the retina and the lumbar spinal cord.

Methods. A generalized form of the activating function together with accurate modeling of the neural membrane dynamics are the tools to analyze the excitation mechanisms initiated by neural prostheses. Sometimes analysis is possible with a linear theory, in other cases simulation of internal calcium concentration or ion channel current fluctuations is needed to observe irregularities in spike trains. Many of the presented results are based on a two step procedure: (i) calculation of the electric field with finite elements or analytically for an infinite homogeneous medium approach and (ii) simulation of a target neuron response with a compartment model where every 'active' compartment is simulated with ion channel gating mechanisms of the Hodgkin - Huxley type.

Results. A set of 12 spike initiation rules is deduced by analyzing several model neurons under stimulating conditions relevant for neural prostheses. Moreover, for a cochlear implant it is shown that spike initiation site can easily change within a single target neuron even under constant stimulation conditions and this way irregularities in the temporal pattern are expected which deteriorate, e.g., speech understanding. Poor myelinisation in the soma region that is unique for the bipolar human cochlear neurons causes firing characteristics differing from any animal recordings. Retinal ganglion cells also will generate propagating spikes within the dendritic tree. Bipolar cells in the retina are expected to respond with neurotransmitter release, before a spike is generated in the ganglion cell even when they are rather far away from the electrode. A new method for focal retina stimulation is presented. Furthermore, it is shown that epidural stimulation of the human lumbar spinal cord predominantly stimulates large sensory axons in the dorsal roots which induce muscle reflex responses, but there are no neural structures within the spinal cord that are directly stimulated.

Conclusions. Presently neuroprostheses uses few active contacts and generate spiking patterns much more synchronized and with reduced information content in comparison to the natural ones. The successful operation of such devices is possible by the robustness and plasticity of the nervous system.

Kurzfassung

Ziele. Die besonderen elektrischen und geometrischen Charakteristika neuronaler Substrukturen führen oft zu überraschenden Effekten wenn Nervensignale künstlich gesteuert werden sollen. Anerkannte Daumenregeln zur Stimulation langer peripherer Axone halten nicht mehr sobald die Stimulation im Zentralnervensystem erfolgt. Das wird durch einen Vergleich theoretischer Ergebnisse mit Tierexperimenten und Patientendaten dargestellt, besonders im Hinblick auf Fallstudien der elektrisch stimulierten Cochlea, der Retina und des lumbalen Rückenmarks.

Methoden. Eine verallgemeinerte Form der Aktivierungsfunktion zusammen mit einer genaueren Simulation der elektrischen Nervenzellmembrandynamik wird eingesetzt, um den von Neuroprothesen ausgelösten Erregungsmechanismus zu analysieren. Manchmal ist diese Analyse schon mittels einer linearen Theorie möglich, in anderen Fällen müssen etwa intrazelluläre Kalziumkonzentration oder stochastische Fluktuationen der Ionenkanalströme miteinbezogen werden, um Irregularitäten in den Zeitreihen der Feuerungen zu verstehen. Viele der präsentierten Resultate basieren auf einem zweistufigen Verfahren: (i) Berechnung des elektrischen Feldes mit Finiten Element-Methoden oder durch eine analytische Darstellung unter der Annahme eines unendlich großen homogenen Mediums und (ii) Antwort eines ausgewählten Neurons, das als Kompartimentmodell simuliert wird, wobei in jedem aktiven Kompartiment die Ionenkanaldynamik nach einem Modell vom Hodgkin - Huxley Typ beschrieben wird.

Resultate. Ein Satz von 12 Regeln zur Nervenimpulsentstehung wird durch Analyse einiger Modellneurone hergeleitet, und zwar für Stimulationsbedingungen, die für Neuroprothesen relevant sind. Außerdem wird für ein Cochleaimplantat gezeigt, dass auch unter konstanten Stimulationsbedingungen der Ort der Aktionspotentialbildung innerhalb einer Nervenzelle leicht wechseln kann, was wegen der damit verbunden Laufzeitänderungen zur Störung des neuronalen Zeitmusters führt, sodass es damit zu einer Verschlechterung z. B. des Sprachverständnisses kommt. Der einzigartige minimale Myelinisierungsgrad in der Somaregion der bipolaren menschlichen Cochlearneurone bewirkt Feuerungscharakteristika, die bei Tierversuchen nicht beobachtet werden können. In Ganglionzellen der Retina können auch dendritische Aktionspotentiale ausgelöst werden. In bipolaren Zellen der Retina werden Neurotransmitterausschüttungen erwartet bevor durch die Elektrostimulation in Ganglionzellen eine Nervenaktivierung einsetzt, auch wenn die Bipolarzellen weiter von der Elektrode entfernt sind. Eine neue Methode zur Fokalstimulation von Retinabereichen wird präsentiert. Außerdem wird gezeigt, dass im Menschen bei der üblichen epiduralen Stimulation des lumbalen Rückenmarks zuerst die dicksten sensiblen Fasern der dorsalen Bündel antworten und dadurch Muskelzuckungen ausgelöst werden und dass primär keine Strukturen innerhalb des Rückenmarks stimuliert werden.

Schlussfolgerungen. Derzeit nützen Neuroprothesen nur wenige aktive Kontakte und erzeugen damit im Vergleich zur natürlichen Situation viel stärker synchronisierte Nervensignale mit geringem Informationsgehalt. Die trotzdem einigermaßen erfolgreiche klinische Elektrostimulation beruht somit teilweise auf der Robustheit und Plastizität des Nervensystems.

Summary

The presented work is supposed to close a gap in understanding electrophysiological phenomena important for modern neuroprostheses. The direct excitatory influence in electrical CNS stimulation is analyzed with a linear and a nonlinear modeling approach. Both methods are based on an electrical network model of a target neuron that simulates the membrane voltage in every neural substructure as answer to the applied field. The presented theory and computer simulations demonstrate how the site of spike initiation depend (i) on the applied electric field, (ii) the geometry of the neuron and (iii) the voltage sensitive ion channel dynamics of the cell membrane.

A first approach of the relation between the electric field and the cell geometry results from the activating function concept. The activating function f , introduced 1986 by Rattay for long nerve and muscle fibers, identifies with $f > 0$ the primarily excited regions and with $f < 0$ the hyperpolarized regions. A generalized form of this activating function that is applicable for arbitrary cell geometry is described in Chapter 2 and the following conclusions of the theory are deduced:

1. The myelinated axon is the most excitable part of a neuron.
2. In neurons with myelinated axons the soma is difficult to stimulate.
3. Excitation with electrodes in the vicinity of the axon is up to 4.2 times easier with negative currents compared to positive stimuli.
4. The relation between positive and negative threshold current varies extremely, and it strongly depends on electrode position and on the neuron's parameters.
5. The maximum value of the activating function is a good indicator for finding the most excitable compartment.
6. Generally, excitation is easier with negative currents. However, this does not hold for (all) electrode positions within the dendritic region. Positive currents from electrodes positioned in front of the dendritic tree will generate spikes at the beginning of the axon. Negative stimulation needs very strong currents, if stimulation is possible at all.
7. The propagation of unwanted natural neural activities towards the axon may be stopped by applying a sequence of negative stimuli from an electrode positioned in front of the dendrites because of the strong hyperpolarization which can be produced at the beginning of the axon.
8. Electrode positions at the terminal side will generate spikes in the endings of the unmyelinated axon.
9. High values of the activating function can occur at the endings of the processes which may result in synaptic activities, even if no propagating spike is evoked.
10. The total activating function for several sources can be obtained by summation:
 $f_{\text{total}} = \sum f_j$.
11. High values of the activating functions result from irregularities, either in the extracellular potential along the neuron or in the geometry of neighbored compartments.
12. During electrical stimulation of the brain via surface electrodes on the scalp or during magnetic stimulation, the electric field is rather uniform. In such cases bending of the axon, branching or extreme changes of diameters play the dominant role in determining the site and threshold of stimulation.

The abundance of phenomena that have to be considered in clinical electrical nerve stimulation are demonstrated with three types of neuroprostheses: the cochlear implant (Chapters 3 and 4), the electrically stimulated retina (Chapter 5) and the epidural stimulation of the lumbar spinal cord (Chapter 6).

The unique form of the human bipolar cochlear neuron with its non-myelinated somatic region underlines the importance of findings from computer simulations, that is, the human cases differ essentially concerning spike initiation sites and temporal behavior from our knowledge based on animal experiments (Chapter 3).

The presented model can be used to predict

1. the points of spike generation,
2. the time difference between stimulation and the arrival of a spike at the proximal end of the central axon,
3. the vanishing of peripherally evoked spikes at the soma region under specific conditions,
4. the influence of electrode positions on spiking behavior, and
5. consequences of the loss of the peripheral axon.

Every subunit of the cochlear neuron is separately modeled. Ion channel dynamics are described by a modified Hodgkin-Huxley model. Influence of membrane noise is taken into account. The generalized activating function gives an envision of the origin of spikes in the peripheral and in the central axon without any knowledge of the gating processes in the active membranes. Comparing the reactions of a human and cat cochlear neuron, show differences in spiking behavior, e.g. peripherally and centrally evoked spikes arrive with a time difference of about 400 μs in man and 200 μs in cat.

The influence of the three-dimensional cochlear structure on neural excitability is studied in Chapter 4. A simplified spiraled model of the human cochlea is developed from a cross sectional photograph. The potential distribution within this model cochlea is calculated with the finite element technique for an active scala tympani implant. The method presented in Chapter 3 allows for simulation of the excitation process of selected elements of the cochlear nerve. The bony boundary has an insulating influence along every nerve fiber which shifts the stimulation condition from that of a homogeneous extracellular medium towards constant field stimulation: for a target neuron which is stimulated by a ring electrode positioned just below the peripheral end of the fiber the extracellular voltage profile is rather linear. About half of the cochlear neurons of a completely innervated cochlea are excited with monopolar stimulation at threefold threshold intensity, whereas bipolar and especially quadrupolar stimulation focuses the excited region even for stronger stimuli. In contrast to single fiber experiments with cats, the long peripheral processes in human cochlear neurons cause first excitation in the periphery and consequently, neurons with lost dendrite need higher stimuli.

The problem of selective stimulation with inner eye prostheses is investigated in Chapter 5: Focal stimulation is an unsolved problem for epiretinal implants because of co-activation of bypassing axons originating from ganglion cells of the outer regions. Based on the activating function concept a method for selective stimulation is developed. Long electrodes parallel to the bypassing axons are shown to be good candidates for avoiding the co-stimulation phenomenon. Efficiency of focal excitation depends on the length and resistance of the electrodes. Furthermore, it is analyzed why, with epiretinal prostheses, bipolar retinal cells are easier to stimulate than ganglion cells despite of the fact that the elements of the ganglion cells are closer to the electrode.

In epidural stimulation of the lumbar cord (Chapter 6), the activating function concept demonstrates a strong relation between electrode position and the order of muscle twitches which is based on the segmental arrangement of innervation of lower limb muscles. The proposed strategy allows also identifying the position of the electrode relative to the spinal cord segments.

Most of the results presented in this thesis have been published recently.

In particular, some material of Chapter 1 is found in

F. Rattay, R. J. Greenberg, S. Resatz. 2003. Neuron Modeling. In Handbook of Neuroprosthetic Methods. Eds. W.E. Finn and P.G. LoPresti. CRC Press, 39-71

with reference to

F. Rattay 1986. Analysis of models for external stimulation of axons. IEEE-Trans. Biomed. Eng. BME-33, 974-977,

F. Rattay 1990. Electrical Nerve Stimulation: Theory, Experiments and Applications. Springer Wien,

F. Rattay and M. Aberham 1993. Modeling axon membranes for functional electrical stimulation. IEEE-Trans. Biomed. Eng. BME 40, 1201-1209

Parts of Chapter 2 are published in

F. Rattay 1998. Analysis of the electrical excitation of CNS neurons. IEEE-Trans. Biomed. Eng. 45, 766-772,

F. Rattay 1999. The basic mechanism for the electrical stimulation of the nervous system. Neuroscience 89, 335-346

Parts of Chapter 3 are published in

F. Rattay, P. Lutter and H. Felix. 2001. A model of the electrically excited human cochlear neuron. I. Contribution of neural substructures to the generation and propagation of spikes. Hear. Res. 153, 43-63

Parts of Chapter 4 are published in

F. Rattay, R. Naves Leao and H. Felix. 2001. A model of the electrically excited human cochlear neuron. II. Influence of the 3-dimensional cochlear structure on neural excitability. Hear. Res. 153, 64-79

Parts of Chapter 5 are published in

F. Rattay, R. J. Greenberg, S. Resatz. 2003. Neuron Modeling. In Handbook of Neuroprosthetic Methods. Eds. W.E. Finn and P.G. LoPresti. CRC Press, 39-71,

S. Resatz and F. Rattay. 2003. Excitability of bipolar and ganglion cells with retinal prosthesis: A modeling study. Engineering in Medicine and Biology Society, Proceedings of the 25th Annual International Conference Cancun, Mexico, p2039-2042,

F. Rattay and S. Resatz. 2004. Effective electrode configuration for selective stimulation with inner eye prostheses. IEEE-Trans. Biomed. Eng., 51, 1659-1664

Parts of Chapter 6 are published in

F. Rattay, K. Minassian and M. R. Dimitrijevic 2000. Epidural electrical stimulation of posterior structures of the human lumbosacral cord: 2. quantitative analysis by computer modeling. Spinal cord 38, 473-489,

F. Rattay, S. Resatz, P. Lutter, K. Minassian, B. Jilge and M.R. Dimitrijevic. 2003. Mechanisms of electrical stimulation with neural prostheses. Neuromodulation, 6, 42-56,

F. Rattay, K. Minassian, B. Jilge, C. Hofer, H. Kern, M. Dimitrijevic. 2004. Neuromodeling and the human spinal cord motor control: Neural responses to epidural stimulation. Proc. 8-th Vienna int. workshop on functional electrostimulation. 8-11,

F. Rattay. 2004. Central Nervous System Stimulation. In Neuroprosthetics: Theory and Practice. Eds. K. Horch and G. Dhillon World Scientific Publishing, 429-444

1. Introduction

As a consequence of the refinement of neuroprosthetic techniques, functional electrical stimulation (FES) has expanded successfully from the peripheral to the central nervous system (CNS) [Horch and Dhillon 2004]. Neural prostheses are used for the stimulation of cochlear [Moore 2003, Zeng 2004] and retinal neurons [Margalit et al. 2002], in Parkinson treatment [Krack et al. 2003] or for the suppression of neurogenic pain [Shealy et al. 1967, Cook and Weinstein 1973, Long and Erickson 1975, Lindblorn et al. 1977, Barlot 1998] or spasticity in spinal cord stimulation [Barolat et al. 1988, Gybels et al. 1991, Dimitrijevic 1998, Pinter et al. 2000] as well as ongoing developments in brain computer interfaces [Wolpaw et al. 2004, Tregoubov and Birbaumer 2005, Brunner et al. 2005]. In contrast to peripheral nerve stimulation, these prostheses are not exclusively operating by stimulating long axons anymore.

The responses of an externally stimulated neuron depend on: the geometry, the electrical cell parameters (dynamics and composition of the ion channels, degree of myelination, membrane capacity, calcium buffering, etc) and the strength and polarity of the extracellular potential along the neuronal structure. The excitation characteristics can easily be analyzed with a compartment model if the structure of a target neuron is homogeneous in the region close to the stimulating electrodes. Such a situation is typical for many applications of peripheral nerve stimulation where the first response of long homogeneous fibers was shown to be proportional to the second derivative of the electric potential along the fiber. This result follows from the activating function for non-myelinated axons, whereas myelinated fiber responses are close to the second difference quotient of the extracellular potential.

The theory of the activating function [Rattay 1986, 1987, 1989, 1990] explains that for external stimulation of long fibers (i) spike initiation with small electrodes is much easier with cathodic than anodic currents, (ii) thick fibers are more excitable, (iii) myelinated fibers respond earlier than the unmyelinated, (iv) the curvature of a target fiber influences its threshold, and there are conditions which favor (v) selective stimulation or (vi) unidirectional firing that stop unwanted spike trains by collision block.

In CNS stimulation different neuronal sub-structures are involved in the excitation process. The peripheral nerve stimulation rules (i-vi) cannot be applied in order to analyze such cases, because an important condition is not fulfilled by the nerve cell geometry, namely branching processes and changes in compartment diameters makes the cell unequal to a homogeneous cable. The important result that, for homogeneous fibers, the activating function value in one compartment becomes proportional to the second external potential difference is based on constant geometric parameters and the same inner-axonal resistance to the left and right neighbor compartment. However, a generalized form of the activating function allows handling the CNS excitation analysis [Chapter 2, Rattay 1999].

Moreover, predictions about electrically evoked CNS responses need careful modeling of the involved processes, for example for the individual simulation of the nonlinear ion channel currents in the soma region and at the synapses. Dissimilarities found in CNS responses are in contrast to peripheral FES where usually every applied pulse with parameters (amplitude, duration, polarity) from an operating window causes spike initiation in a motorneuron and consequently, with some delay, a synchronous twitch in the connected muscle unit. Several examples which are explained in more detail in the following chapters demonstrate characteristic differences between evoked responses in peripheral and central nervous system: A long weak stimulus will cause a sequence of spikes in the soma region of a retinal ganglion cell, spikes can also be generated within dendrites but not every dendritic

spike propagates across the soma. Electrical stimulation can initiate neurotransmitter release without producing an action potential, because synaptic endings are sensitive candidates for neuronal excitation. In epidural stimulation of the lumbar spinal cord a train of constant pulses causes a network of neurons to change its responses in a characteristic way which produces in the first phase tonic muscle activation and in the second phase rhythmic activities of the lower extremities [Chapter 6, Dimitrijevic et al. 1998, Minassian et al. 2004].

Comparing a bipolar cell of the retina with a cochlear neuron demonstrates the variety in architecture and neural signal processing principles. Some neuron types like the afferent bipolar cochlear neurons are effective transmission lines where nearly all of the spikes initiated at the synaptic contact with an inner hair cell arrive with some delay and small temporal variation (jitter) in the terminal region. In contrast to the cochlear neuron, a bipolar retinal cell does not generate action potentials but answers with graded potentials to synaptic stimulation from photoreceptor cells.

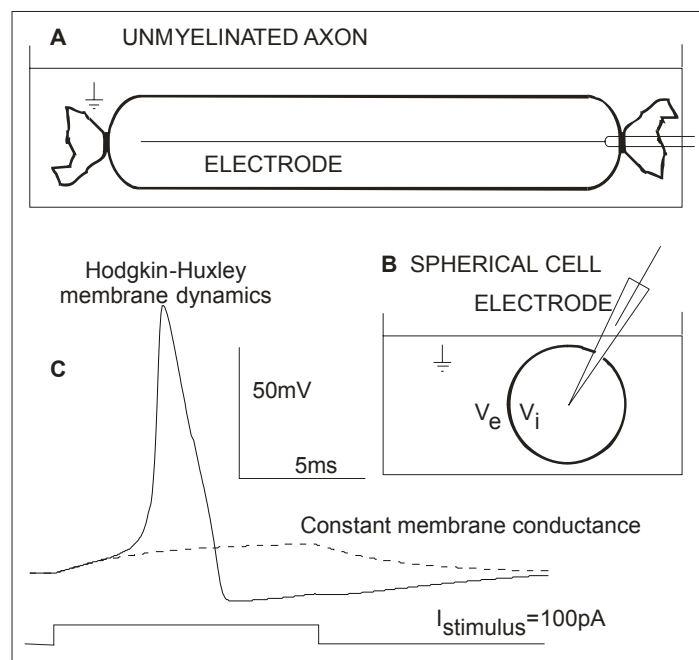


Fig. 1.1. Stimulation without signal propagation (space clamp). A stimulating electrode in form of a non-insulated wire inserted along an unmyelinated nerve fiber (A) or current injection in a spherical cell (B) cause the same inside voltage V_i for every part of the cell membrane. (C) In the first sub-threshold phase the voltage across the cell membrane follows the simple constant membrane conductance model (dashed line). Simulation of a $30 \mu\text{m}$ spherical cell sheltered by a membrane with squid axon ion channel distribution, i.e. by solving the Hodgkin-Huxley model with original data. Membrane voltage V is the difference between internal and external voltage: $V = V_i - V_e$, $V_e = 0$. After Rattay et al. 2003.

Internal cell stimulation by current injection

A breakthrough in our understanding of the physics of neural signals which propagate as membrane voltage along a nerve fiber (axon) was achieved by the ingenious work of Hodgkin and Huxley (1952) on the non-myelinated squid axon. This work helps explain the action potential or “spike” that conveys the “all-or-none” response of neurons. To explore the complicated gating mechanism of the ion channels, the stimulating electrode was a long non-insulated wire, and thereby every part of the neural membrane had to react in the same way, i.e. propagation of signals was prevented (Fig. 1.1 A). Refinements of their method as

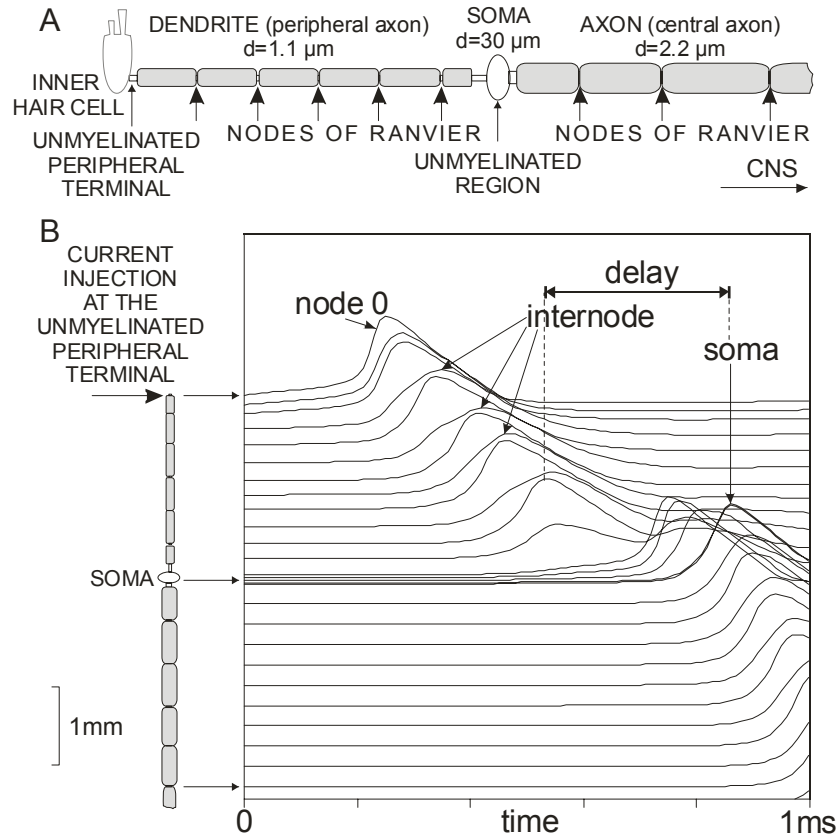


Fig. 1.2. Simulation of the natural excitation of a human cochlear neuron by stimulation with a 50 pA, 250 μ s pulse injected at the peripheral end. This bipolar cell is a non-typical neuron: (i) the dendrite is myelinated and often called peripheral axon, (ii) in contrast to animal cochlear neurons the soma and the pre- and post somatic regions are unmyelinated, (iii) a single synaptic input from the auditory receptor cell (inner hair cell) generates a spike that propagates with a remarkable delay across the current consuming somatic region. Note the decay of the action potential in every internode that again is amplified in the next node of Ranvier.

Simulation: internode with constant membrane conductance, 'warm' Hodgkin Huxley model ($k=12$) in the active membranes of the soma and with 10-fold ion channel density in the peripheral terminal (node 0), all nodes and pre-and postsomatic compartments. The lines are vertically shifted according to their real location of the rectified neuron.

After Rattay et al. 2003; for details see Chapter 3 and Rattay et al. 2001a.

well as the application of patch clamp techniques supply us with models for different neural cell membranes. Reliable prediction of membrane voltage V as a function of time is possible for arbitrary stimulating currents $I_{stimulus}$ with proper membrane models.

The main equation for internal stimulation of the soma or any other compartment where current flow to other processes or neighbored compartments is prevented has always the same form: One part of the stimulating current is used to load the capacity C_m of the cell membrane and the other part passes through the ion channels, that is

$$I_{stimulus} = C_m \frac{dV}{dt} + I_{ion} \quad (1.1).$$

The rate of membrane voltage change, dV/dt , follows as:

$$\frac{dV}{dt} = [-I_{ion} + I_{stimulus}] / C_m \quad (1.2),$$

where the ion currents I_{ion} are calculated from appropriate membrane models. Usually, the membrane models are formulated for 1 cm² of cell membrane and the currents in Eqn. 1.1 become current densities.

A positive stimulating current applied at the inside of an axon or at any other part of a neuron will cause an increase of V according to Eqn. 1.1, if the membrane has been in the resting state ($I_{stimulus}=0$ and $dV/dt=0$) before. In order to generate a spike this positive stimulus current has to be strong enough to reach threshold voltage, which causes many of the voltage sensitive sodium channels to open. By sodium current influx the transmembrane potential increases to an action potential without the need of further stimulating support. This means that as soon as the full line in Fig. 1.1C is some few mV above the dashed line we can switch off the stimulus without seeing any remarkable change in the shape of the action potential.

In general the excitation process along neural structures is more complicated than under space clamp conditions as shown in Fig. 1.1. Current influx across the cell membrane in one region influences the neighbored sections and causes effects like spike propagation (Fig. 1.2). Besides modeling the natural signaling, the analysis of compartment models helps to explain the influences of applied electric or magnetic fields on representative target neurons. Typically such a model neuron consists of functional sub-units with different electrical membrane characteristics: dendrite, cell body, initial segment, myelinated nerve fiber and non-myelinated terminal. Plenty of literature exists on stimulated fibers, but little has been written about external stimulation of complete neurons.

External cell stimulation

In 1976 McNeal presented a compartment model for a myelinated nerve fiber and its sub-threshold response to external point source stimulation. He inspired many authors to expand his model for functional electrical stimulation of the peripheral nerve system, e.g. analysis of external fiber stimulation by the activating function [Rattay 1986,1989], unidirectional propagation of action potentials [Sweeney and Mortimer 1986], stimulation of a nerve fiber within a bundle [Veltnik et al. 1988, Altman and Plonsey 1990], selective axon stimulation [Sweeney et al. 1990, Veraart et al. 1990, Tyler and Durand 1994], and influence of fiber ending [Nagarajan et al. 1993].

Of specific interest is the threshold and place of spike initiation generated with stimulating electrodes which are simulated, e.g. by the near field of a point source or dipole, by finite element calculation for a specific implanted device or when the far field influence from surface electrodes is approximated by a constant field [Rattay 1999]. Stronger electric stimuli or application of alternating currents generate new effects in neural tissue. All effects depend essentially on the electric properties of the neural cell membrane and can be studied with compartment modeling. The ion channel dynamics can be neglected during the first response of the resting cell, but the complicated nonlinear membrane conductance becomes dominant in the supra-threshold phase (Fig. 1.1 C). Consequently the behavior can be analyzed with simple linear models or with more computational effort by systems of differential equations that describe the ion channel mechanisms in every compartment individually.

Modeling the sub-threshold neural membrane with constant conductances allows the analysis of the first phase of the excitation process by the activating function as a rough approach. Without inclusion of the complicated ion channel dynamics, the activating function concept explains the basic mechanism of external stimulation, the essential difference between anodic and cathodic threshold values and its dependence from the geometric situation, the mechanism of one side firing and block of spike propagation by hyperpolarized regions as well as several other phenomena [e.g. Coburn 1989, Rattay 1990].

Beside nerve fiber analysis, the activating function which represents the direct influence of the electric field in every compartment is useful for magnetic stimulation [Basser et al. 1992, Garnham et al. 1995], direct stimulation of denervated muscle fibers [Reichel et al. 1999] or in generalized form for cardiac tissue [Sobie et al. 1997, Efimov et al. 2000] and for neurons of arbitrary shape [Rattay 1998a, 1999].

In previous work we have shown how the geometry of a neuron affects the excitation characteristics and that several surprising phenomena may occur. This is demonstrated e.g. by comparing the threshold current for neurons with small and large sized soma. Whereas thick axons are easier to stimulate than thin ones (known as the inverse recruitment order; [Blair and Erlanger 1933]), this relation does not hold for the size of the soma: a 100 μs pulse from a point electrode 430 μm above the soma needs -2.3 mA to stimulate a 30 μm diameter soma neuron with a 2 μm axon but only -1.1 mA for a 10 μm soma. Increasing the electrode distance to 1000 μm results in the same -2.2 mA threshold for both cases, i.e. the second surprise is that for the large soma neuron excitation threshold increases slightly when the electrode is moved within a specific range towards the soma [Rattay 1999]. The explanation is: the axon, which is generally more excitable than the soma, loses more current to load the larger capacity of the large soma; this effect is more pronounced when the place of spike initiation within the axon is close to the soma.

Comparing a pyramidal cell with a cochlear neuron demonstrates the variety in architecture and signal processing principles in the dendrite and soma region. Some neuron types like the afferent bipolar cochlear neurons are effective transmission lines where nearly all of the spikes initiated at the synaptic contact with an inner hair cell arrive with some delay and small temporal variation (jitter) in the terminal region (Fig. 1.2). In contrast to the cochlear neuron, a single synaptic input at the dendritic tree of a pyramidal cell produces only minimal change in membrane voltage at the soma and at the initial segment and usually the collective effect of many synaptic activities is necessary to influence spike initiation significantly. Typically the pyramidal cell response is dominated by the internal calcium concentration which depends on two types of voltage dependent calcium channels: low voltage activated channels respond in the subthreshold range and may include generation of low threshold spikes and high voltage activated channels in the dendrites respond e.g. to backpropagating sodium spikes [Huguenard 1996, Schiller et al. 1995, Mainen and Sejnowski 1998].

Models for the cell membrane

The cell membrane is not a perfect insulator for ion transport. When one Na-channel opens for a short time some thousand sodium ions may be driven by the high outside concentration into the cell. The second driving element is the voltage across the membrane which requires a Na⁺ current according to Ohms law. The conductance of a patch of cell membrane for a specific ion type depends on the number of open channels and is defined by Ohm's law and a battery voltage according to the Nernst equation. Different internal concentration c_i and external ion concentration c_e causes the membrane voltage E_m when one type of ions is involved:

$E_m = \frac{RT}{zF} \ln \frac{c_e}{c_i}$	Nernst Equation
---	-----------------

with the gas constant $R=8.31441 \text{ J}/(\text{mol.K})$, temperature in Kelvin T , valence z , the Faraday constant representing the charge of one mol of single valenced ions $F=96485 \text{ C/mol}$. Note: At room temperature ($T=20 \text{ }^\circ\text{C}=293.15 \text{ }^\circ\text{K}$) the factor RT/F is about 25 mV.

In their experiments Hodgkin and Huxley found the sodium current proportional to $E-E_{Na}$. Approximating the Nernst equation with their data gives $E_{Na}=45\text{mV}=25 \text{ mV} \cdot \ln(c_e/c_i)$ and results in $c_e/c_i = \exp(45/25)=6.05$, i.e. the outside sodium concentration is six times the

inner one, and $E_K = -82 \text{ mV} = 25 \text{ mV} \cdot \ln(c_e/c_i)$ demands the potassium outside inside concentration to be in the relation 1:26.5.

The Goldman equation defines the steady state membrane voltage $E_m = E_{rest}$ when several ion types are involved. When K^+ , Na^+ and Cl^- ions are considered it reads as:

$$E_m = \frac{RT}{F} \ln \frac{P_K [K]_e + P_{Na} [Na]_e + P_{Cl} [Cl]_i}{P_K [K]_i + P_{Na} [Na]_i + P_{Cl} [Cl]_e} \quad \text{Goldman Equation}$$

where $[K]$ is the potassium concentration and the suffixes i and e stand for inside and external. P_K , P_{Na} and P_{Cl} are permeabilities measured in $[\text{cm}/\text{sec}]$. Note that sodium and potassium are anions, but chloride is cathodic, therefore $[Cl]_i$ appears in the numerator in contrast to the anionic concentrations. In the resting state the membrane is most permeable to potassium ions and therefore the resting membrane voltage of about -70 mV (i.e. the inside is more negative compared to the extracellular fluid) is close to the potassium Nernst potential.

The nonlinear conductance of the neural cell membrane depends on different classes of ion channels [Destexthe et al. 1994] (i-iii) and on the activity of ion pumps (iv):

- (i) Voltage dependent gating dominates excitation and neural signal propagation in the axon; open-close kinetics depend on the voltage across the cell membrane.
- (ii) Calcium dependent gating, mainly at the soma and dendrites; calcium concentration regulates the opening of the channels as opening depends on intracellular calcium ion binding.
- (iii) Transmitter gating and second messenger gating, at the pre- and postsynaptic membrane.
- (iv) Ion pumps are membrane molecules that by consuming energy pump ions across the cell membrane in order to restore the typical high individual ion concentration on one side of the cell, e.g. high external sodium and high internal potassium concentration.

Axon models of the Hodgkin-Huxley type

The Hodgkin-Huxley model (HH-model) was developed from a homogeneous non-myelinated squid axon. It includes sodium, potassium and leakage currents and has the form:

$$\frac{dV}{dt} = \left[-g_{Na} m^3 h (V - V_{Na}) - g_K n^4 (V - V_K) - g_L (V - V_L) + i_{stimulus} \right] / c \quad \text{HH-1}$$

$$\frac{dm}{dt} = [-(\alpha_m + \beta_m) m + \alpha_m] k \quad \text{HH-2}$$

$$\frac{dh}{dt} = [-(\alpha_h + \beta_h) h + \alpha_h] k \quad \text{HH-3}$$

$$\frac{dn}{dt} = [-(\alpha_n + \beta_n) n + \alpha_n] k \quad \text{HH-4}$$

$$k = 3^{0.17 - 0.63} \quad \text{HH-5}$$

V is the reduced membrane voltage, resulting from internal, external and resting potential: $V = V_i - V_e - V_{rest}$, g_{Na} , g_K , g_L are the maximum conductances for sodium, potassium and leakage per cm^2 , m , h , n are probabilities (with values between 0 and 1) that reduces the maximum conductance of sodium and potassium according to experimental gating data, V_{Na} , V_K , V_L are sodium, potassium and leakage battery voltage according to the Nernst equation, $i_{stimulus}$ is the stimulus current in μA per cm^2 , c is the membrane capacity per cm^2 ,

α and β are voltage dependent variables fitted from experimental data to quantify the ion channel kinetics, k is a temperature coefficient which accelerates the gating process for temperatures higher than the original experimental temperature of 6.3 °C, temperature T in °C. Although a temperature conversion is possible, it is interesting to note that unlike real tissue, the Hodgkin-Huxley equations do not propagate action potentials above 31 °C [Rattay 1990].

Parameter values, units and further expressions of the HH-model are listed in Table 1.1

In 1964 Frankenhaeuser and Huxley developed the first myelinated fiber model on the frog axon node (FH-model) assuming a HH like gating mechanisms but derived the ion current formulation from the Nernst-Planck equation [Frankenhaeuser 1960] and added a non specific current density i_P :

$$\frac{dV}{dt} = [-i_{Na} - i_K - i_P - i_L + i_{stimulus}] / c \quad \text{FH-1}$$

$$i_{Na} = P_{Na} m^2 h \frac{EF^2 [Na]_o - [Na]_i \exp(EF / RT)}{RT (1 - \exp(EF / RT))} \quad \text{FH-2}$$

$$i_K = P_K n^2 \frac{EF^2 [K]_o - [K]_i \exp(EF / RT)}{RT (1 - \exp(EF / RT))} \quad \text{FH-3}$$

$$i_P = P_P p^2 \frac{EF^2 [Na]_o - [Na]_i \exp(EF / RT)}{RT (1 - \exp(EF / RT))} \quad \text{FH-4}$$

$$i_L = g_L (V - V_L) \quad \text{FH-5}$$

$$E = V + V_{rest} \quad \text{FH-6}$$

$$\begin{aligned} \frac{dm}{dt} &= -(\alpha_m + \beta_m)m + \alpha_m, & \frac{dn}{dt} &= -(\alpha_n + \beta_n)n + \alpha_n, \\ \frac{dh}{dt} &= -(\alpha_h + \beta_h)h + \alpha_h, & \frac{dp}{dt} &= -(\alpha_p + \beta_p)p + \alpha_p \end{aligned} \quad \text{FH-7-10}$$

Note that membrane voltage is denoted as E in FH-2 to FH-4 and as V (reduced membrane voltage) according to FH-6 in FH-1 and FH-5. Temperature T is measured in °K, for temperatures other than 20 °C=293.15 °K the alpha and beta values in FH-7-10 need to be modified (comp. next section). Parameter values and further expressions of the FH-model are listed in Table 1.1.

Sodium current plays the dominant role in the action potential of the mammalian node of Ranvier and in contrast to the axon model of squid and frog there are almost no potassium currents [Horáckova et al. 1968, Chiu et al. 1979, Schwarz and Eikhof 1987].

The CRRSS model named after Chiu, Ritchie, Rogert, Stagg and Sweeney describes a myelinated rabbit nerve node which was extrapolated from original 14 °C data to 37 °C [Chiu et al. 1979, Sweeney et al. 1987]:

$$\frac{dV}{dt} = [-g_{Na} m^2 h (V - V_{Na}) - g_L (V - V_L) + i_{stimulus}] / c \quad \text{CRRSS-1}$$

$$\frac{dm}{dt} = [-(\alpha_m + \beta_m)m + \alpha_m]k, \quad \frac{dh}{dt} = [-(\alpha_h + \beta_h)h + \alpha_h]k \quad \text{CRRSS-2,3}$$

$$k = 3^{0.1T-3.7} \quad \text{CRRSS-4}$$

Note that the temperature factor $k=1$ for $T=37$ °C. Parameter values and further expressions of the CRRSS-model are listed in Table 1.1

Schwarz and Eikhof obtained a model of FH type from voltage clamp experiments on rat nodes [Schwarz and Eikhof 1987]. From the original data the SE model results by assuming a nodal area of $50 \mu\text{m}^2$ [Rattay 1990, 1993]:

$$\frac{dV}{dt} = [-i_{Na} - i_K - i_L + i_{stimulus}] / c \quad \text{SE-1}$$

$$i_{Na} = P_{Na} m^3 h \frac{EF^2 [Na]_o - [Na]_i \exp(EF / RT)}{RT (1 - \exp(EF / RT))} \quad \text{SE-2}$$

$$i_K = P_K n^2 \frac{EF^2 [K]_o - [K]_i \exp(EF / RT)}{RT (1 - \exp(EF / RT))} \quad \text{SE-3}$$

$$i_L = g_L (V - V_L) \quad \text{SE-4}$$

$$E = V + V_{rest} \quad \text{SE-5}$$

$$\frac{dm}{dt} = -(\alpha_m + \beta_m)m + \alpha_m, \quad \frac{dn}{dt} = -(\alpha_n + \beta_n)n + \alpha_n, \quad \frac{dh}{dt} = -(\alpha_h + \beta_h)h + \alpha_h \quad \text{SE-6-8}$$

Parameter values and additional expressions of the SE-model are listed in Table 1.1.

Schwarz, Reid, and Bostock (1995) derived the SRB model from human nerve fibers at room temperature. Single action potentials are little affected by removing the fast or slow potassium currents, but they report that the slow K conductance was required to limit the repetitive response of the model to prolonged stimulating currents. SRB model:

$$\frac{dV}{dt} = [-i_{Na} - i_{K,fast} - i_{K,slow} - i_L + i_{stimulus}] / c \quad \text{SRB-1}$$

$$i_{Na} = P_{Na} m^3 h \frac{EF^2 [Na]_o - [Na]_i \exp(EF / RT)}{RT (1 - \exp(EF / RT))} \quad \text{SRB-2}$$

$$i_{Kfast} = g_K n^4 (V - V_K) \quad \text{SRB-3}$$

$$i_{Kslow} = g_{Kslow} p (V - V_K) \quad \text{SRB-4}$$

$$i_L = g_L (V - V_L) \quad \text{SRB-5}$$

$$E = V + V_{rest} \quad \text{SRB-6}$$

$$\frac{dm}{dt} = -(\alpha_m + \beta_m)m + \alpha_m, \quad \frac{dn}{dt} = -(\alpha_n + \beta_n)n + \alpha_n, \\ \frac{dh}{dt} = -(\alpha_h + \beta_h)h + \alpha_h, \quad \frac{dp}{dt} = -(\alpha_p + \beta_p)p + \alpha_p \quad \text{SRB-7-10}$$

Additional SRB-model data for 37 °C are listed in Table 1.1.

Axon membrane models for biomedical applications are further discussed in [Rattay 1990, 1993, Rattay and Aberham 1993, Schwarz et al. 1995, Wesselink et al. 1999, Rattay et al. 2001a, Burke et al. 2001]. Some authors neglect the weak K currents in the mammalian axon totally because of their small contributions, but up to five types of K ion channels are shown to have notable influences on axonal signaling, especially in the internode, an element often modeled as perfect insulator with capacity $C=0$. Curious effects like spontaneous switching

between high and low threshold states in motor axons are suggested to be a consequence of K^+ loading within small internodal spaces [Baker 2000]. Phenomena like different excitability fluctuations after action potentials in sensory and motor neurons demand also for more sophisticated modeling. This means that for many applications modeler's work is not finished by selecting the SRB model (as it is based on human data) or by fitting its parameter according to the shape and propagation velocity of a measured action potential.

TABLE 1.1. EXPRESSIONS AND CONSTANTS FOR AXON MEMBRANE MODELS

	HH model	FH model	CRRSS model	SE model	SRB model
α_m	$\frac{2.5 - 0.1V}{\exp(2.5 - 0.1V) - 1}$	$\frac{0.36(V - 22)}{1 - \exp\left(\frac{22 - V}{3}\right)}$	$\frac{97 + 0.363V}{1 + \exp\left(\frac{31 - V}{5.3}\right)}$	$\frac{1.87(V - 25.41)}{1 - \exp\left(\frac{25.41 - V}{6.06}\right)}$	$\frac{4.6(V - 65.6)}{1 - \exp\left(\frac{-V + 65.6}{10.3}\right)}$
β_m	$4 \cdot \exp\left(-\frac{V}{18}\right)$	$\frac{0.4(13 - V)}{1 - \exp\left(\frac{V - 13}{20}\right)}$	$\frac{\alpha_m}{\exp\left(\frac{V - 23.8}{4.17}\right)}$	$\frac{3.97(21 - V)}{1 - \exp\left(\frac{V - 21}{9.41}\right)}$	$\frac{0.33(61.3 - V)}{1 - \exp\left(\frac{V - 61.3}{9.16}\right)}$
α_n	$\frac{0.1 - 0.01V}{\exp(1 - 0.1V) - 1}$	$\frac{0.02(V - 35)}{1 - \exp\left(\frac{35 - V}{10}\right)}$		$\frac{0.13(V - 35)}{1 - \exp\left(\frac{35 - V}{10}\right)}$	$\frac{0.0517(V + 9.2)}{1 - \exp\left(\frac{-V - 9.2}{1.1}\right)}$
β_n	$0.125 \cdot \exp\left(-\frac{V}{80}\right)$	$\frac{0.05(10 - V)}{1 - \exp\left(\frac{V - 10}{10}\right)}$		$\frac{0.32(10 - V)}{1 - \exp\left(\frac{V - 10}{10}\right)}$	$\frac{0.092(8 - V)}{1 - \exp\left(\frac{V - 8}{10.5}\right)}$
α_h	$0.07 \cdot \exp\left(-\frac{V}{20}\right)$	$\frac{0.1(V + 10)}{1 - \exp\left(\frac{V + 10}{6}\right)}$	$\frac{\beta_h}{\exp\left(\frac{V - 5.5}{5}\right)}$	$\frac{0.55(V + 27.74)}{1 - \exp\left(\frac{V + 27.74}{9.06}\right)}$	$\frac{0.21(V + 27)}{1 - \exp\left(\frac{V + 27}{11}\right)}$
β_h	$\frac{1}{\exp(3 - 0.1V) + 1}$	$\frac{4.5}{1 + \exp\left(\frac{45 - V}{10}\right)}$	$\frac{15.6}{1 + \exp\left(\frac{24 - V}{10}\right)}$	$\frac{22.6}{1 + \exp\left(\frac{56 - V}{12.5}\right)}$	$\frac{14.1}{1 + \exp\left(\frac{55.2 - V}{13.4}\right)}$
α_p		$\frac{0.006(V - 40)}{1 - \exp\left(\frac{40 - V}{10}\right)}$			$\frac{0.0079(V - 71.5)}{1 - \exp\left(\frac{71.5 - V}{23.6}\right)}$
β_p		$\frac{0.09(V + 25)}{1 - \exp\left(\frac{V + 25}{20}\right)}$			$\frac{0.00478(V - 3.9)}{1 - \exp\left(\frac{V - 3.9}{21.8}\right)}$
V_{rest} [mV]	-70	-70	-80	-78	-84
V_{Na} [mV]	115		115		
V_K [mV]	-12				0
V_L [mV]	10.6	0.026	-0.01	0	0
g_{Na} [$k\Omega^{-1}cm^{-2}$]	120		1445		
$g_{K,fast}$ [$k\Omega^{-1}cm^{-2}$]	36				30
$g_{K,slow}$ [$k\Omega^{-1}cm^{-2}$]					60
g_L [$k\Omega^{-1}cm^{-2}$]	0.3	30.3	128	86	60
c [μFcm^{-2}]	1	2	2.5	2.8	2.8
$V(0)$	0	0	0	0	0
$m(0)$	0.05	0.0005	0.003	0.0077	0.0382
$n(0)$	0.32	0.0268		0.0267	0.2563
$h(0)$	0.6	0.8249	0.75	0.76	0.6986

p(0)		0.0049			0.0049
T ₀	6.3°C	293.15°K=20°C	37°C	310.15°K=37°C	310.15°K=37°C
Q ₁₀ (α _m)	3	1.8	3	2.2	2.2
Q ₁₀ (β _m)	3	1.7	3	2.2	2.2
Q ₁₀ (α _n)	3	3.2	3	3	3
Q ₁₀ (β _n)	3	2.8	3	3	3
Q ₁₀ (α _h)	3	2.8	3	2.9	2.9
Q ₁₀ (β _h)	3	2.9	3	2.9	2.9
P _{Na} [cm/s]		0.008		0.00328	0.00704
P _K [cm/s]		0.0012		0.000134	
P _P [cm/s]		0.00054			
[Na] _o [mmol/l]		114.5		154	154
[Na] _i [mmol/l]		13.7		8.71	30
[K] _o [mmol/l]		2.5		5.9	
[K] _i [mmol/l]		120		155	
	HH model	FH model	CRRSS model	SE model	SRB model
Faraday constant F=96485 [C/mol]			gas constant R=8314.4 [mJ/(mol.K)]		

The dendrite and especially the soma region are more difficult to simulate [Magee 1999, <http://senselab.med.yale.edu/senselab/NeuronDB/>] because a variety of ion channel types are involved. Some membrane models are available, e.g. [Belluzzi and Sacchi 1991, Winslow and Knapp 1991, McCormick and Huguenard 1992, Traub et al. 1994, DeSchutter and Bower 1994, Fohlmeister and Miller 1997a,b] but even in these models we cannot rely on a precise individual measurement of all the ion components that vary in channel density and open-close kinetics. Repetitive firing (bursting) may occur as response to stimulation or in pacemaker neurons without any input.

Influence of temperature

Most of the membrane model data were gathered at low temperatures but for biomedical applications they have to be extrapolated to physiological temperature. Usually, a specific constant, Q₁₀, is introduced which accounts for the acceleration in membrane gating dynamics when the temperature is increased by 10 °C. Hodgkin and Huxley used Q₁₀=3 as a common coefficient for all gating variables m, n, h (HH-2-4):

$$k = Q_{10}^{(T-T_0)/10} \quad (1.3)$$

Raising the temperature causes shortening of the action potential and increase of spike propagation velocity in the unmyelinated squid axon. The spike duration in Fig. 1.1 with original HH data (6.3 °C) is about ten times longer than that of the cochlea neuron in Fig. 1.2, which also was simulated with HH kinetics. The temporal membrane behavior in cat [Hartmann et al. 1984] was fitted with k=12, corresponding to a temperature of 29 °C (Eqn. 1.2), [Motz and Rattay 1986, Rattay 1990 p165]. The HH spike amplitude becomes rather small for higher temperatures. An essentially reduced amplitude is not able to preserve the excitation process along the fiber and for temperatures higher than 31-33 °C action potentials will not propagate any more in squid axons (heat block) [Hodgkin and Katz 1949, Huxley 1959, Rattay 1990]. Such amplitude reductions are not seen in the membrane models of myelinated axons (FH, CRRSS, SE and SRB model) and the heat block phenomenon is absent both in myelinated and unmyelinated fibers of warm-blooded animals. In all axon models spike duration shortens considerably when temperature is increased e.g. from 20 °C (usual for data acquisition) to 37 °C [Rattay 1990, Rattay and Aberham 1993]. A temperature factor k=12 in the HH-model fits the temporal characteristics of action potentials in unmyelinated axons of man and warm blooded animals at 37 °C [Rattay 1990, 1995, Rattay et al. 2001a].

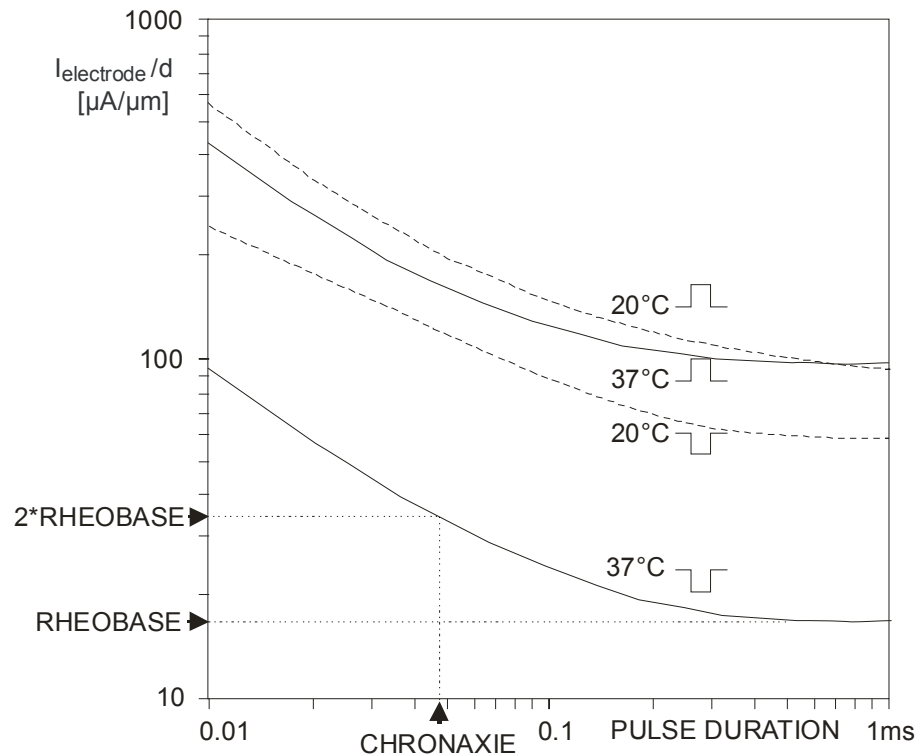


Fig. 1.3. Threshold currents as function of pulse duration (strength duration relation). A myelinated fiber of diameter d and internodal length $\Delta x = 100d$ is stimulated by a point source located in a distance Δx above a node. Excitation is easier for high temperature (full lines) and cathodic pulse. The threshold current for long pulses becomes time-independent and is called rheobase. The pulse duration belonging to the doubled rheobase current is called chronaxie.

Simulations with FH model, internode membrane is assumed as perfect insulator with $c=0$. After Rattay et al. 2003.

The original FH model [Frankenhaeuser and Huxley 1964] incorporates thermal molecular motion according to the laws of gas dynamics (FH2-4) but the authors did not include the necessary Q_{10} values presented in Table 1.1 for the gating variables m, n, h, p . The gating process becomes essentially accelerated for high temperatures and dominates spike duration [Hodgkin and Katz 1949, Frankenhaeuser and Moore 1963, Rattay 1990, Rattay and Aberham 1993]. Therefore the Q_{10} factors have to be involved in functional electrical nerve stimulation modeling. Note that many published results obtained with the original FH model must be corrected to be valid for 37 °C.

2. The activating function concept for CNS neurons

Neural signals can be generated or blocked by extracellular electrodes or magnetic coils. New results about artificial excitation are based on a compartmental model of a target neuron and its equivalent electrical network, as well as on the theory of the generalized activating function. The analysis shows that:

- (i) in most cases, the origin of artificial excitation is within the axon and the soma is much more difficult to excite;
- (ii) within the central nervous system, positive and negative threshold currents essentially depend on the position and orientation of the neurons relative to the applied electric field;
- (iii) in several cases, stimulation with positive currents is easier; and
- (iv) it is possible to excite synaptic activity without the generation of propagating action potentials.

Furthermore, the theory of the generalized activating function gives hints to understanding the blockage of neural activity.

Compartment model of an externally stimulated neuron

Small pieces of a neuron can be treated as isopotential elements and a whole neuron is represented by an electric network (Fig. 2.1). A current injected at the n-th compartment has to cross the membrane as capacitive or ion current or leaves to the left or right side as longitudinal current, i.e. application of Kirchhoff's law is an extension of Eqn. 1.1:

$$I_{injected,n} = C_n \frac{d(V_{i,n} - V_{e,n})}{dt} + I_{ion,n} + \frac{V_{i,n} - V_{i,n-1}}{R_n/2 + R_{n-1}/2} + \frac{V_{i,n} - V_{i,n+1}}{R_n/2 + R_{n+1}/2} \quad (2.1),$$

where n indicates the n-th compartment, C its membrane capacity and R/2 the internal resistance between the center and the border of the compartment. Introducing the reduced membrane voltage $V = V_i - V_e - V_{rest}$ leads to the following system of differential equations for calculating the time courses of V_n in every compartment:

$$\frac{dV_n}{dt} = \left[-I_{ion,n} + \frac{V_{n-1} - V_n}{R_{n-1}/2 + R_n/2} + \frac{V_{n+1} - V_n}{R_{n+1}/2 + R_n/2} + \dots + \frac{V_{e,n-1} - V_{e,n}}{R_{n-1}/2 + R_n/2} + \frac{V_{e,n+1} - V_{e,n}}{R_{n+1}/2 + R_n/2} + \dots + I_{injected,n} \right] / C_n \quad (2.2)$$

The dots in Eqn. 2.2 stand for terms that have to be added in cases of more than two neighbor elements, e.g. at the cell body (soma) or at branching regions. For the first and last compartments Eqn. 2.2 has a reduced form. The membrane surface A_n of every compartment has to be calculated to find $C_n = A_n \cdot c_n$ (c_n is the specific membrane capacitance) and $I_{ion} = A_n \cdot i_{ion}$. The ionic membrane current density i_{ion} is computed with an appropriate membrane model, for cylinder elements (d: diameter, Δx : length) we obtain $A_n = d_n \pi \Delta x_n$, $R/2 = 2\rho_i \Delta x_n / (d_n^2 \pi)$ where the internal resistivity ρ_i is often assumed as $\rho_i = 0.1 \text{ k}\Omega\text{cm}$.

In a spherical cell body with several processes (as in Fig. 2.1) the internal resistances to the neighbor compartments depend on the compartment diameters, that means $R_{soma \rightarrow dendrite1/2} < R_{soma \rightarrow axon/2}$ if $d_{dendrite1} > d_{axon}$, in more detail $A_{soma} = 4r_{soma}^2 \pi - \sum 2r_{soma} \pi h_j$, with (j indicating the j-th process) $h_j = r_{soma} - z_j$, where $z_j = \sqrt{r_{soma}^2 - (d_{process,j}/2)^2}$. The somatic resistance to the border of the j-th process is $\frac{R_{soma,j}}{2} = \frac{\rho_i}{2r\pi} \ln\left(\frac{r_{soma} + z_j}{r_{soma} - z_j}\right)$.

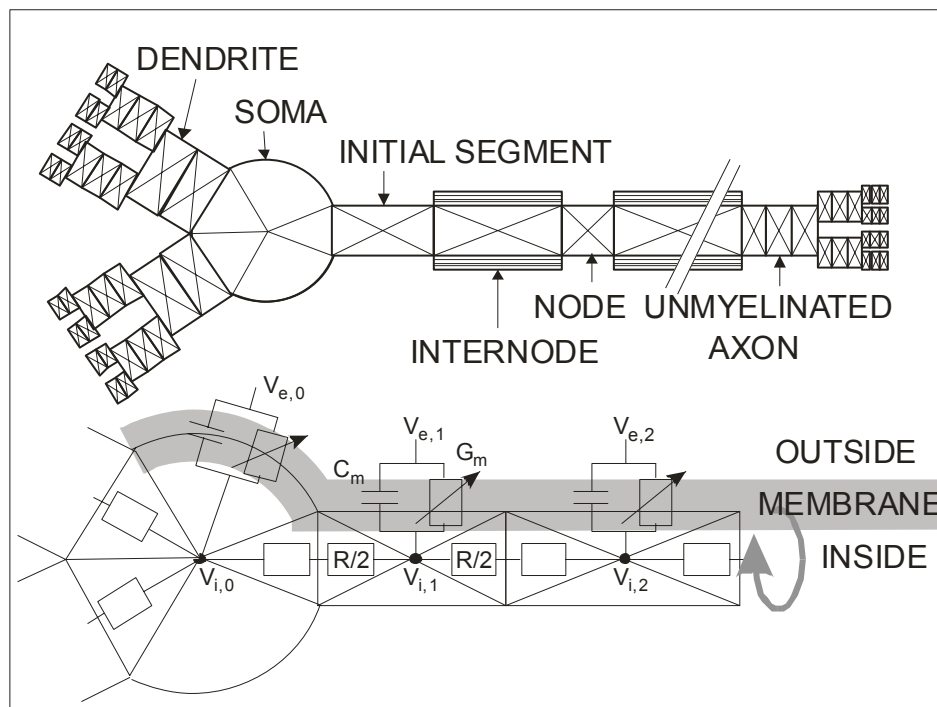


Fig. 2.1. Scheme of a neuron with subunits and part of the simplified equivalent electrical network (batteries resulting from different ion concentrations on both sides of the membrane are not shown).

The electric and geometric properties changes from compartment to compartment and the modeler has to decide about the complexity which should be involved: e.g. the surface area of a dendrite compartment and the soma can be simulated by a cylinder and a sphere or an additional factor is included representing the enlargement by spines or windings. Halter and Clark (1991) and Ritchie (1995) presented detailed ion current data for the internode, whereas many authors neglect internodal membrane currents. A compromise is to simulate the internode as a single compartment with both membrane conductance G_m and membrane capacity C proportional to $1/N$, where N is the number of myelin layers [Rattay 1999].

Synaptic activation of a neuron can be simulated by current injection at the soma or at dendrite compartments (Fig. 1.2). In such cases all external potentials V_e are assumed as 0 in Eqn. 1.3. On the other hand, neuroprosthetic devices generate neural activities by application of electric fields. Instead of current injection the terms including the external potential V_e became the stimulating elements in Eqn. 1.3.

The activating function

The driving term of the external potential on compartment n (Eqn. 2.2) is called the activating function f_n :

$$f_n = \left[\frac{V_{e,n-1} - V_{e,n}}{R_{n-1}/2 + R_n/2} + \frac{V_{e,n+1} - V_{e,n}}{R_{n+1}/2 + R_n/2} + \dots \right] / C_n \quad (2.3)$$

The physical dimension of f_n is [V/s] or [mV/ms]. If the neuron is in the resting state before a stimulating current impulse is applied, the activating function represents the velocity of membrane voltage change in every compartment that is activated by the

extracellular field i.e. f_n is the slope of membrane voltage V_n at the beginning of the stimulus. Regions with positive activating function are candidates for spike initiation whereas negative activating function values causes hyperpolarization.

From which part of a neuron does artificial excitation start?

In this section the generalized activating function concept is tested with two rather simple model neurons, similar to that shown in Fig. 2.1, but with more elements. The temporal pattern generated in model neurons #1 and #2 by a single active electrode is analyzed in the following with the activating function concept. The electrode is assumed as ideal point source in an infinite homogeneous extracellular medium which results in the simple relation

$$V_e = \frac{\rho_e I_{electrode}}{4\pi r} \quad (2.4)$$

where V_e is measured in a point with distance r from the point source and ρ_e is the extracellular resistivity.

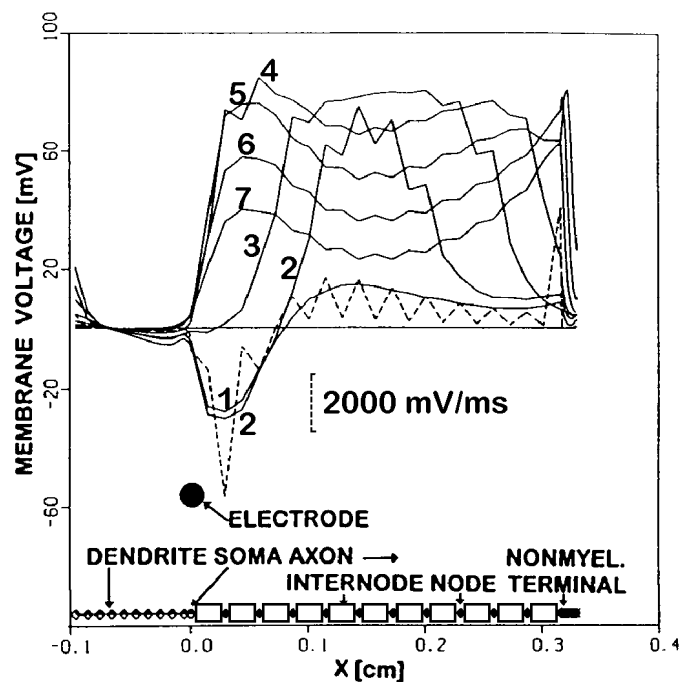


Fig. 2.2. Voltage distribution of model neuron 1 evoked by a positive $100 \mu\text{s}$, 5 mA stimulating pulse. The lower picture indicates the positions of the 40 compartments where membrane voltages are calculated. The positions of the soma and the initial segment coincide in the graph. The electrode is 1 mm just above the soma. The voltage change along the neuron generated by a positive stimulating pulse as predicted by the activating function f is shown as a dashed line. Note that the part of the neuron nearest to the electrode is the soma but there is neither the maximum nor the minimum of f . The strongest negative value of f is at the first node, the strongest positive value of f is at the first element of the unmyelinated part of the axon. Full lines show snapshots of the computed membrane voltage in intervals of $50 \mu\text{s}$, marked by numbers 1-7. Line 1 ($t=50 \mu\text{s}$) is similar in shape to the activating function. Dashed scale bar is for the activating function. (From Rattay 1998a).

Model neuron #1 has 40 compartments and no bifurcations, model neuron #2 consists of 3 dendritic processes with bifurcations, soma, initial segment and a myelinated axon which ends at an unmyelinated branching terminal. Neuron #2 consists of 179 compartments. However, because the branching parts are assumed to be symmetric, only 70 different compartments have to be computed. In both neurons every internode is represented by a single compartment. To reduce numerical calculations all elements of neuron #2 are positioned at the x-axis, that is, the angle at bifurcations is 0. The geometric parameters are gathered in Table 2.1. The electric parameters and membrane models used are found in Table 2.2.

The computed reaction of model neuron #1 to a positive current pulse from an electrode positioned just above the soma disproves the hypothesis that the current density in the extracellular medium is strongly related to the point of artificial spike generation: The maximum value of V_e as well as that of the extracellular current density of all the points of the surface of the neuron is at the soma, because this is the part of the neuron nearest to the electrode. However, the activating function f is rather small there, and Fig. 2.2 demonstrates that for this configuration the soma is one of the regions hardly excited by electrode current.

The 7 full lines in Fig. 2.2 represent the computed distribution of membrane voltage along the neuron within the first 350 μ s in steps of 50 μ s. Line 1 ($t=50 \mu$ s) and line 2 ($t=100 \mu$ s, three main peaks corresponding to nodes 4-6) show that the point of origin of spike generation is node 5. Because of the strong hyperpolarizing effect in node 1 and the positive values of f for nodes 6 to 10 the developing action potentials reach node 10 before reaching the soma. The higher propagation velocity at the right side is also reflected in the greater distance between the right falling edges of line 2 and line 3 compared to that at the left side. However, there is a change in propagation velocity seen in the next interval: the left edge of line 4 has traveled further than the right one, because signal propagation from the myelinated into the unmyelinated part is impeded [Rattay 1995]. The close distances of the right edges in the last lines are due to the slow propagation velocity in the unmyelinated axon.

TABLE 2.1: GEOMETRIC PARAMETERS OF THE COMPARTMENTS

diameter	first/last segment	remarks
d_{dendrite}	$4 \cdot 10^{-4} \text{ cm} / 1.55 \cdot 10^{-4} \text{ cm}$	3 (1)* dendrites, every dendrite has 10 segments; $3 \cdot 2^4 = 48$ (1) endings
d_{soma}	$10 \cdot 10^{-4} \text{ cm}$	
$d_{\text{initial segment}}$	$2 \cdot 10^{-4} \text{ cm}$	
d_{node}	$2 \cdot 10^{-4} \text{ cm}$	21 (10) nodes
$d_{\text{internode}}$	$2 \cdot 10^{-4} \text{ cm}$	50 sheets of isolating membranes
$d_{\text{unmyelinated axon}}$	$1 \cdot 10^{-4} \text{ cm} / 0.4 \cdot 10^{-4} \text{ cm}$	bifurcations after every third segment 16 (1) endings
d_{synapse}	$1 \cdot 10^{-4} \text{ cm}$	16 (1) synapses
length		
l_{dendrite}	0.01 cm / 0.006(0.01) cm	
$l_{\text{initial segment}}$	$6 \cdot 10^{-4} \text{ cm}$	
l_{node}	$1 \cdot 10^{-4} \text{ cm}$	
$l_{\text{internode}}$	0.0286 cm	
$l_{\text{unmyel. segment}}$	0.005 cm / 0.002 cm	
l_{synapse}	$1 \cdot 10^{-4} \text{ cm}$	
* values in brackets are for neuron #1 which has no bifurcations		

TABLE 2.2: ELECTRICAL PARAMETERS / MEMBRANE MODELS

intracellular resistivity ρ_i	0.1 kOhm*cm
extracellular resistivity ρ_e	0.3 kOhm*cm
capacity of cell membrane c_m	1 μ F/cm ²
neural subunit	membrane conductance
dendrite	constant: $g_m=10$ mS/cm ²
soma	warm HH-model*, $g_{leak}=10$ mS/cm ²
initial segment	CRRSS-model
internode	$g_m=1$ mS/cm ² , $g_{m,total}=0.02$ mS/cm ² $g_{m,total}=g_m/\text{number}_{layers}$, $\text{number}_{layers}=50$
node	CRRSS-model
unmyelinated axon	warm HH-model*, doubled channel density
synapse	warm HH-model*, doubled channel density
* The original data of the Hodgkin-Huxley model are used, but the right sides of the differential equations for the gating variables m,n,h are multiplied by 12 to take into account the faster gating processes in mammalian axons. The soma membrane was modelled with a higher value for the leakage conductance.	

The shape of the activating function (broken line in Fig. 2.2) is similar to that predicted by a full model computation at the beginning of the stimulation. However, there are additional currents between the segments and currents caused by effects of loading and unloading capacities, which smoothens the spatial zigzag shape of the activating function. The zigzag shape is partly explained by the different sizes of the areas of neighbored compartments that lead to differing values, e.g. for C_n in Eqn. (2.3). Missing the collective effects of neighbored segments is the reason why „needles“ in the activating function have small influences. The absolute maximum of f in Fig. 2.2 is a „needle“ appearing at the beginning of the terminal axonal partition. It only leads to a minor local increase in lines 1 and 2. A similar situation concerning excitability is at the dendritic ending, where $f>0$ is not restricted to a single compartment. Because no active membrane is assumed to exist there, high values of the activating function do not lead to an action potential, even if membrane voltages essentially above normal threshold are reached. Note the decrease in space and time of the left endings of the curves in Fig. 2.2 and pay attention to the fact that the soma is not excited within the first 350 μ s.

Figure 2.3 shows the possibilities to excite model neuron #2 with positive or negative current pulses from an electrode in the vicinity of the neuron. It is demonstrated that the predicted shapes and voltage strengths essentially depend on the electrode position relative to the neuron.

The electrode current needed to generate an action potential is related to the maximum value of the activating function at an ‘active’ compartment. However, computation of the ion currents across the active membranes demonstrates that high isolated peaks (needles), e.g. at an end of neuron #2 (Fig. 2.3), will not propagate as action potentials.

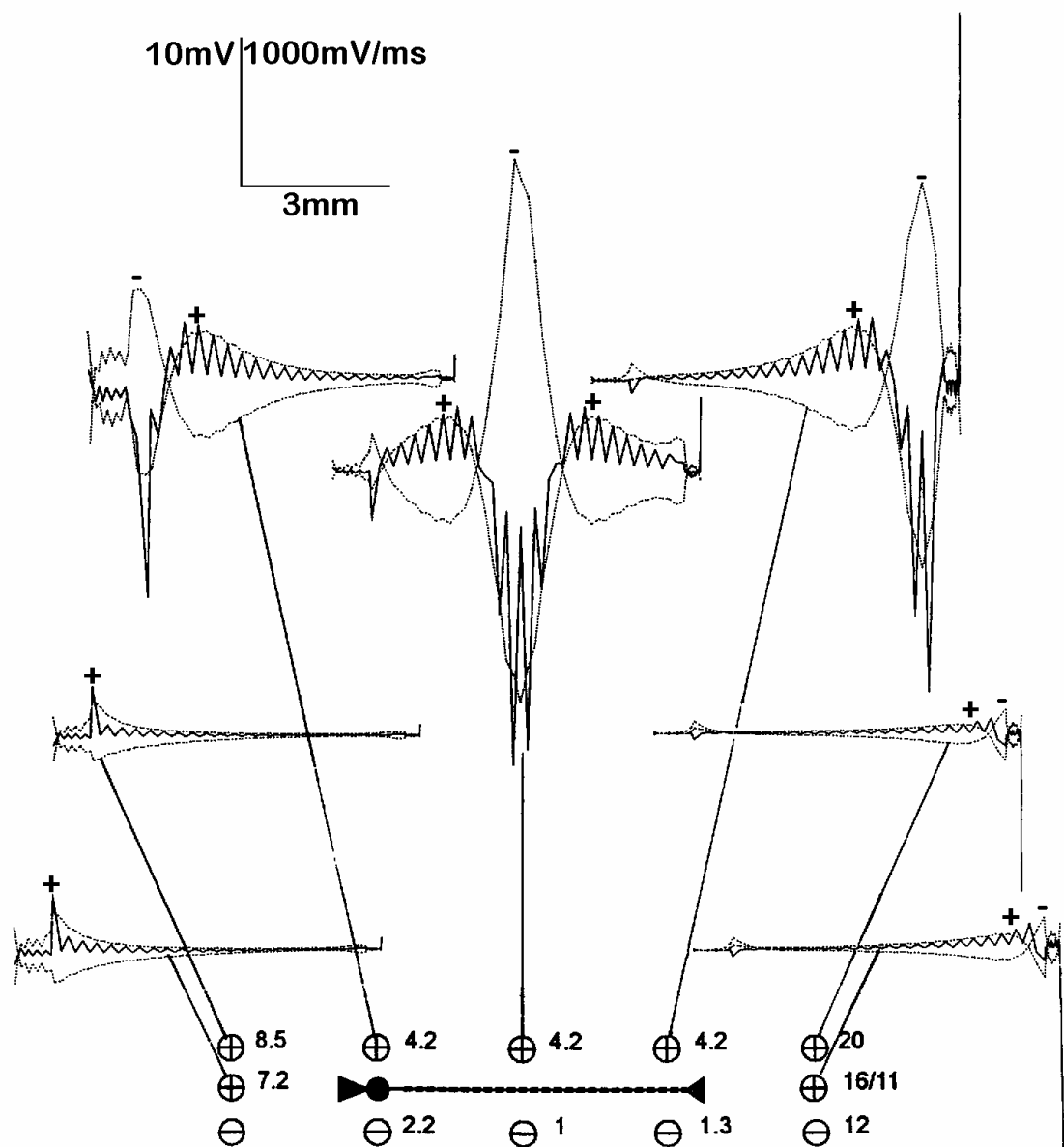


Fig. 2.3. Excitation of model neuron #2 with a 1 mA, 100 μ s pulse from an electrode moved along the neuron. The lower part shows the position of the neuron, which consists of dendritic tree, soma, initial segment, myelinated axon and the branching terminal (the lengths of soma, initial segment and node are not in scale). The neuron is placed on the x-axis of the coordinate system with center of soma at (0/0) and the positions of electrode in cm are (-0.3/0), (-0.3/0.1), (0/0.1), (0.3/0.1), (0.6/0.1), (0.9/0.1), (0.9/0). For these electrode positions full lines in the upper traces show membrane voltages changes as predicted from the activating function for a 1mA stimulating current. The dotted lines with a similar shape represent membrane voltages at the end of a 1 mA, 100 μ s pulse, computed with the full set of differential equations for dynamic membrane behavior. Computed reactions are also shown for cathodic stimuli (-1 mA), they are quite similar to the inverted 1mA responses. The signs + and - show the points where artificial spike generation is expected by the full system computation for positive and negative stimuli. Note that these points are close to the maxima and minima of the activating function. The numbers at the electrode positions marked by the circled signs + and - correspond to excitation thresholds for anodic and cathodic stimuli, respectively (Comp. Table 2.3). (From Rattay 1999).

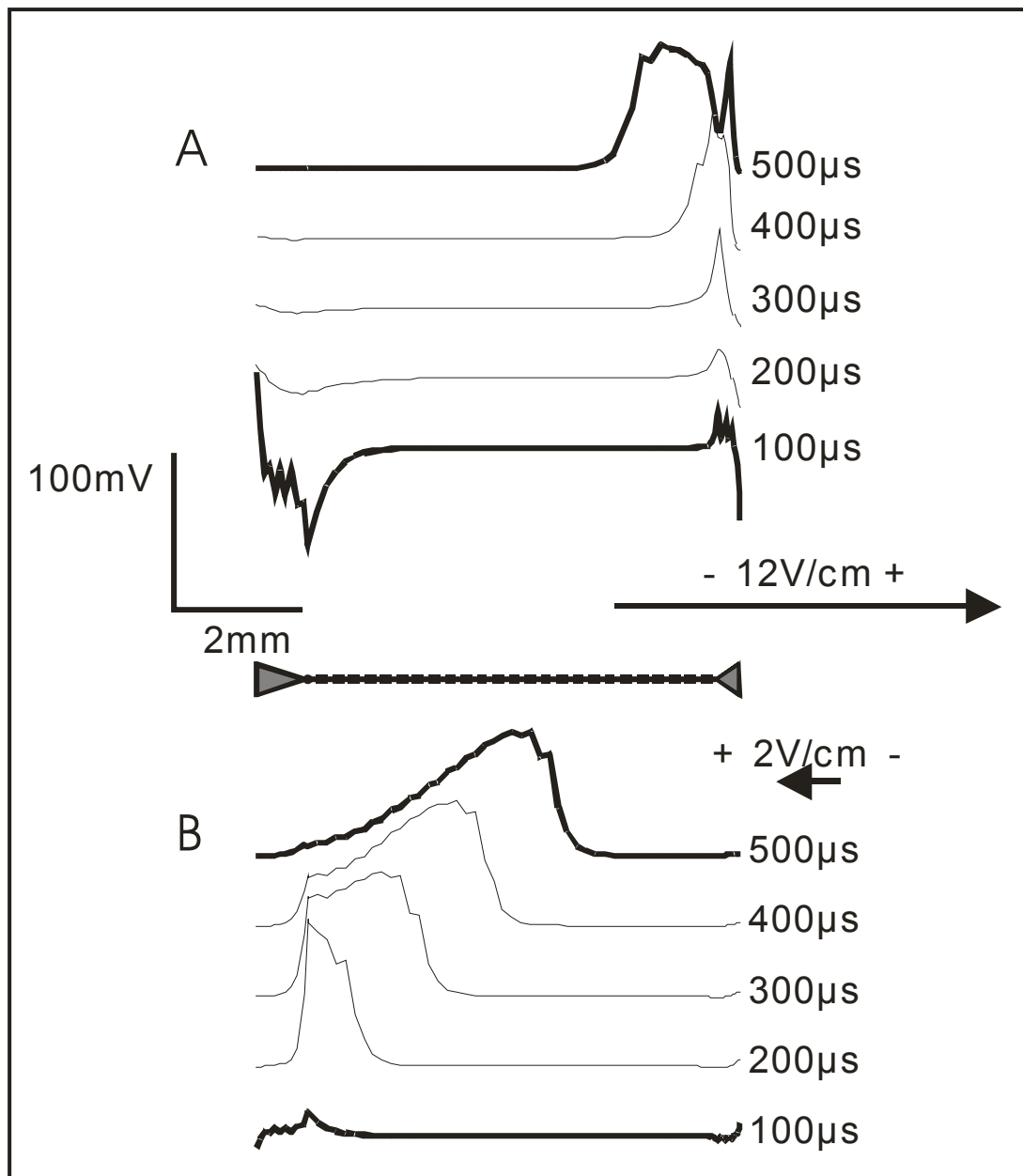


Fig. 2.4. Excitation of neuron #2 by a constant field, applied for 100 μ s. Depending on the orientation and strength of the field, a 'slow velocity' spike is generated in the unmyelinated branching part of the axon (A) or a 'fast' propagating spike is produced in the initial segment (B). The lines that show the membrane voltage along the neuron in intervals of 100 μ s are shifted in x and y direction. (After Rattay 1999).

Neuron #2 is most excited by cathodic currents when the electrode is above the center of the axon ($I_{\text{threshold}} = -1$ mA). In this case, voltage distribution is rather symmetric with a broad high maximum at the center and essentially smaller minima at both sides (Fig. 2.3). An action potential is generated at the place of voltage maximum and bifurcates and propagates to both sides. When polarity is changed, threshold current is 4.2 times larger as a consequence of the smaller maxima that are marked by + in Fig. 2.3, two spikes are generated simultaneously at symmetric positions. Moving the electrode along the axon causes increasing asymmetry of the activating function, +maxima (for positive electrode current) have similar sizes whereas -maxima decrease. This is an explanation why different electrode positions along the axon cause essential changes in the case of cathodic stimulation and

minor changes in the case of anodic stimulation. Different anodal versus cathodal threshold currents in myelinated axons are also reported in experimental studies, e.g. BeMent and Ranck (1969) found 3.19-7.7 (mean 4.57) times stronger thresholds for anodic stimulation and Armstrong et al. (1973) reports a factor between 1.0-3.2. Note, that when placing the electrode very close to the axon (less than internodal length) the relative position of the node has an essential influence which causes additional irregularities in current-distance relations [Rattay 1987, 1990, Roth 1994]. Further data on threshold relations are gathered in Table 2.3.

Many researchers have reported that stimulation with monopolar electrodes in front of the dendrites is often easier with anodic current [Ranck 1975]. The small stimulating effects of cathodic currents, that are restricted to the dendritic endings and to the unmyelinated terminal, can be seen in the two traces on the lower left of Fig. 2.3. With these electrode positions (3 mm in front of soma), excitation of neuron #2 is possible only for positive currents.

TABLE 2.3: THRESHOLDS AND THRESHOLD FACTORS FOR NEURON #2

Position of electrode in cm		Threshold currents in mA		anodic/cathodic
x	y	anodic	cathodic	threshold
-0.3	0	7.2	>80	-
0.9	0	16	11	1.5
-0.3	0.1	8.5	>80	-
0	0.1	4.2	2.2	1.9
0.3	0.1	4.2	1	4.2
0.6	0.1	4.2	1.3	3.2
0.9	0.1	20	12	1.7
-0.3	0.4	36	>80	-
0	0.4	68	54	1.3
0.3	0.4	46	36	1.3
0.6	0.4	71	50	1.4

Electrode positions close to the endings of a neuron will cause extreme values of the activating function in the last compartments that may represent synapses or areas with many synaptic contacts (three right traces in Fig. 2.3, but also left traces in Fig. 2.3 and rather high voltages at the left end in Fig. 2.2). Evaluations with the full set of equations show that synaptic activity can be stimulated at the axonal and dendritic endings: voltage changes >45 mV occur, which are not generating propagating action potentials but are strong enough for reliable synaptic transmission (comp. Katz and Miledi 1967).

Excitation by a constant field

Several years ago the excitation of neurons in a uniform electric field was analyzed. Hause (1975) reports that the strongest effect at a neuron with a straight axon occurs at the presynaptic axonal terminal. For Trachina and Nicholson (1986), the soma seems to be a likely site for action potential initiation. At first glance, these statements sound contradictory, but we will see from the next example that in principle each of the results is correct for a different situation: Neuron #2 becomes excited within the unmyelinated axonal terminal when a uniform field with a longitudinal component of 12 V/cm is applied for 100 μ s and when this field increases from the dendrite towards the terminal end (Fig. 2.4A). Changing

the direction of the field needs only 1/6 of the strength to generate a spike in the initial segment (Fig. 2.4B). The points of spike generation can be seen from the 100 μ s lines in Fig. 2.4. In case A, the compartments in the soma region are strongly negative but by changing the polarity (Fig. 2.4B) this region is able to generate an action potential. It is worth mentioning that the shape of the 100 μ s line of e.g. Fig. 2.4B can already be predicted from the two lowest traces of Fig. 2.3. Simultaneous activation of the electrode in front of the dendrite (this is the electrode marked in Fig. 2.3 by the threshold value 7.2) with a current of 1 mA and the electrode behind the axonal ending (marked by 16/11) with -1mA will cause a rather uniform field. This means that subtracting the 1mA response of the "16/11" electrode (shown in the right low part of Fig. 2.3) from that of the "7.2" electrode results in a curve which predicts the 100 μ s dipole response of neuron #2 and its shape is similar to the 100 μ s answer shown in Fig. 2.4B. Note that the peaks of the activating function close to the + and - marker for the two lower cases in Fig. 2.3 correspond to the points where spike generation is predicted in Fig. 2.4. This means, that the activating function can also be used to predict the origin of spike generation for uniform fields.

Case study on the human cochlear nerve

About 30000 bipolar cochlear neurons connect the inner hair cells from one human ear with the higher centers. Although detailed modeling results are presented in Chapter 3 and Chapter 4 we use now 'real' cell data (in neuron #3) to complete a list of characteristic phenomena which can be explained with the activating function concept. As in the previous examples, the electric field generated by a ring electrode is simplified by assuming constant conductivity of the extracellular medium. The bipolar neuron is assumed to have a weakly myelinated soma with two myelinated processes; we call the thin process a dendrite (1 μ m diameter). It has a 10 μ m long unmyelinated ending (denoted as node 0, Fig. 1.2) that typically makes only one synaptic contact to an inner hair cell. The center of the electrode is close to the center of curvature of the middle part of the dendrite.

The left part of Fig. 2.5 shows strong variations of the activating function with multiple changes of the sign implying small stimulated and hyperpolarized regions that alternate with the neuron's length coordinate, e.g. between node 5 and soma. Therefore, every internode was simulated with five compartments. The consequence becomes obvious by a close inspection of Fig. 2.5A: signs in the slopes of neighboring membrane voltage change at the beginning of the stimulating pulse. However, the term

$$\frac{V_{n-1} - V_n}{R_{n-1}/2 + R_n/2} + \frac{V_{n+1} - V_n}{R_{n+1}/2 + R_n/2}$$

in Eqn. 2.2 has an equilibrating influence for the voltages of neighboring compartments, which quickly smoothens the strong irregularities predicted by f (Fig. 2.5). Therefore, the efforts for this case study can be reduced to 1-3 compartments per internode without loss of accuracy.

Figure 2.5A shows that a positive 100 μ s pulse between 0.74 and 1.12 mA will cause propagating action potentials that are generated at node 2. Stimulation with currents stronger than 1.12 mA additionally generates a neural impulse at node 7. This (case B) action potential propagates from node 7 to both sides, blocks the node 2 spike and arrives earlier at the central destination than the case A spike. Stimulation with cathodic currents is easier and similar to the natural situation: spike generation occurs at the beginning of the neuron in case C. After node 5, the spike has some delay because it is hard to drive the large soma region with the currents from the thin process. Small disturbances of f in the last internode before the soma region disable spike propagation for electrode currents between -0.5 and -0.7 mA (cathodic block, Fig. 2.5D).

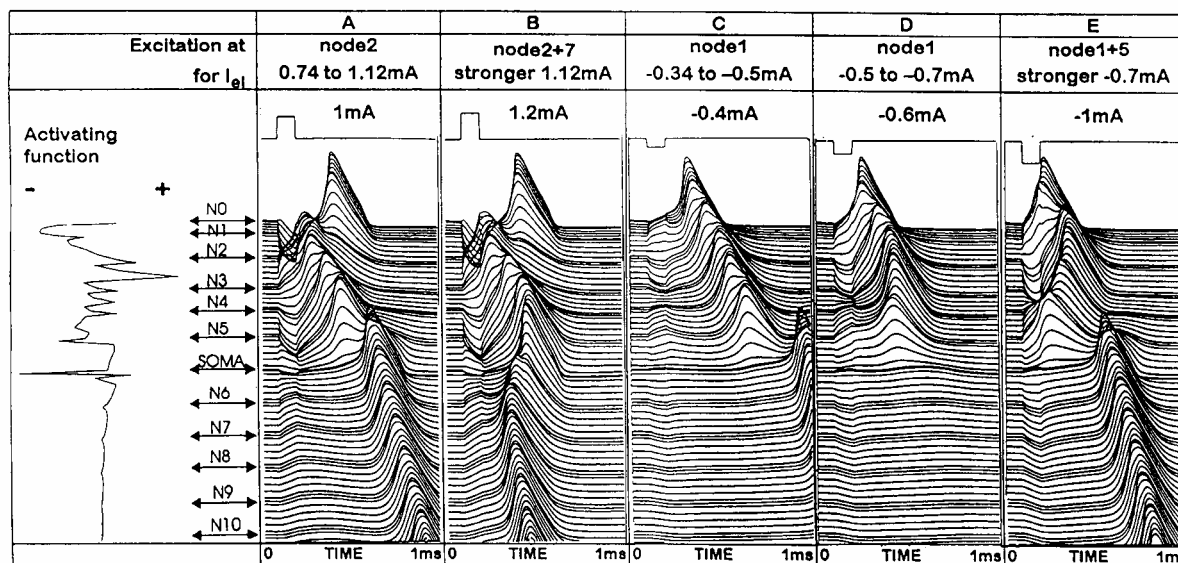


Fig. 2.5. Spike generation of neuron #3 by $100 \mu\text{s}$ pulses. According to the activating function (left), the neuron is most excitable at node 2 for positive stimuli; the maximum of f is within the passive membrane of the third internode. For negative electrode currents, f predicts stimulating influence at node 1, at node 5 and at the unmyelinated part in front of the soma. Firing behavior changes when signal strength is varied. Every line in (A-E) shows membrane voltage for every compartment as a function of time. Soma voltage appears as a single dark line in the center because of the similar signal shape of soma and the two neighbored compartments with a center distance of $12.5 \mu\text{m}$ to the soma; reaction at nodes are center of triple lines. Note the delay in the axonal part when a 'dendritic' action potential passes the soma region (A,C,E). The rather small hyperpolarizing influence in the last dendritic internode hinders spike propagation into the axonal process (D) (From Rattay 1999).

Although the blockage of neural signals is of interest mainly for other clinical applications, I have investigated the blocking behavior in the auditory nerve. Computed model reactions demonstrate that with a -0.6 mA stimulus, as used in Fig. 2.5D, the natural spiking activity can be stopped (Fig. 2.6A). Because a positive 0.6 mA pulse only generates subthreshold activities, this signal strength makes it possible to stop repetitive natural spiking by applying a periodic sequence of negative and positive square pulses that avoid charge accumulation (Fig. 2.7).

TABLE 2.4: THRESHOLDS FOR NEURONS WITH MYELINATED AND UNMYELINATED PROCESSES

Excitation with $100 \mu\text{s}$ pulses	neuron #3 myelinated dendrite	neuron #3a unmyelinated dendrite
Anodic, cathodic thresholds current	+0.74 mA, -0.34 mA	1.12 mA, -2.5 mA
Quotient	$0.74/0.34 = 2.2$	$1.12/2.5 = 0.44$

In a 'Gedankenexperiment', the myelinated dendrite of neuron #3 is substituted with an unmyelinated fiber of the same diameter and shape, and with a HH membrane as assumed for the soma (neuron #3a). The activating function along the neuron is shown in Fig. 2.8A in the same way as in Fig. 2.5: Again, there are multiple changes of the signs in the periphery process. The small values of f are indicators of the fact that much stronger currents are needed to excite an unmyelinated fiber compared to a myelinated (Ruch et al. 1968):

Excitation of this neuron needs $100\ \mu\text{s}$ cathodic electrode currents of at least $-2.5\ \text{mA}$; however, for currents stronger than $-6.6\ \text{mA}$, blockage occurs at the beginning of the central axon (neuron #3 reacts to rather small quantitative differences, if the dendrite is assumed to have the passive neuron #1 membrane). Note that neuron #3a is quite easier to excite with positive currents – exactly opposite to neuron #3 (Table 2.4).

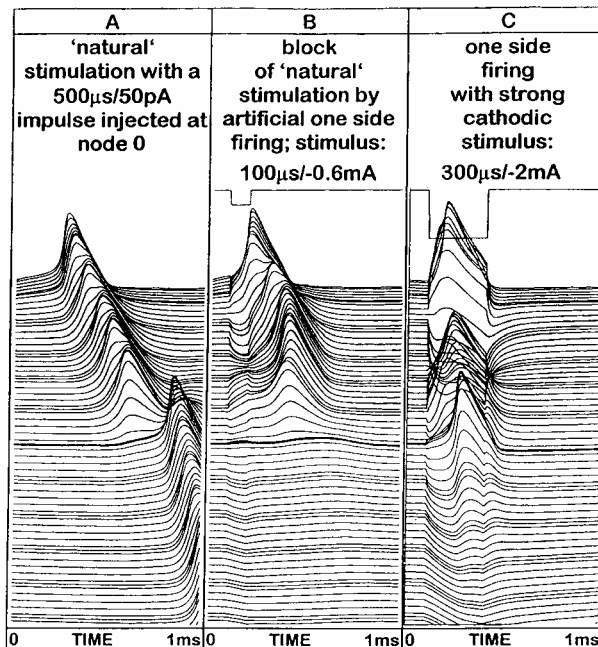


Fig. 2.6. Blockade of neural impulses by cathodic currents. (A) Simulation of synaptic excitation of neuron #3. (B) Applying synaptic current and the block current as shown in Fig. 2.5D hinders excitation of the soma region. (C) A long, strong cathodic pulse produces hyperpolarization of the axon. The soma becomes excited, but not node 6.

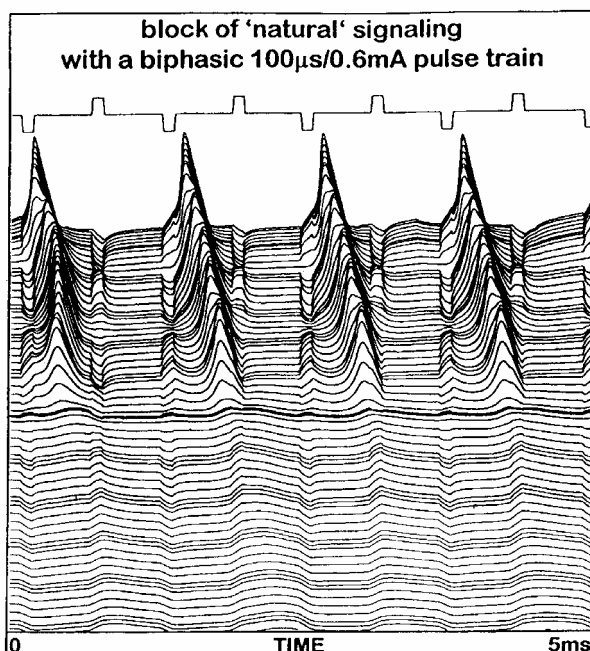


Fig. 2.7. Blockage of action potentials in neuron #3 by pulses with alternating polarity. Node 0 is stimulated periodically every $1.5\ \text{ms}$ by $500\ \mu\text{s}$, $50\ \text{pA}$ current injection as shown in Fig. 2.6A. The additional periodic stimuli (top) with interpulse times of $500\ \mu\text{s}$ are asynchronous to the “natural”, but they force spike generation to be synchronized with the negative stimuli and allow spike propagation only within the dendrite.

Discussion

The activating function gives valuable hints about the influence of structural elements and neural parameters on artificial excitation and blockage of neural activity. Eqn. 2.2 shows

that besides f_n , the contributions from membrane currents and currents to the neighbored compartments are important for the evolution of membrane voltage in the n -th compartment. Even starting in the resting state demands that careful attention be paid to the values of f_n surrounding the maximum. We have demonstrated that a compartment with an isolated high value of f_n and with small membrane area or with low density of sodium channels is not expected to be the generating element of a spike, e.g. the first (comp. Fig. 2.2) or the last (Fig. 2.3, right upper case) compartment of the unmyelinated axonal terminal will not contribute essentially to the excitation process. On the other hand, the presented examples show that when taking into account the collective effects of neighboring compartments, the activating function gives a first impression of the excitation process. The evaluation with the full set of differential equations for the ionic currents (Eqn. 2.2) is recommended for a final decision about the point of highest sensitivity to artificial spike generation.

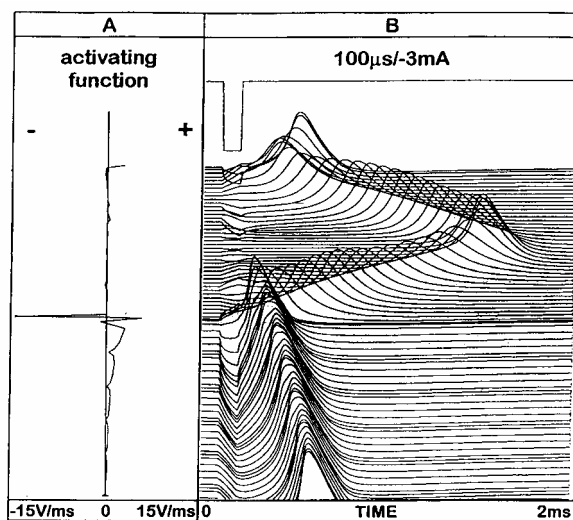


Fig. 2.8. Excitation of neuron 3a with an unmyelinated dendrite needs strong cathodic currents. The values of the activating function within the dendrite (upper part) are essentially smaller than at the central axon. The single high value occurs at the last active compartment before the soma. This element and some compartments at the beginning of the dendrite become excited. Note the low velocity of the neural impulses that propagate in the Hodgkin-Huxley membrane of the thin dendrite.

A surprising result of our analysis is that the direct stimulating effect of the soma membrane is rather small. Nevertheless, special care is necessary for the soma membrane model because the variety in types and numbers of ion channels found in the cell body membranes, needs an adequate description when a specific type of neuron is investigated. For example, we cannot generalize the results obtained from an integrate-and-fire neuron with Hodgkin Huxley dynamics for the case of a pacemaker neuron that is spiking without any electrical stimulus.

Another point which is out of scope of this article is that the high density of excitable elements in CNS stimulation which become active at the same time, cause rather strong membrane currents that may significantly influence the extracellular potential.

Conclusions

The presented examples demonstrate that neural excitability depends heavily on geometric and electric parameters. For several cases, the concept of the generalized form of the activating function gives explanations for the variance found in experiments (comp. Ranck 1975). The following 11 rules of thumb were arrived at by applying the proposed theory and the evaluations of the proposed compartment models with the full set of equations:

1. The myelinated axon is the most excitable part of a neuron. The presumption of Porter (1963) that it is always the axon which is stimulated is shown to be correct for many cases (Figs. 2.2, 2.3, 2.5). We have shown that the strongest changes in the extracellular field in the soma region can cause excitation in the initial segment first.
2. In neurons with myelinated axons the soma is difficult to stimulate because the high soma capacitance causes much smaller values of the activating function compared to that of the nearest axon compartments (comp. Eqn. 2.3); an exception is the case shown in Fig. 2.4B. The activating functions for two neurons with the same shape and diameter show that the excitation threshold increases when the number of myelin sheets is reduced (compare the activating functions of the myelinated peripheral axon in Fig. 2.5 and of the unmyelinated axon in Fig. 2.8, where both axons have the same shape). Therefore, a cell body that is connected with an unmyelinated axon is easier to stimulate directly as compared to the myelinated case.
3. Excitation with electrodes in the vicinity of the axon with negative currents is (at least) up to 4.2 times easier compared to positive stimuli (Figs. 2.3, 2.4; see however Fig. 2.8 and next statement).
4. The relation between positive and negative threshold current varies extremely, and it strongly depends on electrode position (Fig. 2.3) and on the neuron's parameters (Table 2.4).
5. The maximum value of the activating function is a good indicator for finding the most excitable compartment; note however, that neighboring compartments support or hinder excitation in the compartment with the largest f . Therefore, isolated high peaks in the series of f_n may not cause excitation, especially if the membrane activity in that compartment is small (small area, few ion channels). As an example, the high value of f for the first compartment of the nonmyelinated terminal in Fig. 2.2 is isolated and this compartment is not very excited.
6. Generally, excitation is easier with negative currents (Fig. 2.3). However, this does not hold for (all) electrode positions within the dendritic region. Positive currents from electrodes positioned in front of the dendritic tree will generate spikes at the beginning of the axon. Negative stimulation needs very strong currents, if stimulation is possible at all (Figs. 2.3, 2.8).
7. The propagation of unwanted natural neural activities towards the axon may be stopped by applying a sequence of negative stimuli from an electrode positioned in front of the dendrites because of the strong hyperpolarization which can be produced at the beginning of the axon (comp. the two left low traces in Fig. 2.3). Within a rather small range, blockage of spiking is possible for other positions of the electrode (Figs. 2.6, 2.7).
8. Electrode positions at the terminal side will generate spikes in the endings of the unmyelinated axon (Fig. 2.3).
9. High values of the activating function can occur at the endings of the

- processes which may result in synaptic activities, even if no propagating spike is evoked (comp. Fig. 2.3).
10. The total activating function for several sources can be obtained by summation ($f_{total} = \sum f_j$). Often only the nearest electrode contributes to the neuron's behavior, because an electrode's influence decreases rapidly with distance (Rattay 1990).
 11. High values of the activating functions result from irregularities, either in the extracellular potential along the neuron or in the geometry of neighbored compartments. During electrical stimulation of the brain via surface electrodes on the scalp or during magnetic stimulation, the electric field is rather uniform. In such cases bending of the axon¹ (comp. also Tranchina and Nicholson 1986), branching (Fig. 2.4A: zig-zag shape of the 100 μ s line at the axonal terminal and at the dendrites) or extreme changes of diameters (Fig. 2.4B, soma) play the dominant role in determining the site and threshold of stimulation.

¹ The activating function is related to the second derivative of the extracellular voltage V_e along the axon [Rattay 1990] - and therefore the direction and value of the curvature of V_e is associated with the sign and value of f , respectively. A \cup shaped curvature of V_e causes a positive f value; \cap results in $f < 0$.

3. A model of the electrically excited human cochlear neuron

Part I. Contribution of neural substructures to the generation and propagation of spikes

Differences in neural geometry and the fact that the soma of the human cochlear neuron typically is not myelinated are reasons for disagreements between single fiber recordings in animals and the neural code evoked in cochlear implant patients. We introduce a compartment model of the human cochlear neuron to study the excitation and propagation process of action potentials. The model can be used to predict (i) the points of spike generation, (ii) the time difference between stimulation and the arrival of a spike at the proximal end of the central axon, (iii) the vanishing of peripherally evoked spikes at the soma region under specific conditions, (iv) the influence of electrode positions on spiking behavior, and (v) consequences of the loss of the peripheral axon. Every subunit of the cochlear neuron is separately modeled. Ion channel dynamics are described by a modified Hodgkin-Huxley model. Influence of membrane noise is taken into account. Additionally, the generalized activating function is introduced as a tool to give an envision of the origin of spikes in the peripheral and in the central axon without any knowledge of the gating processes in the active membranes. Comparing the reactions of a human and cat cochlear neuron, we find differences in spiking behavior, e.g. peripherally and centrally evoked spikes arrive with a time difference of about 400 μs in man and 200 μs in cat.

3.1. Introduction

With promising new human electrophysiologic measurement techniques as neural response telemetry and auditory brainstem response recordings evolving, a model of the electrically excited human cochlear neuron is a valuable theoretical tool to understand the phenomena encountered during electrical stimulation. A major target is to explain the wide variation in performance across individual implant users. By considering the effects of speech coding strategies at the neural level the patients' reception of speech and music could be considerably improved.

Although the human and animal cochlear neurons essentially differ, modelers have remained focused on animal models to investigate and predict auditory nerve function. As a consequence, wrong assumptions of the nerve fiber's morphometric and electric properties were made. In the following we demonstrate that the characteristic differences in man and cat concerning cochlear nerve geometry and the degree of insulation by myelin - especially at the soma - cause remarkable differences in spiking behavior.

The first attempts to simulate the electrically stimulated cochlear nerve were single compartment models, suited for the prediction of the temporal reactions of an excitable patch of membrane. Calculations were done with the following models described in Chapter 1, that is HH [Hodgkin and Huxley 1952], FH [Frankenhaeuser and Huxley 1964], CRRSS [Chiu-Ritchie-Rogart-Stagg-Sweeney 1979, Sweeney et al. 1987], SE [Schwarz and Eikhof 1987] as well as with the F model [Fitzhugh 1969]. Note that most of the original model data are based on low-temperature experiments. Therefore they have to be adjusted for cochlear implant modeling (for details and review see Rattay 1990): It is recommended that all gating processes be sped up by a common factor of 12 in HH and by individual factors in FH. The F model needs an acceleration factor of 7 to be in accordance with auditory nerve temporal behavior.

Surprisingly, the 'warmed' HH-model (gating processes accelerated), which is based on the unmyelinated squid membrane, gives the best fit to the observed temporal behavior of auditory nerves [Motz and Rattay 1986, Rattay 1990]: (i) Only the HH and the F model are able to produce multiple spiking at low frequency sinusoidal stimulation as described by Hartmann et al. (1984). (ii) The HH and SRB model have an essentially longer chronaxie compared to the other models, the single compartment HH model chronaxie (space clamp condition) is 340 μ s, Parkins and Colombo (1987) report 350 μ s in squirrel monkeys. (iii) If a stimulating pulse is too weak to generate an action potential (AP), the HH model and the SE model are the only ones that can make use of a second weak pulse applied shortly after the first one to give rise to an AP. This cumulative effect has also been reported in a psychophysical experiment with cochlear implant patients by Dillier (personal communication, for details see Rattay 1990, page 217-219).

Several observed phenomena in neural excitation cannot be explained by the response of just a single patch of neural membrane. The temporal information obtained in the spikes of an electrically excited auditory nerve fiber includes, e.g. the spike travel time, which essentially depends on the point of spike generation [Stypulkowski and Van den Honert 1984, Van den Honert and Stypulkowski 1987a,b, Javel 1990, Shepherd and Javel 1997]. In 1987 Colombo and Parkins started spatial modeling for the cochlear neuron. They followed the method of Reilly et al. (1985) and tuned a lumped circuit FH model to represent physiological data from their single fiber recordings in squirrel monkeys [Parkins and Colombo 1987]. Several model parameters were chosen according to the morphometric findings of Liberman and Oliver (1984) in the cat.

The first outstanding three dimensional model that took essential elements of the complex geometry of the inner ear into account was developed by Finley et al. (1990). Using the finite element method potential distributions were calculated for different types of electrodes along the target neurons. In a second step they determined the corresponding activating functions, which is a good first approach of describing the responsiveness of neural fibers to predicted electrical fields: in areas where the activating function is positive a fiber becomes stimulated (depolarized), whereas in regions with negative activating function fibers react in the opposite way, they become polarized or hyperpolarized. Recently, this theory has been generalized for neurons of arbitrary shape, and first results are available for the human auditory nerve [Rattay 1998a, 1999].

Several spatial models were developed to calculate the potential distribution in the cochlea, e.g. Frijns et al. (1995) developed a rotationally symmetric volume conductor model of the second turn of the guinea pig cochlea using the boundary-element method. Nerve fiber responses were calculated with a version of the SE model for a nerve fiber morphology based upon the findings of Liberman and Oliver (1984) in the cat, and Brown (1987) and Gleich and Wilson (1993) in the guinea pig.

We will present a spatial model of the human cochlear neuron that for the first time closely sticks to human morphometric data as known so far. All the neural subunits are individually described by connected electric circuits. Ion channel dynamics is described by the 'warm' HH model. Influence of membrane noise is taken into account. We will compare the reactions of a cat and human cochlear neuron in different case studies.

Investigating the course of synaptically initiated action potentials in man and cat leads to a difference in the propagation process. As for the human case, it takes a spike more than 0.3 ms to get over the unmyelinated soma and to arrive at the central process. This latency correlates well with recent neural response telemetry data from cochlear implant patients, where in few cases double neural response peaks with interpeak times between 0.3 and 0.5 ms have been reported [Dillier 1997, Lai and Dillier 2002, Cohen et al. 2004]. Of course, this time shift phenomenon cannot occur in patients with peripherally degenerated, but centrally intact nerve fibers, as has been observed in material derived from patients with hearing loss [Felix et al., 1997]. Nevertheless, how these people can hear, might be indicated by our

computer simulations of the electrically stimulated cochlear neuron. The results show that slight variations in stimulus configuration can alter the site of stimulation within the same neuron: spikes can arise in the peripheral as well as in the central processes. This phenomenon was observed several times in cat single fiber recordings [e.g. Van den Honert and Stypulkowski 1987a,b, Miller et al. 1999] and it is explained in detail by Javel (1990).

The purpose of this chapter is to supply other modelers with a cochlear neuron model and to analyze excitation and propagation effects that are directly related to the specific architecture of the human cochlear neuron. By computer simulation firing behavior is explored on the single neuron level. Attention is paid to the influence of ion channel current fluctuations in the active membranes and to the loss of peripheral processes. Additionally, it is shown how the generalized activating function can be used to get a quick overview of sites of spike origin. In the next chapter we study excitation effects related to human cochlear geometry.

3.2. Material and Methods

Morphometry

Morphometric measurements of cochlear nerve fibers and spiral ganglion cells in man were either performed in serial celloidin sections [Pollak et al. 1987] or in microdissected cochleae [Felix et al. 1990]. The basic differences between a human and a cat cochlear neuron are illustrated in Fig. 3.1A. Three internodal compartments precede the cat soma [Liberman and Oliver 1984]. In man the internodal lengths have not been investigated systematically. Peripheral internodal lengths were chosen according to Finley et al. (1990), who assumed the cell body positioned after 8 internodes. In our standard human neuron (Fig. 3.1A) the peripheral axon has 6 internodes, resulting in a P0 - soma distance of 2.3 mm. Spoendlin and Schrott (1989) reported that the length of the peripheral axon from the habenula perforata to the spiral ganglion cells is 1.2 mm. These measurements were performed on formalin or glutaraldehyde fixed temporal bones. These fixatives induce shrinkage of about 20-30 % in soft tissue [Romeis 1968]. For that reason we can assume that the peripheral axon as described by Spoendlin and Schrott has an average length of about 1.5 mm. However, the positions of the human cell bodies vary a lot, which is in contrast to the tight packing of cat spiral ganglion cells in Rosenthal's canal. To account for these variations we considered a second soma position (denoted as short dendrite case) at a distance of 1.5 mm from nerve base.

The cell bodies differ not only in size, i.e., 25-30 μm in man [Spoendlin and Schrott 1989] and about 20 μm in cat [Liberman and Oliver 1984], but also in the number of myelin layers surrounding them. According to Ota and Kimura (1980) 94% of human spiral ganglion cells are unmyelinated and mostly surrounded by one to several layers of satellite cells. The pre- and postsomatic areas, the lengths of which vary a lot, are not shielded by myelin, either (Fig. 3.1B). On the other hand, in all mammals studied so far 90 to 95% of the spiral ganglion cells are large in size and myelinated. In cats 95% of spiral ganglion cells are firmly myelinated [Spoendlin 1971]. It is almost a reverse proportion between man and cat. This morphological difference is of major relevance for the propagation of an action potential (AP).

If the soma is hardly covered by any insulating material such as myelin, its membrane acts as a capacitor of high capacitance². Thus, a lot of an AP's energy is needed to load this capacitor, before the AP can propagate to the central compartments. With human somatic

² N-layers of myelin act as N capacitors in series, i.e. the total capacitance becomes the N-th part of the capacitance of a single layer.

capacitance being significantly higher than the somatic capacitance in cat, it is much more difficult for APs to pass the soma of humans than the soma of cats.

Axon diameters of man and cat are rather similar: in man both central and peripheral axon diameters are just slightly larger than in cat. There is a greater variance in diameters in older people compared to young children [Spoendlin and Schrott 1989]. Liberman and Oliver (1984) reported for cats mean central axon diameters of 2.54 and 2.31 μm for high and low spontaneous rate neurons, respectively, the corresponding mean values for the peripheral axons are 1.44 and 1.19 μm . In spite of variations in the axon diameters of cat and man [Felix et al. 1992], we use 1 μm and 2 μm as standard diameter values for peripheral and central axons for both cat and man, respectively. In this way it is easier to demonstrate that essential differences in the excitation between man and cat do not depend on differences of axon diameters.

Fig. 3.1 represents a human cochlear neuron at the upper end of the basal turn. In man the spiral ganglion cells can well be related to the basal turn but the classification within the other turns is much more difficult than in the cat [Hinojosa and Lindsay, 1980].

Compartment model

A cochlear neuron consists of several subunits with individual geometric and electric parameters: the peripheral terminal, the peripheral nodes and internodes, the presomatic region, the soma, the postsomatic region, and the central nodes and internodes are subunits with different membrane compositions according to their physiological tasks. Usually, every subunit is represented by one compartment, which is modeled by an electric circuit (Fig. 3.2). However, the compartment size has to be that small that the compartment's membrane voltage can be represented by an average value without loss of accuracy. If this demand is not met, additional compartments are necessary to describe one single subunit. For details see Rattay (1990, 1998a).

The ion membrane current that is governed by the gating mechanisms of specific voltage sensitive ion channels consists of two components: $I_{ion,n} = A_n \cdot i_{ion} + I_{noise,n}$ where the ionic membrane current density i_{ion} is computed according to the HH equations and $I_{noise,n}$ represents ion channel current fluctuations in the active compartments (unmyelinated terminal P0, nodes, pre- and postsomatic compartment, soma). To account for the fact that the human and cat cochlear neuron operate at higher temperatures and large parts of their fibers are covered by myelin two modifications are undertaken with respect to the original HH model. Firstly, the gating processes are sped up by the common factor 12. Secondly, the sodium-, potassium-, and leakage-conductances are multiplied by the factor 10 to reach 10fold channel density in a node. Model data are listed in Table 3.1 for man and cat. To simulate the reactions of the auditory nerve we use a two-step procedure. In the first step the extracellular voltage is calculated for every compartment. In the second step the time course of the voltages is simulated by evaluation of Eqn. 2.2. 100 μs pulses are used as stimulus signals in all examples with the exception of Fig. 3.3.

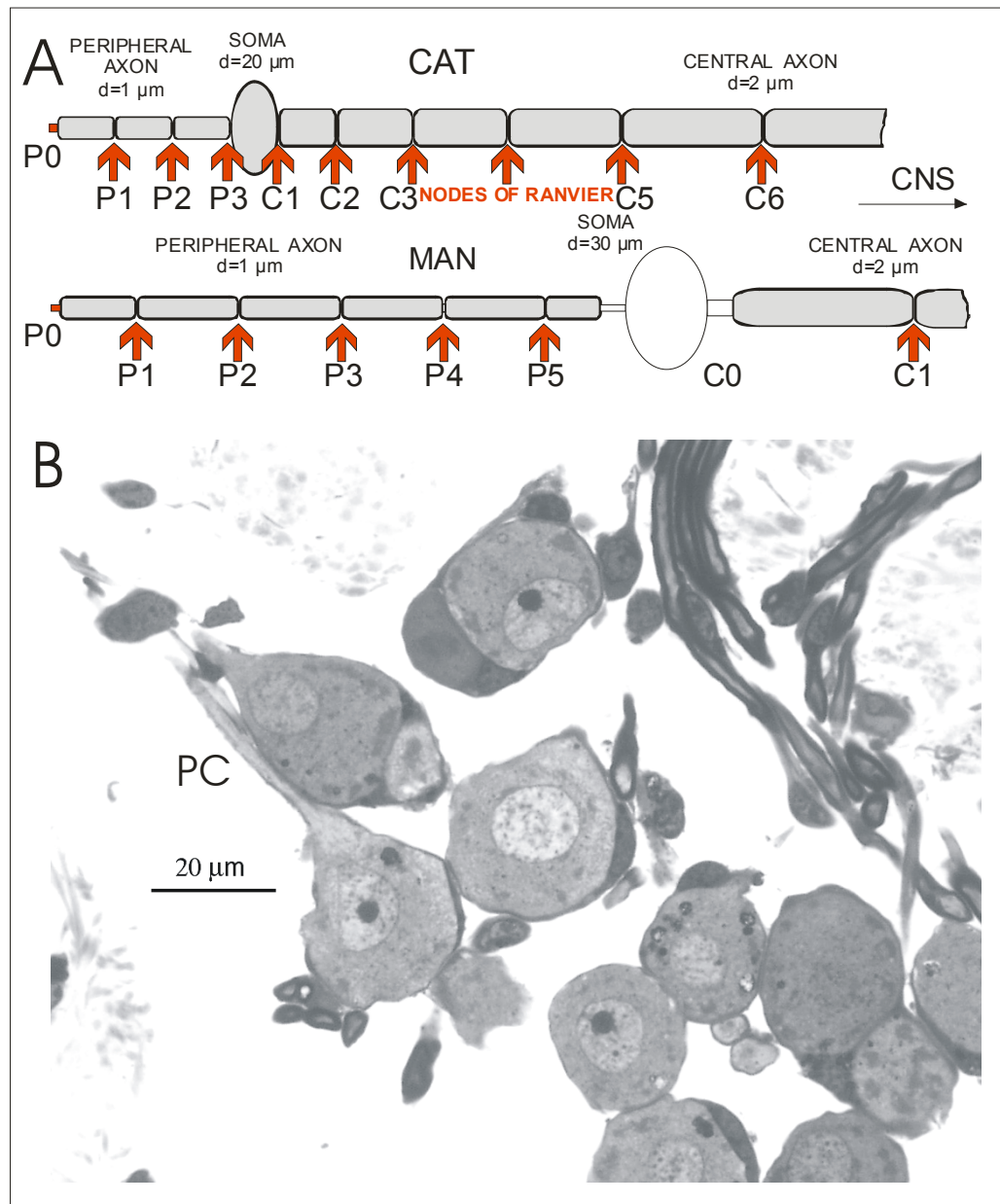


Fig. 3.1. A. Scheme of a cochlear neuron in man and cat. Most parts of the neurons are insulated by myelin (shaded areas). In both cases the synaptic endings of the peripheral axon are unmyelinated (this part, which is denoted as node0 or P0 in the following, is assumed to be $10\ \mu\text{m}$ long). The compartment sequence in MAN is: P0 - first peripheral internode - node - internode - ... internode - presomatic compartment - soma - postsomatic compartment - first central internode - node - ... ; in CAT there are no specific pre- and postsomatic compartments, the soma is between two nodes of Ranvier. Typically, the human afferent cochlear neuron is also unmyelinated in the presomatic, somatic and postsomatic region. The first 3 internodes in cat are about $150\ \mu\text{m}$ long, and length gradually increases in the first part of the central axon, i.e., these internodes are $150, 200, 250, 300$ and $350\ \mu\text{m}$ long (data from the 800-3000 Hz region as reported by Liberman and Oliver 1984). Internodal lengths of the human cochlear nerve have not been recorded systematically, values from Finley et al. (1990) are used. B. Cross section of human cochlear neurons showing unmyelinated somatic regions. Note the ganglion cell in the center of the figure where a part of the unmyelinated presomatic compartment (PC) is visible, before it leaves the plane of intersection.

TABLE 3.1: STANDARD PARAMETERS FOR THE COCHLEAR NEURON

	MAN	CAT
length		
unmyelin. terminal	$10 \cdot 10^{-4}$ cm	$10 \cdot 10^{-4}$ cm
presomatic region	$100 \cdot 10^{-4}$ cm	-
postsomatic region	$5 \cdot 10^{-4}$ cm	-
diameter		
peripheral axon	$1 \cdot 10^{-4}$ cm	$1 \cdot 10^{-4}$ cm
soma	$30 \cdot 10^{-4}$ cm	$20 \cdot 10^{-4}$ cm
central axon	$2 \cdot 10^{-4}$ cm	$2 \cdot 10^{-4}$ cm
node length	$2.5 \cdot 10^{-4}$ cm	$1.5 \cdot 10^{-4}$ cm
Resistivity		
intracellular	0.05 kOhm*cm	0.05 kOhm*cm
extracellular	0.3 kOhm*cm	0.3 kOhm*cm
capacitance of cell membrane (1layer)	$1 \mu\text{F}/\text{cm}^2$	$1 \mu\text{F}/\text{cm}^2$
Membrane conductance		
unmyelin. terminal	HH-model(10)*	HH-model(10)*
presomatic region	HH-model(10)*	-
soma	HH-model*	-
postsomatic region	HH-model(10)*	-
Internode conductance	$g_m = 1 \text{mS}/\text{cm}^2$ number _{layers} =40(80)	$g_m = 1 \text{mS}/\text{cm}^2$ number _{layers} =40(80)
Nodes of Ranvier	HH-model(10)*,	HH-model(10)*;
* HH-model: The original data of Hodgkin-Huxley (1952) are used, but the right sides of the differential equations for the gating variables m,n,h are multiplied by 12 (corresponding to a temperature of 29 °C in the original HH-model) to take into account the faster gating processes in mammalian axons. HH-model(10): the sodium-, potassium-, and leakage-conductances are multiplied by the factor 10 to simulate 10fold channel density.		

The human soma is assumed to have 3 layers of insulating membranes, the cat soma is calculated with 13 layers. 40 shielding layers for the peripheral internode (80 for the central internode) are found from cochlear nerve cross section pictures with the assumption of 8.5 nm per layer [Arbuthnott et al. 1980, Rattay 1990 p.34], which is in the upper region of reported data [Spoendlin and Schrott 1989, Arnesen and Osen 1978].

The standard cat neuron consists of 4 peripheral and 16 central nodes, soma, and 18 internodes (first internodal lengths according to Fig. 3.1A, from the fifth central internode on the internodal length is assumed to be 350 μm), the standard human neuron consists of 6 peripheral and 15 central nodes, 1 postsomatic and 3 presomatic compartments, soma, and 21 internodes (peripheral internodal lengths according to Figs. 3.1A and 3.5, the central internodal length is 500 μm). The geometry of the 'short dendrite' neuron results from skipping the internodes between peripheral nodes P3 and P5. Units in cm, kOhm, etc. allows direct data transformation between the modified HH-model and Eqn. 2.2.

Current fluctuations in the active membrane compartments

The models for the gating processes in the excitable membrane (HH, FH, F, CRRSS, SE, SRB) describe the probability of opening and closing of ion channels in a deterministic way. This means that without introduction of additional noise it is not possible to obtain the observed variance in spiking times in the cochlear nerve [Motz and Rattay 1986]. An accurate model may account for the relation of individual fluctuations in every ion channel [Holden 1976, Sigworth 1980, DeFelice 1981]. Such a model is expected to show most of the noisy behavior in nerve fibers as reported by Verveen and Derksen (1968), e.g., the membrane noise increases with deviation from the resting voltage, and noise becomes greater when a

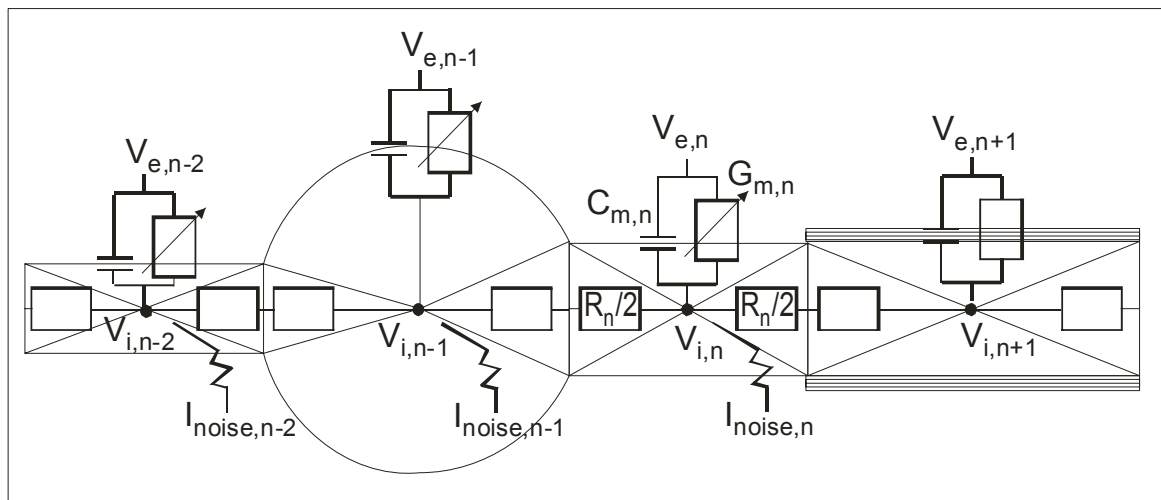


Fig. 3.2. Part of the electric network to simulate a cochlear neuron. Examples given describe the pre- and postsomatic compartment, the soma, and the first central internode of a human cochlear neuron, as e.g., in Fig. 3.1A. The electric components are shown for the postsomatic compartment: axoplasmatic resistance to the neighbors ($R/2$ for cylinders), membrane capacitance C_m , and the membrane conductance G_m , which is only constant in compartments with passive membranes (shielded by myelin). The batteries resulting from differences in ion concentrations between the inside and the outside are not shown. Ion current fluctuations I_{noise} in the active membrane compartments are assumed to be independent from membrane voltages.

fiber is hyperpolarized than when it is depolarized. To reduce computational effort we follow the approach of Rubinstein (1995), who demonstrated that a noise current proportional to the square-root of the number of sodium channels within a compartment reflects the main property causing the irregularities in spike generation and timing.

Thus, our noise term $I_{noise,n}$ in [μA] becomes

$$I_{noise,n} = GAUSS \cdot k_{noise} \sqrt{A_n \cdot g_{Na}} \quad (3.1),$$

where GAUSS is a Gaussian noise current term (mean=0, standard deviation=1) that changes its value every 2.5 μs , k_{noise} [$\mu A \cdot mS^{-1/2}$] is a factor common to all compartments, A_n denotes membrane area in [cm^2], and g_{Na} is the maximum sodium conductance per square unit ($g_{Na}=1200$ $mS \cdot cm^{-2}$ for the regions simulated with 10 fold channel density, $g_{Na}=120$ $mS \cdot cm^{-2}$ for the human soma, $g_{Na}=0$ $mS \cdot cm^{-2}$ for all myelinated internodes and cat's soma, comp. Table 3.1).

We assume that channel densities are constant within the nodes of a target fiber, according to the model neurons of Fig. 3.1 the node area of the central axon has doubled size and, consequently, twice the number of sodium channels in comparison with the peripheral

axon (doubled diameter, same gap width). The double size fiber has the doubled 'regular' ion current, but the noisy current is only increased by a factor $\sqrt{2}$, i.e., large diameter fibers become less noisy.

In this chapter we assume an infinite homogeneous extracellular medium. The extracellular potential becomes

$$V_e = \rho_e I_{electrode} / 4\pi r \quad (3.2),$$

where $\rho_e=0.3$ kOhm.cm is assumed to be the mean resistivity of the extracellular medium. Under these assumptions the isopotentials are spheres, and the decrease of the potential is proportional to $1/r$, where r is the distance between a point of interest and the center of the electrode. In Chapter 4 we assume different conductances according to the different extracellular media and apply 3D finite-element calculations to describe the extracellular potential more precisely.

3.3. Results

Somatic delay

To simulate the natural course of an AP from the periphery to the central process we injected a 50 pA, 250 μ s current pulse at peripheral node P0 (Fig. 3.3). The injected current represents the membrane currents that are - in the natural situation - evoked by synaptic activity. Part of this current is lost within the first internode. Internodes in man are assumed to be longer than in cat. Therefore they cause more current loss, make the signal in the internode weaker, and the next node is harder to excite compared to the situation in the cat. But the real energy problem starts at the end of the human peripheral axon where the myelinated fiber has to supply the adjacent unmyelinated compartments with enough current to reach threshold. This problem was analyzed previously [Rattay 1995], and it was shown that an unmyelinated axon is much more current consuming than a myelinated one, i.e., the active unmyelinated fiber carries large membrane currents per cm fiber length and, consequently, needs a higher inner-axonal current to keep a spike running. In nature two methods are utilized to overcome the handicap sending an action potential from a myelinated axon into an unmyelinated region: in the central nervous system fiber diameters become smaller at the unmyelinated branching terminal, and in the peripheral system the last internodes have a reduced length.³ However, the human cochlear neuron has to overcome a second handicap when the spike has to pass the unmyelinated soma. A part of the incoming current gets lost at the large soma surface due to a lack of insulating myelin, and most of the incoming current is needed to load the somatic capacitance. Our computer simulations indicate that a transmission of the neural impulse is only possible, if the unmyelinated presomatic compartment is essentially longer than a node of Ranvier.

The difficulties arising from crossing the current consuming human somatic region are documented in Fig. 3.3: the time delay of an AP on its way from the periphery to the central axon is essentially larger in man (330 μ s) than in cat, where 118 μ s are needed to overcome the last presomatic internode. Moreover, there is a very small safety factor (compared to the myelinated animal cochlear neurons): even small variations of the geometric and electrical parameters can result in the loss of the spike. In our model the last two peripheral internodes are 0.43 mm and 0.36 mm long, respectively. If we ran our model with a non-reduced last internode length of 0.43 mm, a synaptically evoked spike would not overcome the soma barrier, as the 'regular' length causes just too much current loss in the last internode. The

³ Because of lack of sufficient data we assumed only the last presomatic internode to have a reduced length in our model.

spike is also stopped when the number of soma layers is reduced from 3 to 2, by shortening the unmyelinated presomatic compartment or by enlargement of the soma surface. We have tested also other parameters which make the 'natural' signaling more safe: enlargement of fiber diameter (our fiber is rather thin), reduction of soma membrane capacitance (increased number of shielding layers or smaller soma diameter), increase of axoplasm resistance of the presomatic compartment, and more sensitive sodium gating at the postsomatic compartment (reduction of threshold voltage).

Influence of ion channel current fluctuations

Single fiber recordings show variations in the firing latencies even when stimulated with

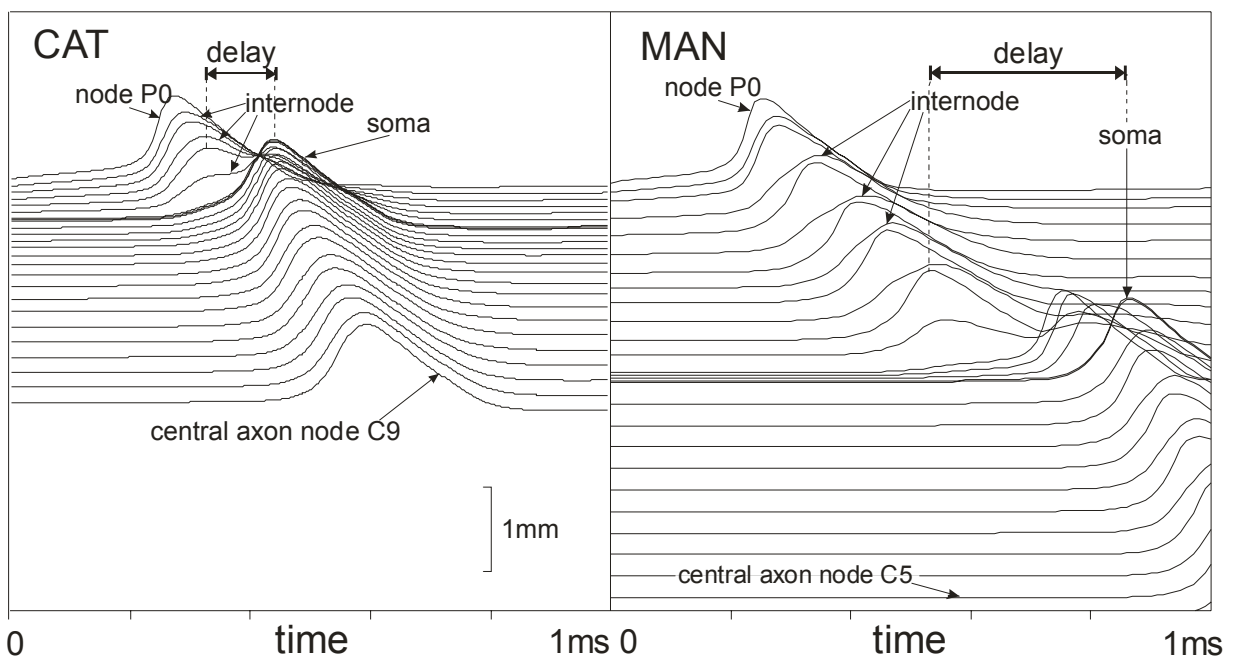


Fig. 3.3. Simulated reactions of a cochlear neuron in response to a 50 pA, 250 μ s current pulse injected at the first compartment. Every line shows the voltage of a compartment as a function of time, every node and internode is represented by a single compartment, node0 is the first unmyelinated part of the neuron. The human presomatic unmyelinated part is represented by three compartments because of numerical reasons. The lines are vertically shifted according to the real location of the compartments. Note the differences in somatic delay between man and cat, delay is measured between maximum voltage values of peripheral node P2 (P5-voltage) and soma in cat and man, respectively. Simulation according to the standard data of Table 3.1, no noise. Due to the small size of the postsomatic human compartment (5 μ m) its reaction almost overlaps with the reaction of the soma, both reactions appear as a single thicker line. In the cat even three compartment reactions are very close (soma, pre- and postsomatic nodes).

constant intensity. Some fibers have a larger spread in the latency than others. Latency variations can be explained by ion current fluctuations. With our standard model data (Table 1) and $k_{noise} = 0.05$ [μ A. $mS^{-1/2}$] the current fluctuations in a node of Ranvier were tested to be in accordance with reported data of Verveen and Derksen (1968) who observed membrane voltage fluctuations with a rms amplitude of 0.4 mV in the clamped node of a 4 μ m myelinated frog fiber and an increase of the fluctuations for smaller diameters.

We found voltage fluctuations of 0.49 mV rms in the resting state of a peripheral human node, and 0.16 and 0.01 mV for the central node and for the soma, respectively. Figure 3.4

shows the situation for a 'nervous' cochlear neuron, i.e., the common noise factor k_{noise} is doubled. Even with this (high) noise current amplitude the ion channel dynamics in the resting state will not cause any spontaneous firing. However, in the 'nervous' cochlear neuron we found that more than 10% of the spikes are hindered by such fluctuations to surpass the soma region, which is a consequence of the small safety factor as mentioned above. As can be seen from Fig. 3.4, the fluctuations in membrane voltage are larger in the nodes of the peripheral axon (small diameter) than in the central nodes (axon diameter is doubled). Hardly any fluctuations are seen at the soma due to its large diameter and the smoothing effect of its large membrane capacitance (comp. Eqn. 2.2).

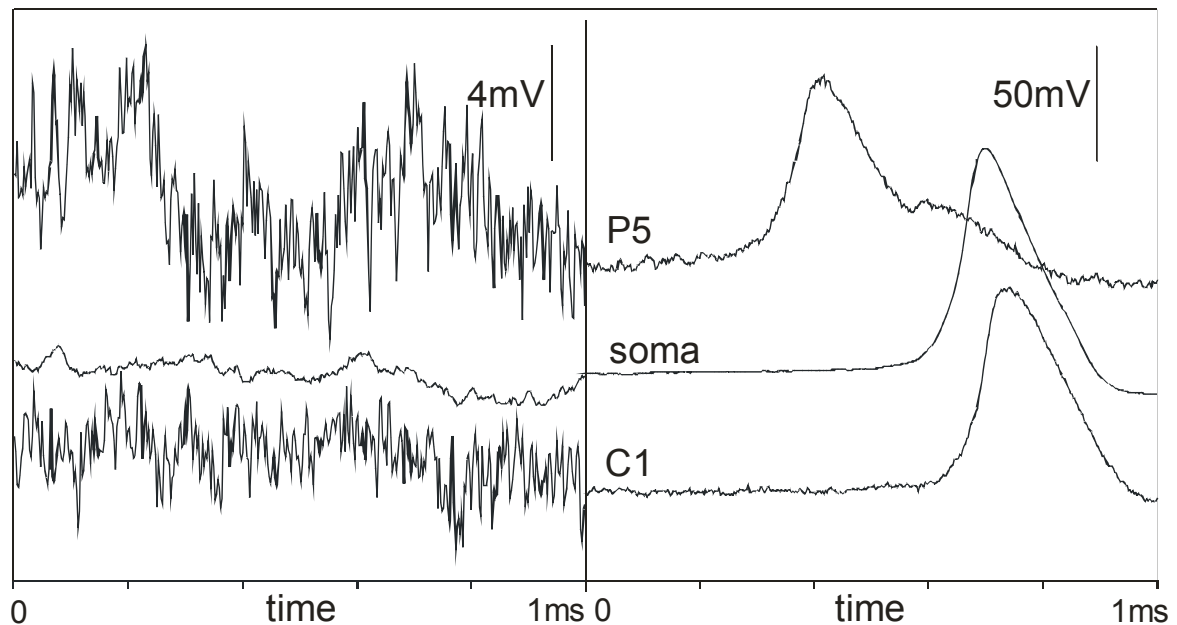


Fig. 3.4. Fluctuation in membrane voltage as a consequence of simulated stochastic channel open-close kinetics for the soma and for the last peripheral (P5) and the first central node (C1). Left panel: the non-stimulated human neuron, right panel: the human neuron as stimulated under the conditions of Fig. 3.3 including noise. Close comparison with Fig. 3.3 (right panel) shows that - as a consequence of the actual random events - the three curves have their maximum values earlier than in the noiseless case. Note that the second 'hill' at P5 is not a consequence of noise. It reflects the delayed excitation of the soma and the activities of the unmyelinated three presomatic compartments.

Several authors have reported that the point of spike generation may jump from the peripheral to the central region e.g., [Stypulkowski and Van den Honert 1984, Javel 1990, Miller et al. 1999]. In some cases of repetitive stimulation with constant current amplitude, half of the spikes in cat rise about 200 μs earlier than the rest. The presomatic 118 μs delay (Fig. 3.3) together with the spike's additional traveling time give an explanation for this phenomenon.

Excitation in the peripheral and central axons

As for the position of a cochlear neuron and a possible place for a monopolar stimulating ball electrode, we will stick to the sketch of Fig. 3.5 for our investigations of the electrically stimulated auditory nerve. The path shows two plausible places for a human soma in a simplified cross section of the upper end of the basal turn. This configuration is also suitable for the simulation of a cat nerve fiber in the basal turn. In comparison to the active electrode, the reference electrode is assumed to have at least a three times greater distance to the

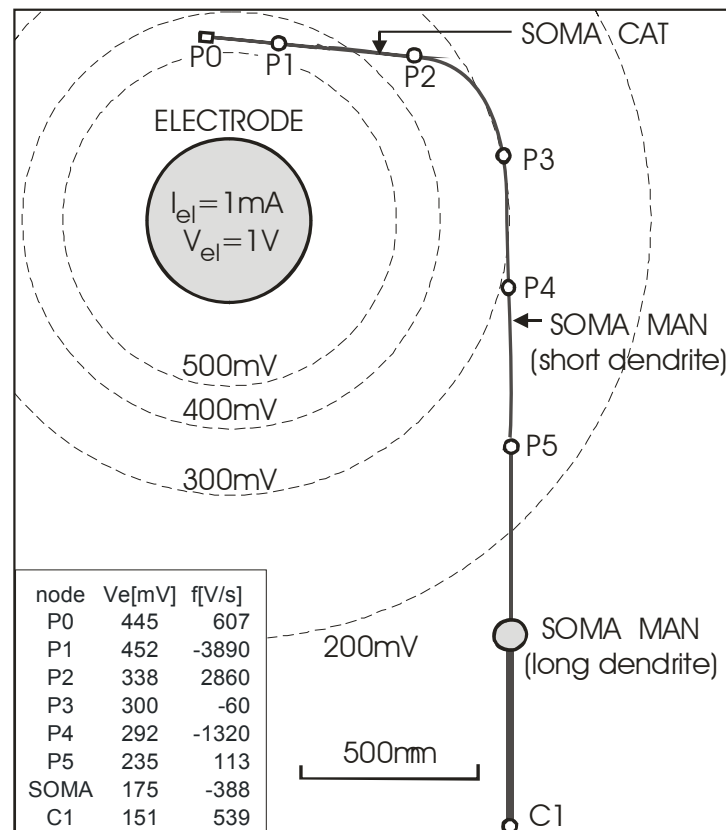


Fig. 3.5 Position of a human primary auditory neuron relative to a stimulating spherical electrode inserted into scala tympani at the upper end of the basal turn. The inhomogeneities in the conductive medium are neglected, therefore isopotential lines become circles. Neglecting capacitive and surface effects at the electrode-perilymph interface results in a linear current voltage relation with 1 mA for the spherical electrode at 1 Volt (electrode diameter: 0.48 mm, conductance of homogeneous medium: 0.3 kOhm.cm). The table shows the values of the extracellular potentials and the oscillating values of the activating function computed for 1 mA electrode current (long dendrite). Neural geometry according to Pernkopf (1960), Finley et al. (1990) and to Rattay et al. (2001b). Arrows mark the position of a cat soma in the basal turn and the alternative position of the human soma.

excited region of the target neuron, under such an assumption the reference electrode's position concerning the activating functions is negligible comp. [Rattay 1990, p. 129].

In order to compute the voltage changes at the membrane of a target neuron we have to determine the values of the extracellular potential V_e for every compartment (Eqn. 3.2). For the peripheral nodes, the soma, and for the first central node of the long dendrite human case these values are listed in the insert of Fig. 3.5. When all the potentials $V_{e,n}$ are known, the membrane reactions can be computed with Eqn. 2.2. The values for the activating function are easy to calculate with Eqn. 2.3. These values (see insert of Fig. 3.5) provide information about the reactions at the very beginning of the stimulus, under the assumption that the neuron has been in rest before. For instance, at the peripheral terminal (P0) the first response to a 1 mA stimulus is an increase of membrane voltage of 607 mV/ms, whereas at the first peripheral node P1 voltage rapidly decreases (-3890 mV/ms). Although V_e extensively changes in the soma region (comp. e.g., voltage changes for {P5, soma, C1} with {P2, P3, P4} in the insert of Fig. 3.5, column 2), f_{soma} is rather low, which is a consequence of the high capacitance of the human somatic membrane.

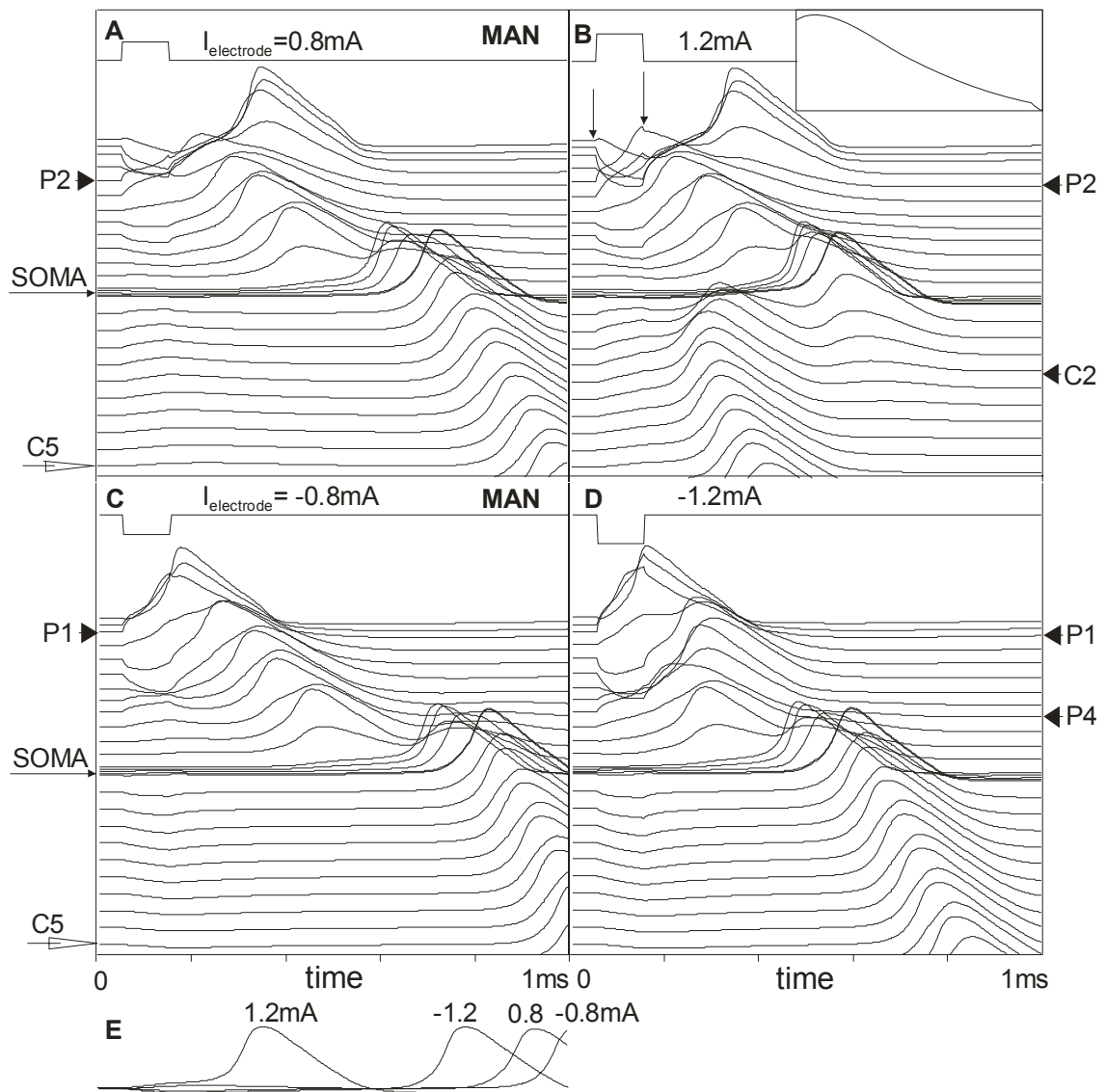


Fig. 3.6. Excitation of the long dendrite human cochlear neuron according to the geometry of Fig. 3.5 with anodic and cathodic current impulses. A. The neuron becomes excited at node P2 (marked by arrow and by slightly thicker line for the voltage curve) when stimulated with an $800 \mu\text{A}$, $100 \mu\text{s}$ pulse (10% above threshold). B. Increase of signal strength to 1.2 mA causes also node C2 (second arrow at the right side) to be a point of spike generation. An essentially shorter delay for the central nervous system is a consequence of skipping the soma zone. With stimulus onset there is a small positive influence as predicted by the activating function in the first compartment. This activity quickly gets compensated by the negative reaction at node P1, see insert, which shows the part of membrane voltage of the first compartment during the stimulus pulse (marked by arrows, 5x magnification). C. $-800 \mu\text{A}$, $100 \mu\text{s}$ pulse causes spike initiation at P1. D. The P4 spike develops after the P1 spike, but nevertheless the P4 activity elicits the excitation process in the central axon. E. The time courses at a simulated measuring electrode in C5 demonstrate the large delay differences in A and B caused by the soma barrier and shorter arrival time differences for the cathodic cases C and D where two spike initiation sites are in the periphery. The unmyelinated presomatic region is modeled by three compartments because of numerical reasons. The reaction of the postsomatic compartment strongly resembles the voltage course of the soma, and therefore the reactions of both compartments appear as a common (thicker) line. Calculation with standard data according to Table 3.1, no noise.

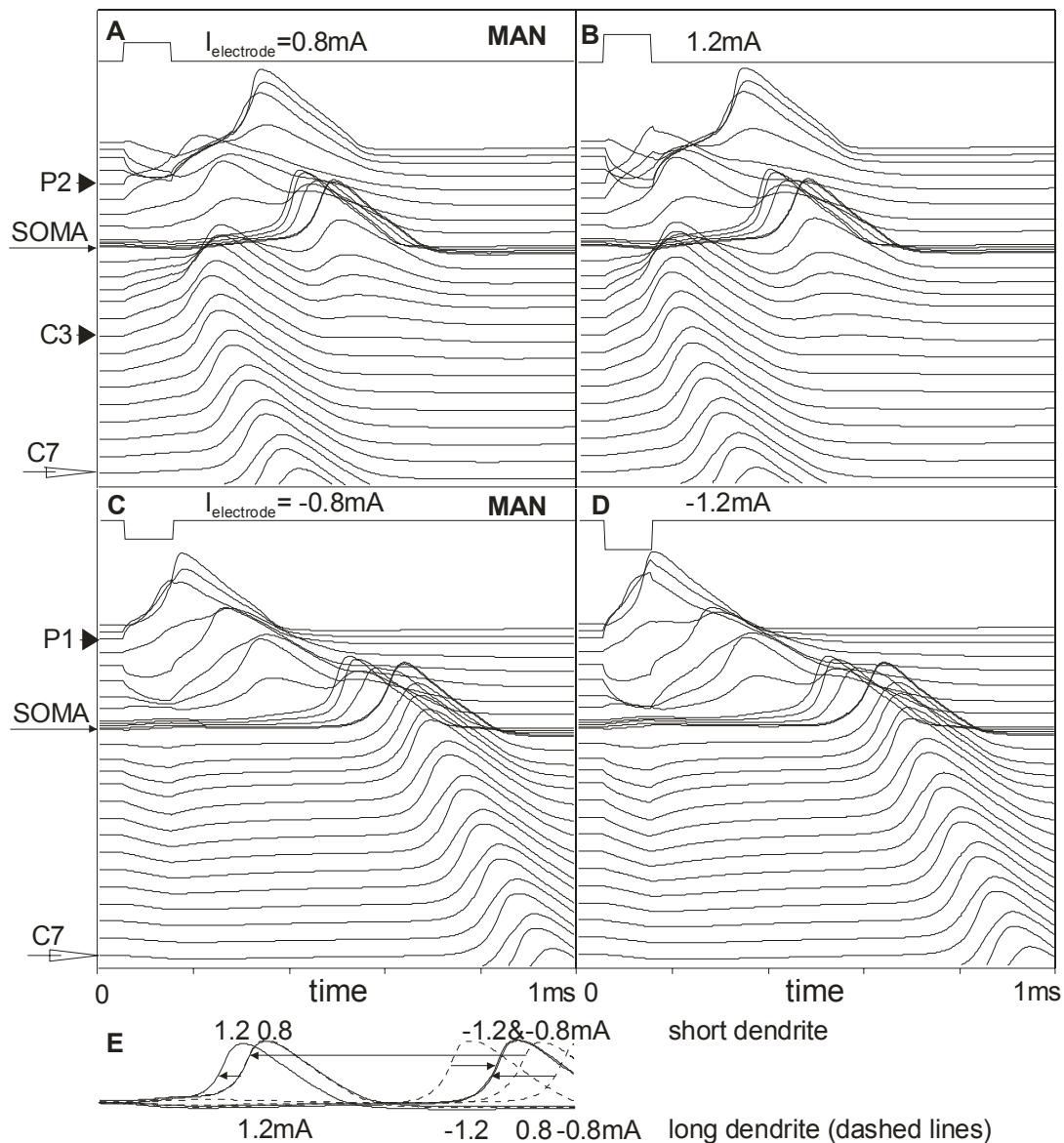


Fig. 3.7. Excitation of the short dendrite human cochlear neuron according to the geometry of Fig. 3.5 with anodic and cathodic current impulses. Note the shift in spike arrival times (denoted by arrows in E) when comparing the short and long dendrite case (dashed lines, copied from Fig. 3.6).

The maximum value of the activating function f is a good indicator for finding the most excitable compartment. Note, however, that neighboring compartments can support or hinder excitation in the compartment with the largest f . Therefore an isolated high peak in a series of f_n may not cause excitation, especially if the membrane activity in the corresponding compartment is small (small area, few ion channels) or if there is an energy consuming neighbor [Rattay 1998a, 1999]. As an example, when a 1.2 mA stimulus is applied the $1.2 \cdot 607$ mV/ms value of f for P0 (insert of Fig. 3.5) produces only a very small uphill movement, as it is seen in the insert of Fig. 3.6B. Quickly, the depolarizing reaction in P0 is suppressed by the much greater dominating negative f value of P1 (line3 in Fig. 3.6.A,B), because the current flow between the compartments smoothes any differences in membrane voltages of neighbored compartments. The strongest positive reaction is at node P2, where an action potential is generated (Fig. 3.6A). This spike propagates to both sides. Note that the soma region is not affected by the stimulus signal at the beginning, which is a consequence of the large somatic capacitance. In the central compartments there are also positive reactions

at the beginning, but they are too small to reach threshold in the 800 μA case. The situation changes with increasing signal strength. At 1200 μA two spikes are generated, the already observed peripheral one at node P2 and a central one at node C2 (Fig. 3.6B). The central spike also propagates in both directions, until it stops the peripheral activity by collision. Note that the centrally evoked spike reaches the central nervous system a lot earlier than the peripherally initiated spike of the 800 μA case.

When polarity in the long dendrite case is changed, rising of action potentials takes place where the activating function in the inserted table of Fig. 3.5 has negative values. In contrast to spike initiation on both sides of the soma the two points of spike initiation in the periphery cause essentially shorter delay differences, because they are on one side of the soma barrier (Fig. 3.6E).

In the short dendrite case stimulus strength has just marginal influence on spike initiation site: C4 at 560 μA (threshold) is shifted to C3 at 800 and 1200 μA , P0 at -260 μA (threshold) is shifted to P1 at -800 and -1200 μA (see Fig. 3.7 and Table 3.2 for details). For this reason variations in stimulus intensity only produce small differences in spike arrival time at the measuring electrode. In Fig. 3.7E the responses at -1200 and -800 μA are almost identical, because the quicker spike development in P1 is compensated by the stronger hyperpolarization at the beginning of the central axon (Fig. 3.7D). As the central axon is more sensitive than the peripheral process for anodic stimulation, the dominant spikes are always generated in the central axon (Fig. 3.7A,B) in the short dendrite case. Large shifts in spike arrival time can only be achieved by changing stimulus polarity (Fig. 3.7E).

Monophasic negative stimuli lead to decreasing membrane voltage in every node of the central axon for both the long and short dendrite case. Consequently, no central spike initiation is possible for our standard electrode position (Figs. 3.6C,D and 3.7C,D). More effects occurring with negative stimuli are reported in Rattay (1999). The specific conditions for spike generation, be it in the periphery or in the central axon, are discussed in detail in section 3.5. Biphasic stimulation effects are investigated in more detail in Chapter 4.

Man versus cat

Now we replace the human neuron by that of the cat, i.e., we use the same path as shown in Fig. 3.5. Extracellular voltages along the neuron stay the same, but the nodes, internodes, and the soma take other positions along the neural path due to the smaller compartment lengths in the cat (the cat's soma position is marked by an arrow in Fig. 3.5). This geometry is an approach for a cat neuron close to an electrode in the first cochlea turn. A good fit is achieved in the most excitable region (from P0 to C3, corresponding to the area between P0 and P4 in Fig. 3.5). The consequences of this change in a neuron's geometry are demonstrated in Fig. 3.8. The left part of the figure shows peripheral spike generation with a cathodic stimulus, and the right part shows central spiking due to a positive stimulus current. Following the peripheral voltage curves in the right-hand part of the figure, it is illustrated that they all decrease within the duration of the stimulating electrode impulse. Consequently, it is not possible to excite the peripheral axon with positive stimuli under these conditions, which is in contrast to the long dendrite human case (compare the positive and negative activities within the duration of the electrode impulse in the peripheral part of Fig. 3.6A with the 600 μA case in Fig. 3.8). There are, however, scenarios to evoke central spikes with negative stimuli, as we will see later.

Figures 3.9-3.12 concern simulated spike arrival times at a measuring electrode, as it is done in single fiber recordings with monophasic stimuli. For humans the reaction is measured at $x_{\text{record}}=0.434$ cm, and with $x_{\text{soma}}=0.231$ cm (long dendrite) the point of recording is in the central axon, about 2 mm away from the soma, soma is compartment #16, and x measures the neuron's length coordinate (distance from nerve base). The values for the cat

are $x_{\text{record}} = 0.263$ cm and $x_{\text{soma}} = 0.048$ cm, soma is compartment #8. In all cases the delay time as well as the variance in delay (jitter) decrease with increasing signal strength, i.e., strong signals will generate sharp post-stimulus histograms. Positive and negative monophasic stimuli are varied in the region of suprathreshold current strength for standard neurons of man (Fig. 3.9) and cat (Fig. 3.10). In the long dendrite human case weaker stimuli cause the 'leading' spike to be generated in the periphery, and for stronger signals it is generated in the central axon. A peripherally initiated spike reaches the central axon with a delay of about 400 μs compared to a spike already generated in the central part (Fig. 3.9, left traces). If the excitability in the peripheral and central axon is of similar magnitude, it is even possible to produce both latencies in one fiber at specific stimulation pulse levels (Fig. 3.9, 900 μA). At 910 μA approximately half of the spikes rise in the central part. Our simulations indicate that this bimodal distribution of spike latencies within a single neuron is a consequence of current fluctuations in the active membrane regions. A smaller latency shift is seen when spike initiation moves within the periphery from P1 at -800 μA to P4 at -1200 μA (Fig. 3.7C-E, Fig. 3.9). Of course, this 'jumping phenomenon' in latency times can be observed in cat as well, both in simulations and experiments e.g., [Miller et al. 1999, Javel and Shepherd 2000].

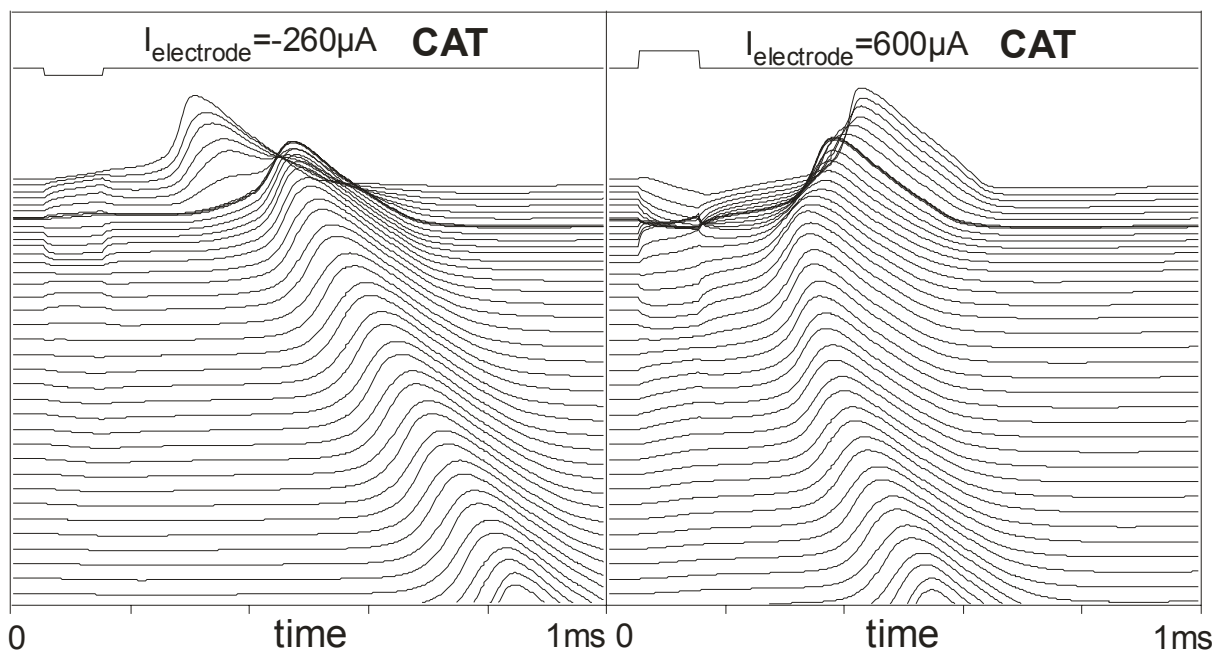


Fig. 3.8. Excitation of the cat cochlear neuron. The neuron is assumed to be in the same position as the human neuron according to the geometry of Fig. 3.5. A cathodic stimulus leads to peripheral spike generation (left part), whereas it is impossible to generate peripheral excitation with anodic stimuli (right part). Stimulus intensities are just above threshold, more than double intensity is necessary for anodic stimulation. Simulation with standard data, no noise.

If the peripheral axon is lost by degeneration, the threshold currents tend to increase in cat and man. As obvious in the 500 μA example, a weak stimulus in cat excites the healthy noisy neuron in 5 out of 10 runs, but the degenerated neuron only in 1 out of 10 runs (comp. lowest traces on the left-hand side in Figs. 3.10 and 3.11). The situation in man is extreme for cathodic stimuli: cathodic threshold increases by a factor of about 6, if the long peripheral axon is lost (comp. lowest traces on the right-hand side in Figs. 3.9 and 3.12). This number is based on the fact that in our model the human somatic membrane is assumed to be excitable according to the 'warmed' HH dynamics, but with normal channel density (channel density in a node is assumed to be 10 times higher). In this case (man, no peripheral axon, cathodic stimulus) excitation starts at the soma. If we assumed, on the other hand, that the somatic

membrane is not excitable, our results concerning intact neurons would not be affected in a remarkable way, for the excitation process in the soma is not crucial to help a spike cross the soma region. Enough current flow into the soma is sufficient for the postsomatic compartment to reach threshold and become active, because this compartment strongly follows the somatic potential. The degenerated case, of course, is different: assuming a non-excitable somatic membrane makes excitation impossible, because now the soma is the only compartment that gets a positive influence. Additional threshold data is summarized in Table 3.2.

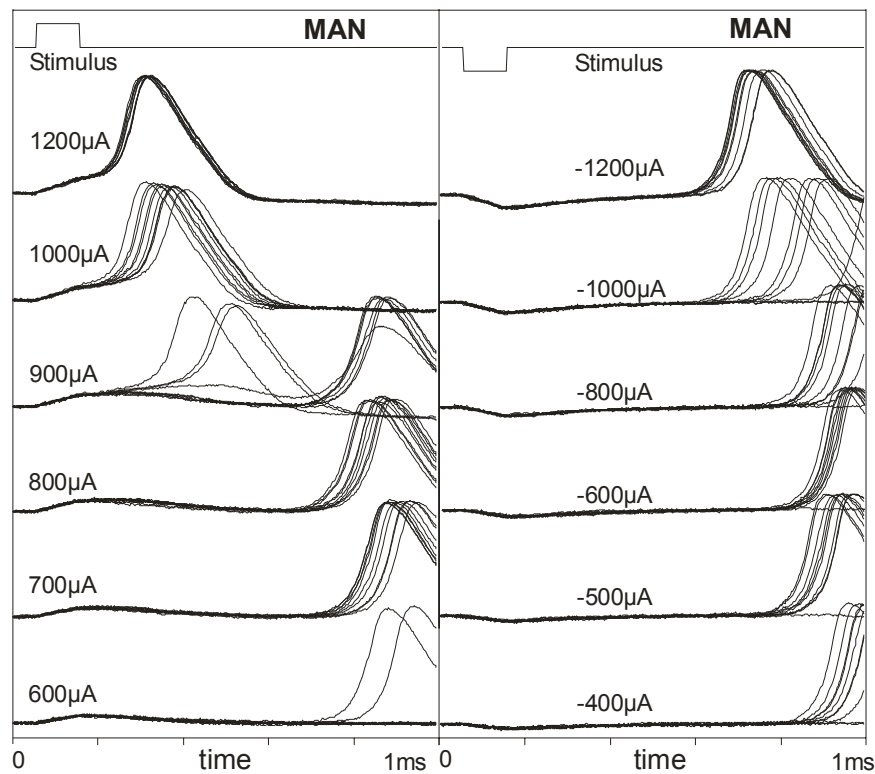


Fig. 3.9. Simulated spiking behavior in compartment #25 (C4) in man. For every signal strength the membrane voltages of 10 runs are shown. Sometimes spike generation fails for weak signals. By increase of stimulus amplitude the latency and its variance are reduced. Note that at 900 μA 7 spikes are generated in the peripheral axon and 3 in the central fiber. Model assumptions as in Fig. 3.6, but with noise.

Biphasic pulses, pulse trains

Pulse trains with 200 pulses per second are often applied, because a period duration of 5 ms makes the experiments comparable with single pulse stimulation with respect to thresholds, spiking probability and delay times. 5 ms after stimulation the simulated neuron is completely recovered, membrane voltage and all gating mechanisms are in the resting state again. Compound action potential data from cochlear implants also indicate that the human cochlear neuron is largely recovered after about 5 ms [Brown et al. 1990].

In a simulated pulse train experiment with a stimulation rate of 200 pulses per second (biphasic, 100 μs per phase) we have found a monotonic increase in discharge rate and a systematic reduction in response latency with increasing stimulus amplitude (Fig. 3.13), which is in accordance with experimental cat data from Shepherd and Javel (1997) and Javel and Shepherd (2000). The standard ($k_{\text{noise}}=0.05 \mu\text{A}\cdot\text{mS}^{-1/2}$) neurons of man (long dendrite) and cat were compared with 'noisy' fibers by doubling the membrane current fluctuations in every node. As a third case, the responses of thicker fibers (peripheral diameter 1.5 μm ,

central diameter 3 μm) were simulated. Additionally, data for a short dendrite human neuron is presented. With spike probability displayed as a function of stimulus intensity (Fig. 3.13A) the simulated standard and thick fiber lines of cat and man all have a similar slope. The computed standard and thick fiber data is comparable to the experimental curve with the second greatest dynamic range (3.19 dB, filled triangles). The 'noisy' fibers have about the same slope as the experimental 'greatest dynamic range' cat example (filled circles). The simulated 'cat' cases are about 1.3 dB easier to excite than the corresponding human neurons. An interesting phenomenon is the zig zag shape of the noisy human spike probability function, which is caused by the loss of peripherally generated spikes on their way crossing the soma region, i.e., increasing electrode current generates systematically more spikes in the peripheral axon, but only a reduced number of them can reach the central axon due to the 'small safety factor' in signal transmission at the soma. Only spike initiation in the central axon (achieved at levels greater than 62.5 dB) will guarantee a one to one response at the proximal end of the 'noisy' human neuron.

TABLE 3.2: THRESHOLD CURRENTS FOR EXCITATION IN MAN AND CAT

	neuron with peripheral axon			neuron without peripheral axon			threshold factor no p.a./with p.a.	electrode position
	threshold [μA]	origin of excitation	pos./neg. threshold	threshold [μA]	origin of excitation	pos./neg. threshold		
MAN long dendrite	130	P2		1500	C2(C1)		11.54	high
	720	P0(P1)		1100	C2(C1)		1.53	normal
	780	C2		800	C4(C2)		1.03	low
	-60	P0(P1)	2.17	-3200	SOMA	0.47	53.33	high
	-260	P0(P1)	2.70	-2400	SOMA	0.46	9.23	normal
	-540	P4	1.44	-1900	SOMA	0.42	3.52	low
MAN short dendrite	130	P2		640	C4(C2)		4.92	high
	560	C4(C2)		560	C3		1	normal
	600	C4		600	C3(C5)		1	low
	-60	P0(P1)	2.17	-1600	SOMA	0.40	26.67	high
	-260	P0(P1)	2.15	-1400	SOMA	0.40	5.38	normal
	-1260	P0(P1)	0.43	-1500	SOMA	0.40	1.19	low
CAT	180	C3(C2)		260	C6(C3)		1.44	high
	580	C6(C3)		640	C9(C8)		1.10	normal
	760	C11(C9)		760	C11(C9)		1.00	low
	-50	P0(P1)	3.60	-150	C3(C1)	1.73	3.00	high
	-230	P0(P1)	2.52	-360	C2(C1)	1.78	1.57	normal
	-350	C4(C6)	2.17	-350	C5(C6)	2.17	1.00	low

Remarks: Position of the neuron and the electrode according to Fig. 3.5, however, electrode positions (last column) can take 3 values, standard (normal), 300 μm above (high), and 300 μm below (low) the standard case. The origin of excitation marks the number of the node that reaches its full spike amplitude quickest (in brackets is the number of the node that is most excited at the end of the 100 μs stimulus), P3 means peripheral node3, C3 central node3. Columns 3 and 6 give the relation between anodic and cathodic thresholds, column 7 gives the absolute value of the threshold relation 'neuron without peripheral process / healthy neuron'. Calculations with standard data, no noise.

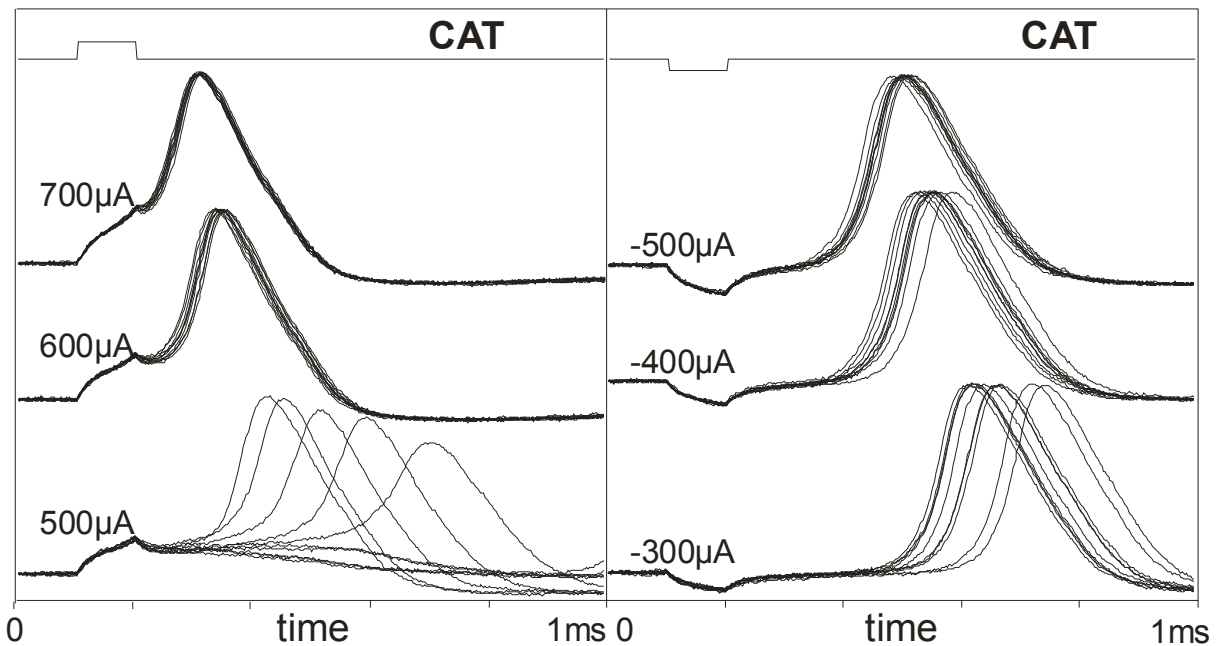


Fig. 3.10. Simulated spiking behavior in compartment #25 (C8) in cat. For every signal strength the membrane voltages of 10 runs are shown. Positive stimuli cause short latencies, because spikes are generated in the central axon. The 500 μA example is an exception, because the rather weak nodal current fluctuations need their time to convert - in 5 of 10 cases - the subthreshold excitations to action potentials, thus causing longer latencies. Negative stimuli only evoke spikes in the peripheral axon. Same assumptions as in Fig. 3.6, but with noise.

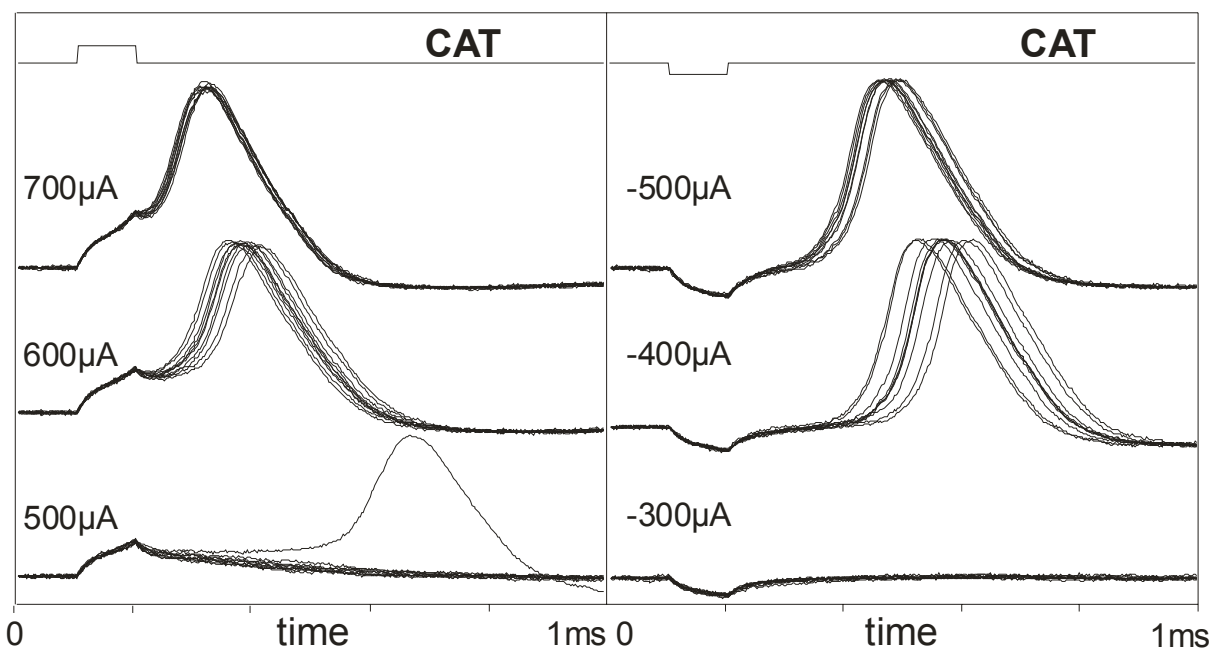


Fig. 3.11. Simulated spiking behavior in a cat neuron with lost peripheral process. Situation as in Fig. 3.10, but without any peripheral compartments. The neuron needs stronger currents, especially in the cathodic case. The long latency in the +500 μA case is due to low stimulus current (comp. Fig. 3.10). Of course, this latency cannot reflect a long time delay resulting from an excitation in the (non existing) periphery.

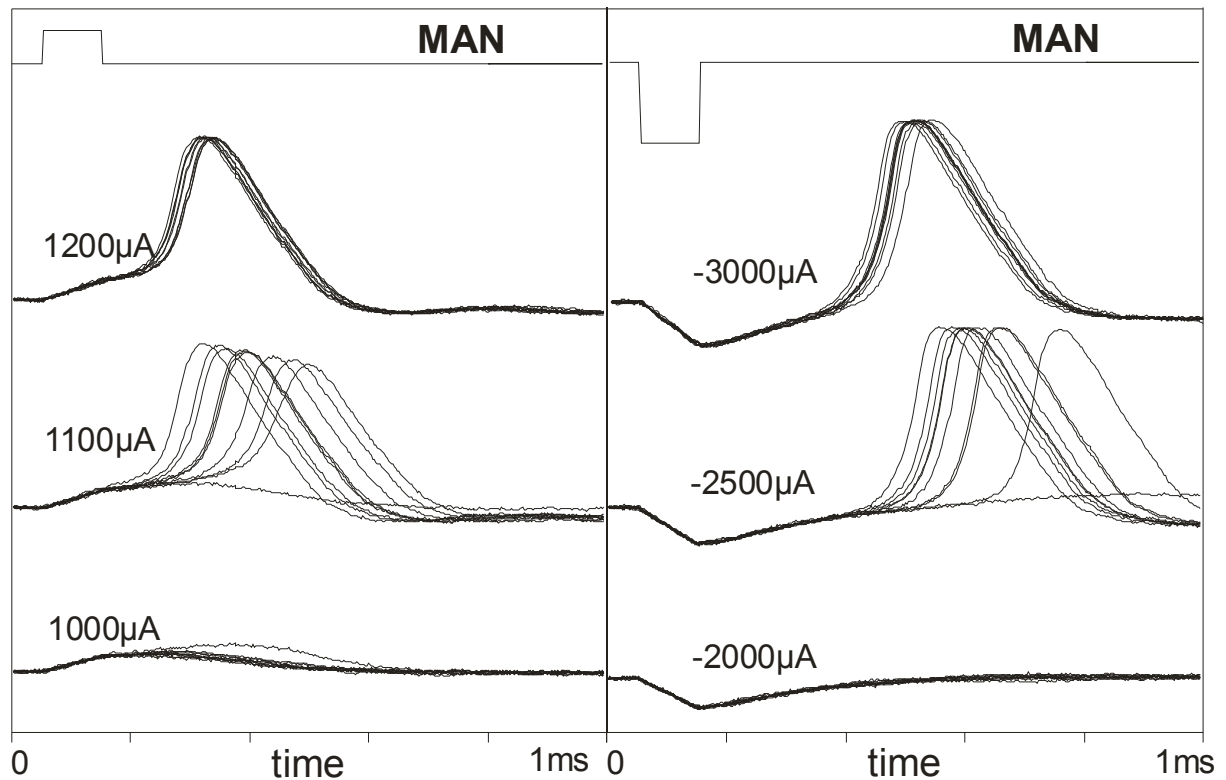


Fig. 3.12. Simulated spiking behavior in a human neuron with lost (long) peripheral process. Situation as in Fig. 3.9, but without any peripheral compartments. More than fivefold cathodic current strengths are needed for spiking.

Figure 3.13B shows examples for human latency curves. First complete spikes for weak stimulation are generated almost simultaneously at the peripheral nodes P0 and P1 with a small advantage for P0 in most cases. A main part of the latency comes from the delayed evolution of the action potential for small stimuli. At the first three points of the latency curve the large values of standard deviation are caused by ion current fluctuations. The delayed spike generation due to weak stimuli is gradually reduced with increasing stimulus strength. For stronger stimuli the formation of new spike initiation regions (closer to the proximal end) dominates the decay of the latency curve by shortening the traveling time (e.g., P1→P4, P2→C2 in the standard human neuron). For weak signals action potentials are generated by the second (negative) stimulus phase. At 1 mA additional spike generation at P2 is initiated by the first (positive) phase, and thus the P4 (second phase) spike is superseded by the distant one (standard and thick human neuron). Note that the form of the delay curve will change with varying stimulating conditions (pulse form, electrode position) and neuron's geometry. Nevertheless, for many configurations the first response will be expected in the periphery, and stronger signals are needed to stimulate the central axon. All these cases will produce a latency curve with a steep descent, as soon as spike initiation crosses the soma region, corresponding to 62.5, 61 and 56.9 dB for the standard, thick, and short human neuron in Fig. 3.13B, respectively. At the stimulus intensity corresponding to the center of this 'step' we have to expect a bimodal distribution in latency: half of the spikes are generated in the periphery, the other part within the central axon. Similar bimodal effects can occur at the smaller steps (see e.g., 56.9 dB [0.7 mA] for the standard human neuron in Fig. 3.13B).

The standard deviation bars oscillate along the latency curves (see e.g., standard human neuron in Fig. 3.13B). At intensities with two regions of spike initiation the standard deviation bars appear to be relatively large. Apart from these regions the deviation generally

decreases with increasing stimulus amplitude and it becomes very small at the right end of all latency curves in Fig. 3.13B.

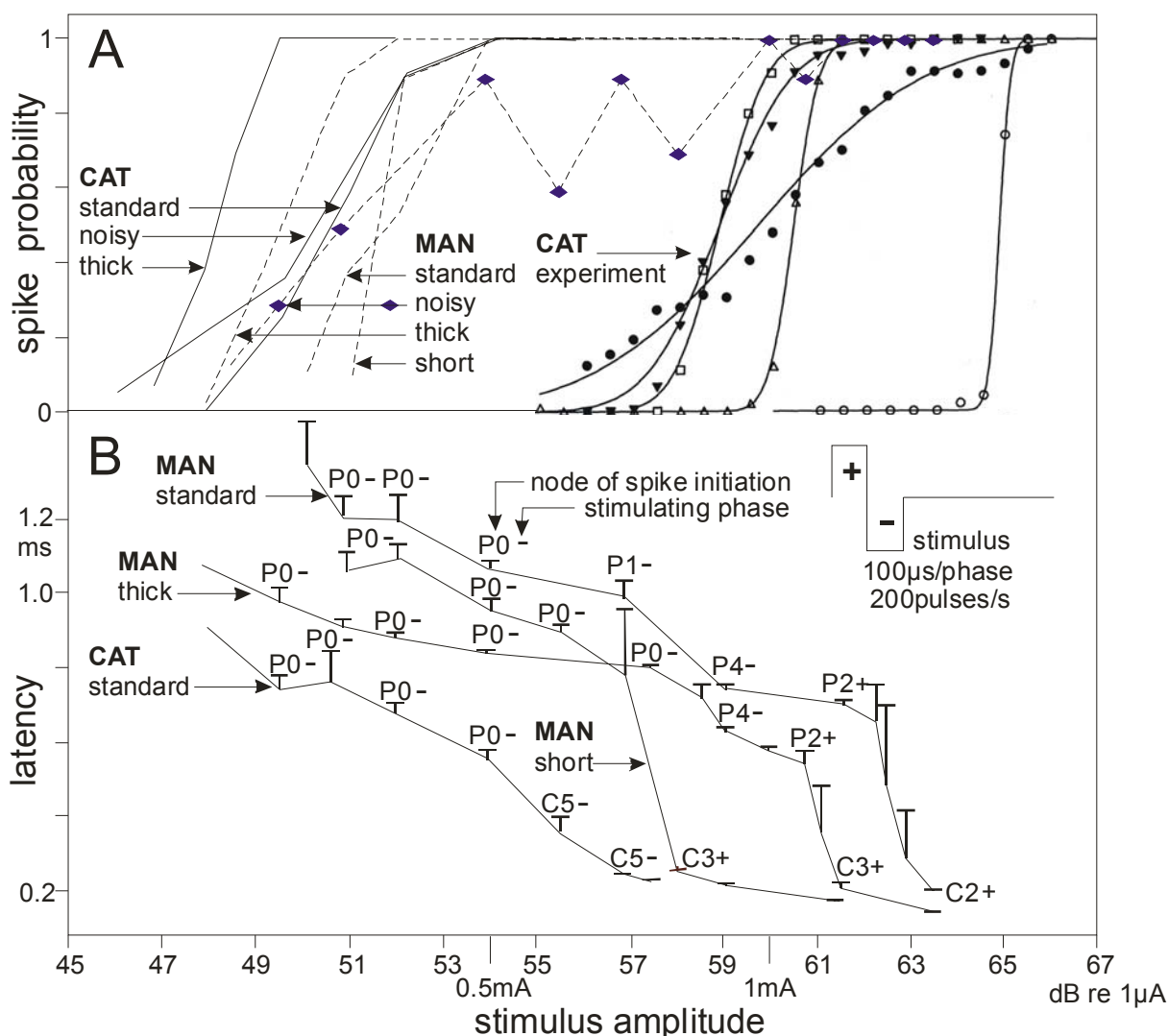


Fig. 3.13. Spike probability and latency as functions of electrode current observed in compartment #25 (C4 and C6 for long and short human dendrite, respectively, C8 in cat). A. Thin lines: cat, dashed lines: man, full lines: least square fit of an integrated Gaussian curve to 5 representative single cat fiber recordings (from Shepherd and Javel 1997, Fig. 15a). B. The four latency curves vary in a much wider stimulus amplitude range than the corresponding spike probability functions. Remarkable are the large steps in the human latency curves when spike initiation site crosses the soma region: 331, 347, and 522 μ s for thick, standard, and short human case, respectively.

When stimulus intensity is increased from 0.7 mA (56.9 dB) to 0.8 mA (58 dB) in the short dendrite human neuron an extreme latency difference of 522 μ s occurs, which consists of three components: (i) spike travelling time from P0 to C3, (ii) crossing the soma barrier, (iii) change of stimulating polarity from second phase (indicated by P0-) to first phase (occurring 100 μ s earlier). The largest steps in the standard and thick human neuron are smaller (347 and 331 μ s), because stimulating polarity does not change and spike travelling time is reduced.

Applying biphasic pulses, the stimulating effect of the first phase is reduced by the second phase. If the second pulse immediately follows the first one, the reduction effect is

even stronger, especially for short stimuli. As a consequence, in most cases stronger currents are needed for biphasic pulse stimulation.

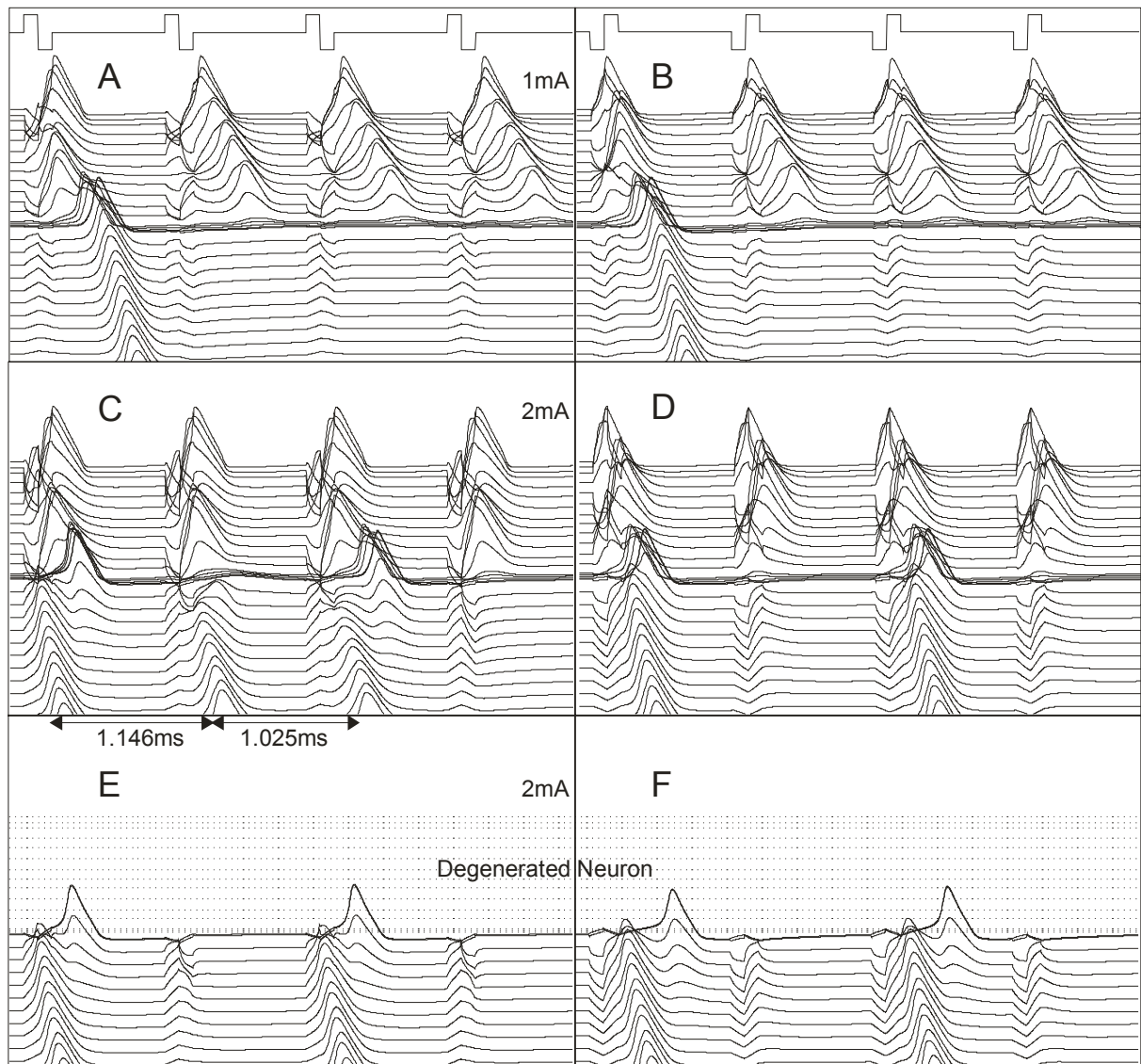


Fig. 3.14. Excitation with biphasic pulse trains in man. On the left side positive/negative 100 μ s pulses - one biphasic pulse per millisecond - are applied, on the right side polarity is changed. Every one of the 1 mA stimuli generates a spike in the peripheral axon (A,B), but only the first spike crosses the somatic barrier, because stimuli of this strength and frequency are within the range of a block window. 2 mA stimuli cause excitation in the central axon. Still some spikes are missed. Because of refractory properties the second activity in the central axon rises with a time delay in C (interspike times are marked by arrows) and fails to reach threshold in D. Additionally, the degenerated neuron even loses spike2 for positive/negative stimulation, because any support from the peripheral axon is missed (comp. C and E). For the degenerated neuron the positions of the lost compartments are marked by dotted lines. All calculations with standard data, no noise, electrode position according to Fig. 3.5 (long dendrite).

Loss of the long peripheral axon results in a degenerated human neuron that needs generally higher stimuli as a consequence of the great distance between the electrode and the excitable structures. When calculated with standard data, no noise, the thresholds for monophasic cathodic stimulation are -2.4 mA and -0.26 mA for the degenerated and healthy

neuron, respectively. But the relation is not that extreme for biphasic pulses: the thresholds become -1.6 mA and -0.33 mA for 'negative phase first' - biphasic pulses. Threshold for the degenerated neuron with 'positive phase first' - biphasic stimulation is 1.4 mA (1.1 mA for anodic monophasic stimulation), the values for the healthy neuron are 0.4 mA (biphasic) and 0.72 mA (monophasic).

As a rule of the thumb we assume that the 'no-noise' threshold values correspond to 50% spiking probability and - according to the 'S'-shape of the spike probability function (Fig. 3.13A) - first (full) responses are achieved by a half dynamic range shift to the left (right). The dynamic range of the standard and thick human neuron with our standard factor $k_{noise}=0.05$ is 3.19 dB (Fig. 3.13A). This way the 100% response is expected by multiplication of the no-noise thresholds with 1.2 and the first response by division with 1.2.

Finally, we want to study how our simulated healthy and degenerated human neuron behaves in reaction to high frequency pulse trains. As shown in Fig. 3.14A,B, a pulse train of 1000 biphasic 1 mA pulses per second will cause synchronous spiking in the peripheral axon. But refractory behavior and unfavorable potentials in the somatic region allow only the first spike of the whole train to pass the soma (high frequency blockade, comp. e.g., Rattay 1990, p. 171f). We found 1.5 ms as shortest interspike times achievable in the central axons for spikes that are generated by current injection at the beginning of the neuron (node0, i.e., in the natural case) when using standard model data. This is a consequence of the high energy barrier of the unmyelinated human somatic compartment. This value is much larger compared to the shortest interspike times of 0.5-0.7 ms known from cat experiments. A biphasic 100 μ s, 2mA pulse train with positive pulses first causes spike generation in the central axon (Fig. 3.14C). Now the interspike times can be shorter, because the somatic energy barrier does not have to be crossed (spike generation is in the central axon). However, the interspike times are still longer than the 1 ms repetitions of the stimuli. In Fig. 3.14C, e.g., refractory behavior causes the second spike to have an additional delay of 146 μ s and the third spike to have a delay of 25 μ s. These time shifts hinder the fourth spike to develop. The situation worsens in the degenerated neuron: without any support from the periphery every second spike is lost (Fig. 3.14E).

3.4. Discussion

We have presented an excitation model of the cochlear nerve capable of both human and animal data, which may simplify the comparison of animal data with advanced measurements from humans. There is, however, a lack of knowledge on morphometry of human neurons, especially concerning the sequence of internodal lengths, and length and shape of the pre- and postsomatic region. Furthermore, exact data for simulating the excitation of the node and the somatic membrane is not available. Consequently, we have focused on new experimental aspects, e.g., the poor grade of myelination of human spiral ganglion cells. Our development of a better method for compartment modeling allows the investigation of the influences of the neural geometry on the excitation process and on firing delays.

We checked the models of Hodgkin-Huxley, Frankenhaeuser-Huxley, Fitzhugh, Chiu-Ritchie-Rogart-Stagg-Sweeney, Schwarz-Eikhof (SE), and Schwarz-Reid-Bostock (SRB) for simulation of the active membranes in the unmyelinated terminal region, at the nodes, in the human pre- and postsomatic area, and at the human soma. It turned out that from these membrane models the HH-model is the appropriate one, if gating processes are sped up with a factor of 12, as suggested by Rattay (1990). Tenfold ion channel density was assumed for the nodes, normal density for the human soma (Table 3.1). Several of our tests indicate that also the SE and the SRB model may represent the cochlear nerve dynamics with a similar accuracy as the HH model. The SRB model was already successfully applied for

human sensory fiber simulations [Wesselink et al. 1999] and cochlear nerve investigations (Frijns, personal communication).

One essential step was the introduction of the generalized version of the activating function f in the field of cochlear neurons [Rattay 1999]: a first prediction of the excited regions of the nerve is possible with Eqn. 2.3, which only needs three values for every compartment: the extracellular potential, the capacitance of the cell membrane, and the intracellular conductance from the compartment center to its edge. This allows an analysis without any knowledge of the composition and the complicated dynamics of ion channels in the areas that are not covered by myelin. In contrast to the simple version of the activating function concept [Rattay 1986] every irregularity in the sequence of compartments is now taken into account. The position, amplitude, and neighborhood of the peaks of f predict which regions are excited by positive and by negative stimuli. For a detailed discussion see section 3.5.

In contrast to all investigated animals most of the cell bodies as well as the pre- and postsomatic regions of the afferent human cochlear neurons are unmyelinated, but still they are protected by some surrounding membranes - and therefore 3 surrounding layers of membrane have been assumed as standard data. Our modeling studies for the natural signal transport from the beginning of the peripheral axon into the central region show two barriers along the way. The main barrier is to load the charge consuming somatic capacitance. The current needed is proportional to the somatic surface and inversely proportional to the numbers of covering membranes. An unmyelinated soma that is essentially larger in diameter than the supplying input axon can only be surpassed by a spike coming from an unmyelinated compartment, because during excitation these types of compartments demand stronger axonal currents than the myelinated ones [Rattay 1995]. If there is not enough current to enter the somatic region, the postsomatic part of the neuron will not reach threshold. It can be speculated that such neurons are designed to be part of a cluster of some units with a common insulation in order to sense synchronization of activities: perhaps a single spike is too weak to pass the soma. However, if another spike arrived at the neighbored soma within a short time interval, one or both neurons could reach suprathreshold potentials in the postsomatic compartments.

The other barrier is to bring enough current from the human myelinated peripheral axon into the unmyelinated presomatic region. The presomatic compartment has to have a large intracellular resistance, which is manifested in a specific minimum compartment length, for two reasons. First of all, it has to concentrate enough current to reach threshold. Secondly, it has to prevent the soma from wasting too much energy, which would occur, if the distance between the soma and the last presomatic node of Ranvier is too short. Altogether, the human peripheral axon must be well designed to manage the natural signal transport to the proximal end. Other mammalian cochlear neurons have a much greater safety factor for bringing the spike from node to node. Nevertheless, there is also a time delay for crossing the soma in these species. Our simulated arrival time differences between peripherally and centrally evoked spikes in the cat gather around 200 μs , which meets experimental data [Miller et al. 1999, 125-245 μs , Stypulkowski and van den Honert 1984 (Fig. 1), 240 μs]. Note that the last citation concerns compound action potentials where non-synchronized spiking activities make interference.

Even with constant stimulation current a bimodal distribution of delay times that corresponds to the generation of spikes that are alternatively generated in the peripheral or in the central axon has been observed in a single neuron [Javel 1990, Miller et al. 1999]. This effect only occurs within a small range (some percent) of the stimulus amplitude. Such a phenomenon is based on current fluctuations in the voltage sensitive ion channels, and this certainly cannot be described with a deterministic membrane model. According to suggestions of Rubinstein (1995) we simulated the membrane current fluctuations by Gaussian noise with an amplitude proportional to the square root of the number of sodium

channels. The noise amplitude was adjusted to measurements by Verveen and Derksen (1968) at isolated nodes of Ranvier. As a consequence, phenomena like the decrease of delay variation for increased stimuli level as well as the bimodal distribution of delay times can be observed in our simulations. Apart from these two phenomena, a model of the electrically stimulated cochlear neuron that reflects stochastic behavior is vital for investigating the temporal spiking pattern [Rubinstein et al. 1999, Rattay 2000].

Degeneration of myelin in the peripheral process will stop signal transport or at least disturb the temporal coding principle [Zhou et al. 1995]. An interesting observation has recently been reported about the maturation process of the rat cochlear neuron: the expression of myelin markers in the peripheral and central part of the intradural part of the VIII-th nerve starts long before the onset of cochlea function. The expression rapidly achieves saturation on the day on which cochlea function commences [Knipper et al. 1998]. This fact is in accordance with our modeling results: signal transport to the proximal end is hindered, before the process of myelinization is finished.

We have shown that it is also possible to stimulate the cochlear nerve when the peripheral axon is lost. For such cases an increase of excitation threshold was observed in animals e.g., [Zhou et al. 1995]. Such an increase is also expected for cochlear implant patients. Our simulations demonstrate that the threshold increase factor for the loss of the peripheral axon essentially depends on the electrode position and the polarity of the stimulus. Even in normal cases excitation sometimes has its origin in the central axon and degeneration of the distal ending hardly influences this excitation process (see section 3.5 for quantitative analysis). However, excitation is essentially harder, if not impossible, when stimulus polarity is changed in the degenerated case.

A mixture of healthy and degenerated neurons can cause alternative points of spike generation that result in delay times gathering around two different values for one stimulus intensity. Note that a similar effect can occur, if only healthy neurons are involved: most of the neurons close to the electrode are stimulated in the central axon, whereas a population of more distant neurons is stimulated in the periphery. Both situations can result in a double peaked histogram of the total nerve response. In some cases telemetry measurements show double peak cochleograms for specific stimulus configurations. Dillier and coworkers (1997) have measured double peak time differences around 300 μs in several cochlear implant patients comp. also [Lai and Dillier 2000]. Cohen et al. (2004) report that in one of four patients they obtained a double peaked cochleogram with 350 μs interpeak time, which also can nicely be related to the results of this chapter (comp. 900 μA case in Fig. 3.9, Fig. 3.13B). Parameter variations have shown that the size of the soma and the number of cell layers surrounding it have major influence on our simulated arrival times. A smaller soma, a higher number of shielding layers, and a bigger dendrite axon diameter (as demonstrated in Fig. 3.13B) shorten the delay of a peripherally initiated spike on its way to the central axon.

We have compared one of Dillier's measurements with the simulated contribution of a single neuron to the human cochleogram [Rattay 1998b] and it was demonstrated that a single peripherally initiated spike propagating to the central axon (assumptions similar to that of this chapter, biphasic signal 100 μs , 0.6 mA, negative phase first) will cause a double peak signal. When a stronger stimulus (e.g., 3 mA) is applied, a dominating second spike is initiated in the central axon. In this case the electrical potential at the measuring point has only one peak. Furthermore, a single peak contribution will be expected from an excited degenerated neuron. Note, however, that summing up the temporally shifted individual contributions of all stimulated neurons can easily result in a single peak signal, even for cases with a majority of double peaked single neuron contributions [Lai and Dillier 2000]. Therefore a single peak cochleogram is not necessarily a consequence of intense loss of peripheral axons. Some investigators have not, at least to any significant extent, reported the occurrence of double-peaked whole nerve wave forms.

Modern speech coding strategies for cochlear implants try to include more temporal elements in order to achieve a better resemblance to the natural spiking pattern. Spike initiation in the periphery and in the central axon together with the relatively large delay caused by the human soma barrier are significant for the electrically evoked time pattern. To account for these phenomena a model has to incorporate individual compartments for the soma and the pre- and postsomatic areas as well as the membrane current fluctuations in the non-myelinated regions. The proposed model may help to analyze the firing behavior in the cochlear nerve for different species and it will be of special use to predict the responses in man when new devices are developed.

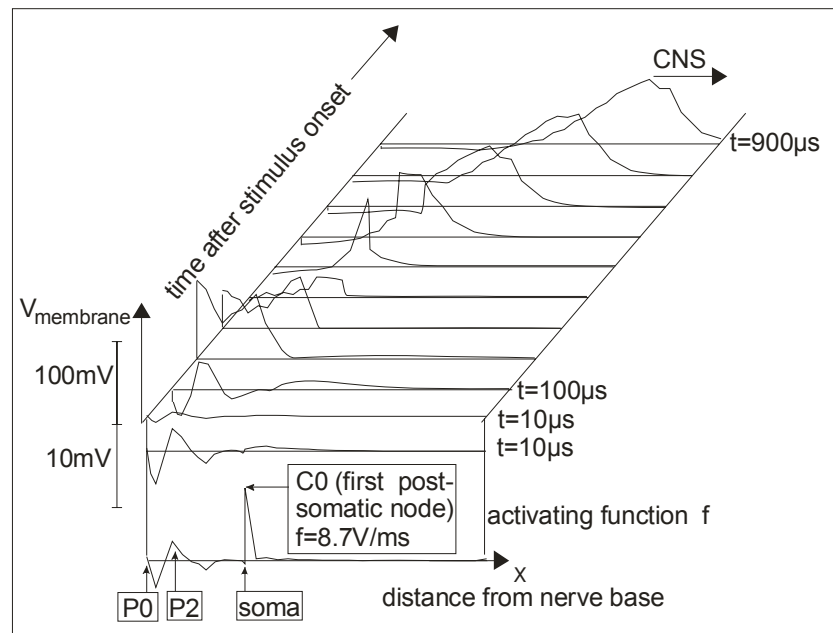


Fig. 3.15. Membrane voltages along a human neuron. Situation of Fig. 6.1 (Stimulus: $800 \mu\text{A}$, $100 \mu\text{s}$), but without noise, is displayed in $100 \mu\text{s}$ steps. To avoid confusion at the crossings every second line is thin. The enlargement of the first reactions ($10 \mu\text{s}$ after stimulus onset, second line from the bottom, larger vertical scale) strongly resembles the activating function (lowest line). Note, however, that the big value of the first post-somatic compartment is missed in membrane voltage. Excitation starts in peripheral node P2, the second highest value of the activating function. The activating function is shown as a continuous curve because of better display. Per definition the activating function (Eqn. 2.3) gives a value for every compartment, equal to the rate of voltage change at the beginning of the stimulus, therefore the activating function should be displayed as a step function according to the length of the corresponding compartments. But in such a scheme one would not recognize the (important) values at the nodes because of the great differences in nodal and internodal lengths.

3.5. The point of spike generation as predicted by the activating function

The use of the activating function (Eqn. 2.2) for analyzing the origin of excitation can be seen from snapshots of the membrane voltage along the neuron (Fig. 3.15). If the neuron is in the resting state, before a stimulus is applied, the very first membrane voltage changes follow the activating function in shape and quantity. Two phenomena will cause quantitative deviations, nonlinear conductance in the active membranes on the one hand and effects from the compensation of intracellular voltage differences in neighbored compartments by intracellular current flow on the other hand. The first effect is not of importance, as we are only interested in the point of spike generation: at the beginning of spike generation voltage

changes are linear, i.e., the threshold will be reached at a location as predicted by the linear theory, i.e., by the activating function. However, the second effect can change the origin of spike generation.

Extreme situations can occur at the border to the soma. An isolated high peak of the activating function should be treated with care, and a closer look to the neighbored compartments is necessary. In the presented case (Fig. 3.15) the postsomatic compartment C0 is the one that becomes most affected at the beginning of the stimulus. The left neighbor, the soma, is stimulated with a small negative value, and most of the current that arrives at C0 will flow antidromically into the soma for two reasons: firstly, the intracellular resistance between C0 and the soma is low, secondly, the soma needs a lot of current to charge its membrane. Taking these facts into consideration, it is nice to see that all the other compartments closely follow the prediction, which is demonstrated by a comparison of the enlarged version of the $t=10 \mu\text{s}$ line in Fig. 3.14 with the activating function below. The situation in the next node (C1) is better suited for an excitation process. Here the value of f is much smaller than that of P2, but if the stimulus is strong enough, this node will reach threshold. It is then the winner, because it is already in the central axon and its spike is already on the way, while the P2-spike has its fight with the soma barrier. This effect can be observed by following the responses when current is increased in the left part of Fig. 3.9.

The peaks of the activating function indicate the possible points of spike generation. Two mechanisms influence the occurrence of peaks, irregularities in the neuron's geometry and in the applied electric field. In order to separate the influence of compartment geometry from that of the extracellular potential along the neural pathway we introduce a pseudo-homogeneous neuron. We construct a hypothetical cat neuron with a peripheral process (1 μm diameter, 14 internodes each 350 μm long, all other values are standard cat data) long enough so that the soma and the postsomatic region will only receive the far field of the stimulating electrode. That way discontinuity in neural geometry can be disregarded, and the influence of the potential along the neural pathway is the center of interest. The activating function for this case (first line in the central column of Fig. 3.16) shows 2 positive and 2 negative regions on the peripheral side of the presomatic node indicating two points of spike generation for positive stimuli and two points for negative stimuli. Because the f peaks at the beginning of the axon are the larger ones, a 'jumping phenomenon' in the delay times will occur for cathodic as well as for anodic stimuli, when stimulus level is increased. (At this electrode position threshold excitation is distal, increase of current causes the more proximal compartments to be the origin of the dominant spike.) The time differences in 'jumping' are rather small, if the extra delay from the soma barrier is not involved, i.e., the two points of spike generation both lie on either side of the soma. The peripheral part of the human activating function (lowest line in the central column of Fig. 3.16) predicts a jump for cathodic stimuli. The delay is of the order of 200 μs , as is seen by comparison of the $-600 \mu\text{A}$ and $-1200 \mu\text{A}$ cases in Fig. 3.9. For anodic stimuli the human 'jump' is essentially longer (about 400 μs , Fig. 3.9), as the soma is between both anodic spike initiation regions (Fig. 3.16, man).

Comparing the first and last lines in the central column of Fig. 3.16 reveals a similar shape of the peripheral activating function in spite of differences in compartment lengths. Thus, these peaks have to be a consequence of irregularities in the electric field surrounding the neural pathway. A look at the neural pathway across the isopotentials of Fig. 3.5 explains the origin of these peaks through irregularities of the field (peak1 corresponding to node P1 is a local maximum of the extracellular potential V_e , comp. inserted table). Additionally, the strong curvature close to node P2 (peak2) and the change from an isopotential pathway between P3 and P4 to a descending potential profile at P4 (peak3) can be treated as irregularities of the field as well. The zigzag shape of f - following peak4 (Fig. 3.16, first line in the central column) - corresponds to gradually decreasing positive node values, which are interrupted by the much smaller f values at the internodes. The positions of the prominent

peaks do not change if the electrode is moved 300 μm down in the y-direction according to Fig. 3.5. Note that the P4 value of f becomes dominant (greater than f at P1, comp. Fig. 3.16, first and third lines, left column). As a consequence, this peak defines the point of first spike generation for cathodic stimuli. Its position closer to the soma makes the 'jumping phenomenon' in the periphery impossible. A double peaked post-stimulus histogram is not expected anymore. Movement of the electrode 300 μm up in the y-direction (Fig. 3.16, first line, right side) makes the beginning of the peripheral neuron prominent, because the electrode is very close to the peripheral axon at a position between P0 and P1. The induced voltages become much stronger (note the different scaling, electrode current is reduced to 100 μA in Fig. 3.16, right cases), and spike origin will take place in one of the first nodes.

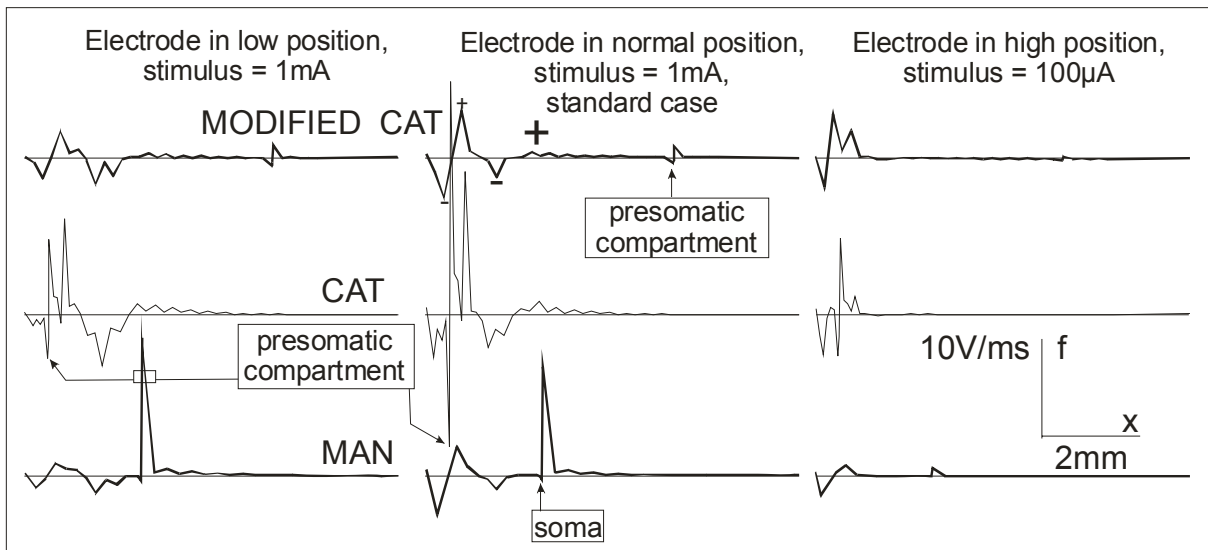


Fig. 3.16. Activating functions for different types of neurons and different electrode positions. The lowest case in the central column describes the same situation as in Fig. 3.15, but for an electrode current of 1 mA. The middle line in the central column (thin) is the activating function for the cat neuron. The first line represents the activation of a hypothetical cat neuron with an extremely long peripheral axon. +/- signs mark the points of spike initiation, the size of the signs represents threshold current. In the left column the electrode is moved in y-direction 300 μm down relative to the standard position shown in Fig. 3.5, in the right column the electrode is moved 300 μm up (a smaller electrode diameter has to be assumed to avoid contact with the neuron, but isopotential lines stay the same, they are independent from electrode diameter, stimulus intensity is reduced to 10%).

Threshold values and the points of spike generation for the human and cat neuron are listed in Table 3.2. Firstly, it is demonstrated that the healthy neuron is almost always easier to excite with cathodic currents. Secondly, for the human cases a peripherally degenerated neuron is hard to excite with cathodic stimuli, if it is possible at all. We have assumed HH dynamics for the somatic membrane. But if the soma has passive membrane behavior (assuming only a small density of sodium channels), excitation with cathodic currents does not seem to be possible with stimuli below the cell damage limit. Thirdly, when positive stimuli are applied, fiber degeneration does not remarkably raise thresholds. An exception is the case when the electrode is close to the beginning of the neural path (high position). Of course, this electrode position is not favorable for the damaged neuron. Fourthly, the degenerated cat neuron reacts in a different manner, because its activating function is cut at another place along the neural pathway compared to man. Note that cutting the peripheral processes in man and cat does neither change the activating function values in the central

axon nor in the postsomatic compartment, the changes are restricted to the soma - and, of course, $f=0$ applies to the peripheral process. But because the soma is hard to excite anyway, there is no need to determine a new f soma value for the degenerated situation. To get a first prediction for the degenerated neuron, it is sufficient to cut out the peripheral part of the healthy neuron's activating function. Consequently, the activating functions of Fig. 3.16 are of use also for the degenerated case.

The origin of spike generation is not always clear to see. Three stages of excitation are of interest: the very beginning of the stimulus pulse, the end of the stimulus pulse, and the moment when the full spike amplitude is reached. In many cases the spike will be generated at that point where f has its maximum (at the very beginning of the stimulus pulse). One exception is the somatic region. We have already discussed that the large peaks at the pre- and postsomatic compartments determine the very first reaction, but the strong influence on excitation immediately decreases, because the somatic membrane has to be charged. Furthermore, the pre- and postsomatic compartments are connected via the high conductance of the somatic region, and they generally have f values with opposite signs. But even the next neighbors are influenced by this current redistribution, and therefore a compartment with a rather small f value can surpass the excitation process of other compartments in the rising phase. As an example, Table 3.2 (column 2) shows first (complete) spikes in the central cat neuron at nodes C3 and C6, but in both cases other nodes (C2, C3) are the most excited elements at the end of the stimulating impulse. The human cases give another example when peripheral node P1 is most excited after 100 μ s stimulus time, but its energy has to drive two neighbor elements. P0 on the other hand is a compartment with no left neighbor, which allows it to become excited more quickly.

4. A model of the electrically excited human cochlear neuron

Part II. Influence of the 3-dimensional cochlear structure on neural excitability

A simplified spiraled model of the human cochlea is developed from a cross sectional photograph. The potential distribution within this model cochlea is calculated with the finite element technique for an active scala tympani implant. The method presented in Chapter 3 allows for simulation of the excitation process of selected elements of the cochlear nerve. The bony boundary has an insulating influence along every nerve fiber which shifts the stimulation condition from that of a homogeneous extracellular medium towards constant field stimulation: for a target neuron which is stimulated by a ring electrode positioned just below the peripheral end of the fiber the extracellular voltage profile is rather linear. About half of the cochlear neurons of a completely innervated cochlea are excited with monopolar stimulation at threefold threshold intensity, whereas bipolar and especially quadrupolar stimulation focuses the excited region even for stronger stimuli. In contrast to single fiber experiments with cats, the long peripheral processes in human cochlear neurons cause first excitation in the periphery and consequently, neurons with lost dendrite need higher stimuli.

4.1. Introduction

A model for the electrically stimulated human cochlear neuron was presented in Chapter 3. This investigation demonstrated that the simulation of the single fiber excitation process needs the extracellular potential along the neuron as input data. In the following, a simplified spiraled three-dimensional (3D) structure based on human geometry is evaluated with a finite element program. The calculated potential distribution can be used to study the stimulating influence of an arbitrary electrode configuration on a target fiber.

Relations between electrode locations, stimulus current and excitation pattern have been investigated both in experiments and theory since the early days of cochlear implant development comp. e.g. [Spelman et al. 1980, Black et al. 1981, Loeb et al. 1983]. Due to the complex cochlear structure the spiraled form was not considered in most of the modeling work.

Resistance networks introduced by von Békésy in 1951 as transmission line models, have been used to calculate the voltage as a function of the distance from the cochlea base in one of the conducting media, e.g., in the scala tympani. Such models are of value to estimate current interactions for multi-channel applications [Strelioff 1973, Jolly et al. 1996, Kral et al. 1998]. However, with this method the potentials along a single neuron cannot be estimated with the resolution necessary to simulate its individual excitation process.

Electric fields along the cochlear neural pathways were calculated with finite elements for humans [Finley et al. 1990], and with the boundary element method for the guinea pig [Frijns et al. 1995, 1996]. Finley and coworkers used a 5.2 mm long section of the uncoiled cochlea, parted it into 12 layers with a higher resolution in the center, and calculated the potential distribution and activating functions in the nodes for seven target neurons stimulated by different types of electrodes. Shortcomings of the activating function as used in their investigation are that the former version predicts the excitation for long fibers of constant diameters, boundary conditions are not considered and constant internodal lengths for myelinated fibers are assumed. Frijns and coworkers simulated the course of the potentials along 95 fibers in a rotationally symmetric cochlea model for bipolar current sources. They calculated neural recruitment characteristics for different electrode positions, as well as the influence of losing the peripheral axon by degeneration.

The first results about the electric field in a rotationally symmetric model of the human cochlea were obtained with the finite element method [Schmidt et al. 1998]. The geometry was based on a photograph of a mid-modiolus cross section of the cochlea (Fig. 4.1). Two dimensional models or even 3D models with rotational symmetry need essentially less computational effort than the spiraled 3D versions. Therefore, the present investigations spared elements by introducing compartments to more simply approximate the cross section compared to our rotationally symmetric model.

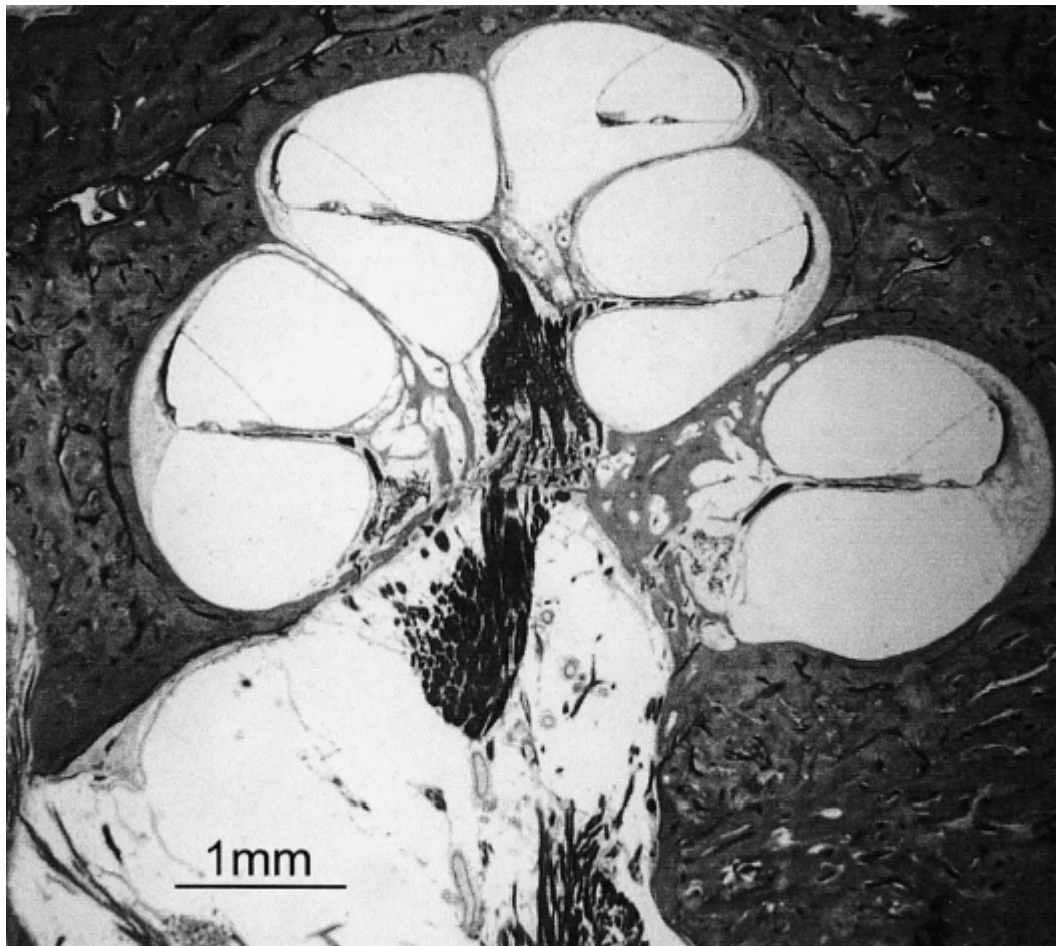


Fig. 4.1. Microphotograph of a midmodiolar horizontal section of a human cochlea.

Three types of scala tympani electrodes are investigated in this article: (i) monopolar (the return electrode is outside of the cochlea; since the ground electrode is far from the target neuron, the stimulating field is essentially that of the mono-pole, the return electrode assumed at the infinity), (ii) bipolar (2 channels, separated by 30 degrees) and (iii) quadrupolar (it is effectively a symmetric tripolar configuration, where the outer poles are half the inverse polarity value of the center electrode, a quadrupole is equivalent to the sum of two dipoles). The electric field is evaluated along 18 representative neural pathways, equally distributed by 30 degree separation within 1.5 cochlear turns. The excitation process of target neurons with long, short, and degenerated (lost) peripheral axon is analyzed for monophasic and biphasic rectangular 100 μ s pulses. Monophasic pulses are instructive to understand the relation between the electric field and the excitation process, but to avoid dangerous charge accumulation biphasic signals are used in all medical applications of functional electrical nerve stimulation. All simulations are calculated with 100 μ s pulse duration per phase.

The temporal information in the spiking pattern of the auditory nerve is an important component for speech understanding [Ghitza 1994, Rattay and Lutter 1997]. In contrast to most other modeling work our simulations are therefore not restricted to the neural recruitment order but investigations on the delay times in the target neurons are included.

Analysis of the responses of cochlear neurons requires a two step procedure: in the first step the extracellular potential along every target neuron has to be calculated. For a rough approach every electrode can be modeled as a point-current source in a homogeneous medium. With an average cochlear conductance of 300 Ohm.cm we have obtained in Chapter 3 a very simple method for calculating the extracellular potential along a given neural pathway (Eqn. 3.2). As expected, the application of the finite element technique provides more accurate potentials for step one of the procedure, nevertheless we will see that some of the voltage profile characteristics are still the same. In the second step we use the electric circuit model and the activating function concept as introduced in the companion paper for predicting and comparing the excitation processes in 15 selected target neurons.

The geometry of the 'long dendrite' target neurons is equal to the human 'standard' cochlear neuron of Chapter 3: The peripheral axon (dendrite) has an unmyelinated 10 μm long terminal, 5 nodes of Ranvier, an axon diameter of 1 μm . The soma has spherical shape, 30 μm diameter, is covered by 3 layers of insulating membranes and neighbored by unmyelinated pre- and postsomatic compartments with lengths of 100 μm and 5 μm , respectively. The diameter of the central axon is 2 μm . The 'short dendrite' neuron has 3 nodes of Ranvier.

4.2. A geometrically simplified model of the human cochlea

In order to calculate the electric field in the spiral ganglion, the cochlea has to be segmented according to the different specific resistances in the main compartments: bone, nerve tissue, perilymph, endolymph, Reissner membrane, basilar membrane and organ of Corti (comp. Table 4.1).

TABLE 4.1. RESISTIVITIES FOR THE FINITE ELEMENT MODEL.

Region	Resistivity [Ohm.cm]	Source: Finley et al. 1990
Electrode	0.1	
Perilymph	70	
Endolymph	60	
Bone	6400	adapted according to Kosterich et al. 1983
Nerve tissue	300	
Basilar membrane+ Organ of Corti	3000	adapted
Reissner membrane	10000	adapted

First we planned to obtain a digitized form of the spatial cochlear structures from a series of photographs showing the structures in distances of 20 μm . This method turned out to be unmanageable because of the following reasons: (i) it needs a high effort in image analyzing, e.g., at the border of bone and nerve tissue, (ii) the geometry is unreliable in areas where the cutting plane has a small angle with the surface of any compartment and (iii) in any case the enormous number of key points has to be reduced drastically before constructing the finite element geometry.

We decided to reconstruct the cochlear shape from a single photograph (Fig. 4.1) of a midmodiolar cross section from an averaged sized human cochlea. In a first step the shapes of the compartments were nicely approximated by polygons with a huge number of keypoints. These polygons were used for our 2D finite element solutions with MATLAB software and for a first 3D finite element investigation with rotational symmetric cochlear shape using ANSYS software [Schmidt et al. 1998]. In a second step the number of keypoints for the polygons in the cross section were essentially reduced (Fig. 4.2), e.g., the borderline of scala tympani just has 7 corners. This borderline changes shape when the scala tympani crosses the central plane for every half turn, but the number of keypoints stays on a constant value of 7. This means, as an example, keypoint 3 can be followed on its way from the base to the upper part of the cochlea. For every keypoint we simulated the spiraled pathway by straight lines that change direction every 30 degrees of turning (Fig. 4.3). In more detail, the coordinates of a group of 5 new corner-points were calculated by linear interpolation of the radius and z-values of those two corresponding keypoints of the cross section picture which are the closest neighbors. The same 'spiral method' was applied to define the outer part of the spiral ganglion. This spiraled outer part was intersected with a rotational symmetric core of neural tissue consisting in order of a cylinder at the base, two conical segments, a cylinder and a cone at the top (Figs. 4.2 and 4.3). Special evaluations for the excitation process were done for an ensemble of cochlear neurons within the nerve tissue compartment which was constructed by the 'spiral method' as described above.

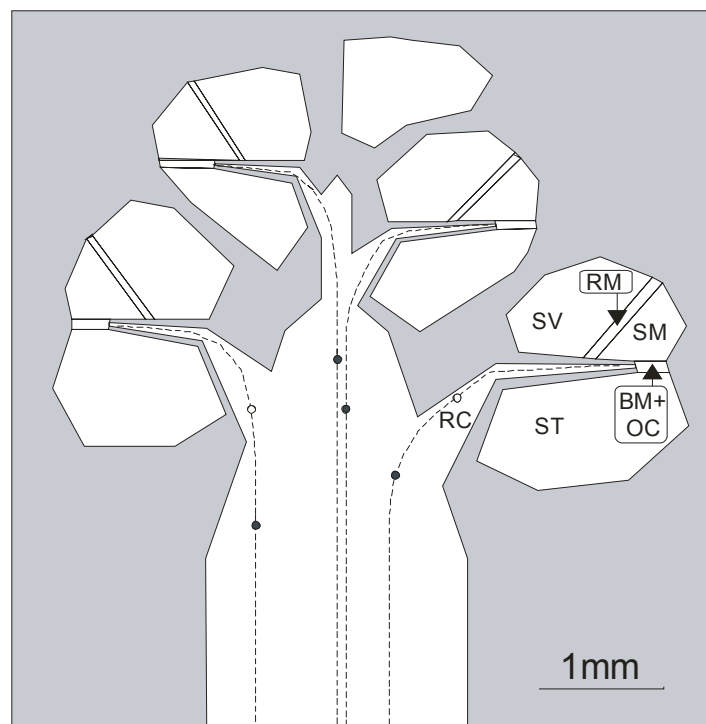


Fig. 4.2. Simplified compartment geometry as used for the 3D finite element calculation. This is an approximation of regions with different conductivities, based on the central cross section of Fig. 4.1. The gray area marks a cube of bone that contains the cochlea. ST: scala tympani, where the electrode is inserted; BM+OC: a single compartment represents basilar membrane and organ of Corti; SM: scala media; RM: Reissner membrane is modeled as a plate, essentially thicker as in reality, but with reduced conductivity; SV: scala vestibuli; RC: Rosenthal canal. Four of the representative neural pathways (N1-N19) are within the cross section area, the positions of their cell bodies are shown as filled circles for peripheral axons of standard length (denoted as 'long dendrite') as well as for cases with short peripheral axon (cell bodies within Rosenthal canal, white circles).

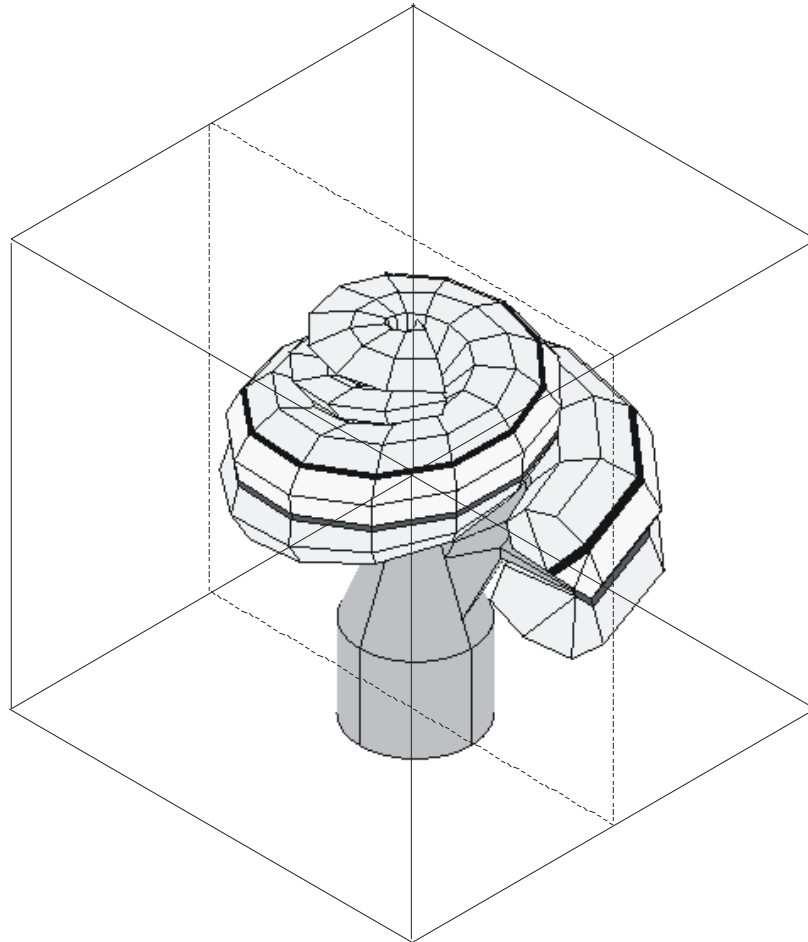


Fig. 4.3. 3D view of the simplified cochlea geometry. The polygons of Fig. 4.2 are linearly interpolated along a spiraled line that makes a corner for every 30 degrees of turning. The gray tone intensity is proportional to the resistivities of the compartments (compare Table 4.1). The dark regions mark the Reissner membrane and the combined compartment that includes the organ of Corti and the basilar membrane. A transparent cube shows the border of the finite element geometry. The bone compartments within the cochlea are also transparent. The dashed lines mark the central plane shown in Figs. 4.1 and 4.2.

4.3. Calculation of the electric field

The cochlea is assumed to be embedded in a cube of bone (Fig. 4.2). In Fig. 4.3 the bony compartment is transparent, all other compartments are shaded according to their specific resistivities. The situation in the highest cochlear turn is simplified at the boundary ending of the spiraled structure, but the scala tympani and scala vestibuli are connected to mimic the electrical short circuit of the real situation at the helicotrema. Furthermore, current flow into the very first part at the basal cochlear ending is neglected by starting the spiraled structure at the lowest cochlear duct segments shown in Fig. 4.2. The basal beginning of the simulated spiral structure is seen at the right side in Fig. 4.3.

The values for the resistivities of cochlear components are listed in Table 4.1 (for references see Finley et al., 1990). The Reissner membrane is approximated by a thicker parallel structure with an adjusted conductivity. In an analogous way the organ of Corti and the basilar membrane are simplified by a single compartment that has only 4 keypoints in the cross section. Because the values for the resistivities of the biological materials may differ from the real ones, we have checked the influence on nerve excitation by doubling the

conductance values for perilymph, bone, organ of Corti and neural tissue, separately (discussion section, Fig. 4.14).

An active multi-channel electrode is modeled in different ways. In the 'standard' 3D case a 0.5 mm diameter ball electrode is intersected by a flexible cylindrical non-conducting carrier material with 0.4 mm diameter. In this way a ring of metal is generated which allows current flow from the electrode's outer surface into perilymph. When the flexible carrier material is inserted into the scala tympani the implant obtains a spiraled form which reduces the cross section area of the conducting cochlear fluid in the scala tympani. The standard position of the active electrode is 180 degrees inserted into the spiraled part that is shown in Fig. 4.3, i.e., the center of the electrode is again in the cross section plane (Fig. 4.2). The geometry of the carrier was constructed by the 'spiral method' as described above. At two positions corresponding to 150 and 210 degrees electrodes of the 'standard' type can be activated in the model to simulate the bipolar or quadrupolar configuration.

Because the system is studied under quasi-static conditions we calculated the potential distribution for a fixed potential of 1 Volt at the surface of the electrode. For a discussion of neglecting capacitive effects see, e.g., Finley et al. (1990). Except for the base, the potential at the outer surface of the bony cube was assumed to be zero. The potential was not defined at the base of the cube where we assumed a condition that is analogue to a long prismatic extension of the cube, with the conductance of neural tissue. It has to be mentioned, that a more precise simulation of the monopolar case with the return electrode positioned somewhere outside of the cochlea causes remarkable deviations from a zero potential in most regions of the cube surface. However, by testing such cases with a 'large' 2D MATLAB model it turned out that any arbitrary position of the return electrode outside of the cube - prism volume has only insignificant influence on the excitability of the target neurons. The small conductivity of the bony surrounding hinders current flow and therefore, potential distribution within that nerve tissue region where excitation is expected is not much influenced by this restriction. The difference in excitability between our model and a 'complete head model' would be even essentially smaller for the investigated bipolar and quadrupolar configuration.

With finite element technique, the field region is divided into small discrete elements. Regional resistivity and a fixed (small) number of nodes (not to mix up with 'node of Ranvier' which is the meaning of 'node' in the following sections) characterize each element. The values at the nodes are defined by the boundary conditions of the problem and a current-voltage relation for volume conductors (for details see, e.g., Johnson 1995). After iterative calculation of the node values the potentials can be evaluated for any arbitrary point or pathway within the defined geometry.

In Fig. 4.2 two positions for the locations of the soma on the pathway of a cochlear neuron are marked which are investigated in this article: Filled circles indicate the soma of the 'long dendrite' neuron which has 5 peripheral nodes P1-P5 with distances from the lateral end as marked in Fig. 4.6, resulting in a peripheral process length that is given by $x_{\text{soma}}=0.23$ cm. Neurons with shorted peripheral axons (reduced by P4, P5 and the last two internodes) have their soma within Rosenthal canal at $x_{\text{soma}}=0.15$ cm (circles in Fig. 4.2). They are called 'short dendrite' neurons in the following.

4.4 Results

Excitation of the most excitable neuron

In the first case study the potential distribution is calculated for the standard electrode position (electrode below neuron 7, comp. Fig. 4.2). We picked up all finite elements within a

slice that contains the central cross section plane shown in Fig. 4.2 (marked by dashed lines in Fig. 4.3) and displayed in Fig. 4.4 potentials according to the boundary conditions (0 V at 5 sides of the bony cube and 1 V at the active electrode) by equi-potential lines in 1 percent steps (10 μ V). The same situation is shown in Fig. 4.5 for the surface of the spiral ganglion compartment. Neuron 7 is closest to the electrode and therefore it obtains the maximum voltage.

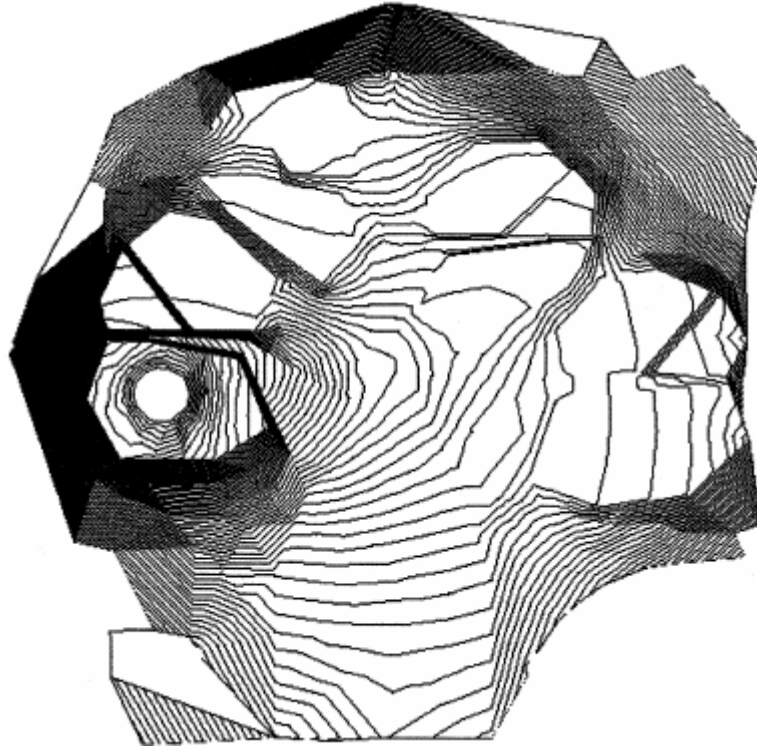


Fig. 4.4. Calculated equipotential lines in the central area of the human cochlea. The electric field results from a scala tympani electrode that appears as a circle in the left side of the picture. The potential at this ring electrode is 1 (arbitrary) unit, e.g., 1 V; the equipotential lines are shown in steps of 1 per cent. The shape of the different compartments can be recognized by breakings in the lines or by narrow spacing (dark areas around the electrode marks the bony structures, the basilar membrane and organ of Corti compartment as well as the Reissner membrane. In some regions the equipotential lines are missed which is a shortcoming of this display; elements which are not entirely within a thin central slice are not displayed, their isopotentials are omitted.

In Fig. 4.6 we compare (A) the finite element solution for neuron 7 (long dendrite) with two simpler models, (B) the homogeneous medium and (C) the constant field, where voltage gradient is constant along the neural pathway, i.e., the graph of the extracellular voltage V_e is a straight line. The curve at the top of Fig. 6A shows V_e along neuron7 for the finite element solution. The largest V_e value of 810 mV occurs at the beginning of the neuron, i.e., at peripheral node P0 which is the unmyelinated terminal at the inner hair cell. Figure 4.6B shows the voltage profile for the same neural pathway and the same electrode position, but for a homogeneous extracellular medium. In Fig. 4.6C it is assumed that V_e uniformly decreases along the neuron, with a value of 1 V/cm. The situation of Fig. 4.6B is very close to that investigated in detail in Chapter 3. In the 'homogeneous' case the extracellular potential is inverse proportional to the distance to the electrode: The two local maximum values in the peripheral region correspond to the nearest points of the neural pathway to the electrode. Under the assumption that the neuron is surrounded by an insulating tube with open endings the potentials between the ends become equally distributed which is the constant field case (Fig. 4.6C). The main reasons for a deviation from the constant field assumption

are: the bone in the cochlea is not a perfect insulator and the nerve tissue cross sectional area is not constant. Nevertheless, the principal effect of the different conducting cochlear compartments is to shift both the extracellular potential and the activating function from the homogeneous medium towards the constant field solution, i.e., the extracellular voltage profile of neurons starting in the vicinity of a scala tympani electrode is a smoothed form of the homogeneous case. Smoothing of the extracellular potential by the bony shielding results in smaller values of the activating function and therefore higher threshold values are expected for the finite element model (Fig. 4.6A) than for the homogenous medium solution (Fig. 4.6B) despite of a 1.77 times larger maximum value of V_e in case A, e.g., the threshold for a cathodic 100 μ s pulse of neuron7 is an electrode voltage of 330 mV in A, compared to only 280 mV in B.

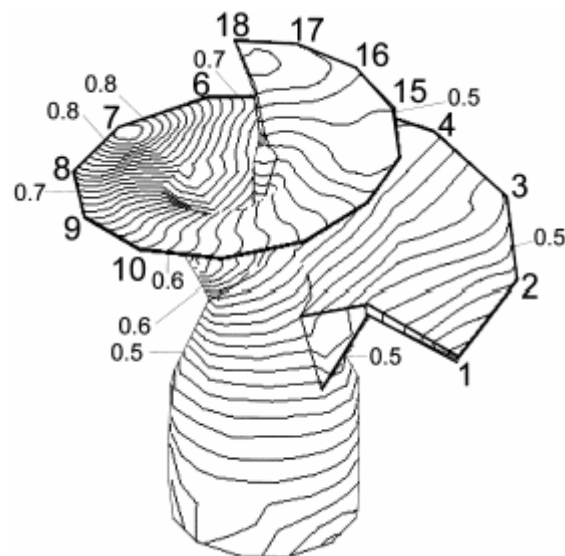


Fig. 4.5. The electrically stimulated spiral ganglion. The equipotentials for the same electrical situation as in Fig. 4.4 are shown at the surface of the neural compartment in a view that corresponds with Fig. 4.3. The numbers 1-18 mark the 30° main sections. The numbers between 0.5 and 0.8 help to find the 10% voltage steps between 0 at the border of the bony cube and the unit potential at the surface of the electrode. The electrode is just below the 180° 'turn' as marked by number 7 and therefore 'healthy' cochlear neurons that are close to position 7 are the most excitable ones. Neuron 7 and the central part of the electrode are within the cross section as shown in Fig. 4.2. The highest equipotential line on the spiral ganglion within the cube is 0.81 and the lowest is 0.41.

The first response in neuron 7 is strongest at peripheral node P1 and the beginning of the excitation process is well fitted by the activating function when the single high value at the post-somatic compartment is neglected (bottom curves in Figs. 4.6A and 4.6B). Figure 4.7 shows the excitation process along neuron 7 in 100 μ s steps for a -360 mV, 100 μ s monopolar stimulus, i.e., the influence of the reference electrode is neglected.⁴ The neural reaction with the 3D finite element data is qualitatively similar to the results predicted by the homogeneous field analysis (comp. Rattay et al. 2000): (i) there are 2 excited regions in the peripheral axon (P1, P3, see bottom curves in Fig. 4.6A and line 3 in Fig. 4.7, corresponding to the voltage profile at the end of the stimulus at $t=0.2$ ms), (ii) the soma is a strong barrier for propagation and causes a time delay for peripheral spikes, (iii) the first reaction in the

⁴ In comparison to the active electrode, the reference electrode is assumed not to be within the scala tympani and to have at least a three times greater distance to the excited region of the target neuron; under such an assumption the position of the reference electrode has only a small influence on the excitation process, (comp. Rattay 1990, p 129).

central axon is smaller than in the periphery (bottom curves in Fig. 4.6A and line 3 in Fig. 4.7), both for cathodic and anodic stimulation.

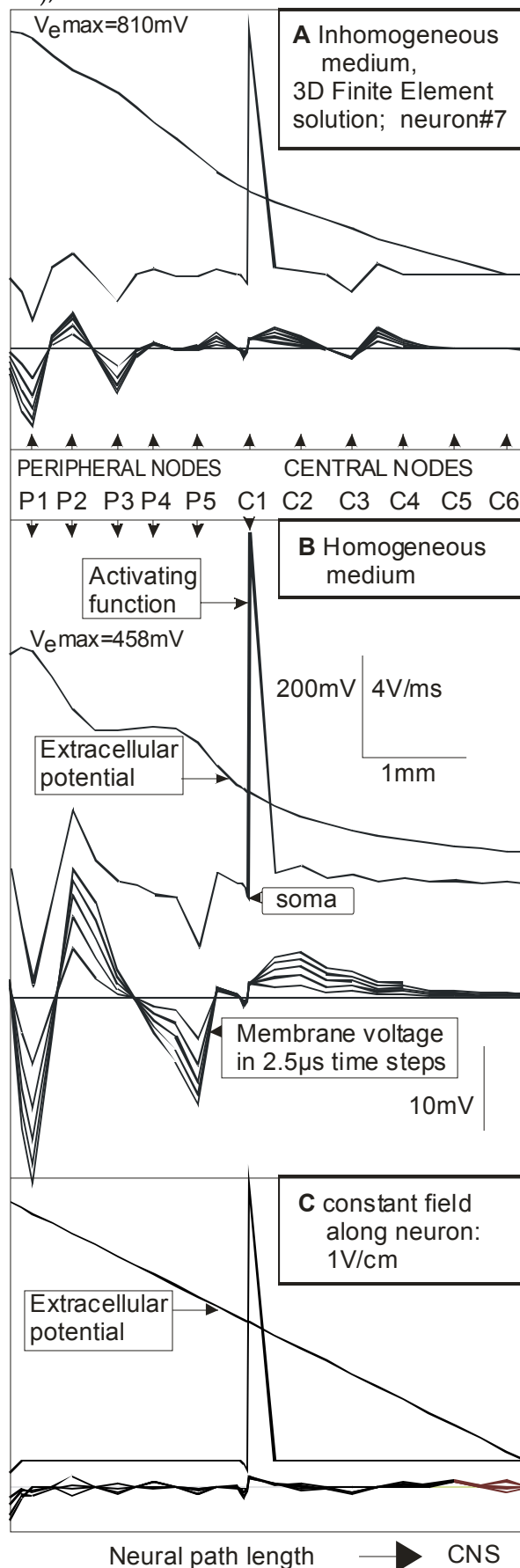


Fig. 4.6. Comparison of the calculated excitability of neuron7 under different assumptions. (A) 3D-finite element conditions as in Fig. 4.5 ($V_{electrode}=1000\text{ mV}$), (B) excitation by the same electrode position but within an homogeneous medium (assumptions as in the companion article: spherical electrode, diameter 0.48 mm; $I_{electrode}=1\text{ mA}$, $V_{electrode}=1000\text{ mV}$, $\rho_e=300\text{ Ohm.cm}$), (C) a constant field of 1 V/cm is applied along the neuron. All cases (A)-(C) include pictures of the activating function, the extracellular potential and the development of the membrane voltage along the neuron; the same scaling is used. All graphs are polygons with breakpoints at the nodes (position marked by arrows) and a point in between, representing the internode reaction. Additionally, there is the soma with 3 unmyelinated presomatic compartments. The high isolated maximum at the postsomatic compartment (=C0) cannot effect the excitation process because of the current consuming neighbored soma. This effect can be observed in the curves below the activating function, which represent the membrane voltages within the first 10 μs of an applied stimulus.

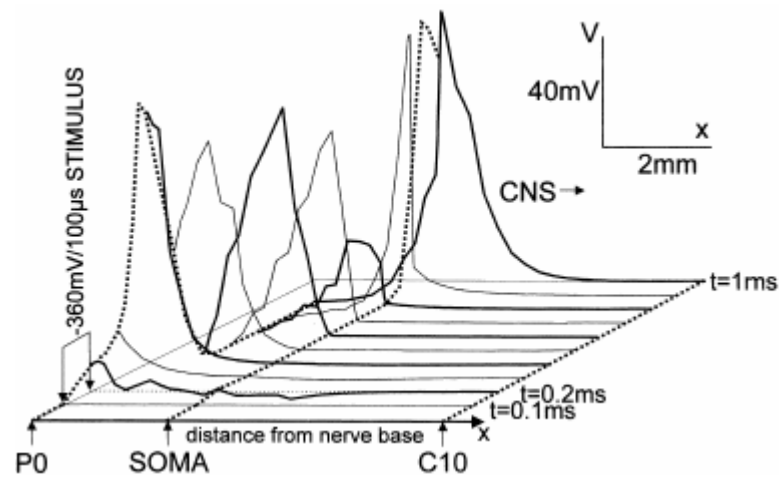


Fig. 4.7. Excitation of 'long dendrite' neuron 7 with a monophasic cathodic stimulus, 10% above threshold. Every line shows the membrane voltage V as function of the neuron's length coordinate. Separation of time steps: $100 \mu\text{s}$. At the end of the $100 \mu\text{s}$ stimulus maximum membrane voltage is at node P1 and node P0. Excitation develops faster in P0 because the P1 compartment loses current to the right side. For clarity every second line of the voltage profile is thin. The dotted lines represent the membrane voltages in P0, soma and C10 as functions of time. Note that the large soma capacity hinders the propagation of the excitation process which can be observed by the 'sharp' corners at the soma of the voltage distribution curves corresponding to times 0.6-0.8 ms (lines 7-9).

Figure 4.8 shows the membrane voltage of the neuron 7 compartments as functions of time for mono- and biphasic monopolar stimuli. For all types of stimuli three regions of excitation can be recognized during stimulus pulse period: two regions in the periphery and one in the central axon. However, under the assumptions of Fig. 4.8 all spikes are generated at the lateral end of the cochlear nerve. Comparison with Fig. 3.6 demonstrates again the relationship of the excitation process in the homogeneous and inhomogeneous medium: the responses of corresponding compartments during the stimulating period are qualitatively similar but the 'smoothing effect of the extracellular potential by the bony shielding' reduces the excitability within the inhomogeneous medium and causes sub-threshold response for the 1000 mV case in Fig. 4.8, whereas 720 mV are enough for spiking in the homogeneous volume conductor.

Excitation of neurons 3-15, monopolar, bipolar and quadrupolar stimulation

The excitability of neurons, especially the long dendrite cases, were tested in steps of 30 degrees along the spiraled cochlea; especially neurons in the positions 3-15 according to Fig. 4.5 were investigated. For monopolar stimulation extracellular voltage decreases more in the basal turn because the good conducting cochlear fluid compartment increases its cross section area there, e.g., neurons 6 and 5 have lower maximum values than the corresponding neurons 8 and 9 (Fig. 4.9). This phenomenon is documented also in other modeling work and by experiments [Jolly et al. 1996, Kral et al. 1997]. Neurons more distant from the stimulating electrode have their maximum extracellular voltages not at the peripheral ending but within the cone of the modiolus or in the Rosenthal canal (neuron 3-5 and 10-15, see Fig. 4.9).

Putting the electrode below neuron 6 and 8 and using the principle of superposition we obtain the finite element data for bipolar and quadrupolar stimulation with a 30 degree distance for the separation of the electrode centers. In the bipolar stimulation standard case +1 Volt is applied at the electrode with position 7 and -1 V at position 8. For quadrupolar stimulation the electrode voltages are -0.5 V, 1 V, -0.5 V for positions 6, 7, 8, respectively.

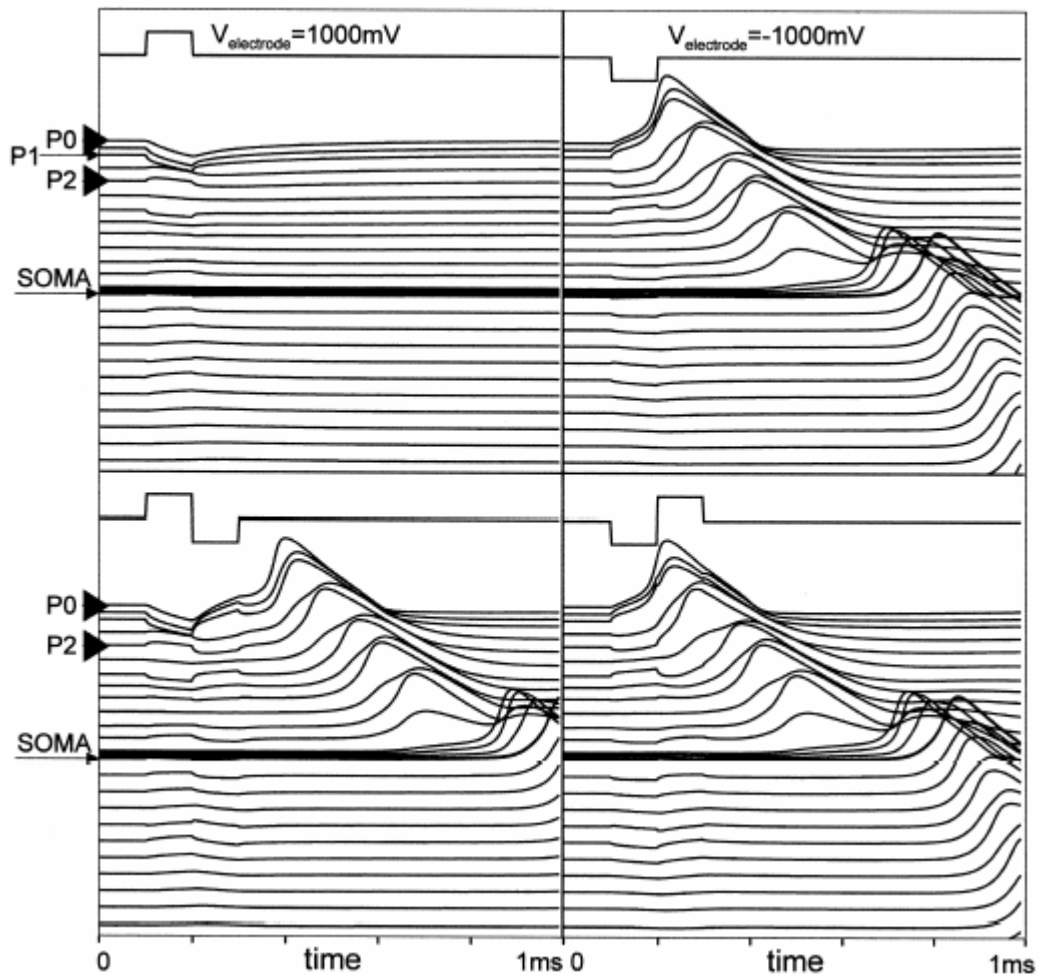


Fig. 4.8. Neuron 7 response to mono- and biphasic 1000 mV stimuli. Every line represents the evolution of membrane voltage of a single compartment. The +1000 mV monophasic stimulus cannot generate an action potential. There are some primary reactions in the central axon, but they are too weak to produce a spike in any of the four cases or even to influence the arrival time of the spike at the CNS. The cathodic pulse is responsible for spiking in all cases.

Figure 4.10 allows to compare the first reactions of neurons 3-15 for monopolar, bipolar and quadrupolar stimulation. Membrane voltages evoked by 1 V monopolar stimulation are rather large for all neurons both in the peripheral and in the central axons; the shapes of membrane voltages does not essentially change from neuron to neuron. Neuron 7 is closest to the electrode and is the most excitable of all 18 selected neurons in the spiral ganglion for positive as well as for negative stimuli; neuron 7 has the greatest positive and negative activating function values (Fig. 4.10). Bipolar stimulation causes opposite signs of membrane voltages and activating functions in corresponding compartments of neuron 7 and neuron 8 and therefore a single stimulus pulse will generate spikes at different node positions in both neurons. Excitation decreases quickly with distance, but there is also a non excitable region between neuron 7 and neuron 8. The quadrupolar electrode configuration as a combination of 2 dipoles ($-V/2$ at 6 $+V/2$ at 7 plus $+V/2$ at 7 $-V/2$ at 8) avoids the strong asymmetry of a single dipole but restrains the spread of excitation along the spiral.

The subthreshold reactions of target fibers in different positions and under different types of stimulus modes (Fig. 4.10) give an impression on the points of spike generation and individual thresholds. Figure 4.11 and Table 4.2 present more details on monophasic and biphasic stimuli. Monopolar stimulation with -990 mV, 100 μ s pulses (3x threshold) causes as

much as 2/3 of the investigated 'long dendrite' cochlear neurons to be spiking (12 representatives from 18; comp. Table 4.2, column 2), stimulus increase to 315% of threshold causes spiking also in neurons 9, 10 and 18.⁵ The fact that threefold threshold currents excite most of the cochlear neurons holds also for other cases of monopolar stimulation (Fig. 11D; Table 4.2). In contrast, bipolar and especially quadrupolar stimulation focuses the population of excited fibers even for strong stimuli (Fig. 4.11). Different possible points of spike generation as predicted by the activating function (Fig. 4.10; Table 4.2) cause the travelling spikes to be at different locations along their way to the central nervous system CNS (Fig. 4.11). With a velocity of 14 m/s in the central axon as predicted by the model the spike arrival times vary between 47 and 410 μs ⁶ (Fig. 4.11). In the monopolar case of Fig. 4.11D, 4 of 9 spikes are initiated in the central axon whereas, e.g., for the bipolar stimulation (Fig. 4.11E) this relation is 5 of 6.

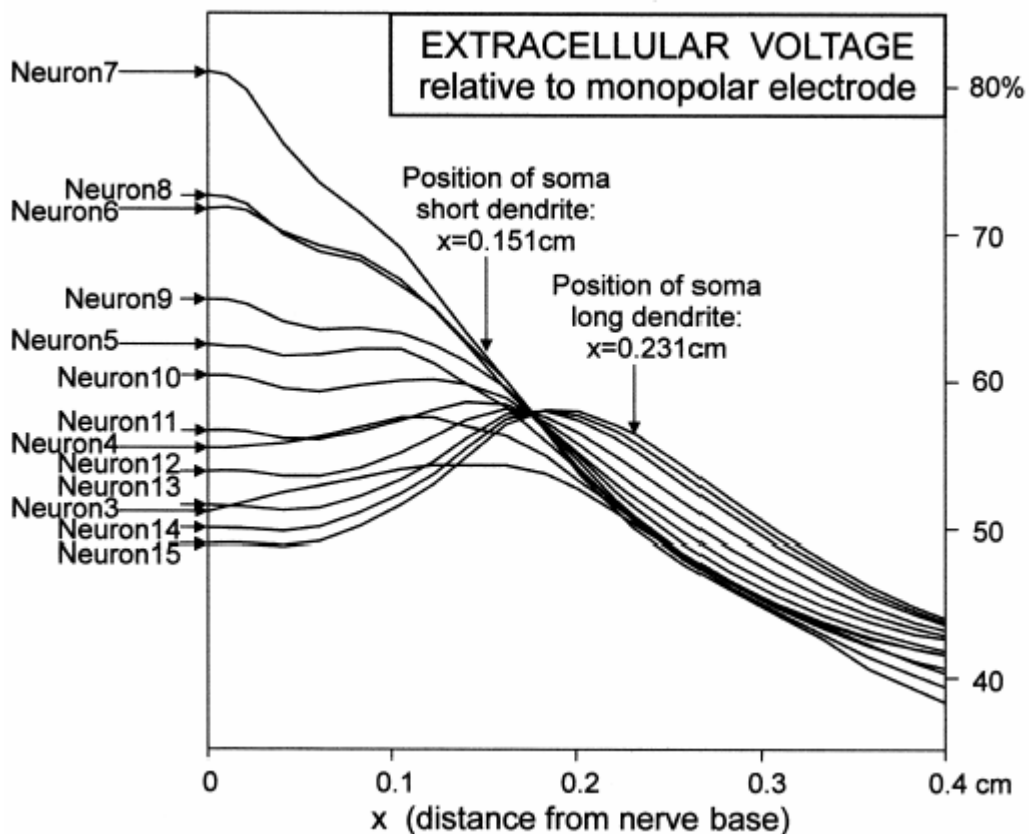


Fig. 4.9. Voltage distribution along neurons 3-15. The active electrode is below the most influenced neuron 7 which feels 81% of electrode voltage at the unmyelinated terminal ($x=0$). Extracellular voltage is calculated at compartment center-points; soma is compartment 16 for the 'long dendrite' and compartment 12 for the 'short dendrite' case.

Threshold voltages of 'short dendrite' and 'long dendrite' target neurons are listed in Table 4.2 for monopolar stimulation. Spike initiation is marked by the node which develops the action potential most quickly. When stimulated monophasically with negative voltage neuron 6, 7 and 8 develop their responses at P0 with similar thresholds for the short and long dendrite case (column 2). At changed polarity the activation of node P2 is hindered because

⁵ Extrapolation of these data to all turns causes about 50% of normally innervated nerve population of the human cochlea to fire when stimulated with threefold threshold intensity.

⁶ Other effects that influence the CNS arrival times are the degree of polarization or hyperpolarization of nodes in the vicinity of the arising action potential, and - not included in this simulation - variations in axon diameter and fluctuations in membrane currents.

both neighbors P1 and P3 have strong negative activating function values (comp Figs. 4.6A and 4.10D) and spikes are initiated in the central axon. The 'long dendrite' neuron 7 gets a rather high positive value of the activating function f at the internode between C2 and C3 (Fig. 4.6A), with small values of f at C2 and C3. This explains why neuron 7 needs a 7.9 times higher voltage for anodic (compared to cathodic) stimulation - and in spite of the fact that neuron 7 is closest to the electrode - it has the highest anodic threshold value of all the target neurons. The central axon of 'short dendrite' neurons in the vicinity of neuron 7 is closer to the electrode and therefore these neurons are essentially easier to stimulate with anodic pulses when compared with the corresponding 'long dendrite' cases. 'Short dendrite' neurons 1-6 and 8-12 have smaller threshold for anodic than for cathodic stimulation.

TABLE 4.2. THRESHOLDS OF ELECTRODE VOLTAGE IN [mV] FOR CATHODIC AND ANODIC MONOPHASIC PULSES AS WELL AS FOR BIPHASIC PULSES.

Neuron	monophasic(-)		monophasic(+)		biphasic(-/+)		biphasic(+/-)	
	threshold	node #						
1	940(1400)	C1(P4)	740(760)	P0(P0)	1080(1120)	C3(P0)	1000(1020)	P0(P0)
2	1100(1300)	C1(P4)	1040(1040)	P0(P0)	1240(1560)	C4(P0)	1280(1380)	C2(P0)
3	1700(1240)	C1(P4)	1260(1200)	C4(C3)	1700(1620)	C4(P5)	1500(1540)	C2(C3)
4	1940(1100)	P3(P4)	920(1320)	C3(C2)	1700(2500)	C4(P4)	1220(1320)	C4(C3)
5	1220(900)	P3(P3)	800(1140)	C4(C2)	1440(1180)	C2(P3)	1080(1480)	C4(C2)
6	760(730)	P0(P0)	700(1640)	C3(C3)	1100(1120)	C3(P0)	920(2000)	C3(P0)
7	330(330)	P0(P0)	640(2600)	C3(C3)	460(480)	P0(P0)	660(620)	P0(P0)
8	700(620)	P0(P0)	660(1560)	C3(C2)	900(900)	P0(P0)	860(1320)	C3(P0)
9	1400(1020)	P0(P3)	700(1100)	C0(C3)	1200(1360)	C3(P2)	940(1400)	C3(C3)
10	2200(1000)	P4(P4)	700(760)	C0(C3)	1360(1280)	C4(P4)	900(1000)	C4(C4)
11	2400(940)	P4(P4)	900(960)	C5(C3)	1800(1220)	C4(P4)	1220(1260)	C4(C3)
12	1240(920)	C1(P5)	1220(1100)	C5(C4)	1360(1160)	C4(P5)	1350(1440)	C2(C3)
13	740(860)	C1(P5)	1300(1060)	P0(C4)	840(1060)	C3(P5)	880(1300)	C1(P5)
14	600(840)	C3(P5)	1200(980)	P0(C3)	700(1040)	C4(P5)	740(1240)	C2(P5)
15	520(840)	C2(P5)	1100(900)	P0(C3)	620(1020)	C2(P5)	640(1200)	C2(C3)
16	460(860)	C2(P5)	960(860)	P0(C4)	540(1040)	C2(P5)	580(1160)	C2(C3)
17	420(920)	C2(P5)	880(880)	P0(C3)	500(1100)	C3(P5)	540(1160)	C2(C3)
18	400(1040)	C2(P5)	860(880)	P0(C3)	480(1240)	C2(P5)	520(1100)	C2(P0)

Node number defines the node with the first complete action potential. Monopolar stimulation with 100 μ s pulses from an electrode below neuron 7 (standard position). Long dendrite data in brackets.

The activating function is related to the second derivative of the extracellular voltage V_e along the axon [Rattay 1990] - and therefore the direction and value of the curvature of V_e is associated with the sign and value of f , respectively⁷. The systematic change of the shape of the extracellular voltage V_e in Fig. 4.9 causes the negative P3 peak of f in neuron7 (comp. Fig. 4.6A) to be shifted closer to the soma and become more dominant for cathodic stimulation when neuron number moves from 7 in both directions (Fig. 4.10D). This effect is seen by a

⁷ A \cup shaped curvature of V_e causes a positive f value; \cap results in $f < 0$. This relation can be observed, e.g., in Fig. 4.6B.

shift of spike initiation site from P0 to P3 and P4 for 'long dendrite' neuron5 and neurons 4-1 as well as to P3, P4 and P5 for neurons9, neurons 10, 11 and neurons 12-18, respectively (Table 4.2, column 3, values in brackets). The 'short dendrite' neuron has some difficulties with the same shifting task, because the corresponding regions are close to the soma barrier. P3 is the last node of Ranvier which has to support the current consuming presomatic compartment, resulting in a threshold of -1940 mV (double anodic threshold value) for neuron4, whereas the 'long case' is easier to stimulate with cathodic stimuli. The situation is even more extreme for the 'short dendrite' neuron10 and neuron11 which are excited in the first of three unmyelinated presomatic compartments (denoted as P4 in Table 4.2, column 3, lines 10,11) and they need about threefold anodic intensity to generate spikes.

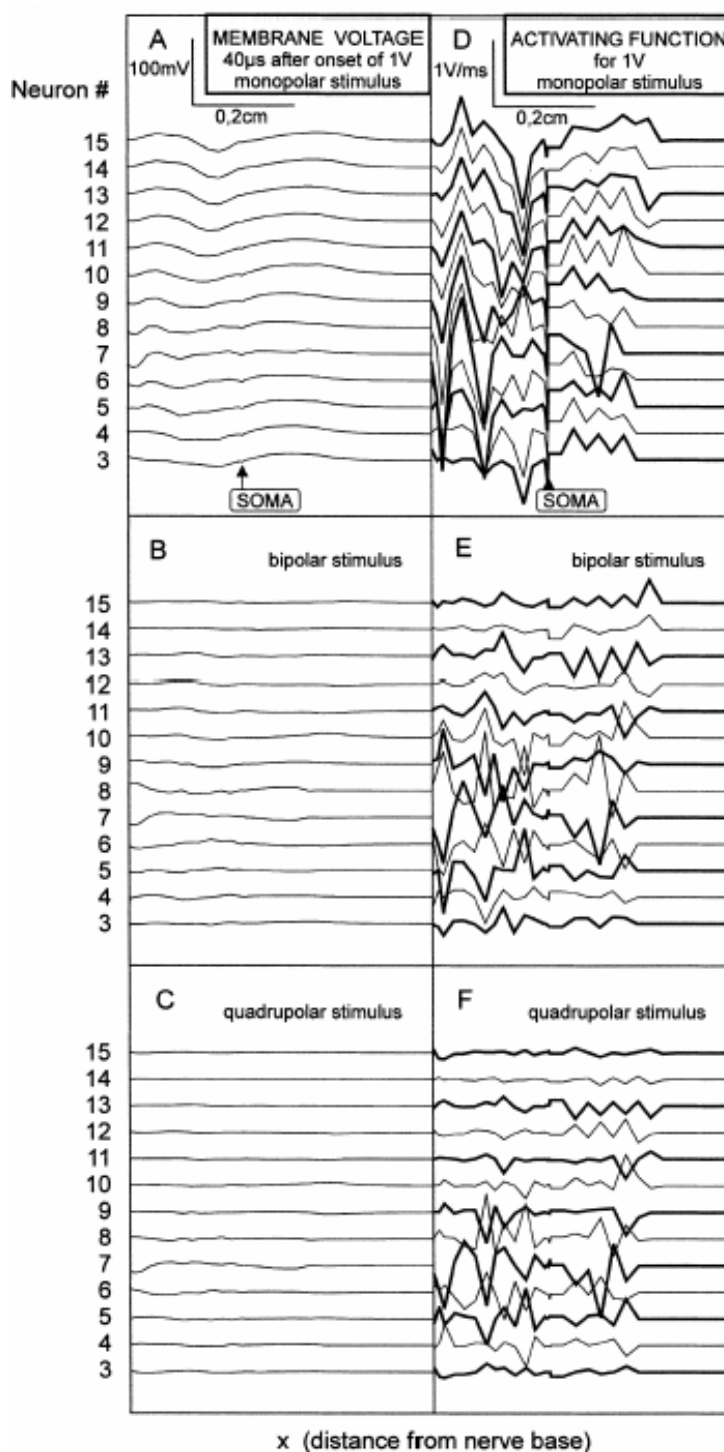


Fig. 4.10. First reactions of neurons 3-15 to a $+1$ V monophasic stimulus. Membrane voltages along the neuron are computed with the electric circuit model (left curves) and predicted by a modified activating function (right curves), where the single high peak of the postsomatic node C0 is generally omitted, because it has solely a small influence on the excitation process (comp. e.g., text in Fig. 4.6 and Chapter 3). $40 \mu\text{s}$ after stimulus onset all curves at the left part of the figure show subthreshold membrane responses. These smoothed versions of the activating functions confirm that the maximum points of the 'modified' activating functions are good indicators for the most excited regions which are the candidates for spike origins. The electrodes are below neuron 7 (monopolar stimulation), below neurons 7 and 8 (bipolar stimulation) and below neurons 6, 7 and 8 (quadrupolar stimulation); anode is always below neurons 7. Note the rather symmetric reactions on both sides of neuron 7 for monopolar and quadrupolar stimulation and the anti-symmetry (axis at 7.5) for bipolar stimulation. Deviations from pure symmetry and anti-symmetry are mainly caused by changes of electrical conductance along the spiral since cochlear compartment sizes become smaller from base to apex. For clarity every second activating function is represented by a thick line.

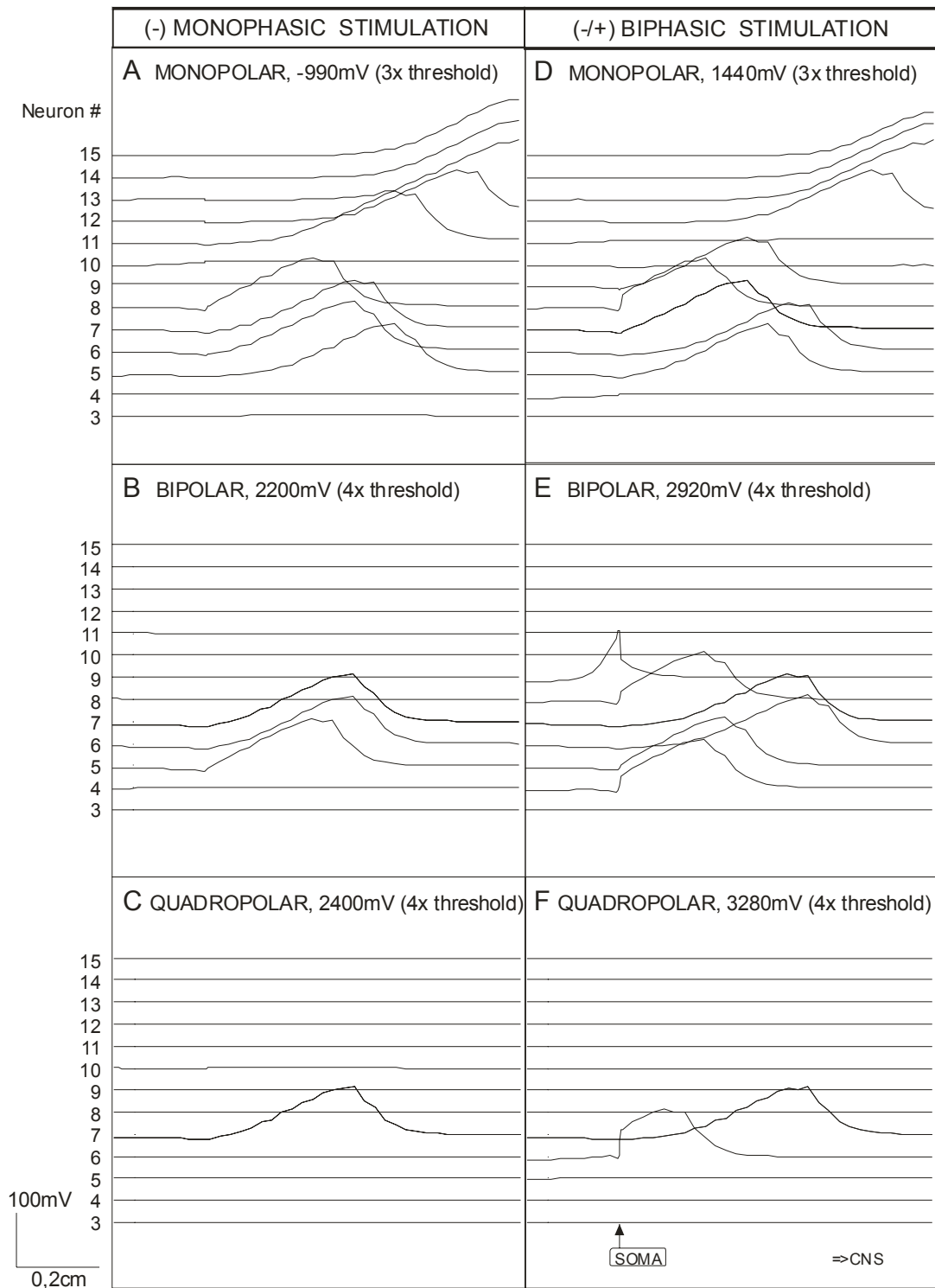


Fig. 4.11. Membrane voltages along neurons 3-15, 0.98 ms after stimulus onset. Stronger stimuli (3x threshold) activates most neurons for monopolar stimuli (A, D), fewer for bipolar electrodes (4x threshold; B, E) and fewest in the quadropolar case (4x threshold; C, F). Action potential positions differ up to 0,6 cm on their way to the CNS. Note the soma barrier effect (comp. Fig. 4.7) that causes a time delay and large voltage steps in the soma region, e.g., in E neuron 9 spike starts to propagate into the central axon whereas the neuron 6 and 7 spikes have completely passed the soma region. Irregularities in spike shape are caused by different dynamics in node and internode compartments. Stimulation with cathodic 100 μ s pulses (A-C) and biphasic 100 μ s + 100 μ s pulses, negative pulse first, no delay between pulses (D-F); electrode positions as in Fig. 4.10.

The range of excitation thresholds for biphasic pulses is generally smaller when compared with monophasic stimulation. An interesting exception is the second highest value in Table 4.2: neuron 4 threshold for (-/+) biphasic stimulation is 2500 mV. Note, that 1400 mV causes already a peripherally initiated spike, but by unfavorable circumstances (hyperpolarized postsomatic region) this spike is just blocked by the soma barrier. All the threshold values in this article are calculated without considering ion current fluctuations in the active membranes. By including current fluctuations with the standard noise value as introduced in the companion article we found spike propagation in the central axon in 8 of 10 cases for 1400 mV biphasic stimulation in neuron 4.

Excitation of degenerated neurons

In deaf people the number of peripheral axons is often drastically smaller than the number of central axons. This implies the loss of the periphery in many of the cochlear neurons [Felix et al. 1997]. Excitability of such degenerated neurons essentially depends on the distance between electrode and soma.

Figure 4.12 shows the excitation of degenerated neurons in the positions 3-15, stimulated with biphasic pulses. Generally these spikes will arrive earlier at the CNS since they spare the travelling time in the periphery and the soma barrier delay. The loss of the peripheral process always causes maximum excitation of the first nodes of the central axon and therefore there is little variance in action potential positions and arrival times for the normal degenerated human cochlear neuron; compare e.g., Figs. 4.12D and 4.11D. Long delays (350-400 μ s, comp, Chapter 3) resulting from crossing the soma barrier cannot occur when the peripheral process is lost. The activation of degenerated neurons needs higher stimulus currents because their excitable structures in the central axon are rather far from the electrodes, particularly for the 'long dendrite' neuron. However, threshold differences between a degenerated neuron and its healthy neighbor decrease with the distance of the neuron to the electrode. This fact can be analyzed by comparing the activating function maximum values of the peripheral and the central axon (Fig. 4.10). Figure 4.13 displays the thresholds for monopolar stimulation of healthy and degenerated neurons. The vicinity of neuron 7 to the electrode is the basis for low thresholds for excitation with biphasic pulses but the assumptions about the pathway of its central axon paradoxically causes maximum threshold values for the degenerated case (Fig. 4.13). The excitability of neurons 3-5 and neurons 9-15 is within a small range, even when degenerated neurons are included, because the excitation starts within the central axons and the extracellular potentials along these fibers are rather similar (comp. Figs. 4.9 and 4.13).

4.4 Discussion

The main task of this chapter is to present a rather simple 3D model that takes into account the spiral shape and the dimensions of the human cochlea. The conductance values for the various compartments, the size of the volume included in the model, and the assumptions about the boundary conditions have to be chosen in a way that allows for analysis of the current to distance relations relevant to artificially evoked neural signals in cochlear implants.⁸ The electrical tissue properties within the living human cochlea are difficult to evaluate and large differences are found in the published conductances, e.g., for bone [Suesserman and Spelman 1993, Kosterich et al. 1983]. There exist data from saline tank measurements and from animal experiments that can be used in resistor networks in order to

⁸ In Chapter 3 we neglected capacitance and resistance effects at the electrode-perilymph interface and we obtained a simple relation: for a 0.48 mm diameter ball electrode, 1 mA current flow is reached at 1 V electrode voltage in an infinite homogeneous medium with a specific resistance of 300 Ohm.cm. Current-voltage relations depend on specific electrode properties and can be found by tank measurements.

find a first approach to the voltage distribution generated by cochlear implants [Strelhoff 1973, Jolly et al. 1996, Kral et al. 1998]. With such investigations voltage profiles along the electrode carrier are found but only few modeling work deals with the voltage profile and the points of excitation along the neural pathway.

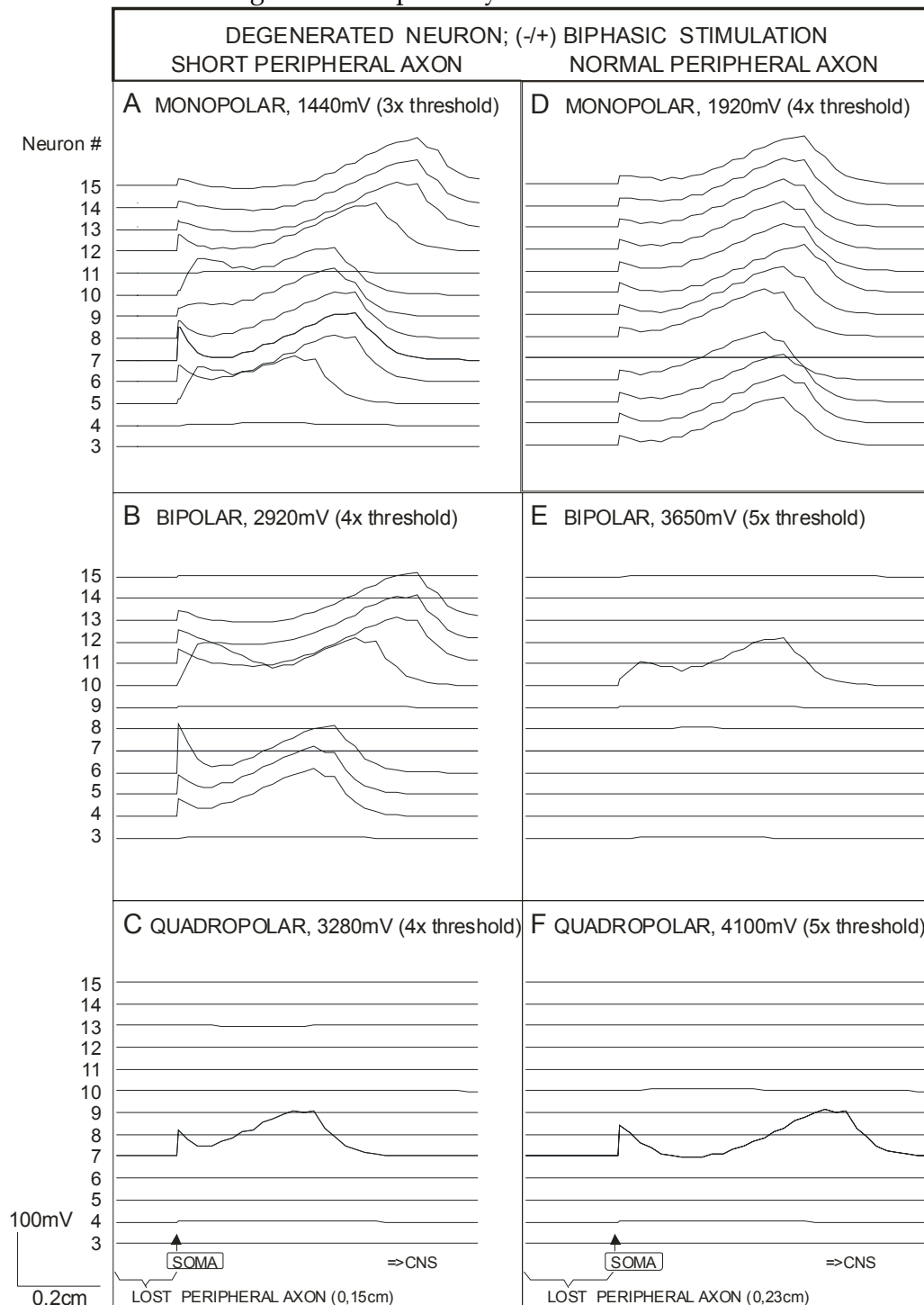


Fig. 4.12. Membrane voltages along degenerated neurons 3-15, 0.48 ms after stimulus onset. Compared with the excitation of healthy neurons (Fig. 4.11) spiking of the central axon in the degenerated case is earlier, more synchronized and needs higher stimuli; note, for example, the high stimuli in (E) and (F) that cause only one of the 13 neurons to fire. Solely in the quadropolar cases (C, F), neuron 7, which is closest to the electrode, is easiest to stimulate and will be excited (Fig. 4.13). Threshold values (e.g. 3times threshold) are relative to the healthy neuron.

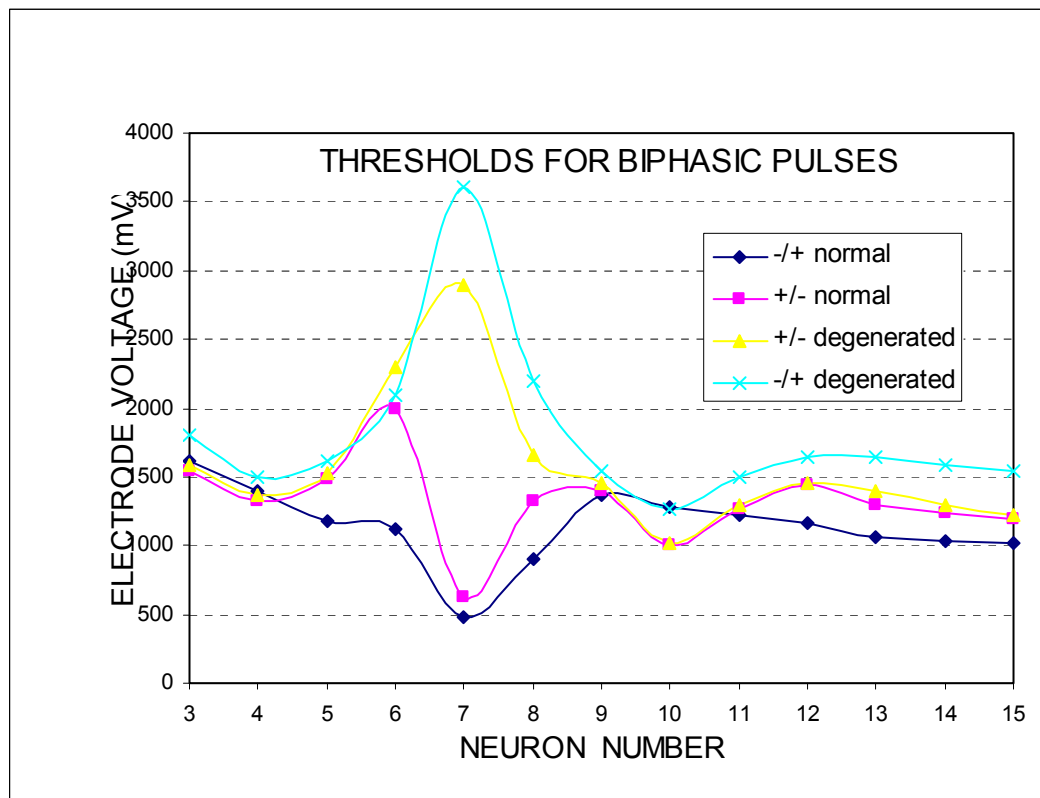


Fig. 4.13. Thresholds of neurons 3-15 for stimulation with monopolar electrode. There is a threshold increase in the order of 6 dB when the most excitable healthy neuron 7 is compared with the '30° neighbor' neurons 6 and 8. Outside of this region the threshold-distance relation becomes flat and especially between the +/- normal and +/- degenerated cases there are minor differences only. Note however the rendered excitation of the degenerated neurons in the vicinity of location 7 which marks the position of the electrode.

In order to check the sensitivity of the model to the assumptions - especially concerning the influence of the electrical conductances - we have compared the proposed results for neuron 7 with a 2D MATLAB finite element model evaluation. The 2D simulation corresponds to a specific case of a 3D geometry where the cross section is moved along an infinite line perpendicular to the plane of the cross section. The resulting prismatic volume can be divided into identical slabs. With the boundary conditions of our 3D model but assuming in the scala tympani constant conducting surface along the implant, no current flow will be observed between the slabs and therefore, the 3D and 2D solutions become identical with these assumptions. For the pathway of the neuron which is closest to the electrode, i.e., neuron 7, the 2D and the spiral 3D voltage profile are of similar shape (comp. Fig. 4.14 with Figs. 4.9 and 4.6A). However, in contrast to the spiral 3D model the voltages in Fig. 4.14 are generally higher, because in the 2D model electrode currents are not allowed to flow out of the cross section region.

Doubling separately the conductances of nerve-tissue, cochlear fluids, bone or that of the basilar membrane and organ of Corti compartment does not essentially influence the shape of the extracellular voltage along the neural pathway (Fig. 4.14). Consequently, we assume that the presented results represent a substantial contribution for the simulation of the electrically stimulated human cochlea - in spite of the fact that the conductivity data are not fully reliable. As presented in the result section, we demonstrated that the low conductance of the bone compartment is responsible for a nearly constant field along the peripheral axon of neuron 7 (Figs. 4.4 and 4.6). However, the rather linear voltage drop in the periphery gets

closer to the shape of the homogeneous medium if the conductivity of bone is doubled (Fig. 4.14). For our computations we used 80% of the resistivity value reported by Kosterich et al. (1983) for fluid saturated bone – but this resistance is still essentially higher than suggested by Suesserman and Spellman (1993). In summary this means: (i) changing the conductance of any region by a factor between 0.5 and 2 will not fundamentally influence the voltage profile and – as a consequence – the excitation of the cochlear nerve; (ii) if we follow Finley et al. (1990), assuming a bone conductance more close to that of nerve tissue, all results concerning voltage distribution are moved towards the homogeneous field solution and we can deal with the simple current-distance relation as used in Chapter 3 to obtain a first approach (see Rattay et al. 2000).

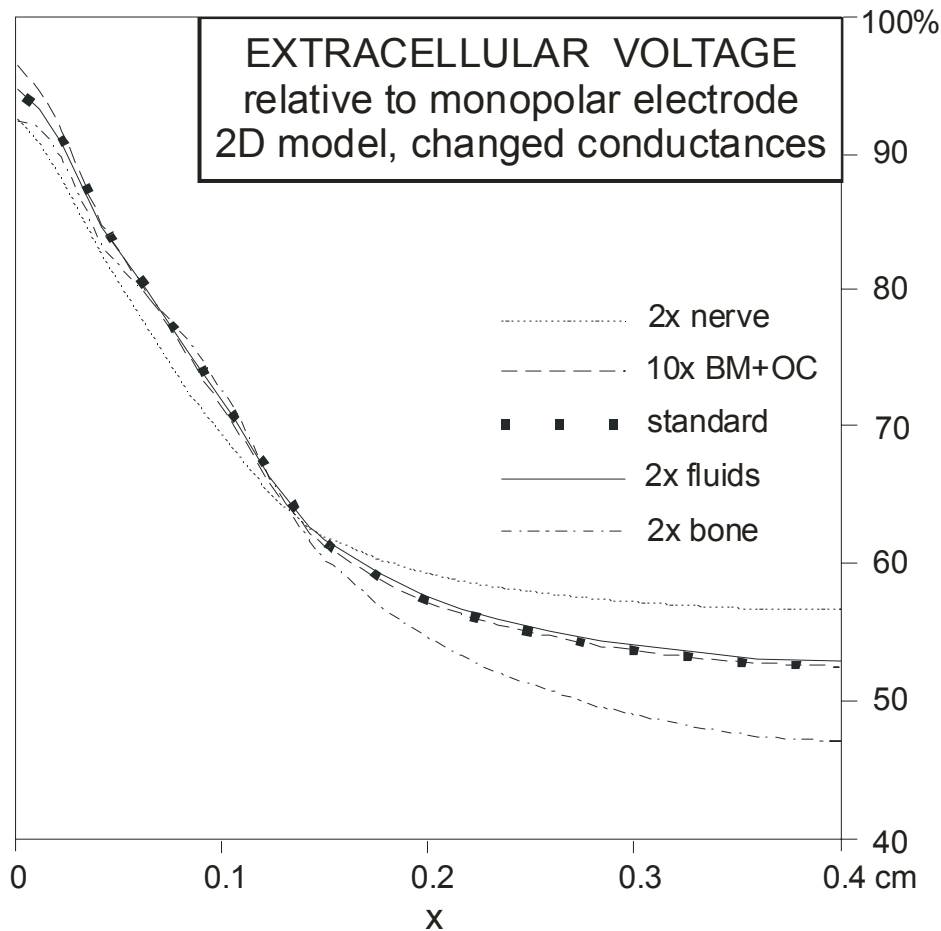


Fig. 4.14. Influence of conductance changes on voltage distribution along neuron7, calculated with a 2D finite element model. The extracellular voltage along the neural pathway for standard conductances (Table 4.1) marked by squares are comparable with the neuron7 values of the 3D model in Fig. 4.9. Note the higher voltage for the 2D solution. Doubling the conductance of the cochlear fluids and even multiplying the conductance of the Basilar Membrane and Organ of Corti compartment (BM+OC) by ten does not essentially change the voltage profile. The influence of conductances for the bone and the nerve compartment is slightly stronger, especially in the soma region and for the central axon. Calculations with a scheme similar to Fig. 4.2, but with more keypoints that result in a closer approach to the real cross section shown in Fig. 4.1.

According to our simulations remarkable differences are expected in electrically stimulated cochlear neurons between man and the animals used for experiments. The reason is the long peripheral human axon. For example, Miller et al. (1999) report about single fiber

recordings with monopolar monophasic stimulation in cats: (i) Threshold stimulus level is polarity dependent, with relatively lower cathodic thresholds, e.g., a mean value of 1 mA for 26 μ s anodic stimuli and a -0.88 dB lower value for cathodic pulses – in comparison, our simulations demonstrate essential differences when polarity is changed, especially for neurons close to the electrode (Table 4.2, columns 2 and 4). (ii) Miller and coworkers assume that in the cat, with monopolar intracochlear stimulation, most fibers are stimulated at axonal (modiolar) sites and a minority of fibers nearest the electrode are stimuable at their peripheral processes – whereas by cathodic stimulation the 'long dendrite' human cochlear nerve is always excited in the periphery and the 'short dendrite' human neuron in 8 of 18 cases (Table 4.2, columns 3). (iii) They observed bimodal post-stimulus-time histograms only in a small number (2%) of fibers, supporting the hypothesis that both the peripheral and central processes are excitable with the same stimulus polarity, in a limited number of cases – however, our simulations show that in contrast to the morphometry of cats in a great part of non-degenerated cases the human cochlear geometry make the peripheral process easier excitable – but application of stronger stimuli will generate additional spikes in the central fibers (Chapter 3; Table 4.2). Therefore, cochlear implant patients have to expect a confusing temporal fine structure of their neural code when an input signal (speech) generates spikes in some central axons whereas other peripherally evoked action potentials arrive with a longer delay. However, this effect cannot occur in a population of degenerated fibers.

Comparison of a fine structured rotationally symmetric human cochlea model [Schmid et al. 1998] with the presented spiral geometry show similar voltage profiles for neural pathways in the vicinity of the stimulating electrode. Therefore, representing the geometry by more keypoints was not necessary. In our opinion, a refined model should be concentrated on two effects that advance excitation. (i) The natural neural pathway is not planar and not as smooth as in our assumptions; details about the pathway should be included because regions with strong curvatures (comp. e.g., Fig. 3.1) are excitable more easily. (ii) focusing electrodes should be designed and tested in a simulation study.

5. Effective electrode configuration for selective stimulation with inner eye prostheses

The quality of visual perception with retinal prostheses strongly depends on the local selectivity. Electrode arrays at the surface of the retina should excite exclusively cells within a local area but they are expected to co-stimulate bypassing axons originating from ganglion cells of the outer regions. Long electrodes parallel to these axons are shown to be good candidates for avoiding the co-stimulation phenomenon. Efficiency of focal excitation depends on the length and resistance of the electrodes. Furthermore, optimal dipole distance is calculated and it is analyzed why, with epiretinal prostheses, bipolar retinal cells are easier to stimulate than ganglion cells despite of the fact that the elements of the ganglion cells are closer to the electrode.

5.1. Introduction

Two main types of retinal prostheses for the blind are currently in development [Margalit et al. 2002, Warren and Normann 2002]. Concerning the position of the stimulating electrodes, the subretinal prosthesis [Chow et al 2001, Zrenner et al 2001] is rather similar to the natural situation as the degenerated photoreceptor cells are substituted by an array of electrodes and the cells of the retinal network closest to the photoreceptors are the first candidates to become stimulated (Fig. 5.1) [Stett et al. 2000].

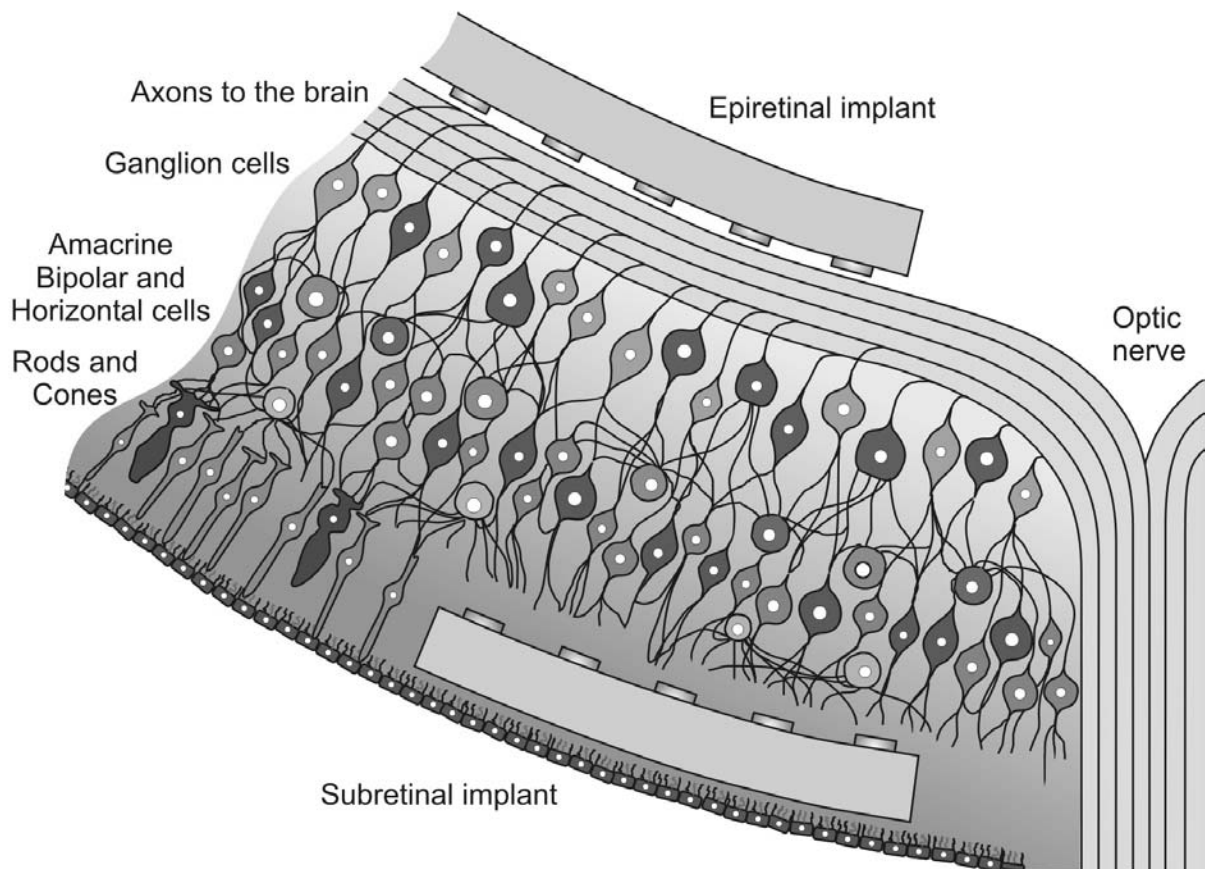


Fig. 5.1. Scheme of retinal cross section with the two available types of inner eye prostheses: epiretinal and subretinal implant. The axons of the ganglion cells are the excitable elements closest to the epiretinal electrodes.

Epiretinal prostheses [Eckmiller 1997, Humayun et al. 1999, Grumet et al. 2000] are mounted on the inner retinal surface and the closest excitable elements are axons from ganglion cells. Computer simulations of electrically stimulated ganglion cells show no significant threshold dependence when a small spherical cathode is moved at the retinal surface from a position above the soma along the pathway of the axon but stronger stimuli are necessary for dendritic spike initiation [Greenber et al. 1999, Rattay et al. 2003]. Therefore, the current from an electrode of an epiretinal prosthesis which is intended to excite a nearby ganglion cell must be expected to initiate spikes also in passing axons from distant ganglion cells (Fig. 5.2).

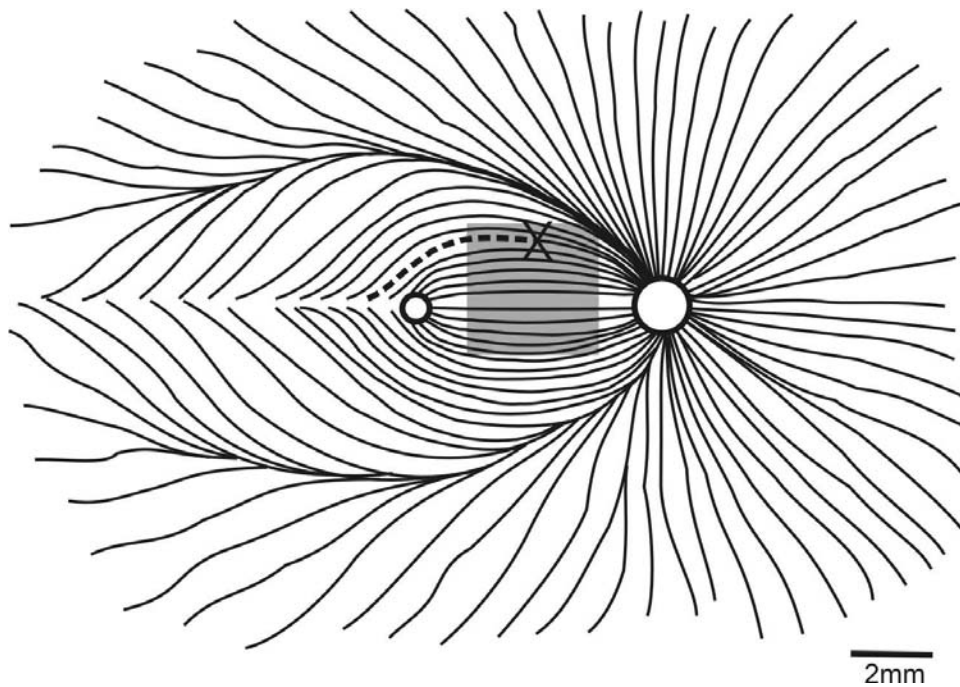


Fig. 5.2. Selected pathways of ganglion cell axons in a rectified human retina with a 3 mm x 3 mm electrode array placed at the inner surface of the retina (gray square). Many fibers have their origin close to the fovea (small circle) but all axons leave the retina at the optic disk forming the optic nerve (right circle). An active small disk electrode marked as X can excite all axons from ganglion cell bodies placed along the dashed line instead of a focused region below the electrode. (Redrawn after J. Rizzo.)

Electrodes at the inner retinal surface are reported to activate rabbit ganglion cells easier directly than by synaptic inputs from the retinal network: 37 and 7.7 times higher currents for indirect stimulations are needed for 5 μm and 125 μm diameter electrodes, respectively at 100 μs pulses which reduce to factors 9.3 and 2.0 for 2 ms pulses [Jensen et al. 2003]. These results and the fact that cell bodies are generally rather difficult to stimulate extracellularly [Chapter 2 and Rattay 1998, 1999] imply sophisticated strategies for focal stimulation with epiretinal implants.

The aim of this chapter is to analyze the possible influence of electrode geometry on selective stimulation of a target ganglion cell by avoiding co-activation of passing axons. In the following we refine an approach of Grumet (1994) who concluded from theory and preliminary experiments that long stimulating elements parallel to the main directions of bypassing axons are appropriate for this task. The presented results reflect the evolving insight from small disk electrodes, via rectangular electrodes, to a sophisticated implant geometry.

5.2 Material and Methods

The excitability of retinal ganglion cell axons is compared concerning their positions relative to different forms of stimulating electrodes. Straight axons and a traced cell are analyzed with the activating function and computer evaluation of a compartment model. Transmembrane voltage is also calculated for two bipolar cells.

Potential distribution of an epiretinal implant with an active dipole is computed with Finite Element software FEMLAB[®] (COMSOL, Sweden) for a simplified prismatic geometry, consisting of several $2000\mu\text{m} \times 2000\mu\text{m}$ layers (the investigated volume is smaller compared to Fig. 5.2 in order to spare elements): electrode carrier ($100\mu\text{m}$ thick), aqueous body layer (i.e. distance between implant and retina surface: $0\mu\text{m}$ or $20\mu\text{m}$), retina ($200\mu\text{m}$), sclera ($200\mu\text{m}$). The first layer is an insulating plate (electrode carrier) where the $10\mu\text{m} \times 10\mu\text{m}$ metallic contacts of an electrode array are embedded. Each line of electrodes which is designed to be placed parallel to the axonal main paths (Fig. 5.2) is in contact with a conducting material filling a $10\mu\text{m}$ wide and $50\mu\text{m}$ deep slot in the lower region of the implant (Fig. 5.3). Two electrodes in different slots are assumed to be active at the same time resulting in a dipole distance of, e.g. $400\mu\text{m}$ or $1000\mu\text{m}$. In a first investigation retinal ganglion and bipolar cell excitation is simulated without the conducting interface medium by simple long rectangular electrodes or $10\mu\text{m}$ diameter disk electrodes mounted at the surface of the electrode carrier which is faced to the retina.

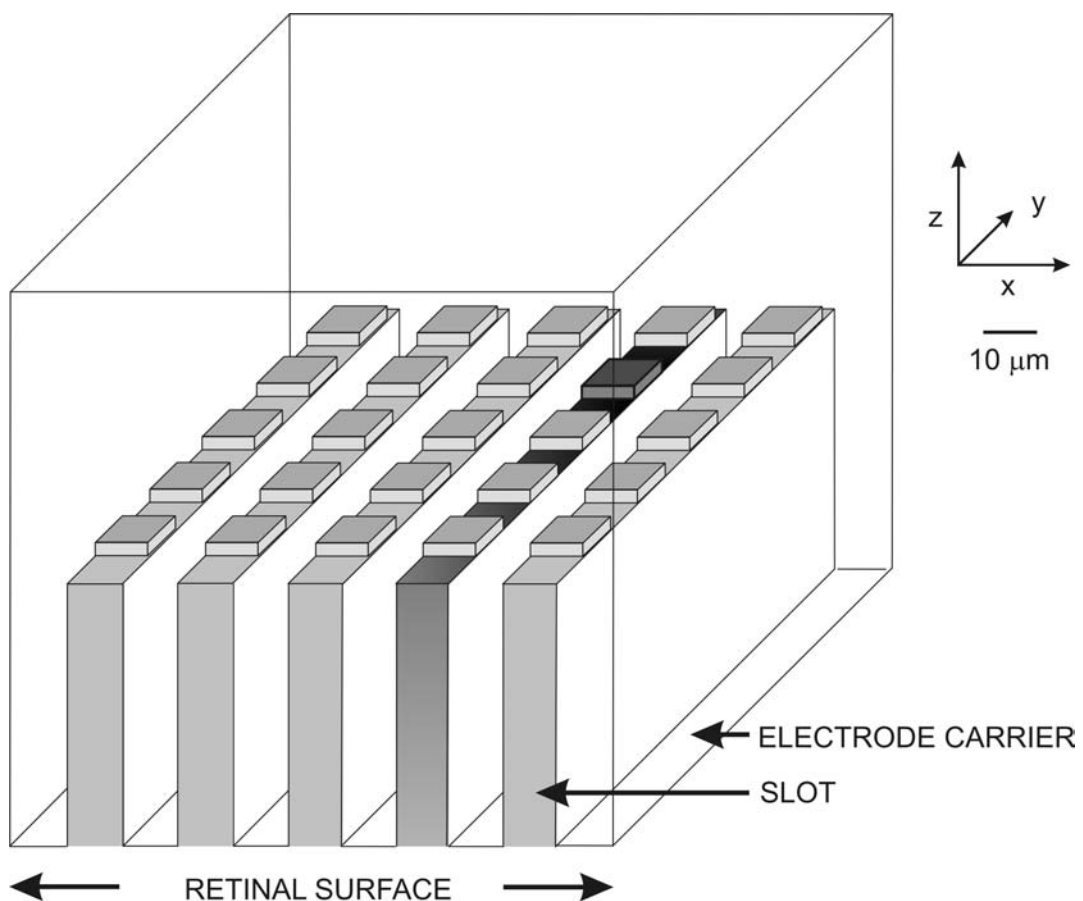


Fig. 5.3. Section of the proposed epiretinal implant. The slots are filled with conducting material (gray). The electrode carrier is transparent, the dark square symbolizes the active electrode. The second electrode (not shown) has a x -distance of $400\mu\text{m}$ and $1000\mu\text{m}$, respectively. The lower part of the implant is either assumed to be in direct contact with the inner retinal surface or it has a distance of $20\mu\text{m}$.

The specific resistances of all tissue and technical materials are defined relative to the retina with $\rho_{\text{retina}}=57 \text{ Ohm.cm}$ [Doslak et al. 1980, Geddes and Baker 1967] by the following factors: electrode carrier (1000), conducting slot medium (0.001, 0.003, 0.01), aqueous body layer (1), sclera (10). The thickness and specific resistance of the sclera was found to have minor influence on the extracellular potential along the investigated cells.

The investigated ganglion cell (819 compartments) and bipolar cell #1 (340 compartments) are human substitutes based on traced salamander data. Their three dimensional coordinates and diameters have been supplied by Toby Velte. Cell #2 is a bipolar rod cell with 14 compartments only, no bifurcations and an orientation perpendicular to the electrode carrier. The ganglion cell soma diameter was assumed to be $10 \mu\text{m}$, differing to the traced $24 \mu\text{m}$ soma, as this is a better approach for the human case. This modification is of minor relevance as our simulation showed only minimal threshold dependence on soma size (not published) for the following case studies. Additionally, a smaller ganglion cell type (69 compartments) was simulated by cutting four main branches of the dendritic tree.

The transmembrane voltage V_n of the n -th compartment of a target cell is calculated according to Eqn. 2.2, with an intracellular resistivity of 110 Ohm.cm [Coleman and Miller 1989]. For the linear analysis ion membrane current $I_{\text{ion},n}$ is assumed to be proportional to V_n with membrane conductance $g_m=0.02 \text{ mS/cm}^2$ [Coleman and Miller 1989] and $g_m=0.042 \text{ mS/cm}^2$ [Usui et al 1996] for ganglion and bipolar cells, respectively. Thresholds for ganglion cell body and axon are calculated with the Fohlmeister-Colman-Miller FCM-model [Fohlmeister and Miller 1997a,b]; see also [Rattay et al. 2002, Resatz and Rattay 2004] for details.

The Fohlmeister - Coleman - Miller (FCM) model

The FCM model includes five nonlinear ion channels and one linear leakage channel [Fohlmeister et al., 1990, 1997a, b]. The kinetic model was constructed on the basis of voltage clamp data in retinal ganglion cells of tiger salamanders and rats [Lukasiewicz and Werblin 1988, Lipton and Tauck 1987]. The model consists of I_{Na} , I_{Ca} , the delayed rectifier I_K , $I_{K,A}$, and the Ca -activated K current $I_{K,Ca}$. $I_{K,Ca}$ was modeled to respond to Ca influx, and a variable-rate Ca -sequestering mechanism was implemented to remove cytoplasmic calcium. I_{Ca} and $I_{K,Ca}$ do play an important role in regulating firing frequency.

The basic mathematical structure for voltage-gating is based on the Hodgkin-Huxley model:

$$C_m \frac{dE}{dt} = -\bar{g}_{Na} m^3 h (E - E_{Na}) - \bar{g}_{Ca} c^3 (E - E_{Ca}) - \bar{g}_K n^4 (E - E_K) - \bar{g}_A a^3 h_A (E - E_K) - g_{K,Ca} (E - E_K) - \bar{g}_l (E - E_l) + I_{\text{stimulus}} \quad \text{FCM-1}$$

$$\bar{g}_{Na} = 50 \text{ mS/cm}^2, E_{Na} = 35 \text{ mV}, \bar{g}_{Ca} = 2.2 \text{ mS/cm}^2, \bar{g}_K = 12 \text{ mS/cm}^2, E_K = -75 \text{ mV}, \\ \bar{g}_A = 36 \text{ mS/cm}^2, \bar{g}_l = 0.05 \text{ mS/cm}^2, E_l = -60 \text{ to } -65 \text{ mV}.$$

The gating of $I_{K,Ca}$ is modeled as

$$g_{K,Ca} = \bar{g}_{K,Ca} \frac{([Ca^{2+}]_i / Ca_{\text{diss}}^{2+})^2}{1 + ([Ca^{2+}]_i / Ca_{\text{diss}}^{2+})^2} \quad \text{FCM-2}$$

where $\bar{g}_{K,Ca} = 0.05 \text{ mS/cm}^2$ and the Ca^{2+} -dissociation constant, Ca_{diss}^{2+} , is $10^{-3} [\text{mmole/l}]$. $[Ca^{2+}]_i$ is allowed to vary in response to I_{Ca} . The inward flowing Ca^{2+} ions are assumed to be distributed uniformly throughout the cell and the free $[Ca^{2+}]_i$ above a residual level,

$[Ca^{2+}]_{res} = 10^{-4} [mmole/l]$, are actively removed from the cell, or otherwise sequestered with a time-constant ($\tau = 1.5 ms$). Thus, $[Ca^{2+}]_i$ follows the equation:

$$\frac{d[Ca^{2+}]_i}{dt} = \frac{-sI_{Ca}}{2vF} - \frac{[Ca^{2+}]_i - [Ca^{2+}]_{res}}{\tau} \quad \text{FCM-3}$$

where F is the Faraday constant, s/v is the ratio of surface to volume of the concerning compartment, and the factor of 2 on v is the valency. For a spherical soma with $r=12 \mu m$ Eqn. FCM-3 reads as:

$$\frac{d[Ca^{2+}]_i}{dt} = -0.000013 I_{Ca} - 0.666667 ([Ca^{2+}]_i - 0.0001)$$

E_{Ca} is modeled as variable according to the already mentioned Nernst equation.

$$E_{Ca} = \frac{RT}{2F} \ln \frac{[Ca^{2+}]_e}{[Ca^{2+}]_i} \quad \text{FCM-4}$$

where $[Ca^{2+}]_e$ the external calcium ion concentration is $1.8 [mmole/l]$.

Similar to the Hodgkin-Huxley model the rate constants for m, h, c, n, a, h_A solve the first order kinetic equation (Table 5.1):

$$\frac{dx}{dt} = -(\alpha_x + \beta_x)x + \alpha_x \quad \text{FCM-5}$$

The multi-compartment model includes representations for dendritic trees, soma, axon hillock, a thin axonal segment, and axon distal to the thin segment. On these parts the five ion channels were distributed with varying densities, which is simulated by varying the value of g_{max} (mS/cm^2) for each channel (Table 5.2)

TABLE 5.1. FCM MODEL:
RATE CONSTANTS FOR VOLTAGE-GATED ION CHANNELS

$\alpha_m = \frac{-0.6(E+30)}{e^{-0.1(E+30)} - 1}$	$\beta_m = 20e^{-(E+55)/18}$
$\alpha_h = 0.4e^{-(E+50)/20}$	$\beta_h = \frac{6}{e^{-0.1(E+20)} + 1}$
$\alpha_c = \frac{-0.3(E+13)}{e^{-0.1(E+13)} - 1}$	$\beta_c = 10e^{-(E+38)/18}$
$\alpha_n = \frac{-0.02(E+40)}{e^{-0.1(E+40)} - 1}$	$\beta_n = 0.4e^{-(E+50)/80}$
$\alpha_A = \frac{-0.006(E+90)}{e^{-0.1(E+90)} - 1}$	$\beta_A = 0.1e^{-(E+30)/10}$
$\alpha_{hA} = 0.04e^{-(E+70)/20}$	$\beta_{hA} = \frac{0.6}{e^{-0.1(E+40)} + 1}$

TABLE 5.2. FCM MODEL CHANNEL DENSITIES AT SOMA, DENDRITE, AND AXON (% TOTAL AXON LENGTH MEASURED AS DISTANCE FROM SOMA) IN mS/cm². TOTAL AXON LENGTH APPROXIMATELY 1 MM.

g_{max}	Soma	Dendrite	Axon(0-3%)	Axon(3-9%)	Axon(9-100%)
g_{Na}	70 mS/cm ²	40	150	100	50
g_{Ca}	1.5	3.6	1.5	0	0
g_K	18	12	18	12	15
g_{Ka}	54	36	54	0	0
$g_{K(Ca)}$	0.065	0.065	0.065	0	0

5.2 Results

Avoiding co-stimulation of by-passing axons

Fine visual resolution with epiretinal microelectrode arrays is hindered by the co-stimulation of superficial passing axons originating in distant retinal regions. In order to overcome this problem we simulated dipolar stimulation with long rectangular electrodes parallel to the orientation of passing groups of axons. Such electrodes will cause a nearly constant potential along an axonal segment that is close and parallel to the electrode. Within this segment the activating function is almost zero and therefore the neural membrane is hardly excitable. Retinal cells with somas proximal to the electrode are assumed to have lower thresholds caused by excitable structures transverse (i.e. not parallel) to the electrode.

We have evaluated this hypothesis by three axons oriented parallel or perpendicular to the electrode: the axon of the traced ganglion cell in connection with the soma and dendrites, a straight perpendicular and a straight parallel axon (Fig. 5.4A,B). All the axons pass the same region close to the center of the cathode and therefore they get similar maximum V_e values (Fig. 5.4C). However, the perpendicular axon becomes about four times more excited as shown both by the activating function (Fig. 5.4D) and the evaluation of the passive membrane model (Fig. 5.4E and Table 5.3, which for comparison contains also the results for small electrodes and the responses of both bipolar cells). Threshold current generates a spike resulting from the positive parts of f below the cathode endings (Fig. 5.4D), which quickly merge to a single excited region of transmembrane voltage (Fig. 5.4E). This effect is rather strong because the 200 μm cathode length is small compared to the fiber's length constant (λ is about 800 μm).

In order to obtain more significant threshold differences between structures parallel and transverse to the electrode the amplifying effect can be reduced by longer electrodes. Additionally, the electrode surface should be separated several, e.g. 20, micrometers from the retinal surface to get a better distance relation between the close bypassing axons (which should not be stimulated) and the deeper retinal elements (Fig. 5.1). Furthermore, the dipole distance was enlarged to 1000 μm in order to reduce threshold current, which actually approximates a monopolar stimulation mode. The traced ganglion cell was reduced by elimination of some large dendrites to spare computational effort. Such a cell is a good substitute for a human midget ganglion cell. This cell, which is called in the following the 'small ganglion cell', was stimulated with 10 μm x 400 μm electrodes in three positions (Fig. 5.5). Previous simulation showed that this cell is most excitable with the cathode above the proximal end of the thin segment (position B in Fig. 5.5), which is consistent with the investigations of Fohlmeister et al. 1997b and Carras et al. 1992. Threshold for positive and negative single 100 μs pulses are listed in Table 5.3 for 400 μm and 1000 μm dipole distance. Usually symmetric biphasic pulses are applied in neural prostheses, e.g. Laube et al. 2003,

Schanze et al. 2002 report that a cathodic-anodic pulse sequence is more effective for epiretinal stimulation than anodic first stimulation. Table 5.4 demonstrates that the cathodic stimulus has essentially lower thresholds for positions A, B, C and position B has a 1.43 lower threshold than C. Threshold ratio for B is even better: 1.57. Increasing the dipole distance from 400 μm to 1000 μm causes generally lower thresholds, but the threshold ratio C/A and C/B is not as good.

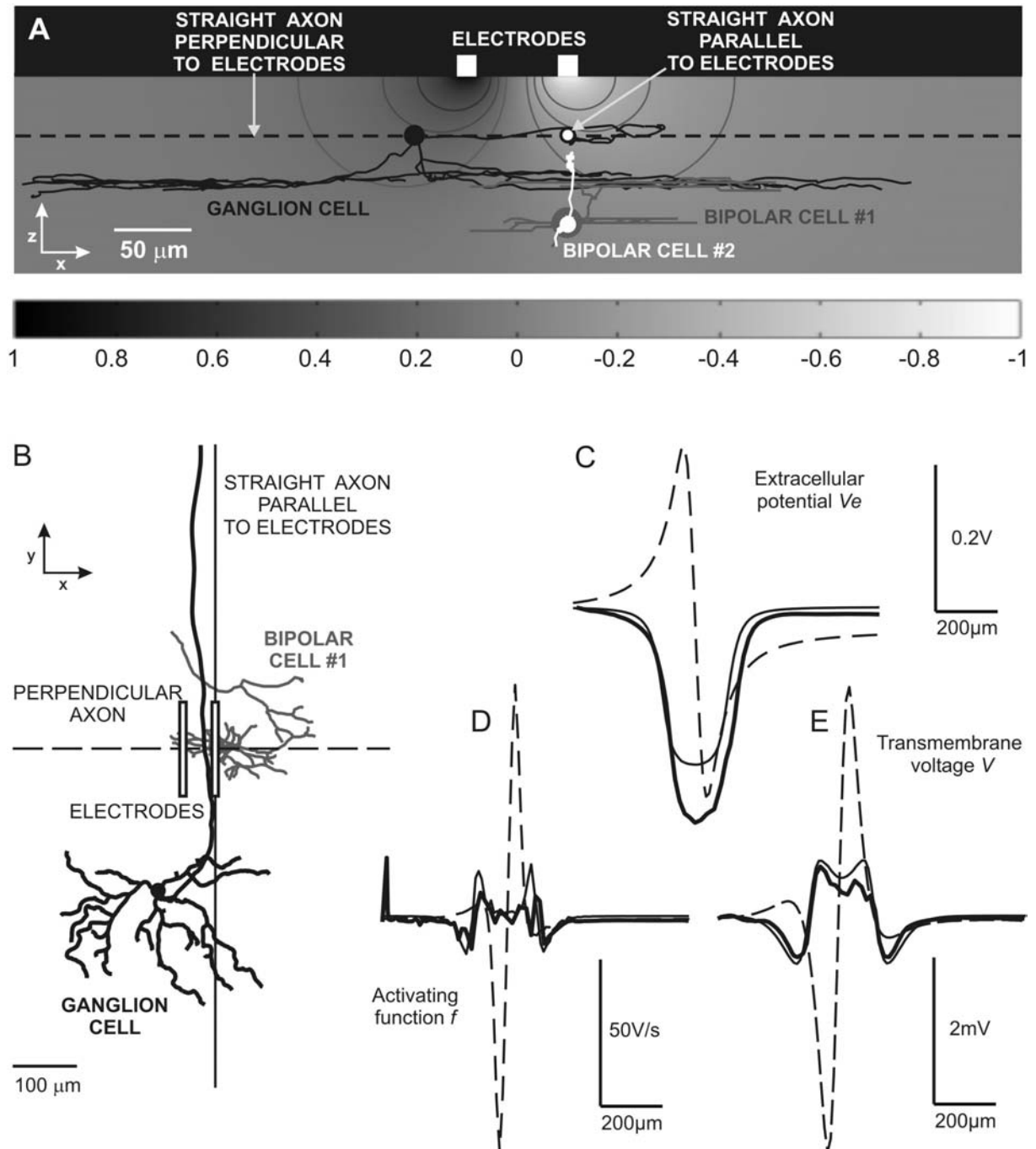


Fig. 5.4. Dipole stimulation with rectangular electrodes (10 μm x 200 μm , center distance 50 μm) parallel to the axon of a ganglion cell. Front (A) and top view (B) with cell positions. Parallel axons and both bipolar cell bodies are below the cathode (-1 Volt). The excitation of two straight axons, parallel to the electrode (full line) and perpendicular to the electrode (dashed line), are compared with the traced ganglion cell. Extracellular voltages along the three axons are of similar magnitude (C), but the axons parallel to the electrodes are barely excited (D,E). Thick lines mark the ganglion cell related curves.

TABLE 5.3. MINIMUM AND MAXIMUM TRANSMEMBRANE VOLTAGES IN MV AT THE END OF A 0.1MS, 5 μ A STIMULUS FOR THE SITUATION SHOWN IN FIG. 5.4

Electrodes		Perpendicular axon	Parallel axon	Ganglion cell axon	Bipolar cell #1	Bipolar cell #2
Disk d=10 μ m	vmin	-5.23	-5.62	-7.00	-1.52	-7.98
	vmax	5.23	1.36	1.93	3.05	2.08
Rectangular 10 μ m x 200 μ m	vmin	-3.17	-0.65	-0.53	-2.01	-0.94
	vmax	3.17	0.75	0.70	0.76	2.59

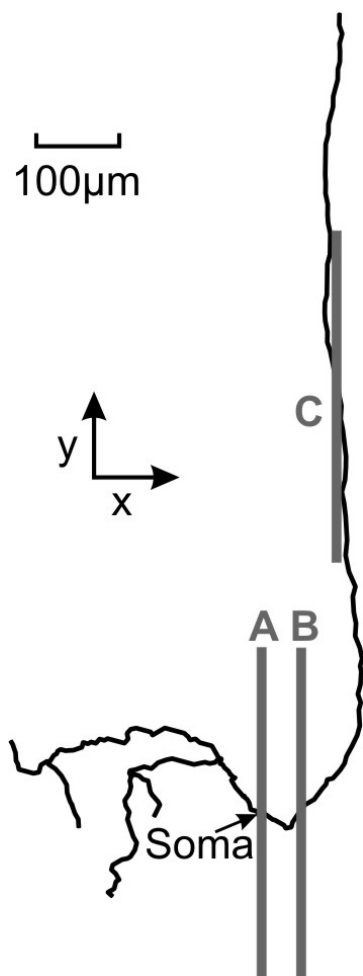


Fig. 5.5. Small ganglion cell with 10 μ m x 400 μ m electrodes centered above the soma (A), the thin segment (B) and the straight axon part representing a bypassing fiber (C). The z-distance between soma and thin segment to the electrode is 50 μ m, whereas the C position is only 30 μ m above the axon because the bypassing axons are closer to the surface of the retina (comp. Fig. 5.1), i.e. 20 μ m z-distance between retina and implant surface is simulated. The second electrode of the dipole has the same size and is shifted 400 μ m or 1000 μ m to the left.

TABLE 5.4. THRESHOLD CURRENT IN μ A FOR 10 μ M X 400 μ M LONG ELECTRODES (POSITIONS SHOWN IN FIG. 5.5)

	Electrode positions			Threshold ratio	
	A	B	C	C/A	C/B
Positive stimulus	267 (235)	295 (268)	434 (308)	1.63 (1.31)	1.47 (1.15)
Negative stimulus	-196 (-123)	-178 (-110)	-280 (-145)	1.43 (1.18)	1.57 (1.32)

Dipole distance 400 μ m; threshold values for 1000 μ m in brackets.

The above described method avoids the co-stimulation of bypassing axons under the electrode but it has the disadvantage to loose selectivity in the direction of the electrode. Moreover spikes can be generated at the edges of the electrodes, where the curvature of the potential distribution will increase, as will the activating function. Hence, for preventing co-stimulation of passing axons, it is important that excitation of these neurons will not occur at the edges. To minimize the edge effect and to improve focalization in y-direction we suggest a design according to Fig. 5.3, where an additional conducting medium is filled in, e.g. 1000 μm long slots below an active 10 μm \times 10 μm electrode. This causes a flat gradient of extracellular potentials for the bypassing axons parallel to the slots (Fig. 5.6A). Comparing the results of Fig. 5.6, the case $\rho=0.57$ Ohm.cm corresponding to 100 fold retina conductance is recommended because it results in a good combination of two conditions: (i) a local maximum of the extracellular potential along the slot (Fig. 5.6A) in order to obtain a focal effect for transverse neural elements both in x and y direction and (ii) similar small sizes of the transmembrane voltage extrema along the parallel axon (Fig. 5.6C) in order to avoid spiking in the parallel axon. For this case the threshold currents for monophasic 100 μs pulses are listed in Table 5.5.

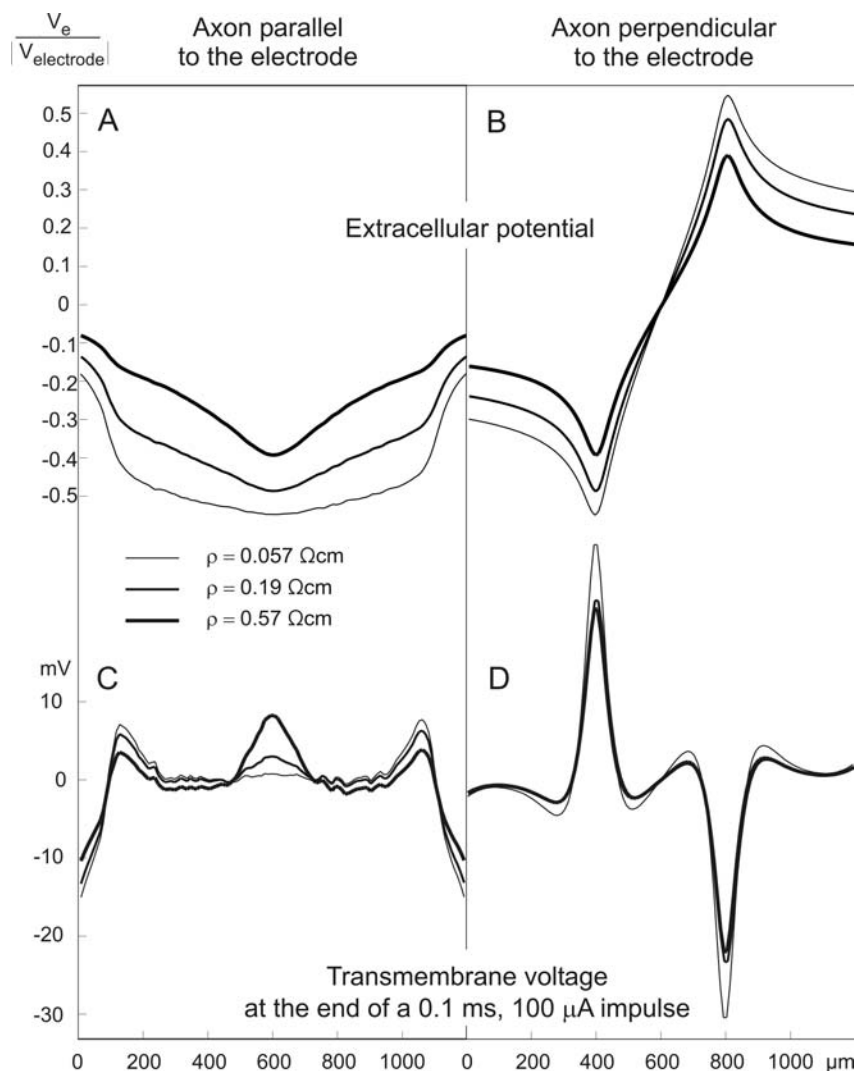


Fig. 5.6. Dipole stimulation of straight axons with electrode array as in Fig. 5.3. Extracellular potential and transmembrane voltages at the end of a 100 μA , 100 μs pulse are shown as functions of the axonal length coordinate for three specific resistances of the slot medium of the implant. Dipole distance: 400 μm , slot length 1000 μm .

TABLE 5.4. THRESHOLD CURRENT IN μA
FOR ELECTRODES AS IN FIG. 5.3 (POSITIONS AS IN FIG. 5.5)

	Electrode positions			Threshold ratio	
	A	B	C	C/A	C/B
Positive stimulus	837 (1033)	874 (994)	874 (776)	1.04 (0.75)	1 (0.78)
Negative stimulus	-454 (-446)	-323 (-333)	-763 (-747)	1.68 (1.67)	2.36 (2.24)

Excitation threshold for an active $10\ \mu\text{m} \times 10\ \mu\text{m}$ electrode in a $10\ \mu\text{m} \times 1000\ \mu\text{m}$ slot positioned above the small ganglion cell. The second electrode is shifted $400\ \mu\text{m}$ to the right; $1000\ \mu\text{m}$ to the right for the values in brackets. Specific resistance of the slot medium: $\rho=0.57\ \text{Ohm.cm}$ corresponding to 100 fold retina conductance.

Influence of dipole distances on axonal excitability

Sometimes neuroprostheses operate in a dipole mode where both electrodes effectively stimulates the same target neuron, which is generally not the case if one electrode's distance is more than tree times greater than the other (comp. Fig. 5.7)

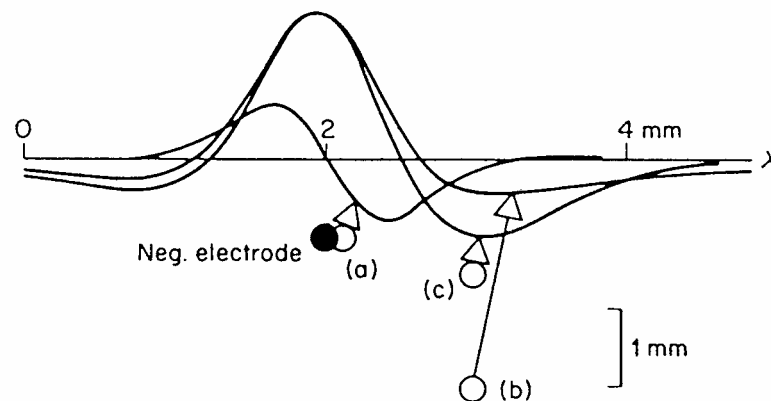


Fig. 5.7. Activating functions for three dipoles (a-c) with the same cathode marked as filled circle in 1 mm distance to a straight axon in a homogeneous extracellular medium. Case b (the second contact has a distance of 3 mm) has a nearly symmetric activating function similar to that of the monopolar stimulation by the cathode itself.

Figure 5.8 shows the top view of the ganglion cell (cell body and first part of the axon, same as in Figs. 5.4 and 5.5 but 90° rotated) and the direct influence of the electric field for four electrodes (same anode, three cathode positions always above the center of an axon compartment). Axonal compartments have variations in diameters and distances to the retina surface which result in small deviations of the monopolar activating functions. For small dipole distances an intersection of the main peak regions of the monopolar activating functions occurs and causes substantially higher thresholds (Fig. 5.8).

Minimum threshold is supported by a dipole distance where both the cathodic and anodic monopolar activating functions contribute with positive values as marked by the red regions in Fig. 5.8. However, the strong negative peak of the anodic pole causes inner-axonal current flow from the excited region and therefore the minimum dipole current is reached after a shift of the cathode to the right side. The dipole separation for minimum threshold current depends on the electrode distance as predicted from the positive peaks of the

activating function and on the fiber's length constant, but it is rather independent from the electrode type and the boundary conditions used in this project (Fig. 5.9).

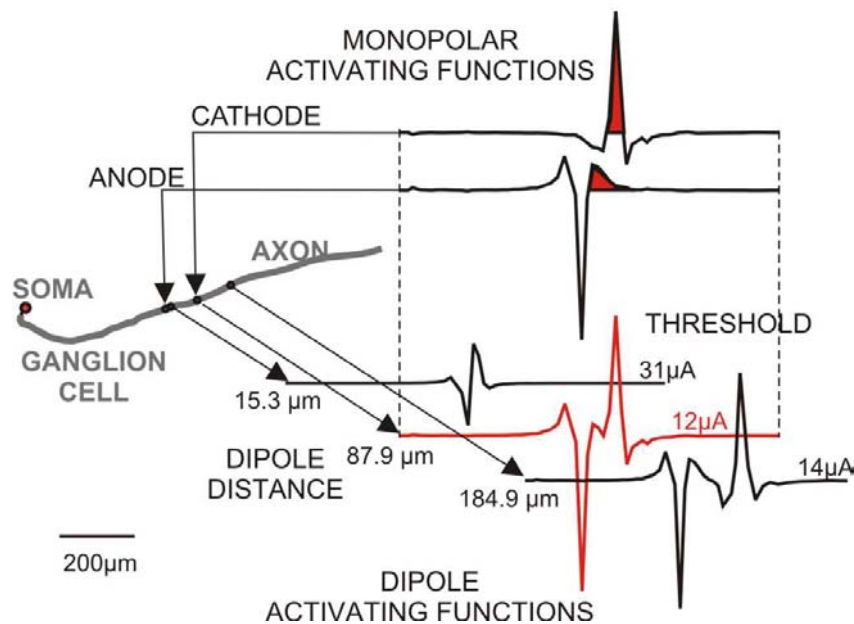


Fig. 5.8. Activating functions for hemispheric electrodes moved at the retina surface along the axon of a ganglion cell. The activating function for a dipole configuration is the sum of the monopolar components as demonstrated by the 87.9 center-center distance case (red curve). Simulated for semi-infinite retina, threshold calculation with the FCM model.

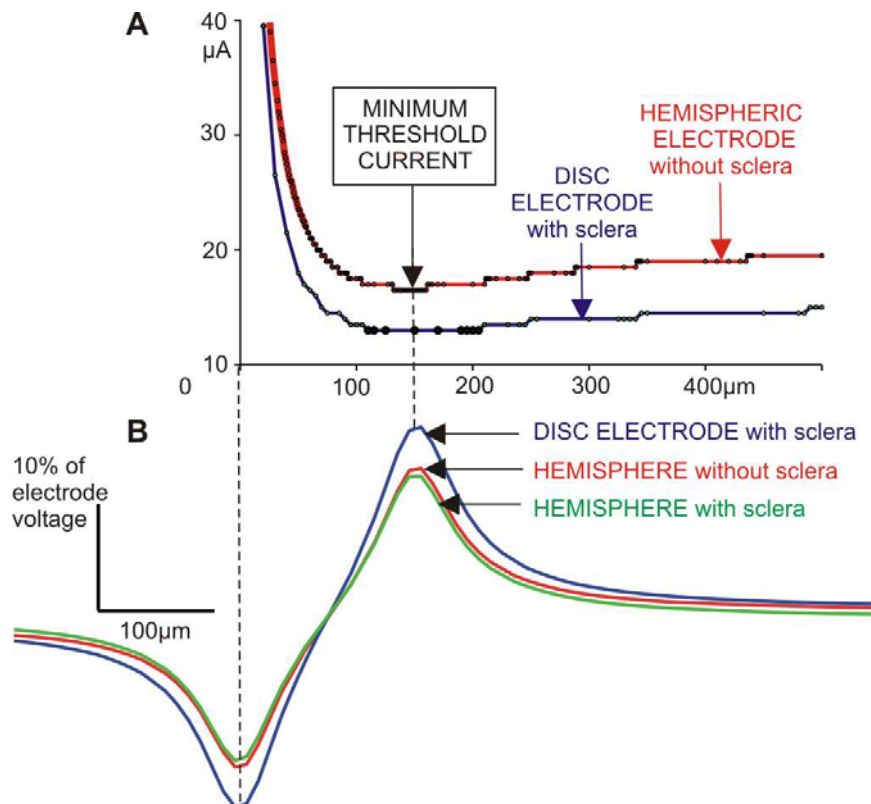


Fig. 5.9. A: Threshold current as function of dipole distance for a straight axon ($1 \mu\text{m}$ diameter, $30 \mu\text{m}$ below electrode centers). B: extracellular voltage along the axon for $150 \mu\text{m}$ electrode center-center distance, a value within the flat minimum threshold current region.

Comparison of bipolar and ganglion cell responses

Every compartment of the bipolar and ganglion cell has its individual f_n value (compare Eqn. 2.3, Fig. 5.10A). Extreme changes of compartment diameters as well as terminal endings and branching points cause irregularities in the sequence of f_n . There is a quick smoothing effect of the transmembrane voltages comparable to the 'minimum threshold shift' phenomenon described above, which causes the loss of the zig-zag shape of the activating function (Fig. 5.10), a phenomenon known, e.g., from Figs. 2.2 and 2.3.

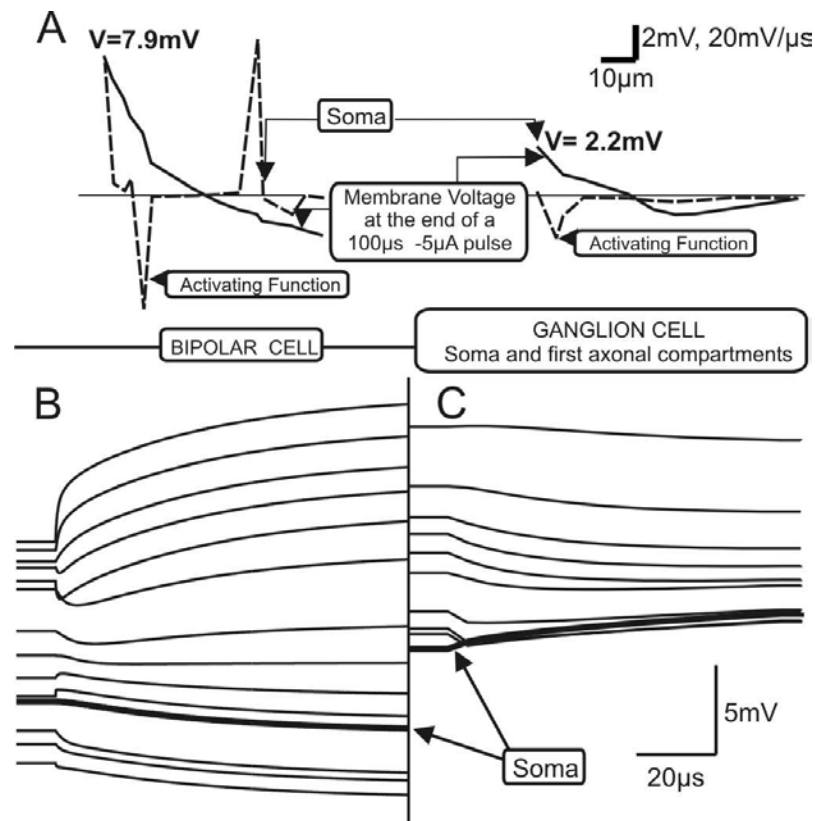


Fig. 5.10. Comparison of bipolar cell #2 (left) and ganglion cell (right) responses when stimulated with a hemispheric $10 \mu\text{m}$ diameter cathode $30 \mu\text{m}$ above the ganglion cell soma center, i.e. situation as in Fig. 5.4 but with other electrode shape. Transmembrane voltages at the end of the stimulus are smoothed forms of the activating function along the neurons (A). Membrane voltages of the neuronal compartments as functions of time (B) and (C); thick lines: transmembrane voltages of the soma compartments. The values of the activating function correspond with the slopes of the voltage curves in (B) and (C) at stimulus onset.

The ganglion cell is flat and the soma - axon connection is close to an equipotential surface when the electrode is positioned above the soma (Fig. 5.4) which results in rather small values of the activating function and transmembrane voltages when compared with bipolar cell #2 (Fig. 5.10A): At the end of a $-5 \mu\text{A}$ $100 \mu\text{s}$ pulse the terminal of the bipolar cell has a transmembrane voltage of 7.9 mV whereas the maximum at the ganglion cell soma becomes only 2.2 mV. With such a stimulus, the bipolar cell is expected to respond with neurotransmitter release, whereas the ganglion cell is far away from a spiking response. However, the maximum membrane voltage relation between ganglion and bipolar cells becomes less extreme for bipolar cell #1 because this cell type has - similar to the ganglion cell - horizontal oriented processes.

5.3 Discussion

The aim of a sophisticated stimulation method for epiretinal implants is to excite local areas below the electrodes without axons originating in other regions. We have investigated this problem with three target cells. Instead of one cell with 3 electrode positions, the results of Table 5.4 and 5.5 can be interpreted as one electrode that stimulates three different ganglion cells of the same shape shifted to three positions (A, B, C): cell C represents the bypassing axon, cell B has the thin axonal segment below the center of the electrode and cell A soma is below the electrode. To avoid charge accumulation we assume application of a train of 100 μ s pulses with equal positive and negative amplitudes and interpulse intervals of some ms. According to Table 5.5, e. g. a 460 μ A stimulus is subthreshold for cell C but initiate spikes both in cell A and B. Cell C has a 2.36 (2.24) times higher threshold than B but this relation is reduced to a 'safety' factor of 1.57 (1.32) for the 'simple' rectangular electrodes as listed in Table 5.4. Note that the soma is not the most excitable cell region but the smallest thresholds are observed for cathodic stimulation above the thin axonal segment (Table 5.4 and 5.3) [Rattay 1999, Resatz 2002].

The activating function concept was helpful for designing the 'sophisticated' electrode: a higher slot medium resistance causes a stronger curvature in the central part of the extracellular potential profile (Fig. 5.6A) resulting in (i) increase of f implying smaller thresholds for the bypassing axons and (ii) sharper focal effect in slot direction. The y-resolution with the proposed parameters is still rather poor and the question arises: How much we can support the sharpening effect on cost of the 'safety' factor reduction ?

The 'safety' factor for avoiding bypassing axon stimulation has a second component contributing to ganglion cell soma excitation in form of synaptic activities from other stimulated retinal cells. Bipolar retinal cells do not generate action potentials but operate by changing the amount of neurotransmitter release within a rather small range of membrane voltage (5 mV) [Teeters et al. 1997]. From Table 5.3 data it can be concluded that even with the investigated disk electrodes the response of bipolar cells can be influenced with stimulus amplitudes being subthreshold to all bypassing axons.

By in-vitro experiments with subretinal electrodes ganglion cell spiking can be initiated by synaptic activities from the electrically stimulated retinal network without direct stimulation of the ganglion cells or their axons [Stett et al. 2000]. However, in epiretinal implants the distances to the excitable structures are in reversed order, i. e., the bypassing axons are the elements closest to the electrodes. Indirect activation was observed for epiretinal stimulation [Jensen et al. 2003]. As reported in the introduction, the synaptic component depends on stimulus duration: it is rather small for 100 μ s pulses, but increases by a factor 4 for 2 ms pulses. According to this relation 1 ms pulses are applied in a blind subject in order to support the local ganglion cell activities [Humayun et al. 2003]. The contribution of a bipolar target neuron depends essentially on two factors (comp. bipolar cell #2 in Fig. 5.4A and Table 5.3) [Rattay et al. 2003]: (i) a cell geometry with small terminal region and cell orientation perpendicular to the electric field causes strong transmembrane voltage, (ii) stimulus polarity.

Threshold currents in patients and animal experiments seem to be generally smaller than in computer simulations of the presented type. As an example, the calculated threshold for the small ganglion cell stimulated with a 10 μ m disk electrode 25 μ m above the thin segment (corresponding to $z=30$ μ m for the soma) is -30 μ A for a 100 μ s pulse, -11 μ A for a 400 μ s pulse and -3.4 μ A for 5 μ m electrode distance (400 μ s pulse). For situations similar to the last case Grummet (1999) reports sub-microampere threshold currents based on his own experiments and reviewed data.

Several phenomena not included in the simulation can reduce the threshold currents, but they will not change the presented qualitative results:

- (i) The amount of neurotransmitter release e.g. from bipolar cells, which helps to activate the ganglion cells increases with pulse duration and electrode size [Jensen et al. 2003].
- (ii) The spontaneous activity of ganglion cells [Sakmann and Kreutzfeldt 1969] is expected to be influenced by a weak electrical field.
- (iii) Ion current fluctuations across the cell membrane [Verveen and Derksen 1968], which can be modeled proportional to the square root of the number of the sodium channels involved [Rattay 2000].
- (iv) An orientation of the thin axonal segment similar to bipolar cell #2 in Fig. 5.4, i.e. nearly perpendicular to the isopotentials could be much better than in our case. Note that the bipolar cell #2 is more excited (Table 5.3) than the axonal segment of the ganglion cell which is parallel to the isopotential.

The technical realization of the proposed electrode array is not planed in detail. One possibility is to use doped semiconductors as conducting medium in the slot material, another one is to generate the calculated potential distribution with a line of active electrodes instead of the approach with the slots. In all cases presented in this article the threshold current densities are within safe limits of available electrodes, e.g. a current of $460 \mu\text{A}$ (super-threshold to positions A and B according to Table 5.3) causes a mean value of $460 \mu\text{C}/\text{cm}^2$ for the $10 \mu\text{m} \times 1000 \mu\text{m}$ slot, which is in the range of experimental data reviewed by Grumet (1999).

6. Neuromodeling and the human spinal cord motor control: Neural responses to epidural stimulation

Bipolar electrodes placed in the dorsomedial epidural space within vertebral level T10 down to L1 stimulate only sensory fibers of the spinal rootlets when amplitudes of 210 μ s pulses are restricted to 10 Volt. For bypassing axons spike initiation occurs close to the cathode. Sensory fibers below the cathode level are stimulated at their spinal cord entry point. Dorsal column axons and other neural elements within the spinal cord are not directly stimulated even when they are closer to the electrodes than the excited afferent axons.

In subjects with chronic, complete spinal cord injury single pulses and low frequency stimulation causes synchronized short latency muscle twitches via monosynaptic pathways. In contrast, 5-50 Hz stimulation produces postsynaptic potentials in spinal interneurons that control the motoneuronal discharge and the transmission trough reflex pathways thus can elicit at 5-15 Hz sustained tonic activity and at 25-50 Hz lower limb extension or stepping like lower limb movements.

6.1 Introduction

Computer simulation of the stimulating influences from electric fields on neural structures, the analysis of the muscle response latencies and the analysis of EMG shapes are useful tools for understanding the evoked activities in the isolated spinal cord circuitry.

Figure 6.1 shows (A) the arrangement of the stimulating dipole and that of the electrodes for EMG recordings, (B) a scheme for a monosynaptic pathway that causes short latency muscle twitches of constant strength and a polysynaptic pathway that activates a patterned muscle response and (C) the differences in the EMG for both neural pathways in respect to the envelope, latency and shape of the measured signal.

In order to explain the measured effects [Dimitrijevic et al. 1998, Minassian et al. 2004] we use a compartment model of a single neuron and a simplified network model [Graham and Redman 1994, Jilge et al. 2004].

6.2 Material and Methods

Data were obtained from ten subjects with accidental, motor complete SCI at low cervical or at thoracic level (8 x ASIA A, 2 x ASIA B). At vertebral levels ranging from T10 down to L1 they had an implanted epidural electrode array which was operated as a bipolar electrode with a contact separation of 27 mm. The stimulator (ITREL 3, Model 7425, MEDTRONIC) delivered continuous, non-patterned stimulation with 1-10 V at 2.2-100 Hz and asymmetric biphasic pulses with a 210 μ s main pulse and a long second pulse for avoiding charge accumulation. Electromyographic activity was recorded with pairs of silver-silver chloride surface electrodes. For details see e.g. [Dimitrijevic et al. 1998, Minassian et al. 2004].

Electric fields were calculated with finite element software ANSYS. The compartment models of the target neurons are based on the CRRSS (Chiu-Ritchie-Rogart-Stagg-Sweeney) model in the form described in Chapter 1. The resulting differential equations were evaluated with software ACSL. Spike initiation points were also analyzed with the activating function concept [Chapter 2]. The shape of the rootlets and other details are reported in Rattay et al. 2000.

The longer delays of polysynaptic pathways were simulated with a simple model consisting of a single interneuron that modulates the output by presynaptic inhibition [Rattay 2003, Jilge et al. 2004].

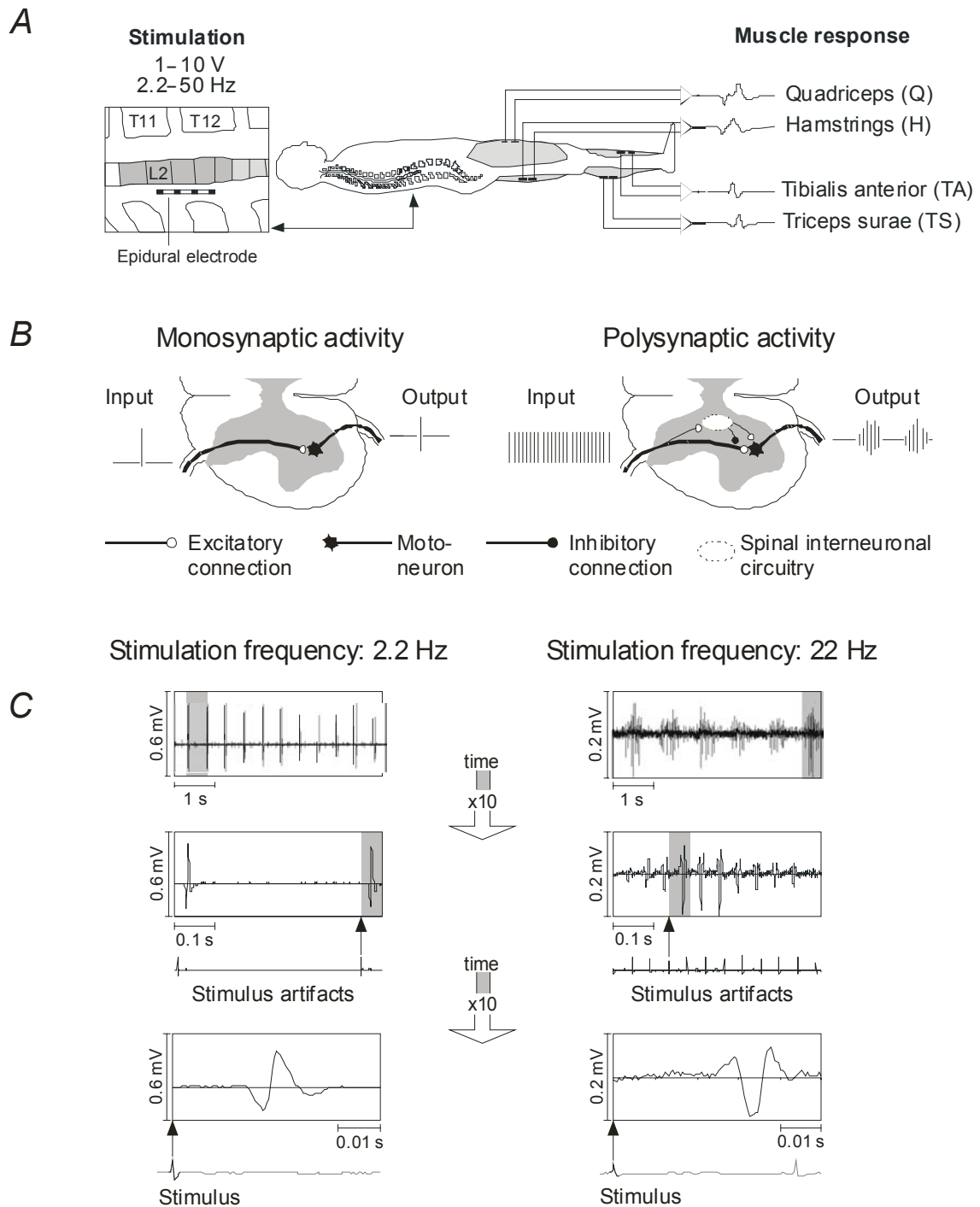


Fig. 6.1. Outline of the assessment design and analysis of stimulus-evoked EMG responses. (A) all recordings were conducted with the patients in a supine position. Pairs of surface EMG electrodes were placed over the lower limb muscles to assess the effects of epidural stimulation. (B) Neural path diagrams in cross-sections at lumbar segmental levels. Left: single pulse (2.2 Hz-) stimulation activates segmental primary sensory axons and affects monosynaptic excitatory action on motoneurons; right: same afferent structures repetitively stimulated at higher frequencies activate lumbar neuronal circuits that modulate the afferent flow through monosynaptic pathways by putatively presynaptic inhibitory mechanism and control motoneuronal discharge by excitatory oligosynaptic pathways. Sustained stimuli at 25–50 Hz organize the lumbar spinal interneurons by temporarily combining them into locomotor centers that project over several segments and coordinate the neural activity. (C) EMG responses of triceps surae to epidural stimulation at 2.2 Hz and 22 Hz. Potentials marked by gray backgrounds are shown in extended time scale ($\times 10$) on the top of the original EMG. Stimulus artifacts allow the identification of the onsets of applied voltage pulses.

6.3 Results

In a first step the electrical field in the vicinity of the dipolar electrode was calculated in order to find the primarily stimulated neural elements (Fig. 6.2). In the second step the extracellular potential along a neural target pathway is used as input for a compartment model. Two hot spots in the afferent rootlet fibers are closely neighbored: the regions with sharp curvature before the entry point in the spinal cord and the entry point itself where irregularities in medium conductance support the initiation of action potentials. Both cases result in large values of the activating function, which is proportional to the second derivative of the extracellular potential along the neural pathway for axons with constant fiber parameters [Rattay 1986, 1990, 2000].

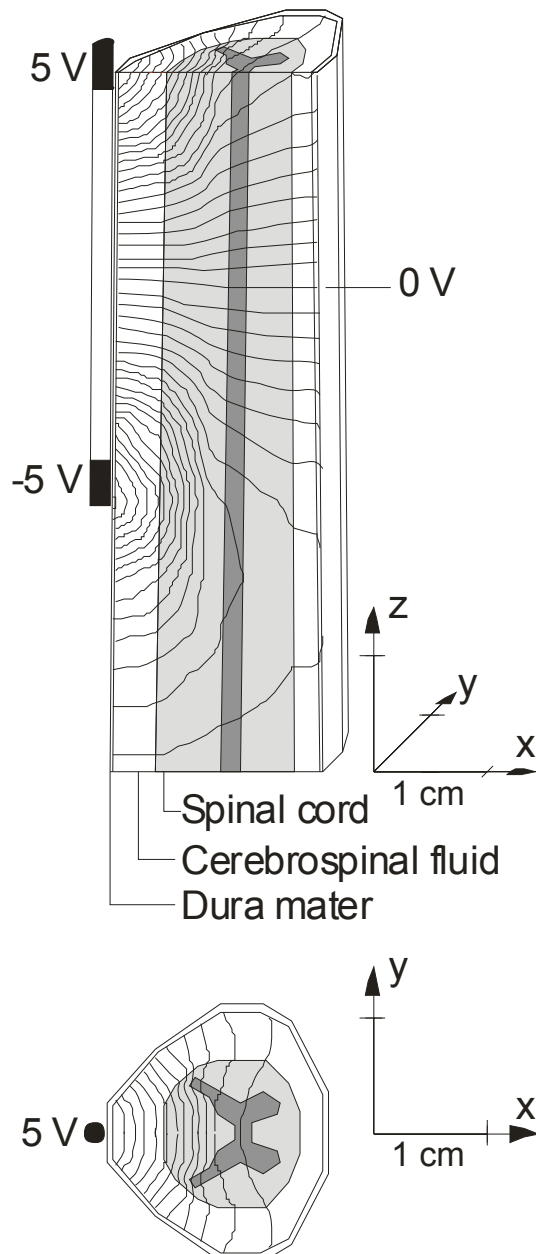


TABLE 6.1 CONDUCTIVITIES

Biological material	Conductivity ($\Omega \cdot \text{cm}$) ⁻¹
Grey matter	0.0025
White matter, transversal	0.00083
White matter, longitudinal	0.0072
Cerebrospinal fluid	0.0167
Dura mater	0.0003
Fat in the epidural space	0.0005
Vertebral bone	0.00025
Surrounding layer	0.0025

The conductivities are according to Coburn and Sin 1985 and Geddes and Baker 1967, dura mater as in Struijk et al. 1993.

Fig. 6.2. Computed potential distribution within the dural sac in midsagittal and transversal plane generated by a bipolar electrode with 10 V potential difference between the two contacts.

With the applied stimulus intensities typically spikes are generated in the large diameter sensory fibers of rootlets which enter the spinal cord not too far below the level of the cathode (Figs. 6.3 and 6.4) or in sensory fibers that pass the level of the electrode before entering the spinal cord, (Fig.6.5) but there is no spike initiation in the dorsal columns (indicated by vertical black arrow in Fig. 6.3A, see also Minassian et al. 2004).

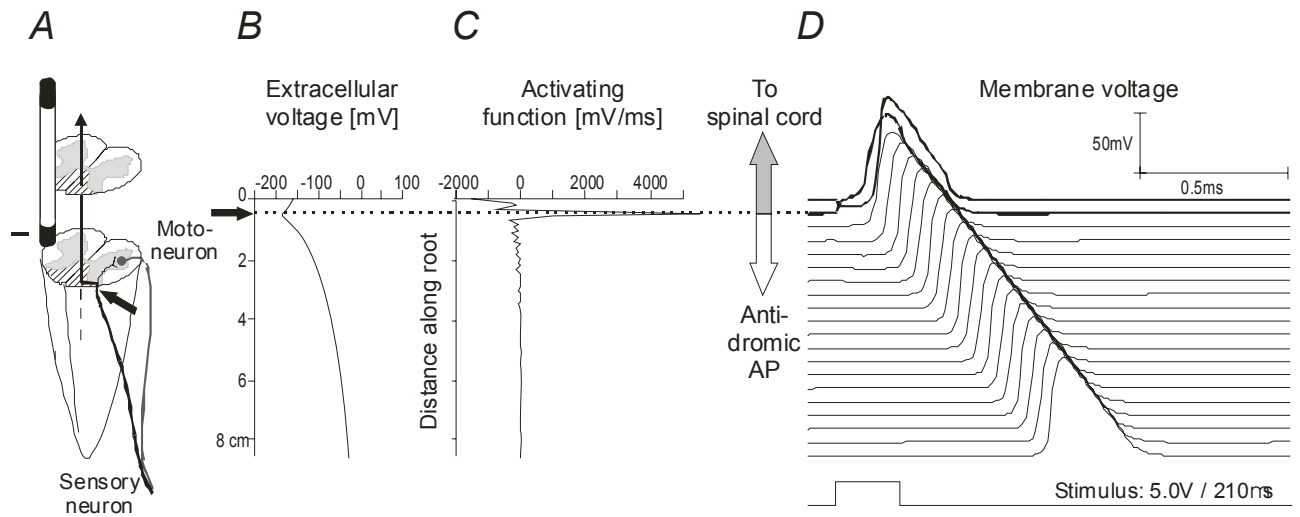


Fig. 6.3. (A) 3-dimensional view of the lower spinal cord with a sensory fiber (within the posterior root, curved trajectory) and its axonal branches in the back side of the spinal cord (that makes synaptic contact to posterior columns; hatched area, vertical arrow) with a single synaptic connection to a motoneuron. Black arrows and the dotted line indicate the “hot spot” for the spike-initiation at the site where the posterior root fiber enters the spinal cord. (B) Extracellular voltage generated by epidural stimulation, (C) activating function and (D) membrane voltage for an S1-posterior root fiber stimulated 4% above the characteristic fiber threshold with a midsagittal electrode at L4-spinal cord level. Note that the positive part of the activating function is restricted to a single node (peak). In this hot spot an action potential is generated that propagates into the spinal and in antidromic direction. Internodes and every second node are not displayed in D.

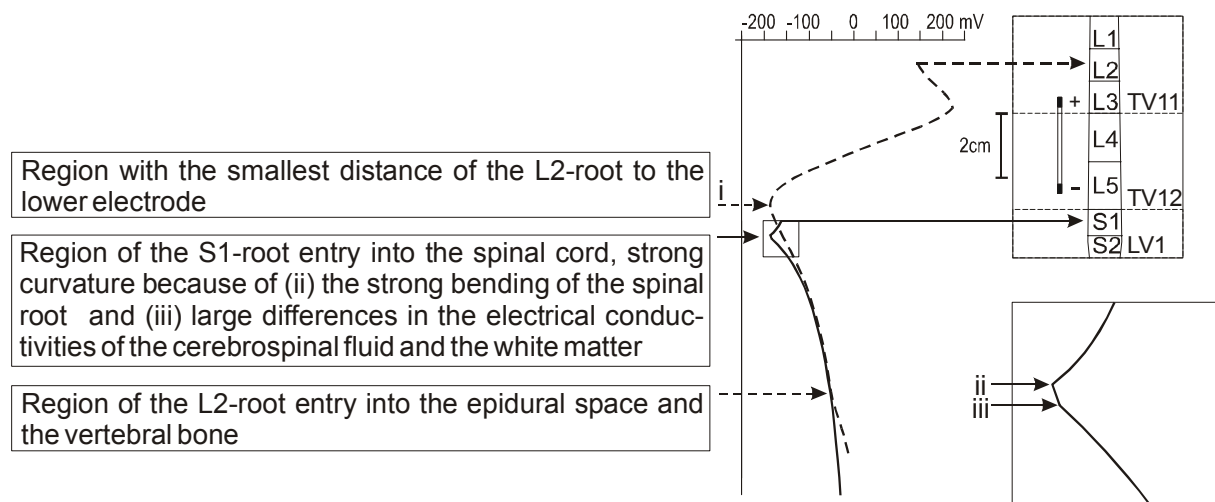


Fig. 6.4. Comparison of the extracellular voltage along a S1 fiber (full line) and a L2 fiber (dashed line) as shown in Figs. 6.3 and 6.5C. Because the S1 fiber origin is about 0.95 cm caudal to the cathode and 4.9 cm below the L2 entry the influence of the positive electrode on S1 is rather small. The extracellular potential within a part of the trajectories of both fibers is nearly identical. Note that differences in curvature (indicated by arrows and numbers i-iii) result from different influences. TV and LV marks thoracic and lumbar vertebrae levels, L and S lumbar and sacral spinal cord levels.

The spike initiation site can be explained with the activating function concept if a single pulse is applied. The single pulse model simulates indeed the real clinical situation, because the second pulse, applied for avoiding charge accumulation, is much longer (see method section) and it was checked with the full system of equations that the second pulse has negligible influence on the neural response.

Figure 6.3 shows the position of the bipolar electrode relative to a sensory fiber that enters the spinal cord at the level of the first sacral segment S1 (A). The part of the axon closest to the cathode, marked with arrows in (A) and (B), defines the minimum of the extracellular voltage (B) and the maximum of the activating function (C). Therefore this position generates the strongest neural response, which is an action potential for superthreshold intensities (D).

Three conditions favor the place of spike initiation in an axon (Fig. 6.4): (i) the smallest distance to the electrode, (ii) strong curvature of the axon and (iii) irregularities in the electrical conductance. The bypassing L2 axon with a minimum distance to the electrode that is comparable to the S1 case has therefore a similar minimum extracellular voltage value (dashed line in Fig. 6.4) but it has a higher threshold because conditions (ii) and (iii) support the S1 axon. Moreover, electrode polarity is an essential parameter. This is demonstrated with an axon with an entry point above both electrode contacts which describes the situation for a L2-dorsal root fiber with the electrode positioned as indicated in Fig. 6.5. The relations between extracellular voltage, activating function and the membrane voltages resulting in a propagating action potential are shown when stimulated just above threshold. In case A the potential of the upper contact (cathode) is -2.9 V with respect to the anode, whereas change of the polarity has a higher threshold value of 5 V (case C). This effect can be explained in the following way: The curved trajectory of the nerve fiber causes some asymmetry in the extracellular voltage profile. There is a stronger curvature at the upper contact (cathode in case A is at a position with length coordinate $s = 1.4$ cm along the L2 posterior target fiber) than at the lower contact (anode in case A at $s = 4.4$ cm). Therefore the maximum value of the activating function f is larger than its minimum value. As mentioned above, the value of the activating function represents the temporal membrane voltage change at stimulus onset, i.e. it defines the slope in every membrane voltage curve (lines at the right part of Fig. 6.5) at the beginning of the stimulating pulse. The arrow in Fig. 6.5A marks the maximum value of f and - because the strongest slope value causes the quickest rise of membrane voltage - the arrow marks also the place of spike initiation for supra-threshold stimulation. Comparison of the first part of every line of the membrane voltages in Fig. 6.5A shows that the negative excursions are always smaller than the positive ones (arrow). Changing the polarity of case A therefore results in a subthreshold response (Fig. 6.5B). Reversed polarity needs 72% higher stimulus to reach threshold and the spike initiation site has moved to the 4 cm region (Fig. 6.5C).

If both active poles of the implant are caudal to the origin of a spinal root fiber we have to expect a similar situation as in Fig. 6.5, i.e. both poles contribute significantly - with alternating polarity - to the extracellular voltage profile along the fiber. Quite different is the 'unipolar' voltage profile for a fiber which originates caudal to the dipole (Fig. 6.3). By comparison of Fig. 6.5C and Fig. 6.3 ($5\text{V}/210\mu\text{s}$ stimulus in both cases) the first 4,9 cm influence on the extracellular voltage in S1 fibers is lost (see also Fig. 6.4). This has minor effect for positive stimuli. However, change of polarity causes quite different results when the influence of one contact is lost: With negative monophasic stimuli we cannot excite the S1 fibers with voltages below 100 Volts, because this fiber has a small negative part of the activating function at the first nodes only (Fig. 6.3). Extracellular voltage changes insignificantly from compartment to compartment, but the activating function has a zig-zag shape because of variations in the nodal and internodal influences (in general the larger values belong to the nodes; for details comp. Chapter 2).

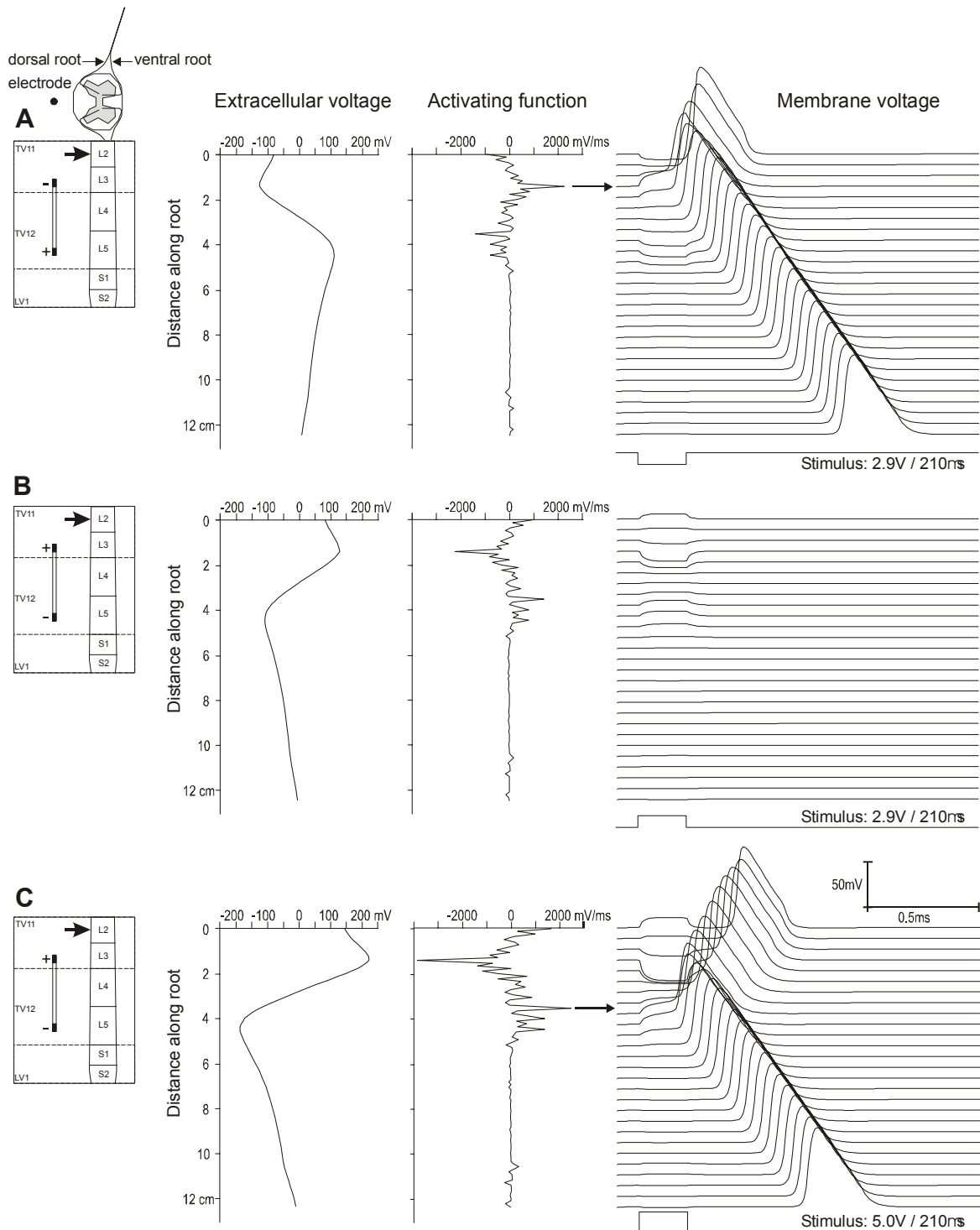


Fig. 6.5. Input data (extracellular voltage) and excitation patterns for a dorsal L2 fiber stimulated with a midsagittal electrode at L4 spinal level (center of the dipole is 2.5 cm caudal to the L2 root, left pictures). Extracellular voltage and the activating function are displayed as functions of fiber's length coordinate – starting point is within the spinal cord. (A) Excitation with negative threshold stimulus (-2.9 V) i.e. the standard polarity is changed and the upper contact which corresponds to a path-length of 1.4 cm becomes the cathode of the dipole. Arrow marks the maximum value of the activating function and the position of spike initiation. B: Change of polarity (2.9 V; subthreshold response) causes mirror pictures of the voltage profile, the activating function and the membrane voltages in the first part of every line (right). C: threshold increases to 5 V for the presented configuration; spike generation at a more caudal position of the root relative to the region in A.

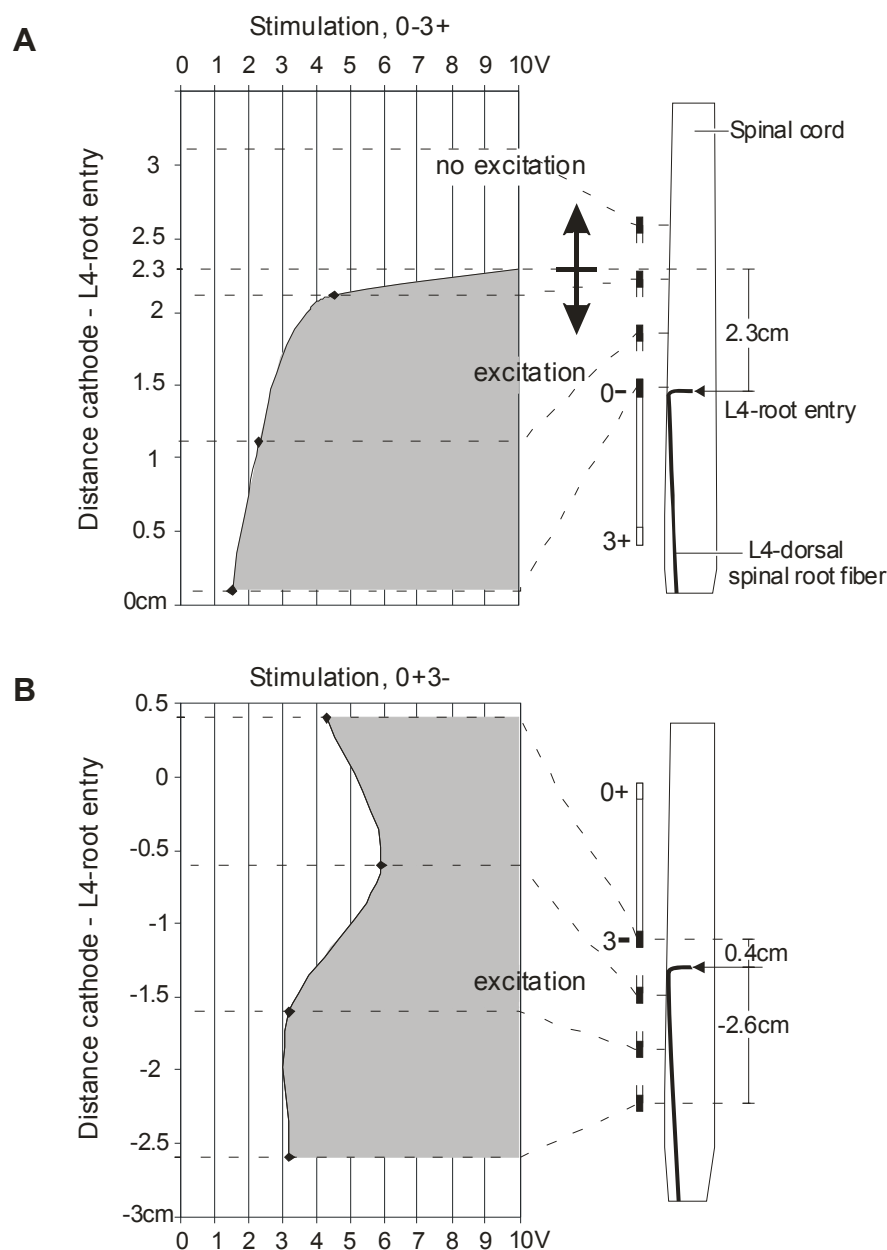


Fig. 6.6. Excitation region of a posterior L4 root fiber. Threshold values are calculated for four electrode positions, polynomial interpolation for other positions. Positions of the electrode with the black marked cathode, L4 spinal root fiber and spinal cord from a side view (right side). The threshold function pictures are zoomed according to the dashed lines.

Now, a midsagittally positioned electrode is moved in the rostro-caudal direction (Fig. 6.6). In all displayed cases the entry of the fiber into the spinal cord is between the levels of the two contacts of the stimulating electrode. The excitation is always dominated by the position of the cathode. For the 0-3+ configuration of the quadropolar electrode which is used as dipole (active upper contact: 0, active lower contact: 3) the L4 fiber will not be excited in the 10 V range when the cathode is more than 2.3 cm cranial to the entry level (Fig. 6.6A). The specific form of the voltage/distance relationship shows rather low thresholds when the cathode is near the entry level and an extreme increase beyond 2 cm (50 V would be required at 3.1 cm). This nonlinear phenomenon causes a sharp border for the excitation region (gray area in Fig. 6.6A) and is a good indicator for determining the fiber entry level.

When polarity is changed (0+3-) the L4 root fiber will always be excited with low or medium threshold values (Fig. 6.6B). Here the cathode is always close to some excitable

region of the fiber. Because of the caudal course of the posterior root trajectory the excitability is not much changed when the electrode is moved several cm caudal to the entry point. All posterior fibers arising from the L4 segment come close together on both sides and therefore all large diameter L4 fibers have similar thresholds for the low positioned electrode. Similar fiber behavior is expected for other lumbosacral spinal levels.

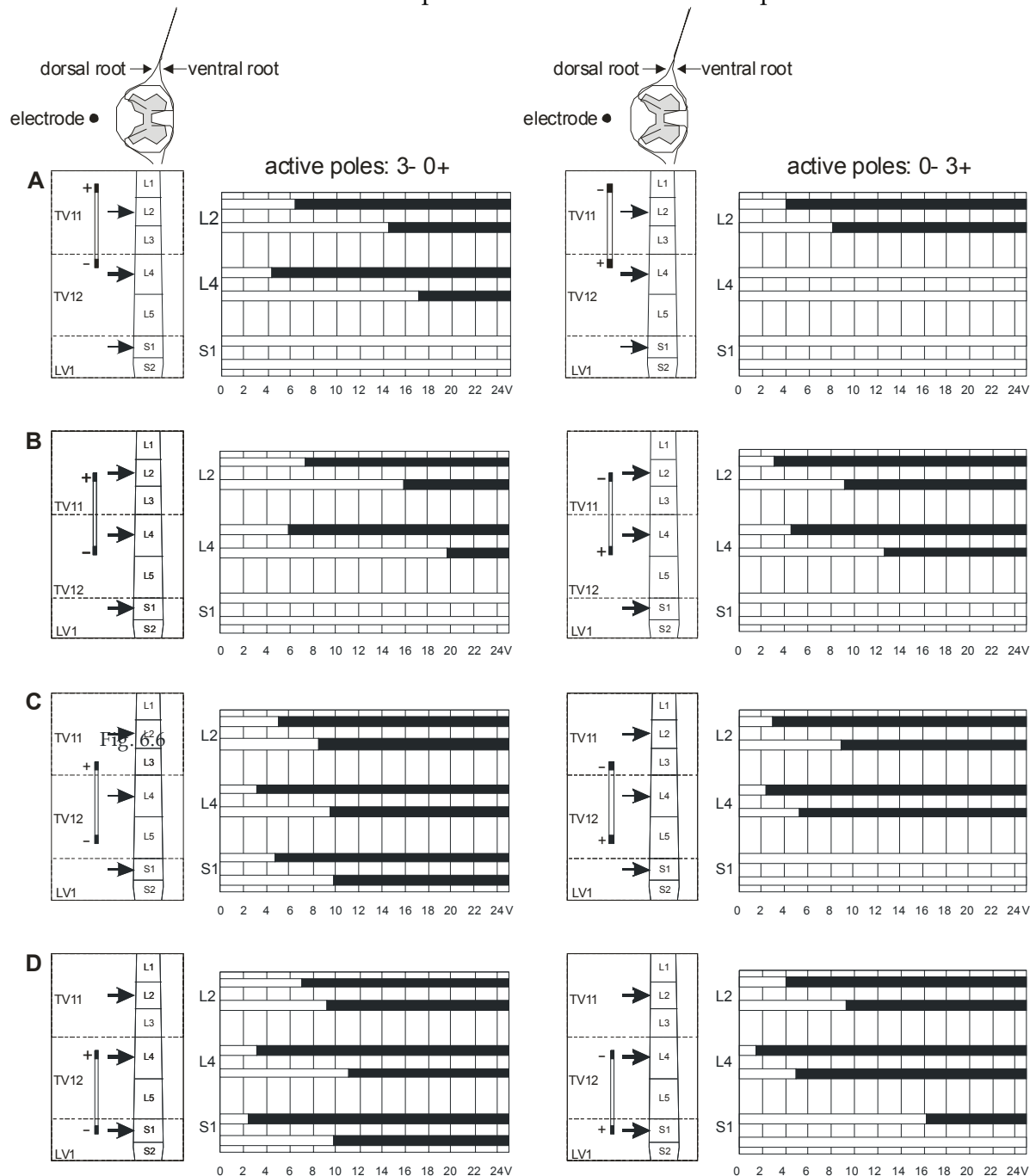


Fig. 6.7. Activation of spinal root fibers for midsagittal electrodes positioned at different spinal levels with single rectangular 210 μ s pulses. The left pictures show the position of the electrode relative to the spinal cord segments. Arrows mark the entries into the spinal cord of the 6 simulated target fibers which are evaluated in the corresponding right pictures. The upper and the lower black bar of each segment marks the simulated excitation range of the dorsal and ventral roots, respectively. Responses of left and corresponding right root fibers are the same because of symmetry. From A to D the electrode is moved in caudal direction in 1 cm steps. The excitation threshold of every target fiber increases drastically when cathode is moved cranially far away from the fiber's entry into the cord.

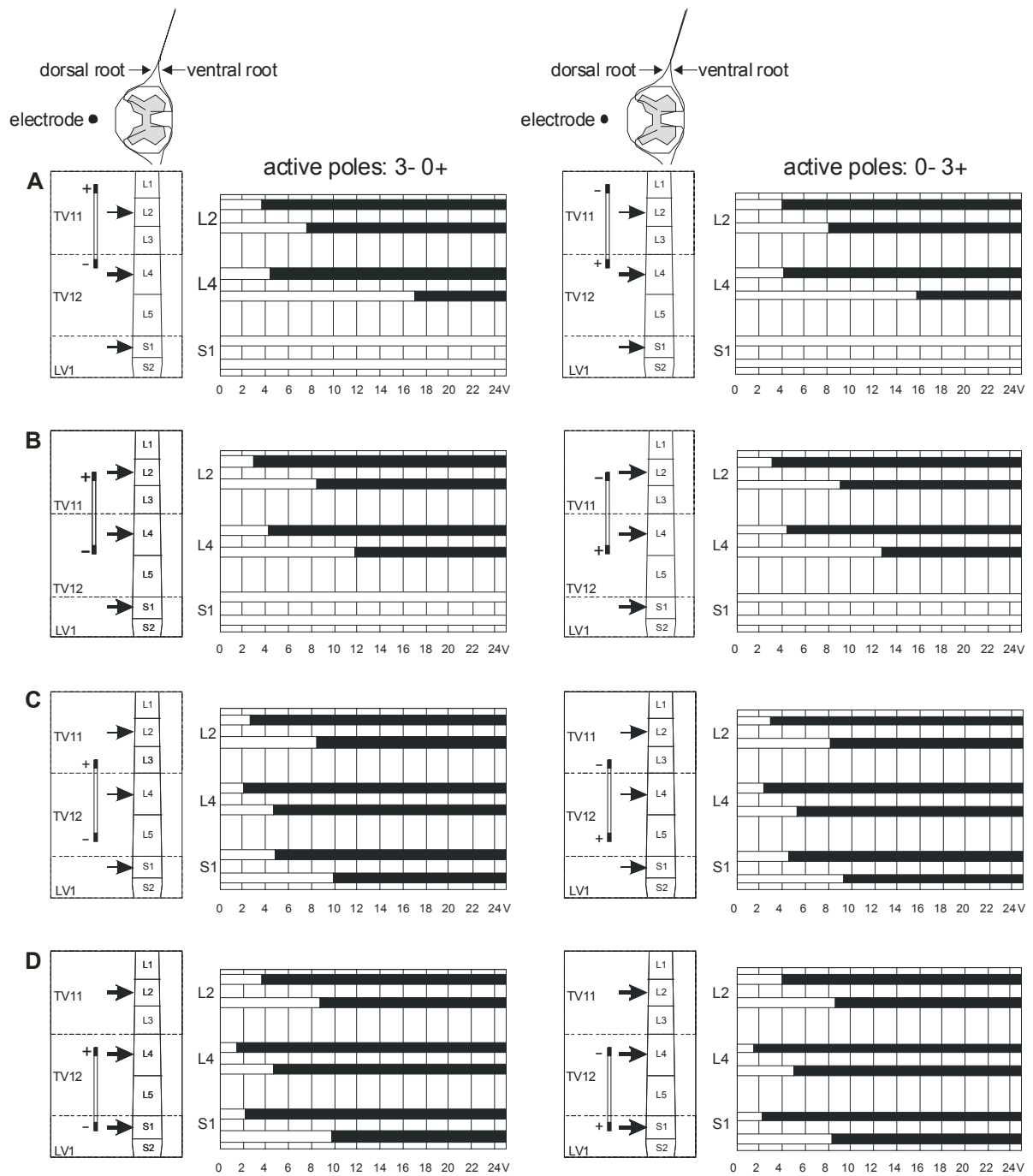


Fig. 6.8. Activation of spinal root fibers for midsagittal electrodes positioned at different spinal cord levels with biphasic rectangular $210 \mu\text{s}$ pulses. Same geometry as for the monophasic case in Fig. 6.7. The length of every black bar is a combination of the maximum values of the two corresponding monophasic situations ($0+3-$ and $0-3+$). Additionally, the effect not starting from the resting state for phase 2, lowers the threshold for all cases where the nerve is excited with the second phase. This effect explains also the small deviations between the $0+3-$ and the $0-3+$ cases when changing the polarity (left and right).

Biphasic stimulation

Both polarities (0+3- and 0-3+) have similar threshold values if the stimulus signal consists of two rectangular phases of the same duration and amplitude (Fig. 6.8). For a given stimulus strength two groups of fibers are stimulated: One group is stimulated by the contact which acts as the cathode during the first phase; when polarity is changed additional fibers become excited by the other contact which is then the cathode. This behavior can generally be expected for midsagittally (Fig. 6.8) as well as for laterally positioned electrodes (Fig. 6.9). Comparisons of corresponding cases in Figs. 6.7 and 6.8 show smaller thresholds for some fibers when stimulated with biphasic rectangular pulses. These fibers profit by being closer to the cathode during the second phase. In the monophasic case (Fig. 6.7) these fibers have the smaller distance to the positive contact of the electrode.

For posterior electrode positions the dorsal roots are usually easier to excite than the ventral ones. This fact is demonstrated in Figs. 6.7 and 6.8 where the lower black bars (corresponding to the ventral roots) are shorter for every calculated root level. Electrodes with an extreme lateral position can lead to a different result. Figure 6.9 shows an example where the ventral roots at the left side of the patient are closer to the electrode and therefore they respond to smaller stimuli.

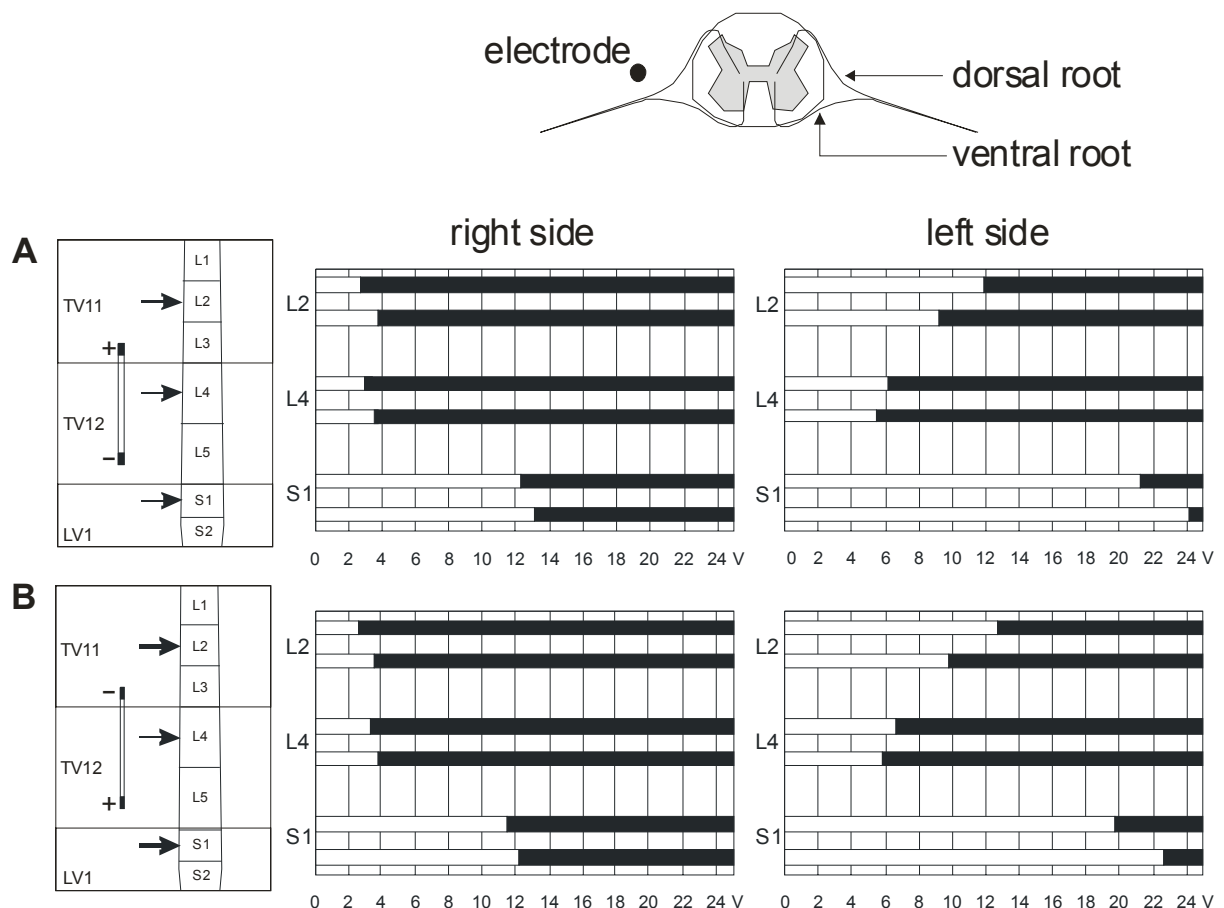


Fig. 6.9. Activation of spinal root fibers for an extreme lateral electrode position with biphasic 210 μ s pulses. Situation as in Fig. 6.8C but with the electrode moved to the right side of the patient; therefore the result is asymmetric: the fibers of the left side have higher thresholds. Note that in this exceptional case the distance between the electrode and the regions of spike initiation at the left side is smaller for the ventral roots and therefore the threshold values of these fibers are lower than those of the dorsal roots.

6.4 Discussion

The presented modeling study demonstrates that epidural stimulation of the lumbosacral cord with electrodes in posterior position activate the large diameter sensory fibers of posterior roots first, when the voltage is gradually increased. Stronger stimuli are needed to excite even the thickest motor neurons of the anterior roots. (Note however a reversed recruitment order for the roots at the opposite site of the electrode if the electrode is in an extreme lateral position Fig. 6.9). The calculated minimum threshold value of dorsal column fibers in the lumbosacral region is 11.2 V. Clinical observations also suggest that dorsal root fibers have the smallest threshold and dorsal column fibers are stimulated only in exceptional cases when voltages close to 10 V are applied.

The lumbosacral cord levels essentially differ from the corresponding vertebral levels with remarkable individual variability. In caudal direction the spinal cord diameter gradually grows to form the lumbar enlargement, then tapers and terminates between the first and second lumbar vertebral segment. The specific structure of the lumbosacral cord requires a three dimensional model with altering cross-sections which is a different approach compared to the prismatic geometries studied with the finite element technique by Coburn and Sin (1985) and to the finite difference method of Holsheimer and coworkers [Holsheimer and Struijk 1991, Struijk et al. 1993, Holsheimer 1998].

For epidural stimulation the region of spike initiation is not restricted to the fiber entry into the spinal cord. As an example L2 posterior root fiber threshold is 3 V for 210 μ s monophasic pulses when cathode is at the L2 cord segment level. The same fiber can still be stimulated for a cathode positioned 5 cm caudal to the L2 level with 7V, while excitation is not possible when cathode is more than 2.5 cm above.

The level of the electrode with respect to the spinal cord is of high importance for several clinical applications, especially in order to reduce spasms [Pinter et al. 2000] and to activate the spinal cord locomotion pattern generator Dimitrijevic et al. 1998]. Usually the electrode position is defined relative to vertebral segments but in living humans the location of the corresponding spinal cord segments cannot be identified by currently available image techniques. A great variance in spinal cord segment lengths has to be considered when simulated results are interpreted (Table 6.2). Our simulations are based on a geometry as published in Fig. 10A of Rattay et al. (2000) which is in some contradiction with the segment levels derived from Lang and Geisel (1983) data.

TABLE 6.2. MEAN VALUES AND RANGES OF SPINAL CORD SEGMENT LENGTHS IN MM ACCORDING TO DIFFERENT AUTHORS.

	Lang and Geisel 1983 old people	Lang and Geisel 1983 young people	Diem 1980	Luderitz 1881
L1	10.33	13.45 (8-24)	15	13.75-15.9
L2	9.88	12.0 (8.5-21)		10.5-13.75
L3	8.75	11.0 (7-21)		9.5-10.25
L4	7.78		9	7.0-8.5
L5	6.29			5.5-7.8
S1	6.89		8	
S2	6.39			
S3	5.41			
S4	3.88			
S5	2.32			

The gray shaded data are used to construct a relation between vertebra and cord levels.

Relationship between fiber thresholds and muscle twitch responses

Muscle twitch measurements are used as a functional method to get information about the electrode position [Murg et al. 2000]. Note however, that the different muscle groups are innervated by several segments and thus there is no direct relationship between EMG responses and excited cord segments, especially for low positioned electrodes.

Action potentials initiated in the large dorsal root fibers seem to pass directly to the motor neuron of the same segment (monosynaptic pathway). The spinal cord segments are between 2 and 24 mm long. The segment separation causes the excitation order of root fibers mainly because of their different distances to the cathode. According to the segmental arrangement of muscle innervation, and considering the mono-synaptic pathways, the recruitment order of dorsal roots is directly related to the sequence of responses of corresponding muscle groups (Fig. 6.10). In our simulation the excitable neural structures of the spinal cord are reduced to 12 target neurons originating from three levels, representing L2-, L4- and S1-root fibers. Applying interpolation methods according to the scheme of Fig. 6.6 allows to predict the thresholds for rootlets which were not considered in the simulation. This principle was used in the case study of Fig. 6.10 in order to estimate the threshold for triceps surae, innervated by the segments L5, S1 and S2. The S1 target fiber (calculated threshold 48V) will not contribute to any activation. However, the most cranial fibers that supply triceps surae arising from the L4/L5 borderline (see segmental arrangement of innervation in Fig. 6.10) have an essentially lower threshold of about 6V as found by interpolation (gray bar for TS in Fig. 6.10). With the same method the thresholds as predicted by the target fibers (black bars) are corrected according to the gray areas by considering the complete innervation region of a muscle of interest.

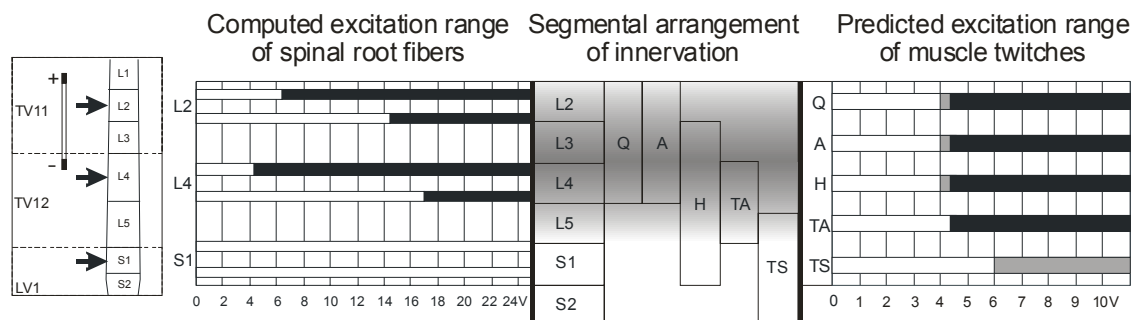


Fig. 6.10. Relationship between computed spinal root fiber thresholds and muscle twitch thresholds. The gray levels in the shaded region indicate the excitability of the 'segmental arrangement of innervation'. The most excitable region for this position of the electrode (same case as Fig. 6.7A) is at the L3/L4 border of the spinal cord. The black bars are computed regions of excitation when innervation is restricted to the standard fibers originating from three levels as indicated by the arrows (left picture). According to the innervation scheme (Table14-1 from Westmoreland 1994; hamstring modified according to clinical observations of Murg et al. 2000) the L4 segment innervates the muscle groups Q, A, H and TA and therefore the black bars indicate the same threshold value of 4.3 V for these muscles. Thresholds for root fibers which were neglected in the simulation are found by interpolation and are used to refine the predicted muscle twitch thresholds by the gray bars. Abbreviations: Q quadriceps, H hamstring, TA tibialis anterior, TS triceps surae.

We have used the same technique to predict muscle twitch thresholds for the four standard levels and both polarities (Fig. 6.11). Of specific interest are those cases where the change of polarity activates an additional muscle group: In Fig. 6.11A right, the cathode (upper contact) stimulates the L2 and L3 cord segments resulting in Q, A and H responses.

Changing polarity to 0+3- activates additionally the L4 and L5 segment, and the muscles TA and TS according to the segmental innervation arrangement, because now the cathode is at the L4 level. Moving the electrode 1cm caudally (case B, right) reduces the cathode distance to L4 for the 0-3+ configuration and thereby allows the activation of TA at 3.5 V; L5 is still beyond the excitation range, there is no TS response. However, the large shift of the cathode position stimulates also TS for the 0+3- polarity. The cathode is able to activate L4 and L5 posterior root fibers for both polarities when the electrode is positioned like in Fig. 6.11C or below; the resulting excitation patterns are similar. All presented calculations are based on activating the outer poles (0, 3) of the electrode. Smaller distances of the poles (e.g. 0-1+) have a better focus effect but higher stimulus voltages are needed.

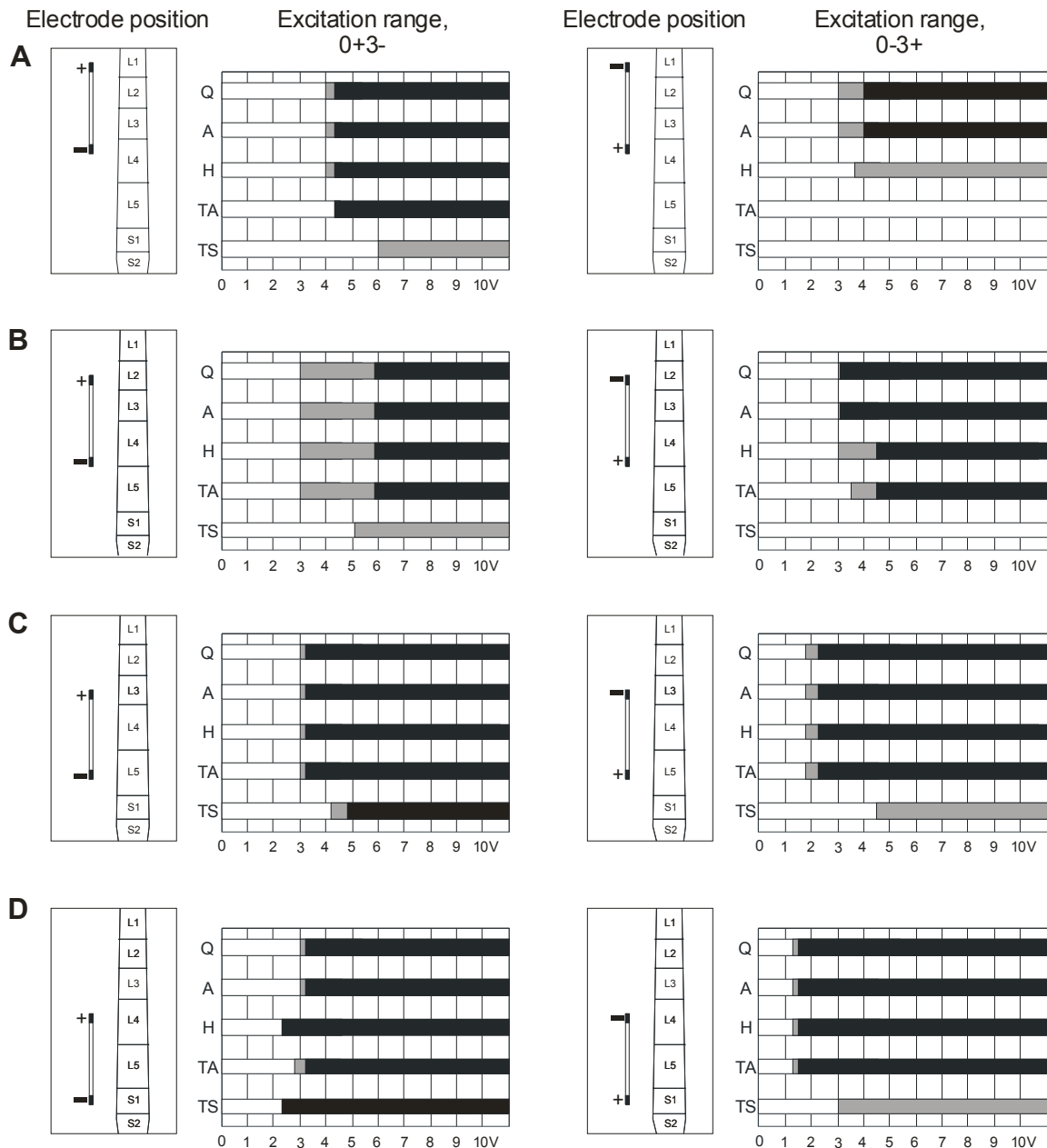


Fig. 6.11. Predicted muscle twitch thresholds for electrode positions of Fig. 6.7, method as in Fig. 6.10.

Comparison of patient muscle twitch data with the predicted muscle activation patterns of Fig. 6.11 informs about individual spinal cord anatomy and helps to determine the position of the electrode relative to cord segments. One example is discussed with the help of

Fig. 6.12 where the muscle twitch responses of one patient recorded with surface-electrode polyelectromyography (pEMG) as reported in Murg et al. 2000 is systematically compared with the four cases A-D of Fig. 6.11. Myograms of different responding muscle regions were systematically recorded while electrode voltage was increased in 1 Volt steps. At first we test if the number of activated muscle groups is reduced when polarity is changed from 0+3- to 0-3+. Such a reduction implies an upper lumbar cord electrode position. Activation of all muscles for 0+3- but missing TA and TS for 0-3+ indicates the correspondence of patients' data with case A. This means the lower contact is positioned at the L4 cord region.

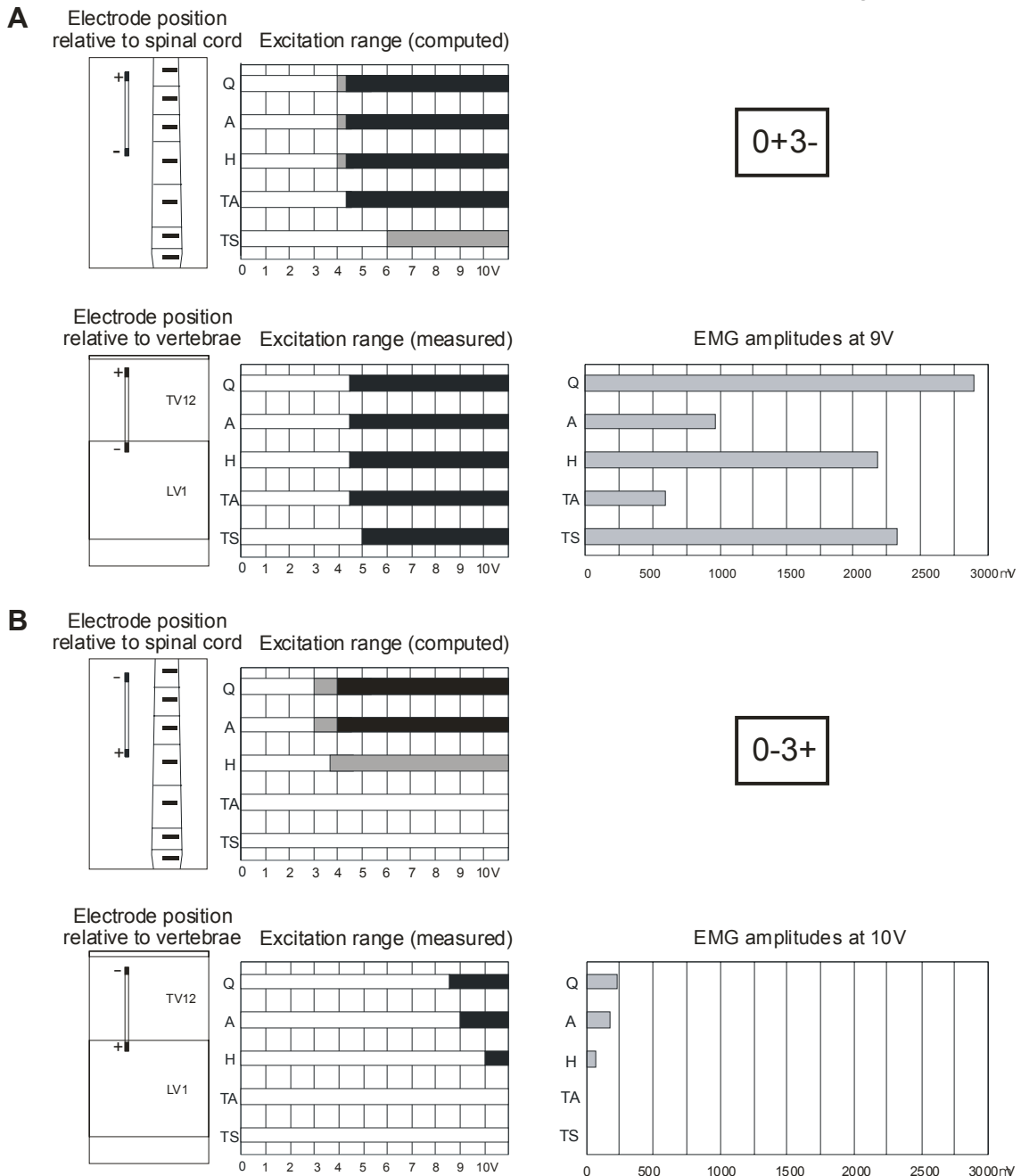


Fig. 6.12. Comparison of computed and measured excitation patterns for a fixed electrode position. Electrode position relative to spinal cord and computed excitation range is same as in Fig. 6.11A. Electrode position relative to vertebrae is according to X-ray picture. White bar lengths are derived from pEMG protocol and correspond to the mean threshold values of the left and right muscle groups of a single patient. EMG amplitudes are mean values between left and right side, measured at the maximum voltage of 10 V or below if the stimulation was uncomfortable.

Considering additional information about the spinal cord termination level (MRI) and deviation from mean segment positions we assume the number 3 contact to be at the lower part of L4. Note the high thresholds (small EMG amplitudes) for 0-3+ which may be caused by a not optimally positioned upper contact (relative large resistance due to tissue placed between electrode and dura). Smaller resistance to the well conducting cerebrospinal fluid would shift the thresholds of all muscle groups to smaller values, TA response could be below 10 V and the position of the electrode relative to the L4 cord segment of this patient between the cases A and B of Fig. 6.11 is also reasonable.

Factors limiting the accuracy of the simulations

A well defined geometry of the volume conductor model is essential for the quality of the computations. Simplified finite element geometry was modeled to represent the complex anatomical compartments. While the spinal canal is treated in detail in the simulation, only a coarse model of vertebral column and its surrounding layer is necessary for simulating the excitation of the neural structures with epidural electrodes [Holsheimer 1998]. The small root filaments, immersed in the well-conducting cerebrospinal fluid, were not modeled as separate compartments in the volume conductor model. This model is valid under the assumption that the potential distribution in the cerebrospinal fluid surrounding the rootlets is not affected by the presence of these filaments. Note however that the lower part of the lumbar cord is surrounded by roots and the cord becomes completely covered by the roots below the twelfth thoracic vertebra [Wall et al. 1990] (see also the cross sections at the left part of Fig. 10 in Rattay et al. 2000). Therefore, a refined model including the insulating property of the roots is assumed to show increase of threshold values for ventral roots and dorsal columns when the electrode is moved to the conus medullaris.

Most tissue conductivities are not exactly known. It is important to estimate the sensitivity of solutions to variations in tissue conductivity in normally accepted ranges. In another spinal cord study (unpublished results mentioned in Holsheimer 1998) these conductivities were increased and reduced by a factor of 2, which is beyond the expected range. The worst case was a change in threshold stimulus of 19% for dorsal column fibers and 27% for dorsal root fibers.

In some clinical cases rather small threshold values were observed as muscle twitches in almost all of the lower limb muscles. These values are lower compared to our calculated data (Fig. 6.11). An explanation is the small distance between electrode and roots by a local narrowing of the cerebrospinal fluid compartment, caused by the electrode pressing against the dura mater. In general we assume geometrical factors (e.g. size of compartments, position of the spinal cord segments relative to the vertebral levels, the trajectories of the roots) to have more influence on the observed range of threshold values than individual differences in the conductances.

Conclusions

Computer simulations demonstrate that thick dorsal root fibers are the most excitable structures for lumbar spinal cord stimulation with posterior epidural electrodes. The recruitment order of lower limb muscles essentially depends on the level of the cathode: For cathode positions at L4 cord level and below all observed muscles (Q, A, H, TA, TS) are expected to respond within a range of about 3-6 V (Fig. 6.11). Changing the polarity has small influence on the pattern of muscle activation for sacral and low lumbar electrode positions, i.e. both poles are below L3 cord level. When the complete electrode is moved superior to L5, change of polarity (a 2.7 cm shift of cathode center in the simulated cases) causes systematical loss of muscle group responses in a characteristic way. This phenomenon

can be used to identify the electrode position relative to the spinal cord segment for levels L2-L5: as shown in Fig. 6.11B loss of the TS response (change from 0+3- to 0-3+) indicates that the lower contact is located close to the L4/L5 border. In an analogous way, additional loss of TA response is a characteristic hint for a 1 cm higher electrode position, i.e. close to the border region L3/L4 (Fig. 6.11A). When the lower contact is at upper L2 cord level 0+3- will activate Q, A and possibly H whereas at changed polarity no muscle groups will be recruited. This method for segment localization works with monophasic pulses and – as in our clinical applications – with biphasic stimuli when a long second phase with small amplitude is used for charge compensation. This method is not suited for biphasic signals with phases of the same duration and amplitude (comp. Fig. 6.8).

Already a rather simple three neuron model (a stimulated afferent axon with a monosynaptic contact to a motoneuron that is influenced from an interneuron by presynaptic inhibition, Fig. 6.13) is able to mimic a stimulus frequency dependent network output as observed in the EMG recordings (Fig. 6.1C, right pictures). For details see [Jilge et al. 2004]. Comparison of the lowest pictures in Fig. 6.1C shows a longer delay for the polysynaptic response and also a change in the EMG shape. Similar to the observed temporal characteristics (lowest pictures in Fig. 6.1C), the model network output switches to the polysynaptic response at higher frequencies as a result of input accumulation at the interneuron which answers with presynaptic inhibition at the sensory-motoneuron contact.

We could show that the changes in the EMG shape occur gradually during stimulation with constant parameters, e.g., in the extension phase of the leg. Every single EMG pattern $f(t)$ within the train of patterns can be approximated by a weighted sum of two temporal components $g(t)$ and $h(t)$: $f = a.g + b.h$, where a and b are slowly changing variables [Jilge et al. 2004a].

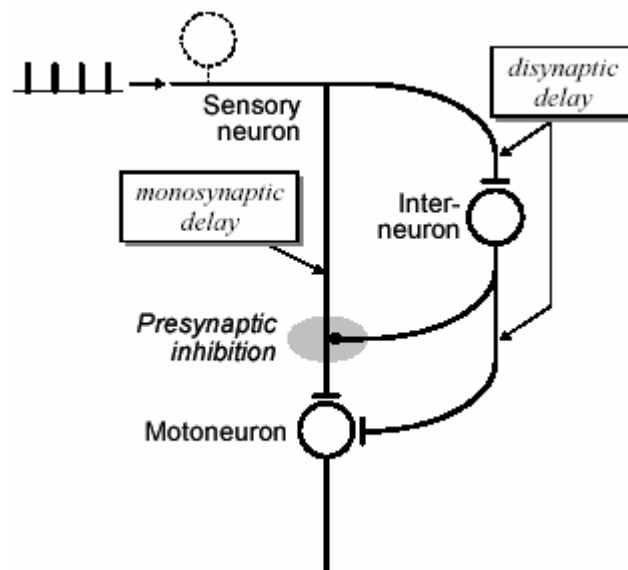


Fig. 6.13. Model network to simulate the neurophysiologically observed transition from short- (monosynaptic) to long-latency (disynaptic) responses to a sustained train of stimuli. An interneuron exerts inhibitory influence on afferent terminals on a motoneuron. Depending on specific parameters of the model neurons and the frequency of the sensory volley, the network output is either solely mono- or disynaptic or includes both components.

In general, the complex interneuronal network of the spinal cord is not easy to simulate. However, in epiretinal stimulation of the human lumbar spinal cord we found rather simple relations between the network input, that is, spike initiation in the afferent axons are sharply synchronized to a train of cathodic pulses, and the output. This motoneuronal output, which

is indirectly recorded as EMG, switches from monosynaptically generated muscle twitches at low frequencies to well defined complex patterns for the extension or for rhythmic stepping like movements of the lower limbs for 5-15 Hz and 25-50 Hz stimulation, respectively [Dimitrijevic et al. 1998, Minassian et al. 2004]. In all these cases the motoneuronal firing is always synchronized with the stimuli.

References

- Abbas PJ, Brown CJ, Shallop JK, Firszt JB, Hughes ML, Hong SH and Staller SJ (1999) Summary of results using the nucleus CI24M implant to record the electrically evoked compound action potential. *Ear Hear.* 20, 45-59
- Altman KW and Plonsey R (1990) Point source nerve bundle stimulation: effects of fiber diameter and depth on simulated excitation, *IEEE Trans. Biomed. Eng.* 37, 688-698
- Amstrong DM, Harvey RJ and Schild RF (1973) The spatial organization of climbing fibre branching in the cat cerebellum. *Exp. Brain Res.* 18, 40-58
- Baker MD (2000) Axonal flip-flops and oscillators, *Trends Neurosciences* 23, 514-519
- Barolat G (1998) Spinal cord stimulation for persistent pain management. In: Goldenberg PL, Tasker RR (eds) *Textbook for Stereotactic and Functional Neurosurgery*. McGraw-Hill, New York, pp. 1519-1537
- Barolat G, Myklebust JB and Wenninger W (1988) Effects of spinal cord stimulation on spasticity and spasms secondary to myelopathy. *Appl Neurophysiol.* 51, 29-44
- Basser PJ, Wijesinghe RS and Roth BJ (1992) The activating function for magnetic stimulation derived from a 3-dimensional volume conductor model, *IEEE-Trans. Biomed. Eng.*, 39, 1207-1210
- Békésy G. von (1951) The course pattern of the electrical resistance in the cochlea of guinea pig (electro-anatomy of the cochlea). *J. Acoust. Soc. Am.* 23, 18-28
- Belluzzi O and Sacchi O (1991) A five conductance model of the action potential in the rat sympathetic neurone, *Progr. Biophys. molec. Biol.* 55, 1-30
- BeMent SL and Ranck JB (1969) A quantitative study of electrical stimulation of central myelinated fibers with monopolar electrodes. *Exp. Brain Res.* 24, 147-170
- Black RC, Clark GM and Patrick JF (1981) Current distribution measurements within the human cochlea. *IEEE-Trans. Biomed. Eng. BME-28*, 721-725
- Blair EA and Erlanger J (1933) A comparison of the characteristics of axons through their individual electrical responses, *Am. J. Physiol.* 106, 524-564
- Bower J and Beeman D, (1997) *The book of GENESIS*, 2nd ed., New York: TELOS.
- Brown CJ, Abbas PJ and Gantz B (1990) Electrically evoked whole-nerve action potentials: data from human cochlear implant users. *J Acoust Soc Am.* 88, 1385-1391
- Brown MC (1987) Morphology of labeled afferent fibers in the guinea pig cochlea. *J. Comp. Neurol.* 260, 591-604.
- Brunner C, Graimann B, Huggins JE, Levine SP and Pfurtscheller G (2005) Phase relationships between different subdural electrode recordings in man. *Neurosci Lett.* 28, 375, 69-74.
- Bugbee M, Donaldson NN, Lickel A, Rijkhoff NJ and Taylor J (2001) An implant for chronic selective stimulation of nerves, *Med. Eng. Phys.* 23, 29-36
- Bulling A, Castrop F, Agneskirchner J, Rumitz M, Ovtcharoff W, Wurzinger LJ and Gratzl M (1997). *Body Explorer 2.0*, An interactive program on the cross-sectional anatomy of the Visible Human Male. Springer Verlag Heidelberg
- Burke D, Kiernan MC and Bostock H (2001) Excitability of human axons, *Clin. Neurophysiol.* 112, 1575-1585
- Carras PL, Coleman PA and RF Miller (1992) Site of action potential initiation in amphibian retinal ganglion cells. *J. Neurophysiol.*, 67, 292-304
- Chiu SY, Ritchie JM, Rogart RB and Stagg D (1979) A quantitative description of membrane currents in rabbit myelinated nerve. *J. Physiol.* 292, 149-166.

- Chow AY, Pardue MT, Chow VY, Peyman GA, Liang C, Perlman JI and NS Peachey (2001) Implantation of silicon chip microphotodiode arrays into the cat subretinal space. *IEEE Trans. Neural. Syst. Rehabil. Eng.*, 9, 86-95
- Coburn B (1985). A theoretical study of epidural electrical stimulation of the spinal cord--Part II: Effects on long myelinated fibers. *IEEE Trans Biomed Eng.* 32, 978-986.
- Coburn B and Sin WK (1985) A theoretical study of epidural electrical stimulation of the spinal cord –Part I: Finite element analysis of stimulus fields, *IEEE Trans. Biomed. Eng.* 32, 971-977
- Coburn B and Sin WK (1985). A theoretical study of epidural electrical stimulation of the spinal cord--Part I: Finite element analysis of stimulus fields. *IEEE Trans Biomed Eng.* 32, 971-977
- Coburn B. (1989) Neural modeling in electrical stimulation. *Critical Reviews Biomed. Eng.* 17, 133-178
- Cohen LT, Saunders E, Richardson LM (2004) Spatial spread of neural excitation: comparison of compound action potential and forward-masking data in cochlear implant recipients. *Int J Audiol.* 43, 346-355
- Coleman PA and Miller RF (1989) Measurement of passive membrane parameters with whole-cell recording from neurons in the intact amphibian retina, *J. Neurophysiol.* 61, 218-230
- Colombo J and Parkins CW (1987) A model of electrical excitation of the mammalian auditory-nerve neuron. *Hear. Res.* 31, 287-312
- Cook AW and Weinstein SP (1973) Chronic dorsal column stimulation in multiple sclerosis. Preliminary report. *N Y State J Med.* 73, 2868-2872
- DeFelice LJ (1981) *Introduction to membrane noise*. Plenum Press, New York.
- DeSchutter E and Bower JM (1994) An active membrane model of the cerebellar Purkinje cell: I. Simulation of current clamps in slice, *J. Neurophysiol.* 71, 375-400
- DeSchutter E and Smolen P (1999) Calcium dynamics in large neuronal models, in *Methods in neuronal modeling: from ions to networks*, 2nd ed., Koch, C. and Segev, I., Eds., MIT Press Cambridge MA, pp 211-250
- Destexhe A, Mainen ZF and Sejnowski TJ (1994) Synthesis of models for excitable membranes, synaptic transmission, and neuromodulation using a common kinetic framework, *J. Comput. Neuroscience* 1, 195-230
- Diem MP (1980). Vergleichende Längenmessungen an vorderen Nervenwurzeln bei Neugeborenen und Erwachsenen. Med. Thesis. Zürich
- Dillier N, Lai WK, Almqvist B, Frohne C, Muller-Deile J, Stecker M and von Wallenberg E (2002) Measurement of the electrically evoked compound action potential via a neural response telemetry system. *Ann Otol Rhinol Laryngol.* 111, 407-414.
- Dillier N, Lai WK, Wyttenbach M, Jakits H, Spillman T, Linder T and Frisch U (1997) First experiences with neural response telemetry (NRT). Report ENT Department University Hospital Zürich
- Dimitrijevic MR (1998) Chronic spinal cord stimulation for spasticity. In: Gildenberg PL, Tasker RR (eds) *Textbook for Stereotactic and Functional Neurosurgery*. McGraw-Hill, New York, pp 1267-1273
- Dimitrijevic MR, Gerasimenko Y and Pinter MM (1998) Evidence for a spinal central pattern generator in humans. *Ann. NY Acad. Sci.*, 860, 360-376
- Doslak MJ, Plonsey R and Thomas CW (1980) The effects of variations of the conducting media inhomogeneities on the electroretinogram. *IEEE Trans. Biomed. Eng.* , BME-27, 88-89
- Eckmiller R (1997) Learning retina implants with epiretinal contacts. *Ophthalm. Res.*, 29, 281-289

- Efimov IR, Aguel F, Cheng Y, Wollenzier B and Trayanova N (2000) Virtual electrode polarization in the far field: implications for external defibrillation, *Am. J. Physiol. Heart. Circ. Physiol.* 279, H1055-H1070
- Felix H, Gleeson MJ, Pollak A and Johnsson L-G (1997) The cochlear neurons in humans. In *Progress in human auditory and vestibular histopathology*, Ed. S. Iurato and J.E. Veldman. Kugler Publ. 73-79
- Finley CC, Wilson BS and White MW (1990) Models of Neural Responsiveness to Electrical Stimulation. In: J.M. Miller and F.A. Spelman (Eds.), *Cochlear Implants: Models of the Electrically Stimulated Ear*, Springer, New York, NY, pp 55-96.
- Fitzhugh R (1969) Mathematical models of excitation and propagation in nerve. In: *Biological Engineering* (Ed. H.P. Schwan), McGraw-Hill, New York, pp 1-85.
- Fohlmeister JF and Miller RF (1997a) Impulse encoding mechanisms of ganglion cells in the tiger salamander retina, *J. Neurophysiol.* 78, 1935-1947
- Fohlmeister JF and Miller RF (1997b) Mechanisms by which cell geometry controls repetitive impulse firing in retinal ganglion cells, *J. Neurophysiol.* 78, 1948-1964
- Fohlmeister JF, Coleman PA and Miller RF (1990) Modeling the repetitive firing of retinal ganglion cells, *Brain Res.* 510, 343-345
- Frankenhaeuser B (1960) Sodium permeability in toad nerve and in squid nerve, *J. Physiol.* 152, 159-166
- Frankenhaeuser B and Huxley AL (1964) The action potential in the myelinated nerve fibre of *Xenopus Laevis* as computed on the basis of voltage clamp data, *J. Physiol.* 171, 302-315
- Frankenhaeuser B. and Moore LE (1963) The effect of temperature on the sodium and potassium permeability changes in myelinated nerve fibers of *Xenopus Laevis*, *J. Physiol.* 169, 431-437
- Frijns JHM, de Snoo SL and Schoonhoven R (1995) Potential distributions and neural excitation patterns in a rotationally symmetric model of the electrically stimulated cochlea. *Hear. Res.* 87, 170-186
- Frijns JH, de Snoo SL and Schoonhoven R (2000) Improving the accuracy of the boundary element method by the use of second-order interpolation functions, *IEEE Trans. Biomed. Eng.* 47, 1336-1346
- Frijns JHM, de Snoo SL and ten Kate JH (1996) Spatial selectivity in a rotationally symmetric model of the electrically stimulated cochlea. *Hear. Res.* 95, 33-48
- Garnham CW, Barker AT and Freeston IL (1995) Measurement of the activating function of magnetic stimulation using combined electrical and magnetic stimuli. *J. med. Eng. and Techn.* 19, 57-61
- Geddes LA and Baker LE (1967) The specific resistance of biological material-A compendium of data for the biomedical engineer and physiologist, *Med. Biol. Eng.* 5, 271-293
- Geddes LA and Baker LE (1967). The specific resistance of biological material - a compendium of data for the biomedical engineer and physiologist. *Med. Biol. Eng.* 5, 271-293
- Ghitza O (1994) Auditory models and human performance in tasks related to speech coding and speech recognition. *IEEE Trans. Speech and Audio Proc.* 2, 115-132
- Gleich O and Wilson S (1993) The diameters of guinea pig auditory nerve fibers: distribution and correlation with spontaneous rate. *Hear. Res.* 71, 69-79
- Graham B and Redman S (1994) A simulation of action potentials in synaptic boutons during presynaptic inhibition. *J Neurophysiol* 71, 538-549
- Greenberg RJ, Velte TJ, Humayun MS, Scarlatis GN and Juan E (1999) A computational model of electrical stimulation of the retinal ganglion cell. *IEEE Trans. Biomed. Eng.*, 46, 505-514
- Grumet AE (1994) Extracellular electrical stimulation of retinal ganglion cells. M.S. thesis, MIT, Cambridge, MA <http://www.mit.edu/people/aegrumet/theses/masters/>

- Grumet AE (1999) Electric Stimulation Parameters for an Epi-Retinal Prosthesis. Ph.D. dissertation, MIT, Cambridge, MA
<http://www.mit.edu/people/aegrumet/theses/phd/index.html>
- Grumet AE, Wyatt Jr. JL and Rizzo 3rd. JF (2000) Multi-electrode stimulation and recording in the isolated retina. *J. Neurosci. Methods*, 101, 31-42
- Gybels J and Van Roost D (1991) Spinal cord stimulation for spasticity, in Sindou M, Abbott R, Keravel Y (eds): *Neurosurgery for Spasticity*. Wien. Springer-Verlag, pp 73-81
- Halter JA and Clark JW (1991) A distributed-parameter model of the myelinated nerve fiber, *J. Theor. Biol.* 148, 345-382
- Hartmann R, Topp G and Klinke R (1984) Discharge patterns of cat primary auditory fibers with electrical stimulation of the cochlea, *Hearing Res.* 13, 47-62
- Hause L (1975) A mathematical model for transmembrane potentials secondary to extracellular fields. In: A. Sances Jr. and S.J. Larson Eds. *Electroanaesthesia: Biomedical and Biophysical Studies*. New York. Academic Press.
- Henriquez CS (1993) Simulating the electrical behavior of cardiac tissue using the bidomain model, *Crit. Rev. Biomed. Eng.*, 21, 1-77
- Hines ML and Carnevale NT (2001) NEURON: a tool for neuroscientists, *Neuroscientist*, 7, 123-135
- Hodgkin AL and Huxley AF (1952) A quantitative description of membrane current and its application to conduction and excitation in nerve, *J. Physiol.* 117, 500-544
- Hodgkin AL and Katz B (1949) The effect of temperature on the electrical activity of the giant axon of the squid, *J. Physiol.* 109, 240-249
- Holden AV (1976) *Models of the stochastic activity of neurons*. Springer, Berlin.
- Holsheimer J (1998). Computer modelling of spinal cord stimulation and its contribution to therapeutic efficacy. *Spinal Cord.* 36, 531-540
- Holsheimer J and Struijk JJ (1991). How do geometric factors influence epidural spinal cord stimulation? A quantitative analysis by computer modeling. *Stereotact Funct Neurosurg.* 56, 234-249
- Horáckova M, Nonner W and Stämpfli R (1968) Action potentials and voltage clamp currents of single rat Ranvier nodes, *Pro. Int. Union Physiol. Sci.*, 7, 198
- Horch K and G Dhillon (Eds.) (2004) *Neuroprosthetics: Theory and Practice*. World Scientific Publishing, Singapore
- Horikawa Y (1993) Simulation study on effects of channel noise on differential conduction at an axon branch, *Biophys. J.*, 65, 680-686
- Huguenard JR (1996) Low-threshold calcium currents in central nervous system neurons, *Annu. Rev. Physiol.* 58, 329-348
- Humayun MS, de Juan E, Dagnelie G, Greenberg RJ, Propst R and Phillips DH (1996) Visual perception elicited by electrical stimulation of retina in blind humans, *Arch. Ophthalmol.*, 114, 40-46
- Humayun MS, de Juan Jr. E, Weiland JD, Dagnelie G, Katona S, Greenberg R and Suzuki S (1999) Pattern electrical stimulation of the human retina. *Vis. Res.*, 39, 2569-2576
- Humayun MS, Weiland JD, Fujii GY, Greenberg R, Williamson R, Little J, Mech B, Cimarusti V, Van Boemel G, Dagnelie G and de Juan E (2003) Visual perception in a blind subject with a chronic microelectronic retinal prosthesis. *Vis. Res.*, 43, 2573-2581
- Huxley AF (1959) Ion movements during nerve activity, *Ann. N.Y. Acad. Sci.*, 81, 221-246
- Javel E (1990) Acoustic and electrical encoding of temporal information. In: J.M. Miller and F.A. Spelman (Eds.), *Cochlear Implants: Models of the Electrically Stimulated Ear*, Springer, New York, NY, pp. 247-295
- Javel E and Shepherd RK (2000) Electrical stimulation of the auditory nerve. III. Response initiation sites and temporal fine structure. *Hear. Res.* 140, 45-76

- Jensen RJ, Ziv OR and Rizzo JF (2003) Thresholds for direct and indirect activation of ganglion cells with an epiretinal electrode: Effect of stimulus duration and electrode size. in *ARVO Conf. 2003*. Abstract 5048.
- Jilge B, Minassian K, Rattay F, Dimitrijevic MR (2004a) Frequency-dependent selection of alternative spinal pathways with common periodic sensory input. *Biol. Cybern.* 91, 359-376
- Jilge B, Minassian K, Rattay F, Pinter MM, Gerstenbrand F, Binder H and Dimitrijevic MR (2004b) Initiating extension of the lower limbs in subjects with complete spinal cord injury by epidural lumbar cord stimulation. *Exp. Brain Res.* 154, 308-326
- Johnson CR (1995) Numerical methods for bioelectrical field problems. In: *The biomedical engineering handbook*. Ed. J.D. Bronzino. CRC press, pp 162-180
- Jolly CN, Spelman FA and Clopton BM (1996) Quadrupolar Stimulation for cochlear prostheses: Modeling and experimental data. *IEEE-Trans. Biomed. Eng.* BME-43, 857-865
- Kameyama T, Hashizume Y and Sobue G (1996). Morphologic Features of the Normal Human Cadaveric Spinal Cord. *Spine* 21, 1285-1290
- Katz B and Miledi R (1967) A study of synaptic transmission in the absence of nerve impulses. *J. Physiol.* 192, 407-436
- Knipper M, Bandtlow C, Gestwa L, Köpschall I, Rohbock K, Wiechers B, Zenner HP and Zimmermann U (1998) Thyroid hormone affects Schwann cell and oligodendrocyte gene expression at the glial transition zone of the VIII-th nerve prior to cochlea function. *Development* 125, 3709-3718.
- Knisley SB, Trayanova N and Aguel F (1999) Roles of electric field and fiber structure in cardiac electric stimulation, *Biophys. J.*, 77, 1404-1417
- Kosterich JD, Foster KR and Pollack SR (1983) Dielectric permittivity and electrical conductivity of fluid saturated bone. *IEEE Trans. Biomed. Eng.* 30, 81-86
- Krack P, Batir A, Van Blercom N, Chabardes S, Fraix V, Ardouin C, Koudsie A, Limousin PD, Benazzouz A, LeBas JF, Benabid AL and Pollak P (2003) Five-year follow-up of bilateral stimulation of the subthalamic nucleus in advanced Parkinson's disease. *N Engl J Med.* 49, 1925-1934.
- Kral A, Hartmann R, Mortazavi D and Klinke R (1998) Spatial resolution of cochlear implants: The electrical field and excitation of auditory afferents. *Hear. Res.* 121, 11-28
- Lai WK and Dillier N (2000) A simple two-component model of the electrically evoked compound action potential in the human cochlea. *Audiol. Neuro-Otol.* 5, 333-345
- Lang J and Geisel U (1983). Über den lombsakralen Teil des Durasackes und die Topographie seines Inhalts. *Morphol. Med.* 3, 27-46
- Laube T, Schanze T, Brockmann C, Bolle I, Stieglitz T, and Bornfeld N (2003) Chronically implanted epidural electrodes in Gottinger minipigs allow function tests of epiretinal implants. *Graefes Arch. Clin. Exp. Ophthalmol.*, 241, 1013-1019
- Lieberman MC and Oliver ME (1984) Morphometry of Intracellularly Labeled Neurons of the Auditory Nerve: Correlations With Functional Properties. *J. Comp. Neurol.* 223, 163-176.
- Lindblom U, Tapper DN, Wiesenfeld Z (1977) The effect of dorsal column stimulation on the nociceptive response of dorsal horn cells and its relevance for pain suppression. *Pain* 4, 133-144.
- Lipton SA and Tauck DL (1987) Voltage-dependent conductances of solitary ganglion cells dissociated from rat retina, *J. Physiol.*, 385, 361-391
- Loeb GE, White MW and Jenkins WM (1983) Biophysical considerations in electrical stimulation of the auditory nervous system. In: *Cochlear prostheses*. Ed. C.W. Parkins and S.W. Anderson. *Ann. N.Y. Acad. Sci.* 405, 123-136
- Long DM and Erickson DE (1975) Stimulation of the posterior columns of the spinal cord for relief of intractable pain. *Surg Neurol.* 4, 134-141.
- Lüderitz C (1881). Über das Rückenmarksegment. Ein Beitrag zur Morphologie und Histologie des Rückenmarks. *Arch. Anat. Physiol.* 423-495

- Lukasiewicz P and Werblin (1988) F A slowly inactivating potassium current truncates spike activity in ganglion cells of the tiger salamander retina, *J. Neurosci.*, 8, 4470-4481
- Magee JC (1999) Voltage-gated ion channels in dendrites, in *Dendrites*, Stuart, G. Spruston, N, and Häusser, M. Eds., Oxford University Press, pp 139-160
- Mainen ZF and Sejnowski TJ (1998) Modeling active dendritic processes in pyramidal neurons, in *Methods in neuronal modeling: from ions to networks*, Koch, C. and Segev, I., Eds., 2nd ed., MIT Press Cambridge, MA, pp 171-209
- Margalit E, Maia M, Weiland JD, Greenberg RJ, Fujii GY, Torres G, Piyathaisere DV, O'Hearn TM, Liu W, Lazzi G, Dagnelie G, Scribner DA, de Juan E Jr, Humayun MS (2002) Retinal prosthesis for the blind. *Surv. Ophthalmol.*, 47, 335-356
- Mascagni MV and Sherman A (1999) Numerical methods for neural modeling, in *Methods in neuronal modeling: from ions to networks*, Koch, C. and Segev, I., Eds., 2nd ed., MIT Press Cambridge MA, pp 569-606
- McCormick DA and Huguenard JR (1992) A model of the electrophysiological properties of thalamocortical relay neurons, *J. Neurophysiol.*, 68, 1384-1400
- McNeal DR (1976) Analysis of a model for excitation of myelinated nerve, *IEEE Trans. Biomed. Eng.* BME-23, 329-337
- Miller CA, Abbas PJ, Robinson BK, Rubinstein JT and Matsuoka AJ (1999) Electrically evoked single-fiber action potentials from cat: responses to monopolar, monophasic stimulation. *Hear. Res.* 130, 197-218
- Minassian K (2000). Excitation of lower spinal cord structures with implanted electrodes: 3D finite element analysis and simulation of neural responses. Diploma thesis. Vienna University of Technology
- Minassian K, Jilge B, Rattay F, Pinter MM, Binder H, Gerstenbrand F, Dimitrijevic MR (2004) Stepping-like movements in humans with complete spinal cord injury induced by epidural stimulation of the lumbar cord: Electromyographic study of compound muscle action potentials. *Spinal Cord* 42, 401-416
- Moore BC (2003) Coding of sounds in the auditory system and its relevance to signal processing and coding in cochlear implants. *Otol Neurotol.* 24, 243-254.
- Motz H and Rattay F (1986) A study of the application of the Hodgkin-Huxley and the Frankenhaeuser-Huxley model for electrostimulation of the acoustic nerve, *Neuroscience* 18, 699-712
- Murg M, Binder H and Dimitrijevic MR (2000). Epidural electric stimulation of posterior structures of the human lumbar spinal cord: 1. Muscle twitches - a functional method to define the site of stimulation. *Spinal cord* 38, 394-402
- Nagarajan SS, Durand D and Warman EN (1993) Effects of induced electric fields on finite neuronal structures: a simulation study, *IEEE-Trans. Biomed. Eng.* BME-40, 1175-1188
- Ota CY and Kimura RS (1980) Ultrastructural study of the human spiral ganglion. *Acta Otolaryngol.* 89, 53-62.
- Parkins CW and Colombo J (1987) Auditory-nerve single-neuron thresholds to electrical stimulation from scala tympani electrodes. *Hear. Res.* 31, 267-286.
- Pernkopf E (1960) *Topographische Anatomie des Menschen*. 4. Band, zweite Hälfte: Topographische und stratographische Anatomie des Kopfes. Urban & Schwarzenberg, Berlin, p 599
- Pinter MM, Gerstenbrand F and Dimitrijevic MR (2000) Epidural electrical stimulation of posterior structures of the human lumbosacral cord: 3. Control of spasticity. *Spinal Cord* 38, 524-531
- Plonsey R, Barr RC (1995) Electric field stimulation of excitable tissue, *IEEE Trans. Biomed. Eng.* 42, 329-336
- Porter R. Focal stimulation of hypoglossal neurons in the cat. *J. Physiol.* 1963; 169: 630-640.
- Ranck JB jr. (1975) Which elements are excited in electrical stimulation of mammalian central nervous system: A review, *Brain Res.* 98, 417-440

- Rattay F (1986) Analysis of models for external stimulation of axons, *IEEE-Trans. Biomed. Eng.*, 33, 974-977
- Rattay F (1987) Ways to approximate current-distance relations for electrically stimulated fibers. *J. theor. Biol.* 125, 339-349
- Rattay F (1988) Modeling the excitation of fibers under surface electrodes, *IEEE-Trans. Biomed. Eng.* BME-35, 199-202
- Rattay F (1989) Analysis of models for extracellular fiber stimulation, *IEEE-Trans. Biomed. Eng.*, 36, 676-682
- Rattay F (1990) *Electrical Nerve Stimulation: Theory, Experiments and Applications*, Springer, Wien - New York
- Rattay F (1993) Simulation of artificial neural reactions produced with electric fields, *Simulation Practice and Theory* 1, 137-152
- Rattay F (1995) Propagation and distribution of neural signals: a modeling study of axonal transport, *Physics of the Alive*, 3, 60-66
- Rattay F (1998a) Analysis of the electrical excitation of CNS neurons. *IEEE-Trans. Biomed. Eng.* 45, 766-772.
- Rattay F (1998b) The contribution of a single neuron to the EEG signal - and an attempt to explain the cochleogram. In: F. Rattay (Ed.) *Brain Modelling Proc. TU-BioMed Symposium*, Vienna, 7-10
- Rattay F (1999) The basic mechanism for the electrical stimulation of the nervous system. *Neuroscience*, 89, 335-346
- Rattay F (2000) Basics of hearing theory and noise in cochlea implants. *Chaos, Solitons and Fractals* 11, 1875-1884
- Rattay F and Aberham M (1993) Modeling axon membranes for functional electrical stimulation, *IEEE-Trans. Biomed. Eng.* BME 40, 1201-1209
- Rattay F and Lutter P (1997) Speech sound representation in the auditory nerve: computer simulation studies on inner ear mechanisms. *ZAMM* 12, 935-943
- Rattay F, Greenberg R and Resatz S (2003) Neuron modeling. in *Handbook of Neuroprosthetic Methods*, W. E. Finn and P. G. LoPresti, Eds. Boca Raton, FL: CRC Press pp 39-71
- Rattay F, Leao RN and Felix H (2001b) A model of the electrically excited human cochlear neuron. II. Influence of the three-dimensional cochlear structure on neural excitability, *Hear. Res.* 153, 64-79
- Rattay F, Lutter P and Felix H (2001a) A model of the electrically excited human cochlear neuron. I. Contribution of neural substructures to the generation and propagation of spikes, *Hear. Res.* 153, 43-63
- Rattay F, Minassian K and Dimitrijevic MR (2000) Epidural electrical stimulation of posterior structures of the human lumbosacral cord: 2. quantitative analysis by computer modeling. *Spinal cord* 38, 473-489
- Rattay F, Resatz S, Lutter P, Minassian K, Jilge B and Dimitrijevic MR (2003) Mechanisms of electrical stimulation with neural prostheses. *Neuromodulation*, 6, 42-46
- Reichel M, Mayr W and Rattay F (1999) Computer simulation of field distribution and excitation of denervated muscle fibers caused by surface electrodes, *Artif. Organs* 23, 453-456
- Reilly JP, Freeman VT and Larkin WD (1985) Sensory effects of transient electrical stimulation: Evaluation with a neuroelectrical model. *IEEE Trans. Biomed. Eng.* 32, 1001-1011
- Resatz S (2002) Electrical stimulation of the retinal ganglion cell: A computer simulation. Master's thesis, Vienna Univ. Technol., Vienna, Austria
- Resatz S and Rattay F (2004) A model for the electrically stimulated retina. *Math. Comp. Mod. Dynam. Systems* 10, 93-106

- Rijkhoff NJ, Holsheimer J, Koldewijn EL, Struijk JJ, Van Kerrebroeck PE, Debruyne FM and Wijkstra H (1994) Selective stimulation of sacral nerve roots for bladder control: a study by computer modeling, *IEEE Trans. Biomed. Eng.* **41**, 413-424
- Ritchie JM (1995) Physiology of axons, in *The axon: structure, function and pathophysiology*. Waxman, S.G., Kocsis, J.D., and Stys, P.K., Eds., Oxford University Press, Oxford pp 68-96
- Roth BJ (1994) Mechanisms for electrical stimulation of excitable tissue. *Crit. Rev. Biomed. Eng.* **22**, 253-305
- Rubinstein JT (1995) Threshold fluctuations in an N sodium channel model of the node of Ranvier, *Biophys. J.* **68**, 779-785
- Rubinstein JT, Wilson BS, Finley CC and Abbas PJ (1999) Pseudospontaneous activity: stochastic independence of auditory nerve fibers with electrical stimulation. *Hear Res.* **127**, 108-18
- Sakmann B and Kreuzfeldt OD (1969) Scotopic and mesopic light adaptation in the cat's retina. *Pflügers Arch.* **313**, 168-185
- Schanze T, Wilms M, Eger M, Hesse L and Eckhorn R (2002) Activation zones in cat visual cortex evoked by electrical retina stimulation. *Graefes Arch. Clin. Exp. Ophthalmol.*, **240**, 947-954
- Schiller J, Helmchen F and Sakmann B (1995) Spatial profile of dendritic calcium transients evoked by action potentials in rat neocortical pyramidal neurones, *J. Physiol.* **487**, 583-600
- Schmidt R, Rattay F and Felix H (1998) FE-Modell zum stationären elektrischen Strömungsfeld des Innenohrs mit Cochlear Implantat. 5. FEM-Workshop, Univ. Ulm (German)
- Schwan HP. and Kay CF (1957). The conductivity of living tissues. *Ann. N.Y. Acad. Sci.* **65**, 1007-1013
- Schwarz JR and Eikhof G (1987) Na currents and action potentials in rat myelinated nerve fibres at 20 and 37°C, *Pflügers Arch.* **409**, 569-577
- Schwarz JR, Reid G and Bostock H (1995) Action potentials and membrane currents in the human node of Ranvier. *Eur. J. Physiol.* **430**, 283-292.
- Shealy CN, Mortimer JT, Reswick JB (1967) Electrical inhibition of pain by stimulation of the dorsal columns: preliminary clinical report. *Anesth Analg* **46**, 489-491
- Shepherd RK and Javel E (1997) Electrical stimulation of the auditory nerve. I. Correlation of physiological responses with cochlear status. *Hear. Res.* **108**, 112-144
- Shepherd RK and Javel E (1999) Electrical stimulation of the auditory nerve. II. Response initiation sites and temporal fine structure. *Hear. Res.* **130**, 171-188
- Sigworth, FJ (1980) The variance of sodium current fluctuations at the node of Ranvier, *J. Physiol.* **307**, 97-129
- Sobie EA, Susil RC and Tung L (1997) A generalized activating function for predicting virtual electrodes in cardiac tissue, *Biophys. J.* **73**, 1410-1423
- Spelman FA, Clopton BM, Pflingst BE and Miller JM (1980) Design of cochlear prosthesis: Effects of the flow of current in the implanted ear. *Ann. Otol. Rhinol. Laryngol.* **89**, 8-10
- Spoendlin H (1971) Degeneration behaviour of the cochlear nerve. *Arch. Klin. Exp. Ohren Nasen Kehlkopfheilkd.* **200**, 275-91.
- Stett A, Barth W, Weiss S, Haemmerle H and Zrenner E (2000) Electrical multisite stimulation of the isolated chicken retina. *Vis. Res.*, **40**, 1785-1795
- Strelhoff D (1973) A computer simulation of the generation and distribution of cochlear potentials. *J. Acoust. Soc. Am.* **54** 620-629
- Struijk JJ, Holsheimer J and Boom HB (1993). Excitation of dorsal root fibers in spinal cord stimulation: A theoretical study. *IEEE Trans Biomed Eng.* **40**, 632-639
- Struijk JJ, Holsheimer J, Barolat G, He J and Boom HBK (1993). Paresthesia thresholds in spinal cord stimulation: A comparison of theoretical results with clinical data *IEEE Trans Rehab Eng.* **1**, 101-108

- Stypulkowski PH and Van den Honert C (1984) Physiological properties of the electrically stimulated auditory nerve. I. Compound action potential recordings. *Hear. Res.* 14, 205-223.
- Suesserman MF and Spelman FA (1993) Lumped-parameter model for in vivo cochlear stimulation. *IEEE Trans. Biomed. Eng.* 40, 237-245
- Sweeney JD and Mortimer JT (1986) An asymmetric two electrode cuff for generation of unidirectionally propagated action potentials, *IEEE-Trans. Biomed. Eng.* BME-33 541-549
- Sweeney JD, Ksienski DA and Mortimer JT (1990) A nerve cuff technique for selective excitation of peripheral nerve trunk regions, *IEEE-Trans. Biomed. Eng.* BME-37, 706-715
- Sweeney JD, Mortimer JT and Durand D (1987) Modeling of mammalian myelinated nerve for functional neuromuscular electrostimulation, *IEEE 9-th ann. conf. Eng. Med. Biol. Soc.* Boston. 1577-1578
- Szentágothai-Schimert (1941). Bedeutung des Faserkalibers und der Markscheidendicke im Zentralnervensystem. *Zeitschrift f. Anatomie u. Entwicklungsgeschichte* 111, 201-223
- Teeters J, Jacobs A and Werblin F (1997) How neural interactions form neural responses in the salamander retina. *J. Comput. Neurosci.* 4, 5-27
- Toris CB, Eiesland JL and Miller RF (1995) Morphology of ganglion cells in the neonotous tiger salamander retina, *J. Comp. Neurol.* 352, 535-559
- Tranchina D and Nicholson C (1986) A model for the polarization of neurons by extrinsically applied electric fields. *Biophys. J.* 50, 1139-1156
- Traub RD, Jefferys JG, Miles R, Whittington MA and Toth K (1994) A branching dendritic model of a rodent CA3 pyramidal neurone, *J. Physiol.* 481, 79-95
- Tregoubov M and Birbaumer N (2005) On the building of binary spelling interfaces for augmentative communication. *IEEE Trans Biomed Eng.* 52, 300-305
- Tyler DJ and Durand DM (1994) Intrafascicular electrical stimulation for selectively activating axons, *IEEE Eng. Med. Biol.* 13, 575-583
- Usui S, Ishihara A, Kamiyama Y and Ishii H (1996) Ionic current model of bipolar cells in the lower vertebrate retina. *Vis. Res.*, 36, 4069-4076
- Van den Honert C and Stypulkowski PH (1987a) Single fiber mapping of spatial excitation patterns in the electrically stimulated auditory nerve. *Hear. Res.* 29, 195-206.
- Van den Honert C. and Stypulkowski PH (1987b) Temporal response patterns of single auditory nerve fibers elicited by periodic electrical stimuli. *Hear. Res.* 29, 207-222.
- Velte TJ and Miller RF (1995) Dendritic integration in ganglion cells of the mudpuppy retina, *Visual. Neurosci.* 12, 165-175
- Veltink PH, van Alste JA and Boom HBK (1988) Simulation of intrafascicular and extraneural nerve stimulation, *IEEE-Trans. Biomed. Eng.* BME-35, 69-75
- Veraart C, Grill WM and Mortimer JT (1990) Selective control of muscle activation with a multipolar nerve cuff electrode, *IEEE-Trans. Biomed. Eng.*, 40, 640-653
- Verveen AA and Derksen HE (1968) Fluctuation phenomena in nerve membrane. *Proc. IEEE*, 56, 906-916.
- Wall EJ, Cohen MS, Abitbol JJ and Garfin SR (1990). Organization of intrathecal nerve roots at the level of the conus medullaris. *J Bone Joint Surg [Am]* 72, 1495-1499
- Warman EN, Grill WM and Durand D (1992) Modeling the effects of electric fields on nerve fibers: determination of excitation thresholds, *IEEE Trans. Biomed. Eng.* 39, 1244-1254
- Warren DJ, Normann RA (2002) Visual neuroprostheses in *Handbook of Neuroprosthetic Methods*, W. E. Finn and P. G. LoPresti, Eds., CRC Press, Boca Raton, FL, 261-305
- Wesselink WA, Holsheimer J and Boom HB (1999) A model of the electrical behaviour of myelinated sensory nerve fibres based on human data. *Med Biol Eng Comput* 37, 228-35
- Westmoreland BF, Bennaroch EE, Daube JR, Reagan TJ and Sandok BA (1994). *Medical Neurosciences*. 3rd edn. Little, Brown and Company. Boston
- Wiley JD and Webster JG (1982) Analysis and control of the current distribution under circular dispersive electrodes, *IEEE Trans. Biomed. Eng.* BME-29, 381-385

- Winslow RL and Knapp AG (1991) Dynamic models of the retinal horizontal cell network, *Prog. Biophys. Mol. Biol.* 56, 107-33
- Wolpaw JR and McFarland DJ (2004) Control of a two-dimensional movement signal by a noninvasive brain-computer interface in humans. *Proc Natl Acad Sci USA.* 101, 17849-17854
- Zeng FG (2004) Trends in cochlear implants. *Trends Amplif.* 8, 1-34
- Zhou R, Abbas PJ and Assouline JG (1995) Electrically evoked auditory brainstem response in peripherally myelin-deficient mice. *Hear. Res.* 88, 98-106
- Zierhofer CM (2001) Analysis of a linear model for electrical stimulation of axons - critical remarks on the "activating function concept", *IEEE Trans. Biomed. Eng.*, 48, 173-184
- Zrenner E, Gekeler F, Gabel VP, Graf HG, Graf M, Guenther E, Haemmerle H, Hoefflinger B, Kobuch K, Kohler K, Nisch W, Sachs H, Schlosshauer B, Schubert M, Schwahn H, Stelzle M, Stett A, Troeger B and Weiss S (2001) Subretinal microphotodiode array as replacement for degenerated photoreceptors? *Ophthalmologe*, 98, 357-363